



THE UNIVERSITY OF QUEENSLAND
A U S T R A L I A

**Trajectory Optimisation of a Partially-Reusable
Rocket-Scramjet-Rocket Small Satellite Launch System**

Sholto O. Forbes-Spyratos

B.Eng. (Mechanical and Aerospace) (Hons. I) & B.Sc. (Physics)

A thesis submitted for the degree of Doctor of Philosophy at
The University of Queensland in 2018

School of Mechanical Engineering

Centre for Hypersonics

Abstract

Declaration by author

This thesis is composed of my original work, and contains no material previously published or written by another person except where due reference has been made in the text. I have clearly stated the contribution by others to jointly-authored works that I have included in my thesis.

I have clearly stated the contribution of others to my thesis as a whole, including statistical assistance, survey design, data analysis, significant technical procedures, professional editorial advice, and any other original research work used or reported in my thesis. The content of my thesis is the result of work I have carried out since the commencement of my research higher degree candidature and does not include a substantial part of work that has been submitted to qualify for the award of any other degree or diploma in any university or other tertiary institution. I have clearly stated which parts of my thesis, if any, have been submitted to qualify for another award.

I acknowledge that an electronic copy of my thesis must be lodged with the University Library and, subject to the policy and procedures of The University of Queensland, the thesis be made available for research and study in accordance with the Copyright Act 1968 unless a period of embargo has been approved by the Dean of the Graduate School.

I acknowledge that copyright of all material contained in my thesis resides with the copyright holder(s) of that material. Where appropriate I have obtained copyright permission from the copyright holder to reproduce material in this thesis.

Publications during candidature

Journal papers

Sholto O. Forbes-Spyratos, Michael P. Kearney, Michael K. Smart, and Ingo H. Jahn. “Trajectory Design of a Rocket-Scramjet-Rocket Multi-Stage Launch System”. In: *Journal of Spacecraft and Rockets - Under Consideration* TBD (2018)

Conference papers

S.O. Forbes-Spyratos, M.P. Kearney, M.K. Smart, and I.H. Jahn. “Trajectory design of a rocket-scramjet-rocket multi-stage launch system”. In: *21st AIAA International Space Planes and Hypersonics Technologies Conference, Hypersonics 2017*. Xiamen, China, 2017. ISBN: 9781624104633

Publications included in this thesis

This thesis comprises partly of publications, as allowed by University of Queensland Policy PPL 4.60.07. The papers that have been included have all been published in peer reviewed journals at the time of submission.

make this table more compact

Sholto O. Forbes-Spyratos, Michael P. Kearney, Michael K. Smart, and Ingo H. Jahn. “Trajectory Design of a Rocket-Scramjet-Rocket Multi-Stage Launch System”. In: *Journal of Spacecraft and Rockets - Under Consideration* TBD (2018)

Contributor	Contribution
Sholto O. Forbes-Spyratos	Performed simulations (%)
	Analysis of results (%)
	Wrote and edited paper (%)
Ingo H. Jahn	Analysis of results (%)
Michael P. Kearney	Analysis of results (%)
Michael K. Smart	Analysis of results (%)
	Wrote and edited paper (%)

Contributions by Others to the Thesis

Except for the contributions by others to publications above, there are no contributions by others to this thesis.

Statement of Parts of the Thesis Submitted to Qualify for the Award of Another Degree

None.

Acknowledgements

Keywords

keyword, keyword, keyword, keyword, keyword

Australian and New Zealand Standard Research Classification (ANZSRC)

ANZSRC code: 090107 Hypersonic Propulsion and Hypersonic Aerodynamics, 20%

ANZSRC code: 090106 Flight Dynamics, 20%

ANZSRC code: 090108, Satellite, Space Vehicle and Missile Design and Testing, 20%

ANZSRC code: 090104 Aircraft Performance and Flight Control Systems , 20%

ANZSRC code: 010303 Optimisation , 20%

Fields of Research (FoR) Classification

FoR code: 0901, Aerospace Engineering, 100%

CONTENTS

List of figures	xvii
List of tables	xix
1 Introduction	1
1.1 Research aims	3
1.2 Thesis Outline and Contributions	5
2 Literature review	7
2.1 Scramjets	7
2.2 Reusable Rocket-Powered Satellite Launch Systems	9
2.3 Small Satellite Launchers	10
2.4 Airbreathing Access-to-Space Systems	14
2.4.1 Small Airbreathing Launchers	15
2.5 Airbreathing Launch Vehicle Ascent Trajectories	16
2.5.1 Single-Stage Vehicles	18
2.5.2 Multi-Stage Vehicles	18
2.6 Hypersonic Vehicle Fly-Back Trajectories	20
2.7 The University of Queensland's Rocket-Scramjet-Rocket Launch System	22
2.7.1 Scramjet Engine Model	23
2.7.2 The Trajectory of the SPARTAN	24
2.7.3 The Third Stage Rocket	25
2.7.4 Exoatmospheric Rocket Engines	25
2.8 Optimal Control	29
2.8.1 Shooting Methods	30

CONTENTS

2.8.2	Collocation Methods	31
2.9	Available Optimal Control Solvers	34
2.10	Aerodynamic Analysis	35
2.10.1	CART3D	37
2.10.2	Missile DATCOM	38
3	Launch Vehicle Design and Simulation	41
3.1	Second Stage Scramjet	44
3.1.1	The SPARTAN Accelerator	44
3.1.2	Propulsion	44
3.1.3	The Aerodynamics of the SPARTAN	48
3.2	First Stage Rocket	59
3.2.1	Aerodynamics Including First Stage	60
3.3	Third Stage Rocket - Baseline	61
3.3.1	Heat Shield Sizing	64
3.3.2	Fuel Tank Sizing	67
3.3.3	The Aerodynamics of the Third Stage Rocket	67
4	LODESTAR	71
4.1	Vehicle Simulation	73
4.1.1	6DOF Equations of Motion	73
4.2	Mission Definition	74
4.3	Optimal Control Problem Structure	76
4.3.1	Trajectory Connection Points	78
4.3.2	III. Second Stage Ascent Trajectory	81
4.3.3	IV. Second Stage Return Trajectory	82
4.3.4	V. Third Stage Powered Ascent	83
4.3.5	VI. Third Stage Unpowered Ascent	84
4.3.6	VII. Hohmann Transfer	85
4.4	Optimal Solution Analysis	87
4.5	The Optimisation Process	89
5	Optimised Ascent Trajectory	91
5.1	Constant Dynamic Pressure Trajectory	92
5.2	Optimised Ascent Trajectory	95
5.3	Sensitivity Analysis	103
5.3.1	Dynamic Pressure Sensitivity	104
5.3.2	Drag Sensitivity Analysis	105

5.3.3	ISP	105
5.3.4	mSPARTAN	106
5.3.5	mFuel SPARTAN	106
5.3.6	m3	107
5.3.7	T3	108
5.4	Cd3	109
5.5	Comparison of Design Parameters	109
5.6	Summary	111
6	Optimised Trajectory Including Fly-Back	113
6.1	Combined SPARTAN Ascent-Descent & Third Stage	114
6.2	First Stage Trajectory	115
6.3	Second Stage Trajectory	115
6.4	Third Stage Trajectory	116
6.5	Fly-Back Trajectory	116
6.6	Fly-Back Trajectory Analysis - paper	116
6.6.1	Return Trajectory	117
6.6.2	Design Sensitivity Analysis	118
6.7	dynamic pressure	119
6.8	Isp	119
6.9	Cd	120
6.10	m SPARTAN	121
6.11	m Fuel	121
6.12	m3	122
6.13	T3	122
6.14	Viscous Drag	122
6.15	Comparison of Sensitivities	122
6.16	Sonic Boom Ground Effects	123
6.17	Alternate Launch Locations	123
6.18	Summary	123
7	Conclusions	131
7.1	Recommendations for future work	131
Library		133
A	Propulsion Interpolation Scheme	147
B	GPOPS-2 Example - Brachistochrone Problem	149

CONTENTS

C Initial Guesses	151
D Trajectory results	153
E CART3D Results	155
E.1 Engine-On Plume Check	155
E.2 CART3D Results	155
E.3 verification	155
F title	159
G Trajectory Plot Comparisons	161
G.1 Cases With No Fly-Back	161
G.1.1 Dynamic Pressure Variation	161
G.1.2 Specific Impulse	162
G.1.3 Drag	164
G.1.4 SPARTAN Mass	165
G.1.5 Fuel Mass	167
G.1.6 Third Stage Mass	168
G.1.7 Third Stage Thrust	170
G.1.8 Third Stage Drag	171
G.2 Cases With Fly-Back	171
G.2.1 Dynamic Pressure Variation	171
G.2.2 Specific Impulse	171
G.2.3 Drag	171
G.2.4 SPARTAN Mass	171
G.2.5 Fuel Mass	171
G.2.6 SPARTAN Viscous Drag	171
G.2.7 Third Stage Mass	171
G.2.8 Third Stage Thrust	171

LIST OF FIGURES

1.1	The scramjet-powered second stage of the SPARTAN[7].	3
2.1	A simple schematic of a scramjet engine[46].	8
2.2	Characteristic performance for airbreathing and rocket engines with Mach number[40].	8
2.3	Comparison of Blue Origin and SpaceX partially-reusable launch systems with existing and historic launch systems[69].	10
2.4	The trajectory of the Falcon Heavy[87].	11
2.5	The trajectory of the Ariane featuring Adeline[125].	12
2.6	The airbreathing vehicle flight corridor [113].	14
2.7	The SKYLON spaceplane [129].	15
2.8	An example of an airbreathing ascent trajectory of the Maglifter RBCC/Rocket launch vehicle[81]. This trajectory shows a constant dynamic pressure section during fanramjet mode[81].	17
2.9	18
2.10	Powell	18
2.11	19
2.12	Wilhite	19
2.13	a) Airbreathing b) Airbreathing/Rocket	19
2.14	The trajectory of the launch system developed by Tsuchiya and Mori [128]	19
2.15	20
2.16	The trajectory of the launch system developed by Mehta and Bowles [74].	20
2.17	The optimised maximum range trajectory of a hypersonic vehicle[16].	22
2.18	An early design of the socket-scramjet-rocket launch system incorporating the SPARTAN [53].	23
2.19	The C-RESTM10 propulsion database, specific impulse.	24

LIST OF FIGURES

2.20	The flight trajectory of the SPARTAN	26
2.21	The elevons of the SPARTAN[93].	27
2.22	The third stage rocket of the rocket-scramjet-rocket launch system[93].	27
2.23	A comparison of single shooting and multiple shooting[60].	31
2.24	Examples of h and p collocation methods[60].	32
2.25	Comparison of optimisation techniques[16]. A hypersonic vehicle is optimised for maximum range. The hp-adaptive method can be observed to have produced the most optimal result.	33
2.26	The Skylon spaceplane, simulated using CART3D at Mach 12.189, $\alpha = 7.512^\circ$ [73]. Cell distribution produced by mesh adaptation is shown.	37
2.27	Comparisons of CART3D with experimental data and the FUN3D Navier-Stokes CFD solver. P1, P2 and P3 indicate pressure tap locations. Modified from Sagerman et al.[107].	38
3.1	The launch process of the rocket-scramjet-rocket launch system, presented in simplified form.	42
3.2	The rocket-scramjet-rocket launch system, top view, showing the SPARTAN and first stage.	43
3.3	The rocket-scramjet-rocket launch system, side view, showing the SPARTAN and fuel tanks, along with the third and first stages.	43
3.4	The locations of conditions relevant to C-REST engine simulation.	45
3.5	Flow conditions after the conical shock generated by the vehicle nose cone. Figure a) shows the Mach number, b) shows the pressure ratio, and c) shows the temperature ratio following the conical shock.	46
3.6	Specific impulse of the CRESTM10 engines with input temperature and Mach number. Available data points are indicated.	47
3.7	Operable equivalence ratio of the CRESTM10 engines with input temperature and Mach number. Available data points are indicated.	48
3.8	Viscous drag coefficient across various Mach numbers.	50
3.9	Viscous drag coefficient across various Mach numbers.	51
3.10	SPARTAN model showing control surfaces.	52
3.11	The forces on the SPARTAN during flight.	52
3.12	Centre of gravity positions throughout the flight of the SPARTAN.	54
3.13	Flap deflection required for trim of the SPARTAN. Negative up.	55
3.14	Process for generating aerodynamic databases.	56
3.15	Surface triangulation of the Baseline SPARTAN, generated using Pointwise[CITEXX].	57
3.16	View of the SPARTAN surface triangulation showing engine outlet boundaries.	57

3.17	The total thrust output of the SPARTAN, including the C-REST database, and Cart3D nozzle and boat tail simulations.	58
3.18	The specific impulse of the SPARTAN, including the C-rest database, and Cart3D nozzle and boat tail simulations.	59
3.19	Engine-on CART3D simulation at Mach 6, 2° angle of attack, and 25km altitude.	60
3.20	Aerodynamic coefficients with the C-REST engines powered on. Coefficients correspond to a reference area of 62.77m ²	61
3.21	Side view of the CART3D flow result for the SPARTAN, at Mach 6, 2° angle of attack.	62
3.22	Top view of the CART3D flow result for the SPARTAN, at Mach 6, 2° angle of attack.	62
3.23	Aerodynamic Characteristics of the SPARTAN with C-REST engine powered off. Coefficients correspond to a reference area of 62.77m ²	63
3.24	Unstarted scramjet engines at mach 3, 2° angle of attack.	64
3.25	Thrust vectoring moment balancing of the first stage.	64
3.26	CART3D result for the SPARTAN and first stage vehicles at Mach 2, -1° angle of attack.	65
3.27	Aerodynamic characteristics of the SPARTAN including the first stage rocket.	65
3.28	The third stage rocket, showing major internal features.	66
3.29	Variation in coefficient of thrust with area ratio [122].	66
3.30	Aerodynamic characteristics of the baseline third stage rocket, for a reference area of 0.95m ²	68
3.31	Thrust vector moment balancing of the third stage.	69
4.1	The optimisation process.	72
4.2	The Earth-fixed components of the geodetic rotational coordinate system.	74
4.3	The vehicle-based components of the coordinate system.	75
4.4	Sun synchronous orbit illustration, passing over the equator at the same time each day[111].	75
4.5	Approximate location of the ELA launch site. Image from Google maps.	76
4.6	Illustration of the segmented launch profile.	78
4.7	The Hohmann transfer manoeuvre.	86
4.8	The process of the rocket-scramjet-rocket trajectory optimisation. Relevant sections are indicated in square brackets at each process step.	90
5.1	Maximum payload-to-orbit trajectory path with the SPARTAN flying at constant dynamic pressure.	93
5.2	The first stage trajectory of the launch system, with the SPARTAN constrained to flight at constant dynamic pressure.	95
5.3	The constant dynamic pressure flight path of the SPARTAN.	96

LIST OF FIGURES

5.4	The third stage trajectory of the launch system, with the SPARTAN constrained to flight at constant dynamic pressure.	97
5.5	98
5.6	99
5.7	101
5.8	Net Isp contours for the SPARTAN at Mach numbers from 5-9, showing optimised trajectory and constant dynamic pressure trajectory.	102
5.9	102
5.10	103
5.11	111
6.1	115
6.2	116
6.3	125
6.4	126
6.5	127
6.6	128
6.7	129
6.8	129
6.9	130
A.1	147
B.1	The solution to the brachistochrone problem, solved in GPOPS-2[CITATIONXX]. . .	150
E.1	156
E.2	Mesh generated by CART3D around the SPARTAN and first stage vehicles.	156
E.3	CART3D flow result for the SPARTAN, at Mach 1.1, 6° angle of attack.	156
E.4	CART3D flow result for the SPARTAN, at Mach 3, 6° angle of attack.	157
E.5	157
E.6	158
E.7	158
F.1	159
G.1	161
G.2	162
G.3	163
G.4	163
G.5	164

LIST OF FIGURES

G.6	165
G.7	166
G.8	166
G.9	167
G.10	168
G.11	169
G.12	169
G.13	170
G.14	171
G.15	172
G.16	172
G.17	173
G.18	173
G.19	174
G.20	174
G.21	175
G.22	175
G.23	176
G.24	176
G.25	177
G.26	177
G.27	178
G.28	178
G.29	179
G.30	179

LIST OF TABLES

2.1	Summary of small satellite launchers, operational and in development	13
2.2	Comparison of upper stage rocket engines, sourced from the Encyclopedia Astronautica reference website[133].	28
2.3	Summary of programs capable of pseudospectral optimisation.	35
3.1	Mass breakdown of the modified SPARTAN vehicle.	44
3.2	First Stage Engine Properties [CITATIONXX].	60
3.3	Third stage heat shield breakdown.	67
3.4	Third stage fuel distribution.	67
4.1	Segment coupling conditions for combined trajectory optimisation.	79
4.2	Optimisation setup of the first stage phase.	81
4.3	Optimisation setup of the second stage ascent. * This is only used in the constant dynamic pressure simulation.	83
4.4	Optimisation setup of the second stage return.	84
4.5	Optimisation setup of the third stage powered ascent.	85
5.1	94
5.2	Summary of key results from the maximum payload-to-orbit trajectory.	100
5.3	104
5.4	105

CHAPTER 1

INTRODUCTION

In recent years, the space sector has seen a significant shift in the paradigm of space launch system design. The sector has moved towards privatisation, with new and innovative launch systems competing to offer the most cost-efficient and reliable launches. The sector has also seen a split between those who produce large satellite launchers and those who produce small satellite launchers. For large payload launchers, reusability is a major focus in the design of new launch systems, with the purpose of making a launch system cost efficient over multiple launches[CITEXX]. For small payload launchers, reusability is more complex than for large launchers, as the additional systems necessary for reusability add a larger fraction of system mass, and require a proportionally larger fuel mass. Consequently, the focus of small launch system design is currently on producing expendable launch systems as cheaply and efficiently as possible, using state of the art technologies such as 3D printing to expedite the process and minimise cost[80]. However, if reusability is able to be successfully integrated into small launch system design, it has the potential to increase the cost efficiency and launch flexibility, potentially opening up the small satellite market significantly.

A potential candidate for integrating reusability into small satellite launch systems is the use of airbreathing engines[62, 116]. Airbreathing engines produce higher specific impulse than rockets, and require far less propellant to be carried on-board a launch vehicle[113]. The higher efficiency and reduced propellant mass of airbreathing vehicles allows the additional mass of the systems necessary for reusability to be mitigated[24]. An airbreathing vehicle can be designed in a similar fashion to a conventional aircraft, with wings, stabilisers and ailerons[110]. A vehicle designed in this fashion has a high lift-to-drag ratio, and good manoeuvrability, allowing for a return flight which uses minimal fuel.

The primary airbreathing engines in consideration for launch vehicles are ramjet and scramjet engines[47]. These engines offer good efficiency and have operational regimes that allow them to effectively accelerate a launch vehicle over a range of Mach numbers. Ramjets and scramjets rely on

CHAPTER 1. INTRODUCTION

the high velocity of the aircraft to compress the flow of air entering the engine before combustion. Ramjets slow the air to subsonic speeds before combustion and are limited to operation at low Mach numbers, whereas scramjets keep the flow supersonic throughout, and operate within the hypersonic regime, above Mach 5. These engines have limited operational regimes, and require atmospheric flight in order to operate. These operational constraints mean that a launch system cannot be solely powered by airbreathing engines. Rocket power is necessary for at least the exoatmospheric portion of the trajectory. As a result, the designs of airbreathing launch systems require rocket stages, usually separated into multiple stages to increase weight efficiency[116]. If a scramjet engine is used as the airbreathing engine of the launch system, rocket power is also desirable for accelerating scramjet accelerator to minimum operational speed, as the alternative is using turbojets and ramjets sequentially[116], which is weight and cost intensive.

Calculating a suitable trajectory for an airbreathing launch system is an integral part of the preliminary vehicle and mission design process. A trajectory must be calculated that allows the launch system to achieve its objectives of placing a payload into orbit, while recovering any reusable stages. Ideally, the calculated trajectory will achieve the maximum possible payload-to-orbit, while adhering to the structural, heating and propulsive limitations of the vehicle. The trajectory design for a partially-airbreathing launch system is complex and requires consideration of each of the individual stages in order to maximise the performance of the launch system, and consequently, its cost efficiency. The airbreathing engines of a ramjet or scramjet-powered stage require high dynamic pressure to operate effectively, and airbreathing stages are generally designed for high lift-to-drag. Conversely, rocket-powered stages produce more thrust at higher altitude, and are generally designed for weight and cost efficiency. For these launch systems, the various stages and engines involved during launch require trade-offs in engine efficiency and thrust generation, stage mass, and vehicle aerodynamics. These factors require the launch trajectory of the system to be thoroughly simulated and optimised, to ensure that the launch vehicle is operating effectively.

Optimal control theory is a general set of techniques which find a control law to maximise a given metric of a system, subject to a set of constraints[10, 97]. Optimal control theory can be used to calculate the optimised trajectory profile for a launch vehicle in a robust and computationally efficient manner, allowing a trajectory to be calculated in which the flight path of each individual stage is considered simultaneously to produce a maximum-payload trajectory[10]. Optimal control is able to produce an optimised trajectory which satisfies the specific structural and flight constraints of the vehicle being simulated, allowing the physical limitations of the vehicle, such as heating and structural loading limits, to be imposed[10]. These constraints also allow any necessary mission conditions to be established, such as reaching orbital velocity and achieving fly-back. An optimal trajectory calculated for multiple launch vehicle stages simultaneously, without predispositions, can offer valuable insights into the performance of a launch vehicle, and drive future design decisions. This concurrent optimisation of multiple stages is particularly important for launch systems incorporating airbreathing

engines, where the performance of each stage is significantly different.

This study applies optimal control theory to a three stage rocket-scramjet-rocket launch system being developed by The University of Queensland. The second stage of this system is a scramjet-powered accelerator, designated The SPARTAN[92]. This launch system is designed to be partially reusable, with at least the second stage scramjet vehicle flying back to the initial launch site, as well as possibly the first stage booster[CITEXX], although this is beyond the scope of this study. In previous studies it has been assumed that by maximising the performance of the SPARTAN, that the performance of the launch system is also maximised[CITEXX]. The trajectory of the launch system has been designed around the SPARTAN flying at its maximum dynamic pressure, and all other trajectory stages have conformed to this assumption. However, these studies did not consider the interaction between stages, or the fly-back of the SPARTAN. This study will develop trajectory planning tools for partially-airbreathing launch systems, and calculate an optimised launch trajectory for the rocket-scramjet-rocket system incorporating the SPARTAN. This optimised trajectory will be calculated with the aim of producing an optimal trajectory profile which may be applied to any multi-stage rocket-airbreathing-rocket system for delivering small satellites to Earth orbit. The impact of the fly-back of the scramjet stage on the optimised trajectory will be studied, and the ability of the rocket-scramjet-rocket system to effectively deliver small payloads to orbit with fly-back will be assessed.



Figure 1.1: The scramjet-powered second stage of the SPARTAN[7].

1.1 Research aims

The aim of this work is to design the trajectory of a rocket-scramjet-rocket small satellite launch system. The purpose of this optimised trajectory is to maximise the payload-to-orbit capabilities of the launch system, thereby also maximising the cost efficiency of the system. The optimal trajectory will be utilised to assess the feasibility of return flight, as well as to determine the impact of key

CHAPTER 1. INTRODUCTION

vehicle design parameters on the performance of the launch system.

These aims will be achieved by addressing the following objectives:

1. *Development of a detailed design and aerodynamic simulation for a rocket-scramjet-rocket launch system.*

A detailed launch system design and robust dynamic simulation are required in order for optimal control to be applied to a launch system. The design must be representative of a standard rocket-scramjet-rocket launch system for the optimal trajectory results to be generally applicable. The dynamic simulation must be high fidelity and robust in order for the optimised trajectory to be meaningful.

2. *Calculation of the maximum payload-to-orbit trajectory for the rocket-scramjet-rocket launch system using optimal control, with and without fly-back.*

The optimal trajectory shape of a multi-stage rocket-scramjet-rocket system is sensitive to the design and aerodynamic characteristics of each stage, and cannot be easily assumed. The use of optimal control techniques allows a maximum-payload trajectory to be calculated with few assumptions as to the general shape of the trajectory. The inclusion of the fly-back of the scramjet stage in the trajectory optimisation allows the impact of the fly-back to be minimised.

3. *Assessment of how key design parameters of the launch system interact with the optimised trajectory.*

The optimal trajectory shape and maximum payload-to-orbit are dependent on the design of the launch system. Assessing the sensitivity of the optimised trajectory shape and payload-to-orbit to key aerodynamic and propulsive properties allows the relative impacts of various design parameters to be calculated and contrasted.

1.2 Thesis Outline and Contributions

Chapter 2 - Literature Review

A review of literature related to the various aspects of this study is presented. The theory behind scramjet propulsion is outlined, followed by a background of reusable and small satellite launch systems. A review of the trajectories of partially-airbreathing launch systems is presented, comparing the optimised trajectories of various conceptual vehicles. An overview of optimal control techniques is presented, with particular emphasis on the pseudospectral method of solving optimal control problems, which is employed within this study. Lastly, an overview of the optimal control and aerodynamic solvers which are used in this study is presented.

Chapter 3 - Launch Vehicle Design and Simulation

The design, aerodynamics and engine models of all three stages are detailed. The SPARTAN scramjet-powered stage is presented first, followed by the first and third stages, due to the external scramjet vehicle design being taken from prior work. The design of each stage is presented, followed by the propulsion model used, and finally the simulated aerodynamic characteristics.

Chapter 4 - LODESTAR

The method used for the simulation and optimisation of the trajectory is detailed, including the creation of the trajectory analysis program, LODESTAR, which has been created for this study. The specifics of the optimal control methodology used are presented, along with relevant examples. The simulation methodology is detailed, along with the construction of the optimal control simulation. The specific set-up of the optimal control program is detailed for each trajectory stage, specifying the costs and constraints which drive the optimal control solver. Finally, the methods for validating the final solutions are specified.

Chapter 5 - Optimised Ascent Trajectory

The ascent of the SPARTAN and third stage rocket are optimised using LODESTAR, for maximum payload-to-orbit. The first stage rocket is optimised to the first-second stage separation point, for minimum fuel usage. The optimal trajectory is analysed. It is found that a pull-up at the end of the scramjet stage trajectory significantly improves payload-to-orbit. The sensitivity of the optimal trajectory to variation of key vehicle design parameters is studied. Optimised trajectories are calculated, and the trends in maximised payload-to-orbit and optimal trajectory shape are analysed to study the relative impact of the design parameters of the SPARTAN.

Chapter 6 - Optimised Trajectory Including Fly-Back

The trajectory of the launch system is optimised for maximum payload-to-orbit, including the fly-back of the SPARTAN to its initial launch location. It is found to be necessary to reignite the scramjet engines during the return flight of the SPARTAN to achieve fly-back. The SPARTAN is found to bank during acceleration to lessen the fuel consumed during the return flight. In a similar fashion to Chapter 5, The effects of key vehicle parameters on the optimised trajectory are studied. The sensitivity of the optimised trajectory and payload-to-orbit are analysed, with emphasis on how the fly-back trajectory is affected by the varied vehicle parameters.

Conclusions

The body of this thesis concludes by summarising the most significant findings from this work. Recommendations for future work are made.

CHAPTER 2

LITERATURE REVIEW

This chapter examines the relevant literature associated with the different aspects of the work conducted as part of this thesis. A brief overview of the theory behind scramjet engines is presented, followed by surveys of the current state of small satellite and reusable launch systems. Next, various conceptual airbreathing launch systems are presented, along with the trajectories and return flights which have been simulated for these systems, with particular emphasis on whether the trajectories were optimised or not. The SPARTAN scramjet-powered accelerator is detailed, followed by a review of the design of the third stage rocket. The theory behind optimal control methods is presented, followed by a survey into currently available optimal control solvers. Lastly, an overview of various aerodynamic modelling methods with emphasis on applicability to preliminary design is detailed.

2.1 Scramjets

A Scramjet, or supersonic combustion ramjet, is an airbreathing engine design which combusts air at supersonic speeds and is capable of high Mach number operation. Across their operating range, scramjets offer much higher specific impulse than rockets, the only other propulsion system capable of operating efficiently at hypersonic speeds[11, 20]. Scramjets compress air without moving parts, using geometry changes within the engine [21], as well as on the forebody of the vehicle to create inlet shocks which provide the compression required for combustion[114]. After combustion, the combustion products are expanded through a thrust nozzle, shown in Figure 2.1. This is similar in operation to a ramjet engine, though a scramjet does not generate a normal shock, allowing supersonic air to enter the combustor. Maintaining supersonic speeds throughout the engine allows scramjets to operate efficiently at Mach numbers of 5 and greater. Scramjets were proposed in the 1940's [22] and found to be capable of positive net thrust in 1993 [85] but have yet to be developed to a level which

would allow for commercial application. Though scramjets are still in-development, the potential advantages which they offer over rockets for certain applications are driving their development in a number of institutions[23].

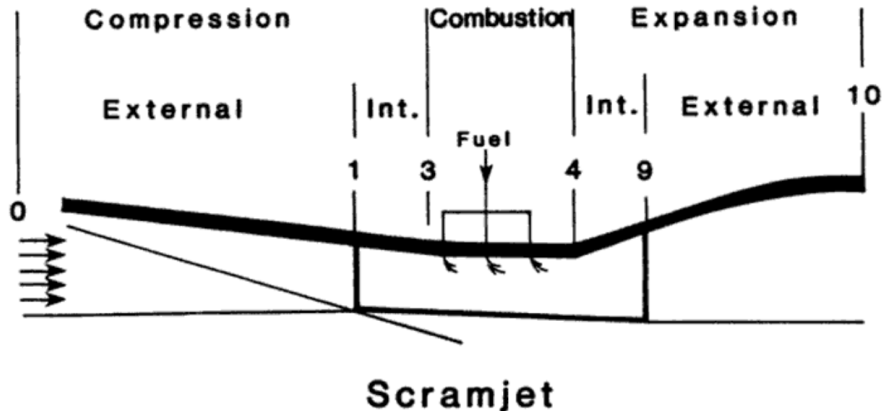


Figure 2.1: A simple schematic of a scramjet engine[46].

Scramjet engines are suitable for a number of applications where sustained flight or acceleration is desired at high Mach numbers. The high efficiency of scramjet engines means that significantly less propellant is used during flight compared to rocket engines, and consequently, that a much smaller fraction of a scramjet-powered vehicle consists of fuel mass[24]. The small fuel mass fraction of a vehicle powered by scramjet engines mitigates the mass of the vehicle systems, allowing features such as wings, control surfaces, landing gear, and passenger transport capabilities to be included in the vehicle design[24].

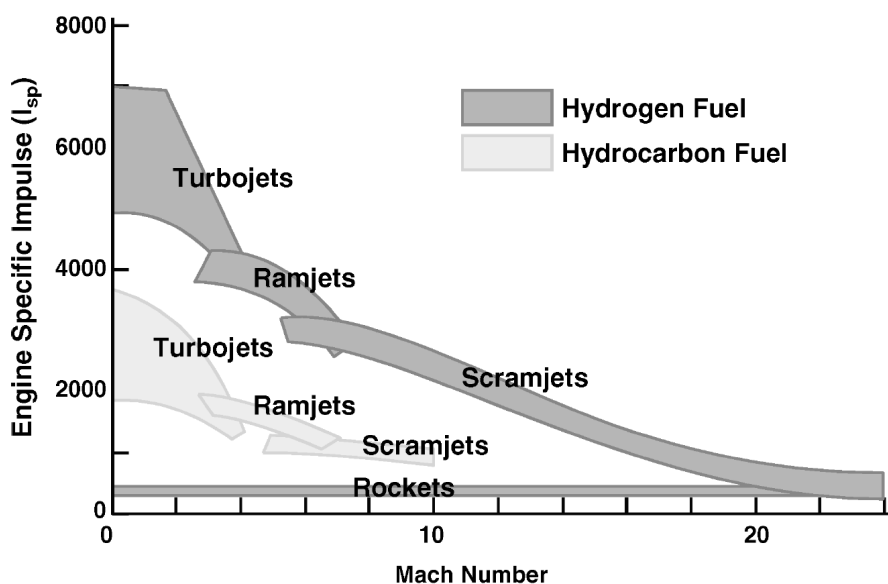


Figure 2.2: Characteristic performance for airbreathing and rocket engines with Mach number[40].

Theoretically, the operable range of scramjets is wide[112]; the specific impulse of a scramjet decreases with velocity, until it is equal to rockets around Mach 19[40], as shown in Figure 2.2. However, in practical designs, the operating range for a scramjet engine is far more limited. For a fixed geometry scramjet, the operable region is constrained by the geometries of the forebody of the vehicle, the inlet, and the combustor of the scramjet engine[113]. The Mach number range of a scramjet engine varies by design, but Mach number ranges of 5-10[90], 7-11[26] and 6-10[14] have been suggested as appropriate operable regimes for scramjet-powered launch vehicles. The operable range of scramjet engines can be improved with mechanisms to vary the geometry of the inlet during flight[25]. However, the systems necessary for variable geometry inlets add weight and complexity to the scramjet engine, and can be detrimental to overall system performance[113].

2.2 Reusable Rocket-Powered Satellite Launch Systems

Launch system technologies have progressed rapidly over the last 60 years. From the early vehicles based on intercontinental ballistic missile technology such as the Thor based launch systems, capable of launching 40-400kg to LEO in the 1960s, to the more modern Atlas V based systems of the 2000s capable of launching 9750-18500kg to LEO[61]. The materials, propulsion technology, aerodynamics and guidance algorithms have all improved significantly, enabling rockets to become more efficient, cheaper to produce, and more reliable. As the demand for satellite launches grows, and the cost of development of launchers becomes cheaper, the potential for profiting from space launches increases. This has driven a large portion of the space flight industry to move towards privatisation, with a heavy focus on reusable technology.

Reusable launch technology has been possible for many years, in the form of the space shuttle. However, the space shuttle was weighed down by large launch costs and operational complexity, and was not a commercial success[68]. Recently, reusable launchers have become the focus of many of the largest private launch companies, as reusability becomes more achievable due to technological advances[39, 75]. The SpaceX Falcon 9 and Falcon Heavy have been demonstrated on multiple occasions, landing booster stages successfully, and re-flying reused boosters multiple times[39]. In the near future the Blue Origin New Glenn is planned[39], with potentially the Airbus Adeline to follow (to be used on the Ariane 6)[3]. The Falcon and New Glenn rockets are shown in Figure 2.3, and the trajectories of the Falcon Heavy and Adeline are shown in Figures 2.4 and 2.5.

The aim of reusing launch vehicles is to reduce the cost-over-time of the reused components drastically, which subsequently allows the cost of individual launches to be reduced[98]. Reducing costs lowers the barrier of entry for space launches, potentially improving the diversity of space-based enterprises. Reusing launch system components also allows faster turnaround times for launches, as refurbishment of stages is much faster than manufacturing stages from scratch. Reduced turnaround times are key for improving mission scheduling, allowing satellites to be launched sooner, on a more

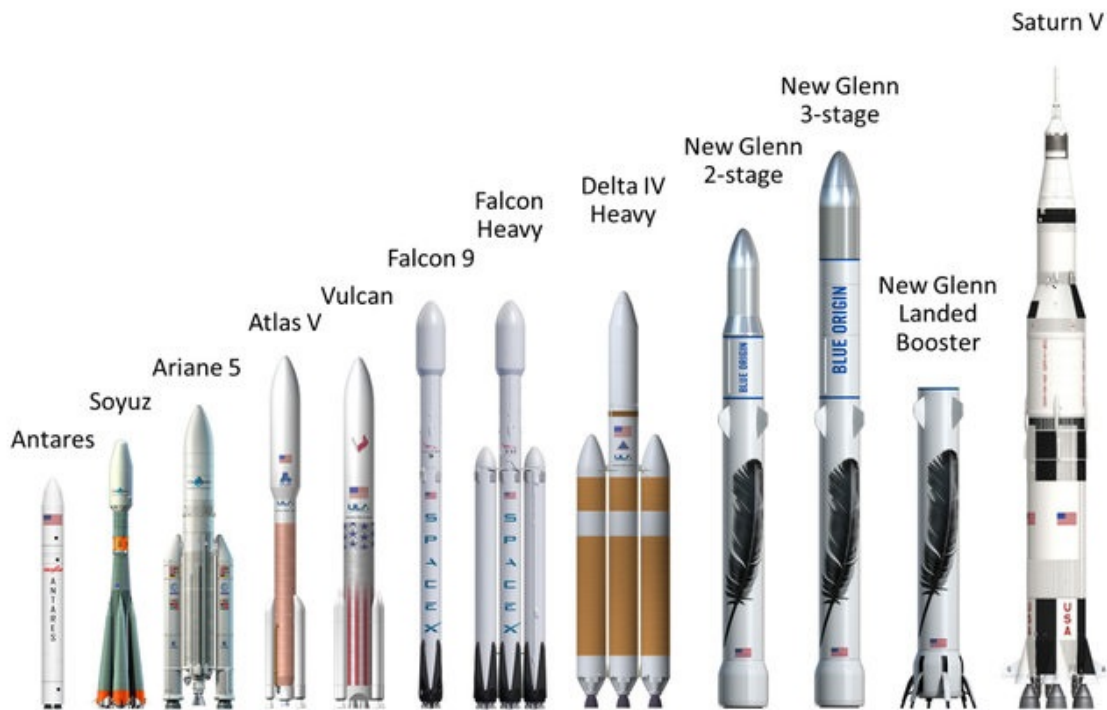


Figure 2.3: Comparison of Blue Origin and SpaceX partially-reusable launch systems with existing and historic launch systems[69].

flexible time frame.

For a launch vehicle to be reusable, it must necessarily have the ability to come back to Earth safely, without damage to major system components. This return flight requires the addition of system components which allow the reusable stage to fly to a specified landing point. Control surfaces[17], structural components[108], additional fuel[108], and in the case of the Adeline, additional engines[3], must be incorporated within a reusable launch vehicle design. The additional weight that these components contribute further increases the fuel and structural mass necessary to initially accelerate the reusable stage. The impact of reusability on the mass and cost of the vehicle is minimised when the velocity at the initiation of the return trajectory is decreased. Because of this mass increase on any stage which is to be designed to be reusable, most current reusable launch vehicle designs include only reusable first stages, with later stages being expendable.

2.3 Small Satellite Launchers

The vast improvements in computational technologies in recent years have allowed satellites to decrease in size and cost to a large degree. These factors have lowered the barrier of entry into small satellite manufacturing significantly, driving a surge in the demand for small satellite launches. Many private and public companies are currently developing small satellite launchers which will allow small

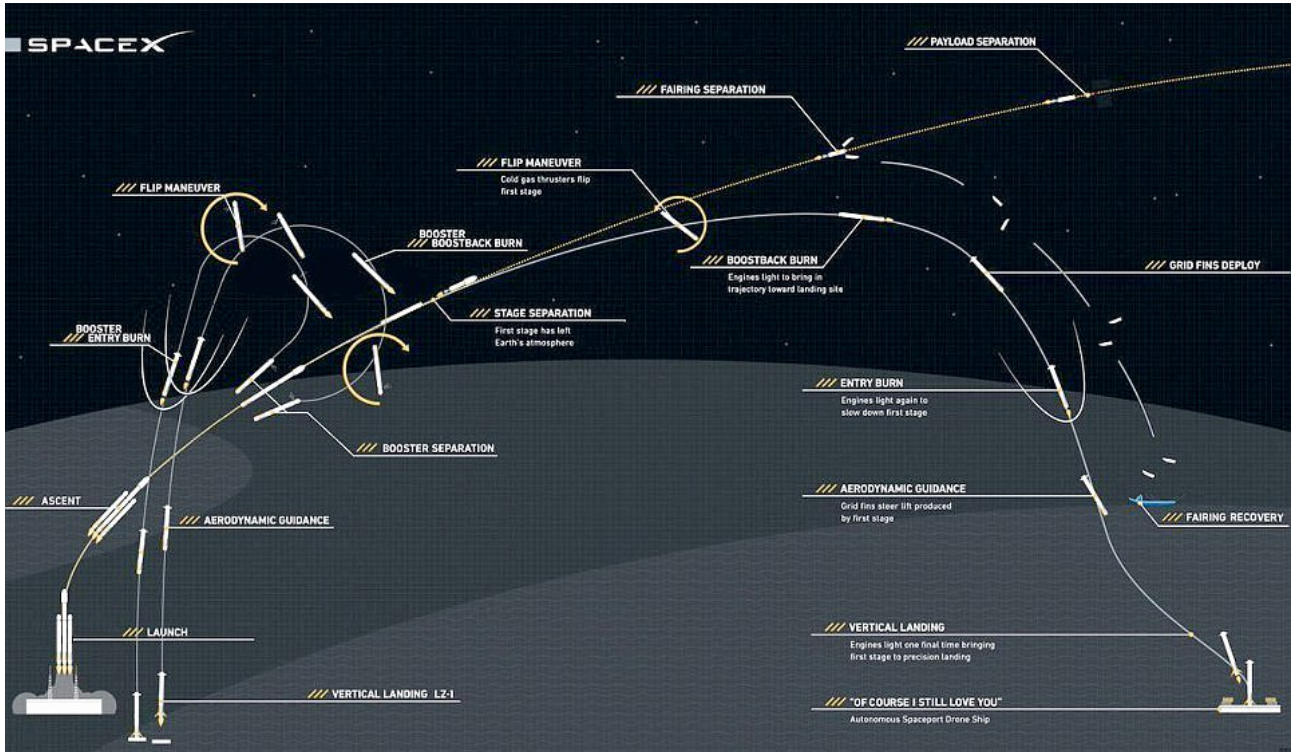


Figure 2.4: The trajectory of the Falcon Heavy[87].

satellites to be launched into bespoke orbits on schedules determined by the customer. A summary of the small satellite launchers currently in active development is shown in Table 2.1. Many of these launchers are projected to be available within the next few years, and will offer cost-per-kg comparable to piggybacking on larger launches.

The majority of the small satellite launchers in development are expendable[80]. These expendable small satellite launch systems aim to reduce costs by creating a launch system which is as cost-efficient as possible to produce and launch[80]. This generally entails making use of conventional, well-tested designs, combined with state of the art manufacturing techniques, such as 3-D printing[42, 80]. This method allows for rapid development, although it has an intrinsic cost limit due to the requirement of manufacturing a new launch system for each launch.

Reusable small satellite launchers have higher initial costs-per-vehicle, but also have the potential for large advantages in the long term[93]. Reusable small satellite launchers have the potential for lower cost-per-launch than expendable systems, with increased launch flexibility[93]. One of the most promising methods of reusability for small launchers is the addition of airbreathing engines[117].

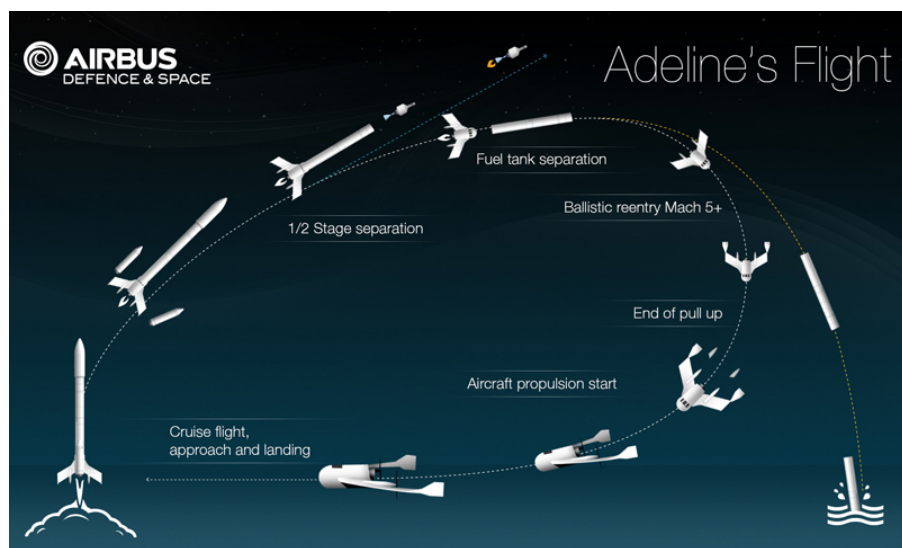


Figure 2.5: The trajectory of the Ariane featuring Adeline[125].

Launcher	Company	Country	Payload Capacity	Cost/Kg (USD)	Availability	Stages & Propulsion	Reusability
Electron [101]	RocketLab	NZ/USA	150Kg to SSO	\$32,600	Available	Rocket-rocket	No
LauncherOne [131]	Virgin Orbit	UK	300kg to SSO	\$33,000	-	Aircraft-rocket-rocket	Aircraft
Bloostar [138]	Zero2Infinity	Spain	100kg to SSO	\$40,000	-	Balloon-rocket-rocket-rocket	No
XS-1 [83]	Boeing	USA	-	-	-	-	First Stage
Eris [42]	Gilmour Space Technologies	Aus/SG	380kg to LEO	\$23,000-38,000	Q4 2020		No
Black Arrow 2 [50]	Horizon	UK	350kg to SSO	-	2019	Rocket-rocket	No
Intrepid-1 [102]	Rocket Crafters	USA	376kg to SSO	\$23,936	Q1 2019	Rocket-rocket	No
KZ-1A [66]	CASIC	China	250kg to SSO	-	-	Rocket-rocket	No
500R [82]	Orbital Access	UK	500kg to SSO	-	-	Aircraft-Rocket	Fully Reusable
Vector-H [130]	Vector Space Systems	USA	160kg to LEO	\$21,875	2018	rocket-rocket-(third rocket optional)	No
SMILE [67]	NLR	EU	50kg	<\$50,000	-	-	-

Table 2.1: Summary of small satellite launchers, operational and in development.

2.4 Airbreathing Access-to-Space Systems

The addition of airbreathing stages to a satellite launch system to allow for partial or full reusability of a launch system has been investigated for a number of years by multiple institutions[14, 44, 74, 88, 93, 100, 127–129, 135, 137]. The reduced fuel usage of airbreathing engines allows for the inclusion of systems which enable fly-back and landing of the stage in a similar manner to a conventional aircraft, potentially offering multi-launch re-use with increased launch flexibility and decreased costs[93]. However, the addition of airbreathing engines to a launch system introduces significant design challenges, and no airbreathing access to space systems have yet been developed.

The technological challenges present for an airbreathing launch system stem from the inherent limitations of jet engines. Turbojets, ramjets and scramjets all operate across different Mach number regimes, and require atmospheric flight to operate[117]. This means that within an airbreathing access-to-space system, a combination of various airbreathing engines and/or rockets must be used during launch. Figure 2.6 shows the operating corridor for an example launch system using turbojet, scramjet, and rocket engines, indicating the point at which engine transition occurs, as well as the lower dynamic pressure limit on engine operation and the upper dynamic pressure limit on the aircraft structure. This operational corridor imposes unique constraints on the design of airbreathing launch systems and their trajectories. An airbreathing access to space system must be capable of resisting high structural and thermal loads, as well as being able to sustain atmospheric flight for long periods, necessitating a high lift-to-drag ratio.

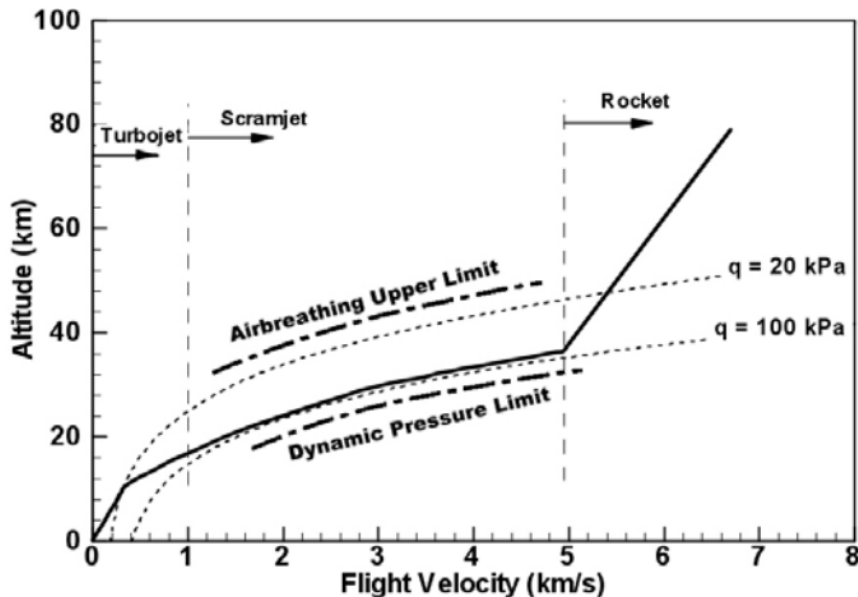


Figure 2.6: The airbreathing vehicle flight corridor [113].

Airbreathing access-to-space systems have been investigated in various forms including; single stage[14, 88, 100, 127, 129, 135, 137], dual stage [44, 74, 128] and tri stage [93] designs. A single

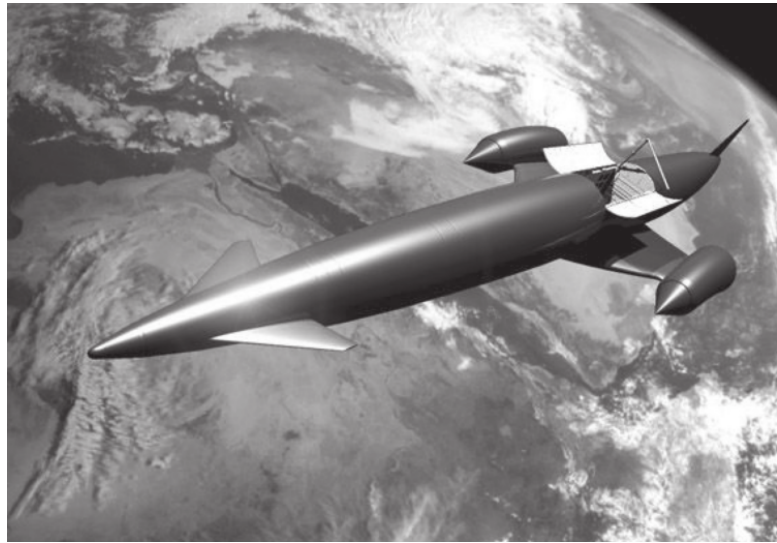


Figure 2.7: The SKYLON spaceplane [129].

stage design has the advantage of being fully contained within one vehicle, which is convenient for reusability and return trajectories however it has been suggested by Smart & Tetlow [117] that these designs suffer from severe limitations as they must contain multiple engines which add mass at later stages of the trajectory and decrease the efficiency of the vehicle. Smart & Tetlow suggest that multistage systems offer significant improvements in payload mass fractions, and have the advantage of using airbreathing stages only within their operable range. Dual stage designs have been investigated in some detail using the 'spaceplane' concept by Mehta & Bowles [74] using life cycle cost analysis in order to take flexibility and reusability into account. Mehta & Bowles conclude that a two stage design is the optimal configuration for reusable hypersonic space access systems, however this study is only based on comparison with single stage to orbit systems, and it is more useful to consider their conclusions as an endorsement of multi stage airbreathing designs in general. They find that multi stage vehicles have higher potential for payload than single stage to orbit (SSTO) systems and have less propellant requirements, partly due to a greater atmospheric cruise capability.

2.4.1 Small Airbreathing Launchers

The use of airbreathing engines has particular applicability to small launch systems. As discussed in section 2.3, incorporating reusability into rocket-powered small satellite launchers is complex, due to the high mass fraction of the systems necessary for re-use at small scales. The use of airbreathing engines may allow a small launch system to incorporate reusable elements without excessive mass penalties. Smart & Tetlow[117] have found that the addition of a scramjet-powered stage may enable the development of a partially reusable small satellite launch system in the near future. Simulations carried out for three stage systems utilising scramjet and rocket engines for small payload delivery show favourable payload mass fractions with a reusable scramjet stage [117]. Scramjet

powered vehicles may also offer the ability to put small payloads into orbit with greatly increased flexibility and launch window when compared to similarly sized rocket systems. This has been assessed in a study by Flaherty[36] comparing the United States Air Force's Reusable Military Launch System all-rocket launch vehicle RMLS102 against the Alliant Techsystems rocket/scramjet launch system ATK-RBCC. These vehicles are similarly sized and comparisons were made for payloads launched to rendezvous with satellites in randomly generated orbits[36]. These vehicles were compared using the range of orbital trajectories that each vehicle was able to rendezvous with within one day, determined by launch vehicle range[36]. The vehicles were compared by their ability to reach a range of trajectories intercept locations in limited time, and the ATK-RBCC vehicle was found to be able to cover at least 1.7 times area of the rocket-powered vehicle[36], in a large part due to the airbreathing vehicle's ability to fly fuel efficiently over long distances. This means in general that a partially scramjet powered accelerator is able to fulfil the specific delivery needs of small payloads over a wider range of orbits within smaller time periods when compared to a fully rocket powered accelerator. This can be advantageous for time critical and orbit dependant payloads which have specific mission requirements to be met.

2.5 Airbreathing Launch Vehicle Ascent Trajectories

The trajectory of an airbreathing launch vehicle is more complex than that of a fully rocket-powered launch system. A airbreathing launch system trajectory must be designed around a number of factors:

- The requirement for the airbreathing stages to fly in-atmosphere
- The variable efficiency of the airbreathing engines
- The relative efficiency of the different types of engines within the system
- The aerodynamic performance of each vehicle or engine-mode of the system
- The structural limitations of the system

A simple way to design the trajectory of an airbreathing launch system is to constrain the flight of the high speed airbreathing section to a constant dynamic pressure[58, 81, 91, 95, 137]. Constant dynamic pressure trajectories can be advantageous for an airbreathing accelerator due to the trade-off between structural loading and engine performance[81]. As dynamic pressure increases so does the structural loading on the vehicle, however the performance of a ramjet or scramjet engine is directly reliant on dynamic pressure[81]. A constant dynamic pressure trajectory is viewed as being an acceptable compromise between these two factors. Figure 2.8 shows an example of a constant dynamic pressure trajectory flown by an airbreathing vehicle.

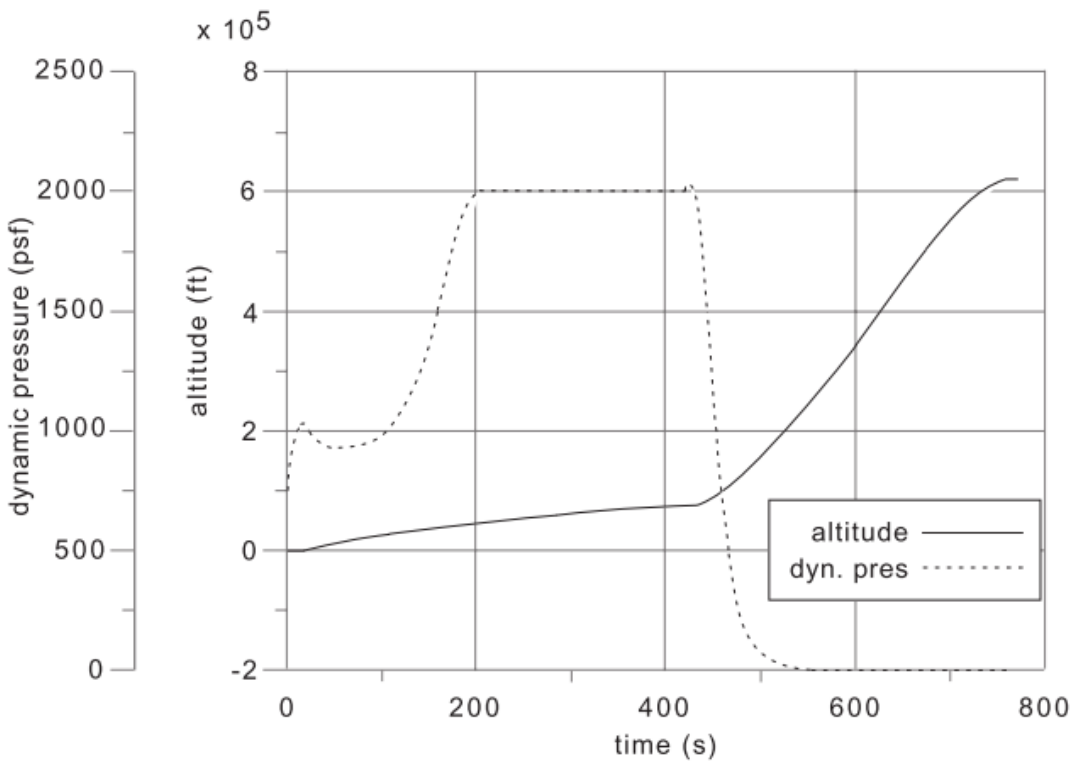


Figure 2.8: An example of an airbreathing ascent trajectory of the Maglifter RBCC/Rocket launch vehicle[81]. This trajectory shows a constant dynamic pressure section during fan-ramjet mode[81].

Although a constant dynamic pressure trajectory is likely to produce high efficiency flight for the high speed airbreathing portion of an ascent trajectory, there are a variety of factors that must be considered in designing the trajectory of a launch system. For example, a constant dynamic pressure flight may produce suboptimal conditions for the switch from airbreathing engines to rocket power for exoatmospheric flight. For a constant dynamic pressure trajectory the transition to rocket power will occur at a very low trajectory angle and altitude[93]. It may be more optimal overall for the vehicle to fly at less than maximum dynamic pressure for a time during airbreathing engine operation, allowing the trajectory angle and altitude to be raised before the rocket engines are powered-on, increasing the efficiency of the rocket engines and reducing the dynamic pressure experienced by the rocket stage[74, 128, 135]. The consideration of all stages and propulsion methods when designing the trajectory of a launch vehicle can produce a more optimal trajectory, which maximises the performance of the launch system, eg. increasing payload-to-orbit, or increasing the range of orbits attainable by the launch vehicle.

2.5.1 Single-Stage Vehicles

Optimal trajectories have previously been developed for launch systems integrating airbreathing and rocket propulsion within single-stage-to-orbit (SSTO) vehicles[14, 71, 86, 88, 100, 127, 137]. These optimal trajectory studies found unanimously that a pull-up manoeuvre before the end of the airbreathing engine cut-off was the optimal flight path for the SSTO airbreathing-rocket vehicles being investigated. A pull-up was found to be optimal for vehicles where the rocket engines are not ignited until circularization altitude [71, 88], vehicles where the rocket engine is ignited immediately after airbreathing engine cut-off [86, 100, 127] as well as for vehicles which operate in combined scramjet-rocket mode[14, 137]. For SSTO vehicles a pull-up manoeuvre is a simple trade-off between the altitude at airbreathing engine cut-off and the velocity achievable at cut-off. Due to the entire vehicle being lifted into orbit, this becomes a relatively simple problem of engine efficiency. The airbreathing engine is used for its high efficiency, until the dynamic pressure drops below the operable limit of the airbreathing engine, or until the thrust provided by the airbreathing engine is significantly counteracted by the effects of drag and gravity.

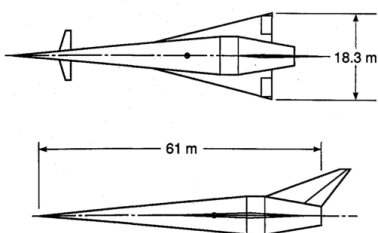


Figure 2.9

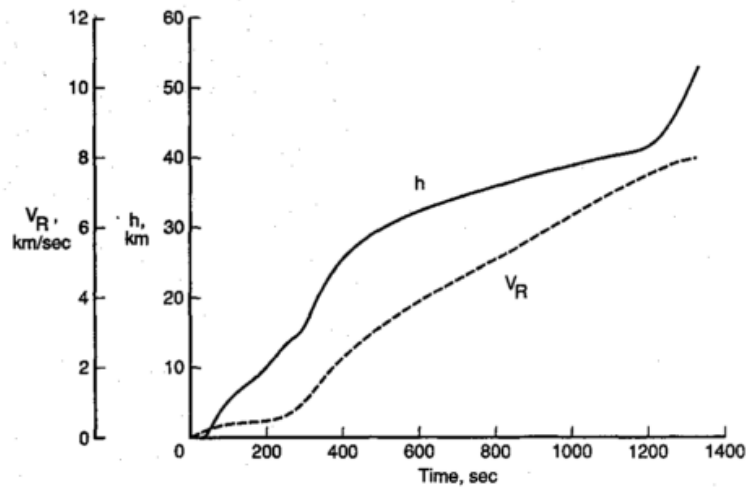


Figure 2.10: Powell

2.5.2 Multi-Stage Vehicles

For a multi-stage to orbit vehicle, calculating the optimal trajectory for maximum payload flight is significantly more difficult. A multi-stage vehicle has one or more stage transition points, where the vehicle separates a component which is discarded or reused later, and does not continue to orbit. At a stage transition point there is a large change in the mass and aerodynamics of the launch system. This change in flight dynamics makes finding the optimal stage transition point more complicated. To find the optimal separation point there is a trade-off between:

- The high efficiency of the scramjet engines

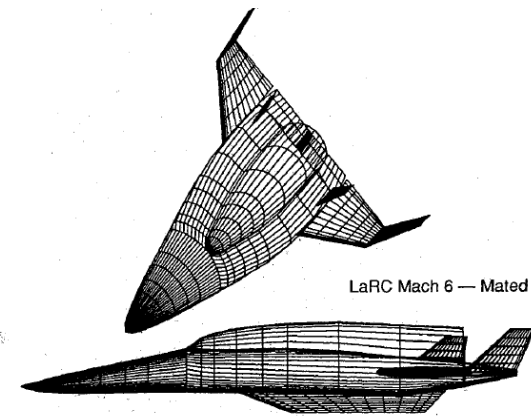


Figure 2.11

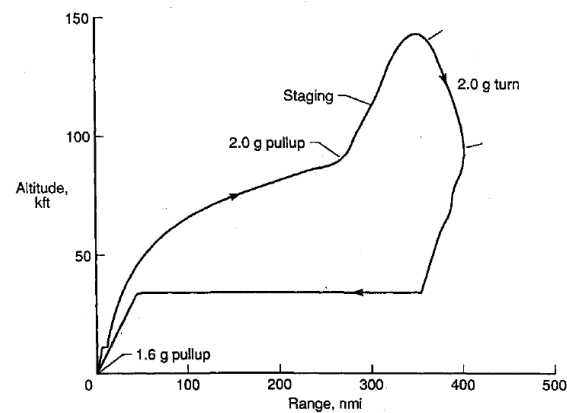


Figure 2.12: Wilhite

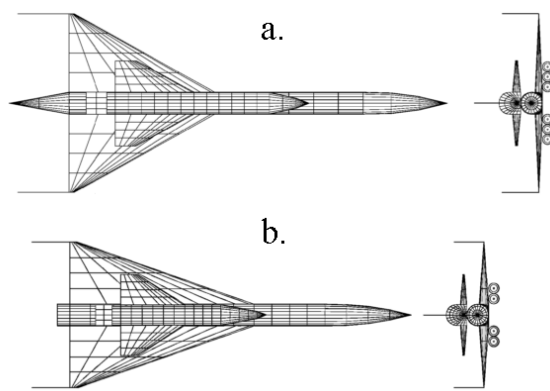


Figure 2.13: a) Airbreathing b) Airbreath-

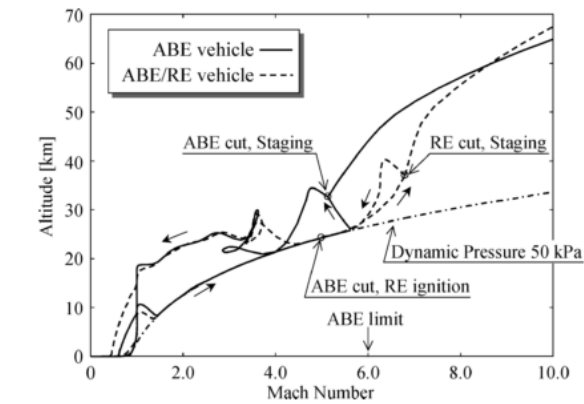


Figure 2.14: The trajectory of the launch system developed by Tsuchiya and Mori [128]

- The thrust produced by the scramjet engines
- The potential thrust of the rocket engines
- The energy necessary to increase the altitude of the scramjet stage
- The aerodynamic efficiency when performing the required direction change

All of these factors must be considered in order to generate an optimal trajectory.

There has been a number of studies which have identified a pull-up manoeuvre as being advantageous for a multi-stage system [74, 128, 135]. However, in these studies a pull-up manoeuvre has been specified in order to decrease the dynamic pressure of the vehicle at airbreathing-rocket stage separation. In the studies by Tsuchiya et al.[128] and Wilhite et al.[135], decreased dynamic pressure is necessary for the successful operation of the orbital rocket stages, of the systems under investigation. In these studies the airbreathing stages pull-up to the maximum allowable dynamic pressure for the rocket-powered orbital stages. When the orbital stages are able to operate, stage separation



Figure 2.15

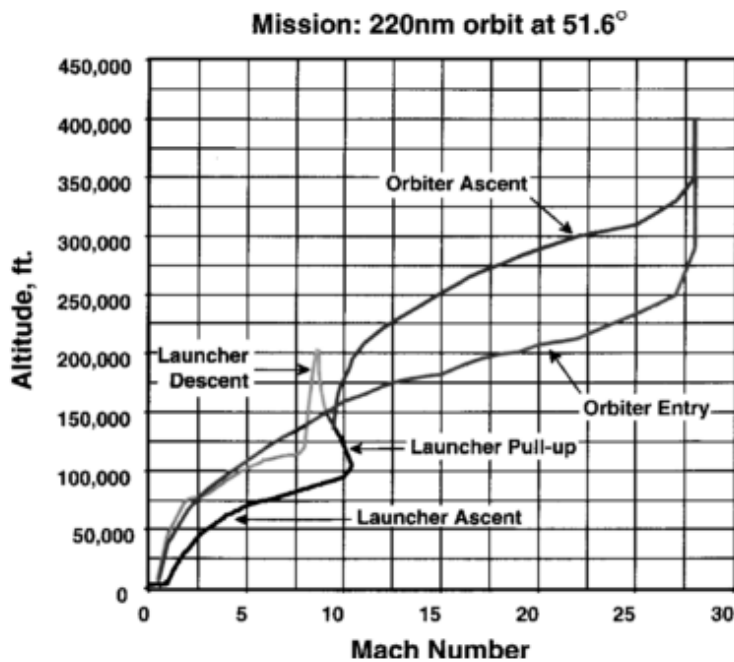


Figure 2.16: The trajectory of the launch system developed by Mehta and Bowles [74].

occurs. These pull-up manoeuvres demonstrate the advantages of a pull-up for the operation of the orbital stages, allowing the aerodynamic and thermal loading on the vehicle to be reduced. However these pull-up manoeuvres are not performed as part of optimal trajectories, instead they are designed to ensure that the performance constraints of the systems are met. Mehta & Bowles [74] prescribe a 2g pull-up at flight conditions of Mach 10, 95000 ft for an airbreathing stage in order to "lower dynamic pressures and to achieve the optimal launching flight path angle for the orbiter vehicle". This indicates that a pull-up manoeuvre before airbreathing-rocket transition is considered the optimal trajectory, however this study does not optimise the shape or magnitude of the pull-up manoeuvre, only considering the increased performance of the rocket vehicle.

2.6 Hypersonic Vehicle Fly-Back Trajectories

The fly-back of an airbreathing launch vehicle is a crucial component of the trajectory. The ability to land a reusable launch vehicle safely in the intended location is a key requirement, and if this fly-back can transport the launch vehicle back to the initial launch location, then transport costs and turnaround times can be significantly reduced.

There are three main methods that have been studied for potential hypersonic vehicle return; glide-back, cruise-back and boost-back. Glide-back involves the hypersonic vehicle returning to base and landing entirely using its aerodynamics. This requires sufficient lift to sustain the hypersonic vehicle

over the entire return range, as well as the controllability to land the hypersonic vehicle in level flight. For a hypersonic trajectory a fully glide-back return flight is most likely unobtainable. This is due to the large downrange distance flown, and the large initial velocity at the beginning of the fly-back trajectory, when the vehicle is oriented away from the landing site. Multiple studies have investigated the maximum staging velocity allowable for the glide-back flight of a booster. In these studies, the maximum separation velocity for glide-back to be feasible has been found to be between Mach 3-4 at 30km-120km downrange distance, with higher initial velocities or longer downrange distances requiring fly-back under power[48, 123].

Cruise-back involves the inclusion of subsonic engines, which are used to power the fly-back of the hypersonic vehicle until landing similar to a conventional aircraft. These engines may be included solely for the fly-back[48], or used in the acceleration phase for low velocity acceleration[74, 123, 135]. The addition of subsonic engines powering a constant velocity cruise-back phase allows the accelerator to return to base with a similar trajectory to that of traditional aircraft, allowing the velocity and altitude of the accelerator to be precisely controlled. However, the addition of subsonic engines necessary for cruise-back increases the mass of the vehicle significantly, leading to decreased mass efficiency and increased design complexity[48].

A preferable mode of powered fly-back is to use the existing hypersonic airbreathing engines during the return trajectory in a boost-back trajectory. Using the existing airbreathing engines allows for range to be added to a return trajectory, without the inclusion of additional engines. The hypersonic airbreathing engines can be operated at appropriate times during the fly-back, when they will be most impactful on the return trajectory range. However, the hypersonic airbreathing engines may only be used within their operating region, and vary in thrust and efficiency dependent on flight conditions. Hypersonic airbreathing engines have maximum efficiency at low Mach numbers[93], with the thrust produced depending on the dynamic pressure and inlet conditions, which vary with the trajectory path and angle of attack of the vehicle. This added complexity requires the use of trajectory optimisation methods to find the most efficient flight path for return to the launch site, and to ensure that the return of the vehicle under its own power is viable.

The possibility of an airbreathing vehicle reigniting high speed airbreathing engines for short periods has been investigated by Tsuchiya and Mori [128]. Tsuchiya and Mori investigate two conceptual launch vehicles; a vehicle powered solely by airbreathing propulsion returning after separation of an orbital stage at Mach 5.1, and an airbreathing/rocket vehicle returning after a separation at Mach 6.8[128]. Both vehicles use the high speed airbreathing engines during return flight. The optimal launch and return trajectories for these vehicles are shown in Figure 2.14. Both vehicles ignite the airbreathing engines at around Mach 3.5 for several tens of seconds to extend the range of the fly-back manoeuvres. After this, the vehicles descend and land at the launch site. These boosters fly to a downrange distance of 600-625km from the launch site, and less than 5% of the vehicles initial propellant was required to return the vehicles to the initial launch sites[128].

If powered fly-back is necessary, the additional fuel weight used during this phase can negatively impact on the potential performance of a launch system. Optimising the fly-back trajectory of the reusable stages of a launch vehicle can decrease the amount of fuel used, and minimise the impact of the return phase. The problem of optimising the fly-back of a launch vehicle for minimum fuel is analogous to maximising the range possible on a small amount of fuel, with manoeuvring. The maximum range trajectory of a hypersonic vehicle operating at high altitudes has been shown to be a 'skipping' trajectory, where the altitude of the vehicle is repeatedly raised and lowered[16, 28, 76, 126]. A skipping trajectory has been shown to be range optimal for hypersonic vehicles able to skip out of the atmosphere [76], as well as vehicles flying entirely within the atmosphere[28, 76, 123, 126]. A skipping trajectory has also been shown to be optimal for an airbreathing hypersonic vehicle thrusting throughout the trajectory[16]. This optimised trajectory is shown in Figure 2.17. The range optimal operation of the scramjet engine is shown to be repeated ignitions at the trough of each skip[16]. The scramjets are ignited as the vehicle climbs after the trough, as the Mach number decreases to the minimum operable conditions of the scramjet engines[16]. Minimising the Mach number during operation in this way maximises the efficiency of the scramjet engines[16].

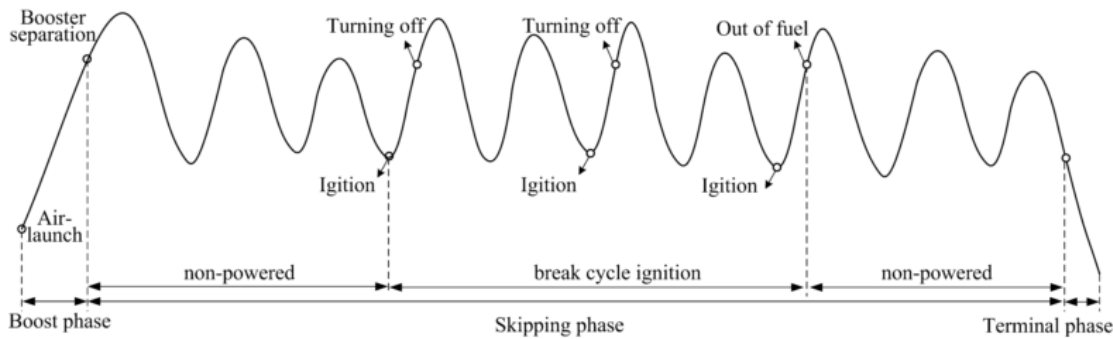


Figure 2.17: The optimised maximum range trajectory of a hypersonic vehicle[16].

2.7 The University of Queensland's Rocket-Scramjet-Rocket Launch System

The three stage, partially reusable, access to space system under development at The University of Queensland utilises the SPARTAN[53] scramjet powered vehicle as the reusable second stage, shown in Figure 2.18. This system is considered in this study as a representative model for three stage, air-breathing access to space system designs. This launch system is designed for small payload deliveries to orbit and will in the future utilise a fly-back rocket booster to accelerate the SPARTAN stage to minimum Mach number required for stable burn, at which point separation occurs and the second stage uses a scramjet engine to accelerate to between approximately Mach 5-9. The first and second

2.7. THE UNIVERSITY OF QUEENSLAND'S ROCKET-SCRAMJET-ROCKET LAUNCH SYSTEM

stages are to be reusable, the first stage via conversion into a propeller powered drone, and the second stage through either a glide or extra scramjet powered flight to a suitable landing site. The third stage

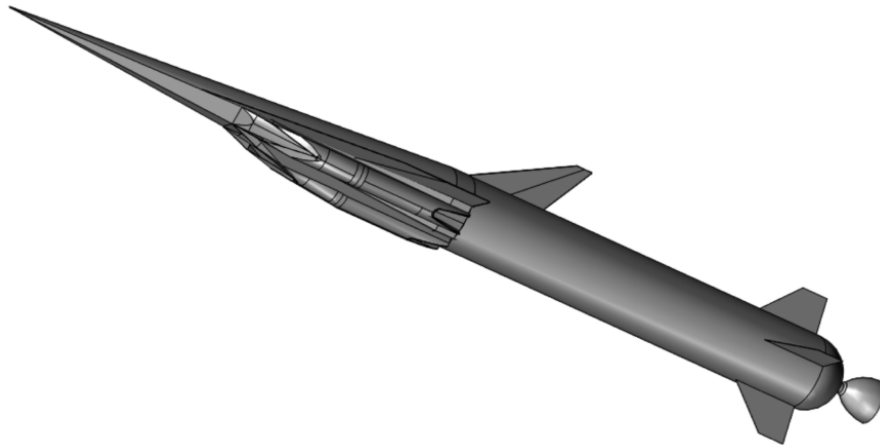


Figure 2.18: An early design of the socket-scramjet-rocket launch system incorporating the SPARTAN [53].

will be a disposable rocket stage, which will then deliver the payload to orbit, exiting the atmosphere and performing a Hohmann transfer. Preliminary designs of the SPARTAN have been completed, with the shape of the SPARTAN optimised for payload delivery to heliosynchronous orbit. Studies have indicated that the expendable third stage makes up only 8.8% of the mass of the launch system, and that if the SPARTAN and first stage rockets are able to be reused, approximately 90% of the launch system mass would be reusable[93].

2.7.1 Scramjet Engine Model

To deliver a payload to orbit, the SPARTAN uses four Rectangular-to-Elliptical Shape Transition (REST) scramjet engines, with inlets configured to allow installation on a conical forebody (C-REST). The C-REST engines which the SPARTAN uses have been configured to fly between Mach 5 and 10, this type of engine is known as a C-RESTM10 engine[93]. The REST engine has been shown experimentally to operate successfully at off design conditions by Smart & Ruf[115].

A C-RESTM10 propulsion database has been used in previous studies to model the scramjet engines of the SPARTAN[93]. This database has been created through separate modelling of the compression within the inlet, combustion within the combustor, and expansion through the internal nozzle[89]. The inlet compression was modelled by performance curved based on a set of CFD solutions[89]. These performance curves were used to obtain the flow conditions at the end of the inlet. The combustor was modelled using quasi-one-dimentional cycle analysis, assuming a combustion efficiency of 80%[89]. Lastly, the properties at the end of the combustor were expanded assuming a nozzle efficiency of 90%[89]. The C-RESTM10 is designed for operation at $M_0 = 10$, and the con-

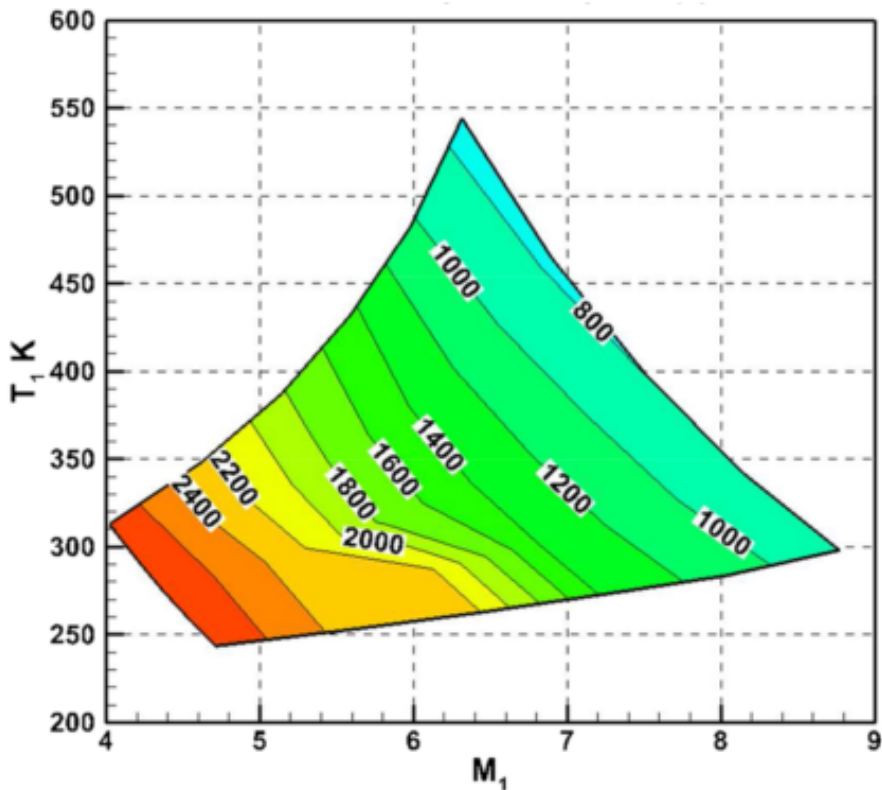


Figure 2.19: The C-RESTM10 propulsion database, specific impulse.

traction ratio and combustor divergence are not optimal for operation at low Mach numbers. At low Mach numbers, an equivalence ratio of 1 may cause the flow to choke and unstart. Consequently, an equivalence ratio of less than 1 was set at low Mach numbers, in order to avoid unstart[89]. At these Mach numbers, the C-REST engines are operating in dual-mode[89].

2.7.2 The Trajectory of the SPARTAN

To date, studies of the SPARTAN have assumed a constant dynamic pressure trajectory[93]. Past studies of the SPARTAN vehicle have assumed that a fly-back to launch site is possible after third stage separation[93]. However, this fly-back has not yet been simulated.

Figure 2.20 shows the trajectory of the SPARTAN, simulated in three degrees of freedom to fly close to a constant 50kPa dynamic pressure, using a pole-placement angle of attack controller[93]. The ascent trajectory of the SPARTAN begins at Mach 5.1, and terminates at Mach 9.46, when the hydrogen fuel is exhausted[93]. The net specific impulse of the SPARTAN varies from 1694s at the beginning of the trajectory, to 377s by the time the fuel is depleted[93]. This significant decrease in efficiency means that by the end of the trajectory, the net efficiency of the SPARTAN is approximately that of a rocket[93].

The SPARTAN is trimmed throughout the trajectory by ailerons on the wing, shown in Figure

2.7. THE UNIVERSITY OF QUEENSLAND'S ROCKET-SCRAMJET-ROCKET LAUNCH SYSTEM

[2.21](#). These elevons were sized through variation of the width, b_E , to have an area equal to 15% of the area of the wing, and to have a cord length, c_E , of 15% of the cord length of the wing[93]. Over the flight of the SPARTAN, the flap deflection changes from -0.8° to 3.0° [93]. The drag contribution of the flap varies from 1.2% to 3.5%, and the lift contribution from -4.0% to 4.2%[93].

This trajectory enables delivery of a 307.1kg payload to low earth orbit[93]. This is a payload mass fraction of 1.17%, which compares well with existing expendable launch systems of similar size, with the advantage of being designed for reusability[93]. This trajectory was designed around the SPARTAN flying a constant dynamic pressure trajectory, with the first and third stage trajectories confirming to this constraint. It has been suggested that for the design of this launch system to be improved, a an optimised trajectory is necessary[93].

2.7.3 The Third Stage Rocket

The third stage rocket of the rocket-scramjet-rocket launch system consists of a rocket motor, fuel tanks, structure, payload and a thermal protection system[93], shown in Figure 2.22. The third stage rocket separates from the SPARTAN at the end of its trajectory, and performs a pull-up manoeuvre to exit the atmosphere. Once the density of the atmosphere is low enough, the thermal protection system separated from the vehicle for mass efficiency, and once exoatmospheric, the third stage performs a Hohmann transfer to reach the desired orbit. The third stage has to this point been designed to be powered by the Pratt & Whitney RL-10-3A[93], and has exhibited good performance when powered by this engine. However, the RL-10-3A is a pump-fed engine, and is likely to be prohibitively expensive for a small launch system.

2.7.4 Exoatmospheric Rocket Engines

The third stage requires a rocket engine with sufficient thrust to accelerate out of the atmosphere, and a diameter small enough to allow the rocket to fit within the fuselage of the SPARTAN. The major factors when choosing a rocket engine are efficiency and thrust-to-weight ratio, as well as cost. It is desirable to use a rocket engine which has already been developed and flight tested, to reduce the costs and potential complications of engine development. Table 2.2 shows a comparison study of small sized upper stage rocket engines which are currently in use, or have been used, for commercial space flight. The cost of these engines is not generally published, however, pressure fed engines cost significantly less than pump-fed engines, due to the cost of the turbopump and the associated complexity of a pump-fed system.

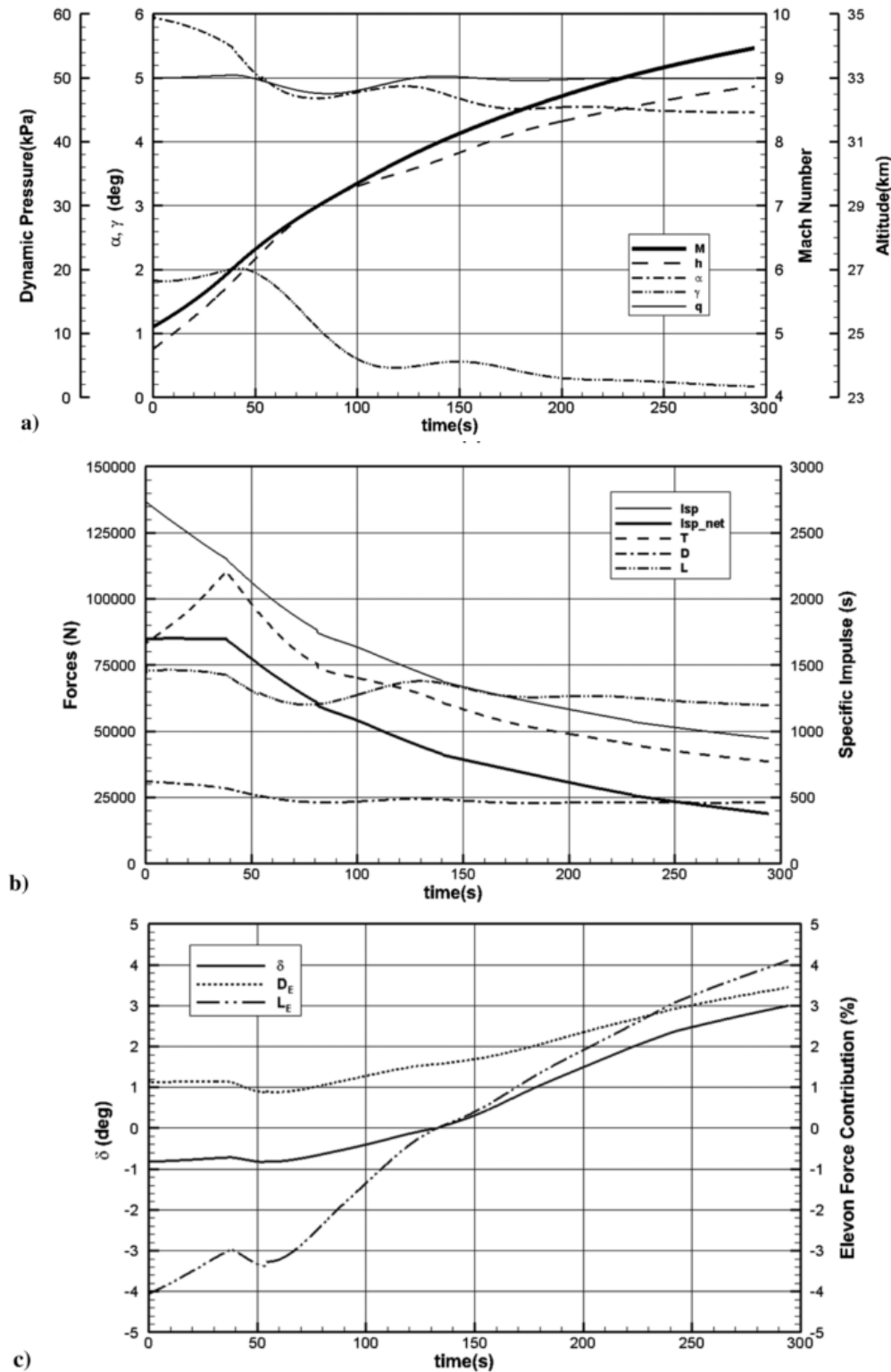


Figure 2.20: The flight trajectory of the SPARTAN

2.7. THE UNIVERSITY OF QUEENSLAND'S ROCKET-SCRAMJET-ROCKET LAUNCH SYSTEM

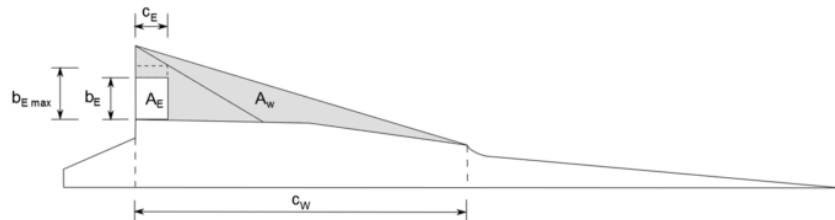


Figure 2.21: The elevons of the SPARTAN[93].

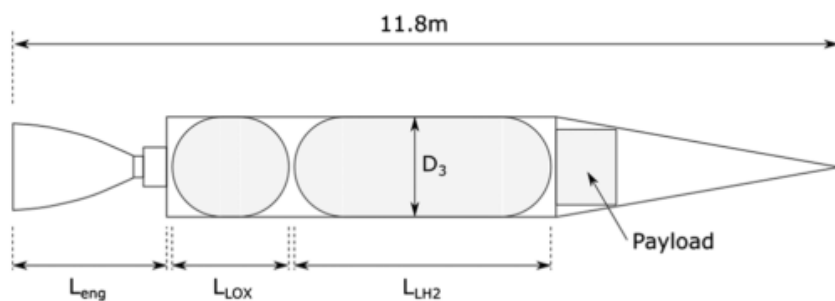


Figure 2.22: The third stage rocket of the rocket-scramjet-rocket launch system[93].

Engine	Fuel Supply	Fuel	Thrust	Isp	Mass	Diameter	Length	Thrust Vector Capability
Rl-10A-3A	Pump-Fed	LOX/LH ₂	73.4kN	444s	141kg	1.01m	1.78m	Yes, Unknown limits
Aestus II	Pump-fed	MMH/NTO	46kN	337.5s	148		2.2m	6°
RS-72	Pump-fed	MMH/NTO	55.4kN	338s	154kg		2.286	6°
ATE	Pump-fed	MMH/NTO	20kN	345s	57.9kg	0.38m	1.4m	15°
AJ10-118K	Pressure-fed	A-50/NTO	43.3kN	320.5s	124.5kg	1.53m	2.7m	Fixed
Kestrel	Pressure-fed	LOX/Kerosene	30.7kN	317s	52kg	1.1m	1.9m	Yes, Unknown limits
Aestus	Pressure-fed	MMH/NTO	27.5kN	320s	110kg	1.27m	2.2m	4° & 4° by mechanical adjustment
OMS	Pressure-fed	MMH/NTO	26.7kN	316s	118kg	1.168m	1.956m	8°

Table 2.2: Comparison of upper stage rocket engines, sourced from the Encyclopedia Astronautica reference website[133].

2.8 Optimal Control

Calculating the optimal trajectory of a launch system with multiple stages and multiple modes of propulsion is a complex process. Defining the trajectory of a launch system purely from vehicle analysis is unlikely to yield a trajectory which maximises the performance of the system. A simulation method is required which is able to calculate a trajectory path which maximises the performance of the launch system, while taking into account the aerodynamic and propulsive properties of each stage and propulsion mode. Optimal control theory is used in situations where an optimal trajectory path must be found with little prior knowledge of the shape of the trajectory. Optimal control theory has been widely used in aerospace applications, including being used to optimise the launch of hypersonic launch vehicles[CITATIONSXX].

For an optimisation of a complex trajectory there are a variety of optimal control methods that are useful for specific problem types. These are separated into two categories: direct and indirect solution methods. Indirect methods are based on the calculus of variations or minimum principle model, and generally result in high accuracy solutions to optimisation problems [15]. However indirect models suffer from the drawbacks of small radii of convergence and the fact that the equations to be solved often exhibit strong nonlinearity and discontinuities. This means that indirect methods will not be solvable unless the problem is very well defined with a minimum of nonlinearity, making indirect methods unsuitable for many complex optimisation problems, such as aerospace vehicle simulations which can exhibit strong nonlinear behaviour and have a wide solution space.

Direct methods transform an optimisation problem into a nonlinear programming (NLP) problem which can be solved computationally [120]. NLP solvers solve the optimisation problem defined as [8]:

$$\text{Minimise} \quad f(x) \quad (2.1)$$

$$\text{Subject to} \quad g_i(x) \leq 0 \quad \text{for } i = 1, \dots, m \quad (2.2)$$

$$\text{and} \quad h_j(x) = 0 \quad \text{for } j = 1, \dots, n \quad (2.3)$$

An optimisation problem that has been discretised in this form can thus be solved using any of a variety of NLP solvers. One of the most effective methods of solving twice differentiable NLP problems is sequential quadratic programming (SQP) [13] for which there is a variety of commercial solvers available such as NPSOL, SNOPT and packages within MATLAB.

In order for these packages to be able to solve an optimisation problem it must be presented in discretised form, and as such must be transformed using approximation techniques. The task of approximating a continuous optimisation problem in discrete NLP solvable form is not simple. SQP

solvers can very easily run into convergence issues when provided with an optimisation problem which has not been well defined. Also, any approximation must be carried out with care that the accuracy of the solution is not compromised. There are multiple ways to approximate a continuous optimisation problem directly as an NLP problem, the most common of which are shooting and collocation methods. The choice of discretisation method can affect the stability and accuracy of the solution as well as the solution time of the problem.

2.8.1 Shooting Methods

Shooting methods in optimal control are forward-time methods of discretisation. Shooting methods explicitly enforce the dynamics of the system, and update the free conditions and system controls to move towards an optimal solution from an initial guess. Shooting methods are generally simple to apply, and require little specialised knowledge to use once they have been implemented.

The Single Shooting Method

The oldest and simplest method of approximating continuous optimisation problems as NLP problems is the direct single shooting method. Direct single shooting discretises the control function over the solution space, and solves this directly as an NLP by integrating the vehicle dynamics, or state variables, along the trajectory at each trajectory guess[10, 34, 60, 97]. Single shooting is simple to apply and has been used since the 1970s for rocket trajectory optimisation [54]. Single shooting methods suffer from nonlinearity problems, ie. an optimisation problem solved using the single shooting method will potentially struggle to solve if the problem exhibits even small nonlinearities, due to being unable to converge to an optimal solution. This makes the single shooting method unsuitable for complex problems such as a scramjet model, as there are many nonlinear factors inherent in atmosphere and airbreathing engine modelling.

The Multiple Shooting Method

Direct multiple shooting solves some of the instabilities of the single shooting method by splitting the trajectory into multiple shooting arcs, and collocating these at specific time points[10, 34, 60, 97]. This creates a system of discontinuities, illustrated in Figure 2.23, which are gradually removed by the solver algorithm until the trajectory is continuous. These discontinuities allow greater flexibility for the solver than is afforded by the single shooting method.

The multiple shooting method has greatly improved convergence compared to the single shooting method, removing much of the susceptibility to instabilities resulting from nonlinear effects. However, the multiple shooting approach still suffers from a relatively small radius of convergence and slow computation times. Radius of convergence is extremely important to this study as the optimal

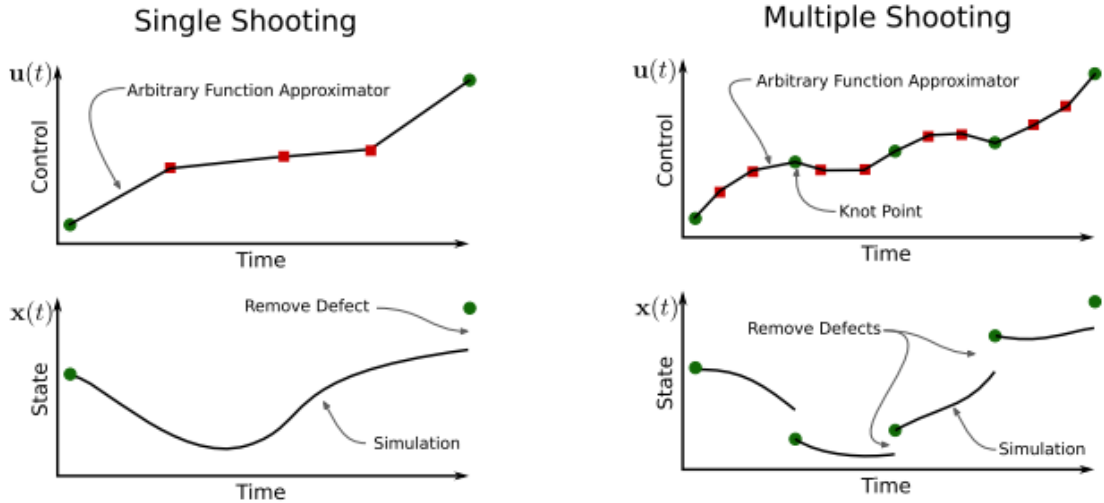


Figure 2.23: A comparison of single shooting and multiple shooting[60].

solution cannot be approximated to a great degree of accuracy, and as such multiple shooting was deemed inappropriate for this study. It was desired to find a method with a global radius of convergence to apply to the optimisation problem being considered.

2.8.2 Collocation Methods

Collocation methods are arguably the most powerful methods for solving optimal control problems[97]. Collocation methods are simultaneous methods, where both the states and controls are approximated using a specific form of functional[60, 97]. In these methods, the dynamics of the system are not explicitly enforced, but instead are constrained at specified points along the trajectory, called collocation points, or nodes[60]. This means that the derivative of the state functions become a constraint within the NLP, being equated to the polynomial approximation functions by the solver algorithm. Collocation methods provide larger radius of convergence, greater robustness, and smaller computational times compared to multiple shooting[34]. However, the solution accuracy of collocation methods is less than that of multiple shooting methods[34], although this can be improved through the choice of basis functions used for collocation[97].

Collocation methods can be represented in two ways; h and p schemes[60]. p schemes, or global methods, represent the entire trajectory as high order polynomials, and converge by increasing the order of these polynomial[60]. This method works well if the underlying solution is smooth, however, if there are discontinuities present, a P scheme will fail[60]. h schemes separate the trajectory into a series of medium order polynomials, stitched together at set points using defect constraints, similarly to the multiple shooting method[60, 97, 104]. These joining points are called knot points[60, 104]. A comparison between h and p methods is shown in Figure 2.24.

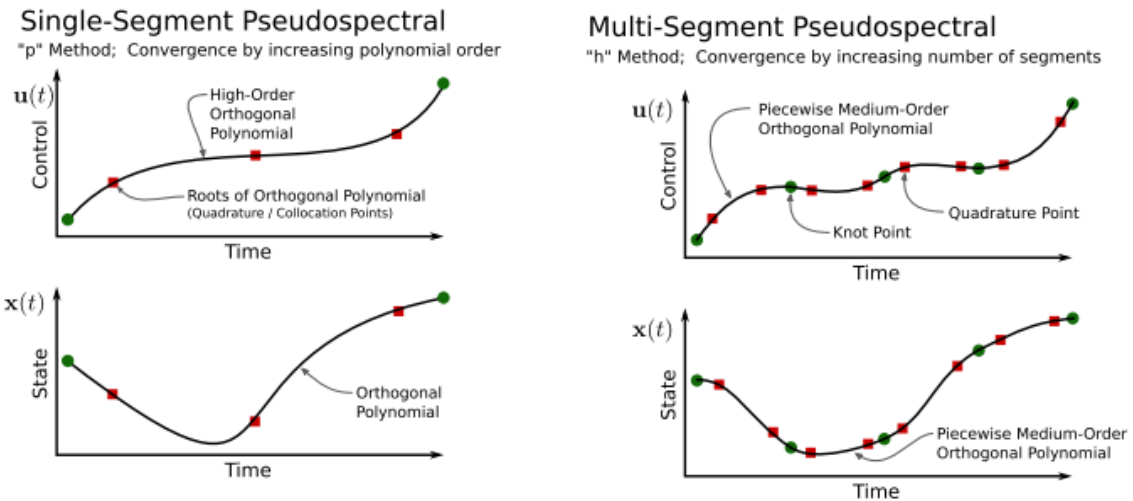


Figure 2.24: Examples of h and p collocation methods[60].

The Pseudospectral Method

The most accurate and effective type of collocation methods use orthogonal polynomials to approximate the state and control functionals[31]. In trajectory optimisation, this type of collocation is referred to as the pseudospectral method[60]. The pseudospectral method was first introduced in 1972 by Kreiss & Oliger [65] as an efficient way to compute meteorology and oceanography problems. The pseudospectral method has recently garnered a large amount of attention for its ability to rapidly and accurately solve a wide variety of optimal control problems. The pseudospectral method employs the use of orthogonal polynomials such as Legendre or Chebychev polynomials to approximate the state and control functions at a specific set of collocation points[31, 52, 60, 97]. When a solution is well behaved and smooth, the pseudospectral method converges at an exponential rate, with a high accuracy known as spectral accuracy[27, 104].

There are multiple types of pseudospectral methods, distinguished by the polynomial and collocation points used. Usually, these polynomials are Chebyshev or Lagrange polynomials[31, 97], and the collocation points are the roots of a Legendre polynomial[41]. Chebyshev polynomials have been used since the introduction of pseudospectral methods in optimal control, but have been superseded in many cases by Lagrange polynomials, which offer simpler collocation conditions[97]. There are many possible types of collocation nodes, although there are three most commonly used sets; Legendre-Gauss (LG); Legendre-Gauss-Radau (LGR); and Legendre-Gauss-Lobatto (LGL)[41, 97]. The choice of collocation type determines how the roots of the problem are calculated, and changes the formulation of the problem slightly[41]. Practically, there is very little difference between these node sets [41].

The pseudospectral method is usually employed as a p method, where a global polynomial is used, and convergence is achieved by increasing the order of this polynomial[97]. Recently, hp-adaptive

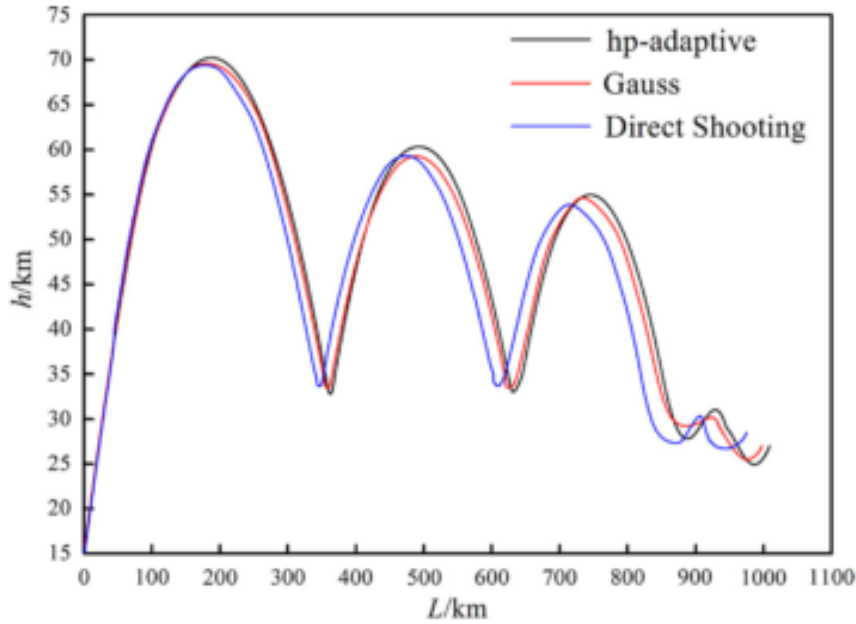


Figure 2.25: Comparison of optimisation techniques[16]. A hypersonic vehicle is optimised for maximum range. The hp-adaptive method can be observed to have produced the most optimal result.

pseudospectral methods have been introduced, which segment the mesh using an h method, whilst also having a variable polynomial degree, as in the p method[27]. These hp methods converge by varying the degree of the approximating polynomial as well as the number of segments simultaneously. Utilising both h and p methods improves the accuracy and robustness of the solution, as illustrated in Figure 2.25, from a study by Chai et al.[16] comparing the single shooting method to p and hp -adaptive pseudospectral methods. Additionally, the hp -adaptive method decreases the computational effort and memory usage necessary during the solution process[16, 27].

A secondary usability advantage of the pseudospectral method is the ability to generate Hamiltonian and costate values easily[32, 45, 97]. The Hamiltonian and costate values allow a solution to easily and quickly be checked to determine if some of the necessary conditions for optimality are being met. This is useful to determine initially if the optimal solution calculated by the pseudospectral solver is valid.

The pseudospectral method has been proven to be extremely effective for simulations in aerospace applications and has been proven in flight applications such as the zero propellant manoeuvre of the International Space Station in 2007, where the ISS was rotated 180 degrees without any propellant used following a pseudospectral method solution [9]. The pseudospectral method has been used successfully in a multitude of studies for the trajectory optimisation of hypersonic vehicles[16, 28, 56, 64, 70, 76, 99, 124, 136, 139]. These results indicate that the pseudospectral method is robust for complex, nonlinear systems, and that the pseudospectral method can be used for systems with many state variables[CITATIONXX].

2.9 Available Optimal Control Solvers

There are a number of optimal control solvers available, both commercially and open source. A summary of the most prominent available solvers is shown in Table 2.3. These programs are mostly general solvers, and must be configured specifically in order to solve a particular optimal control problem. The exception is ASTOS[6], which is a standalone program designed for aerospace trajectory optimisation.

Functionally, most of the available solvers are similar in operation. The states and controls of the optimal control problem are defined to the program by the user, along with any constraints; continuous or endpoint. The cost function of the problem is input, and dynamic model of the system is defined. An initial guess is provided, and once activated, the solver will move toward an optimal solution from this initial guess. The most significant practical difference between the solvers lies in the robustness of the optimal solution, ie. how easily a particular solver is able to converge to the optimal solution. For a simple and continuous optimisation problem all solvers will be able to approach the same solution (though with varying efficiency). However, for a complex and nonlinear optimisation problem, some solvers will converge much more easily than others. Generally, this stems from the underlying transcription method used.

The most common form of discretisation used by these solvers is the pseudospectral method, although other forms of collocation, as well as multiple shooting, are also used. Comparing the benefits of these solvers is difficult, as a particular problem may lend itself to one solver in particular, and all have been used widely. However, it is generally held that hp-adaptive pseudospectral methods are the current state-of-the-art in discretisation methods, and a solver which utilises one of these techniques is likely to have good convergence and accuracy properties[citeXX]. The readily available packages which utilise hp adaptive pseudospectral methods are GPOPS-2[96] and ICLOCS2[79].

ICLOCS2 is a software package in the alpha stages of development, which is based upon ICLOCS, a multiple shooting solver[79]. ICLOCS2 is able to implement a range of transcription methods, including a hp adaptive Legendre-Gauss Pseudospectral method[79]. As ICLOCS2 is relatively new at the time of writing, it has not yet been implemented in any published works and documentation is limited.

GPOPS-2 is a proprietary hp-adaptive pseudospectral method solver, which implements a variety of hp-adaptive pseudospectral methods, so that the best method may be chosen for a given problem[96]. GPOPS-2 is specifically designed to be as flexible as possible, to accommodate for a wide range of problem formulations[96]. GPOPS-2 is well proven in aerospace applications, and has been used for spacecraft orbit optimisation as well as in-atmosphere trajectory optimisation[CITEXX]. GPOPS-2 is well suited to solving multi-phase optimal control problems, which is necessary for efficient multi-stage launch optimisation[96]. GPOPS-2 represents the state of the art in trajectory optimisation software, and as such is used by a number of institutions around the world.

Both ICLOCS2 and GPOPS-2 uses IPOPT[132] (Interior Point OPTimizer) as the standard nonlinear programming solver (with the option of installing others). IPOPT is a widely used open source nonlinear optimisation package which utilises an interior point line search filter method.

Software	Publisher	Platform	Optimisation Type
DIDO[103]	Elissar Global	MATLAB	Chebychev Pseudospectral
GPOPS II[96]	RP Optimization Research	MATLAB	hp Adaptive Legendre-Gauss-Radau Pseudospectral
PROPT (IPOPT) [105]	TOMLAB	MATLAB	Legendre-Gauss Pseudospectral
ICLOCS2[79]	Imperial College	MATLAB	Multiple Shooting / hp Legendre-Gauss Pseudospectral
POST2[18]	NASA	FORTRAN	Direct Shooting
OTIS[33]	NASA	Fortran	Pseudospectral + Various
TRANSWORHP[134]	ESA	Fortran/C++	Full Discretisation
ASTOS[6]	Astos Solutions	Standalone	Multiple Shooting/Collocation
ACADO[51]	Open Source	C++	Direct
JModelica[55]	Modelon AB, Open Source	Modelica/Python	Collocation/ Pseudospectral

Table 2.3: Summary of programs capable of pseudospectral optimisation.

2.10 Aerodynamic Analysis

Simulating the trajectory of access to space systems requires the aerodynamics of each stage of the launch system to be characterised at every flight condition experienced during launch. For this to be possible, it is necessary to create large aerodynamic coefficient databases, which cover the operable region of the vehicle, and include the effects of control surface deflections and propulsion.

There are a variety of tools available to calculate the aerodynamics of aerospace vehicles. These tools are primarily designed towards either accuracy or efficiency, as more accurate methods require more computational power, longer computational times and, usually, more man-hours to produce a solution. This trade off means a tool must be selected which best suits the requirements of a given problem. For a preliminary vehicle design, it is often desirable to select a tool which is as computationally efficient as possible, as the design of the vehicle is liable to change often. Whereas for more advanced stages of vehicle design, an accurate tool is desirable, to assess the design of the vehicle in detail.

The lowest fidelity, and highest efficiency methods include packages which use empirical relations derived from databases of existing vehicles, such as Missile DATCOM[citeXX missile datcom], as well as panel method codes such as HYPAERO, cbaero and HOTSOSE[cite cbaero, HYPAERO, hotsose]. Low fidelity methods offer rapid solutions, with highly variable accuracy. For simple, standard vehicle shapes, low fidelity methods may offer high accuracy, as low fidelity solutions are usually calibrated to higher fidelity simulations or experiments. However, for complex vehicle geometries, for example geometries involving engine through-flow, low fidelity models may be highly inaccurate, and are not acceptable for use[30].

Medium fidelity methods consist of inviscid Euler solvers such as CART3D, FUN3D and AIRPLANE[cite cart3d, AIRPLANE], which are able to provide reasonable accuracy, with medium run times, by neglecting viscous effects within the solution. These solvers are often used in the later stages of preliminary design, or when higher fidelity is necessary due to design features, but rapid solutions are still desired. Neglecting the viscous effects in the fluid flow means that the solution obtained from an inviscid solver will only be an approximation of the real flow, and that the accuracy of the solution varies depending on the type problem being solved. For problems such as lift on a thin airfoil, inviscid Euler methods may be quite accurate, however for a problem such as boundary growth on a flat plate these methods will not accurately model the solution[78]. A particular advantage that many inviscid Euler codes provide is automatic adjoint mesh adaptation, the ability for the mesh to be automatically and rapidly generated, and updated sequentially throughout the solution process, refining areas of complex geometry or flow. This enables multiple solutions to be easily computed, without the need to regenerate meshes manually. For preliminary design purposes, inviscid-flow Euler CFD solvers are used extensively across industry and academia[5].

High fidelity methods consist of Navier-Stokes CFD solvers such as Eilmer3/4, Fluent, CFX, STAR-CD, COMSOL and OpenFOAM [citationsxx]. These solvers will resolve the fluid flow and aerodynamic forces to a high level of accuracy, including viscous effects. However, the mesh for the problem must be generated prior to the calculation of the solution, which increases the working time significantly. Additionally, the computation times are much longer, and require more computational resources than lower fidelity methods. These factors make the generation of an aerodynamic database using high fidelity CFD an extremely time consuming process, which is suited for use on mature vehicle designs, or when accurate flow simulation is absolutely necessary. This is the case for the simulation of scramjet engines, which contain complex flow fields featuring high Reynolds-number flow, complex shock wave structures, and large thermal and composition gradients[109]. For this reason, scramjet engines must be simulated using high-fidelity methods to produce an accurate solution.

2.10.1 CART3D

CART3D is an inviscid CFD package, designed for use during preliminary vehicle design and analysis[5]. CART3D is computationally efficient and requires only a surface triangulation of the vehicle being analysed to initiate a simulation. CART3D features adjoint mesh adaptation, and uses cartesian 'cut-cells' which intersect the surface, allowing complex geometries to be analysed. The mesh automatically refines as the simulation progresses, reducing error. The absence of a requirement for a user generated mesh allows CART3D to be easily applied to complex launch vehicle designs, as well as allowing for simple modification of control surface deflections and flight conditions. CART3D has been used extensively for aerodynamic simulations in preliminary design, including analysis of the plumes of the Skylon spaceplane[73], HIFIRE-5[63], and in low sonic boom shape optimisations[2]. CART3D has shown good agreement when compared to experimental results for winged boosters

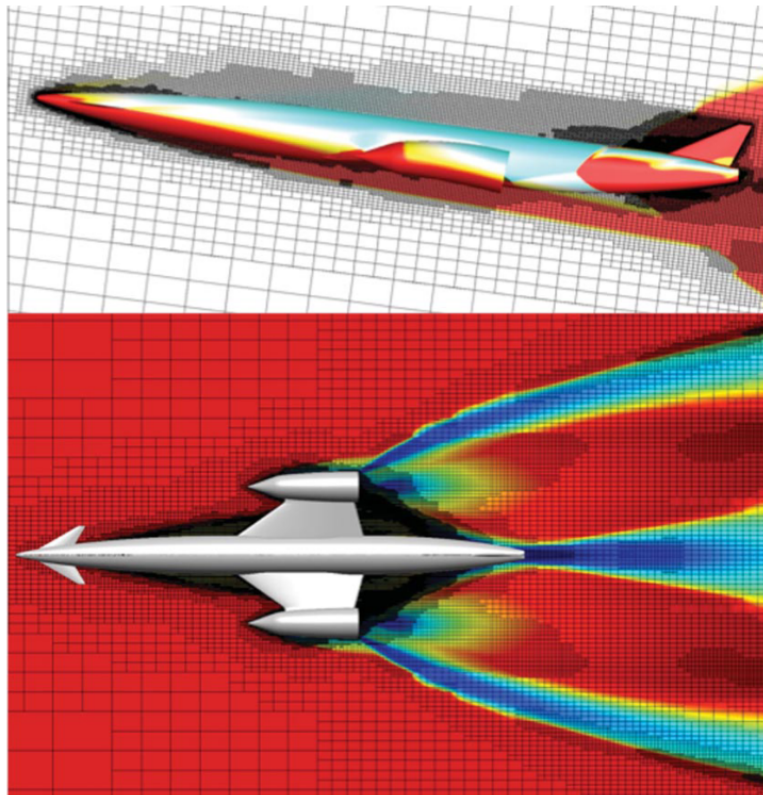


Figure 2.26: The Skylon spaceplane, simulated using CART3D at Mach 12.189, $\alpha = 7.512^\circ$ [73]. Cell distribution produced by mesh adaptation is shown.

at hypersonic speeds[107], as well as supersonic missiles[1] and aircraft[2], and lifting bodies across wide Mach number ranges[4]. In addition, good agreement has been shown between CART3D, experimental results, and full Navier-Stokes solutions for the HIFIRE-1 hypersonic test payload[107]. In this case, the exception to close agreement was at an identified area of shock-induced boundary layer separation, which an inviscid solution does not capture[107]. The model of the HIFIRE-1 and pressure

coefficient results at each pressure tap are shown in Figure 2.27. Finally, in a comparison between CART3D and the Overflow-D Navier-Stokes solver, it was shown that both codes produce similar pressure distributions for simulations of the space shuttle fuel tanks at low Mach numbers[43]. The Overflow-D simulations were stated to require at least 20 times more CPU time than CART3D[43], an example of the efficiency afforded by CART3D.

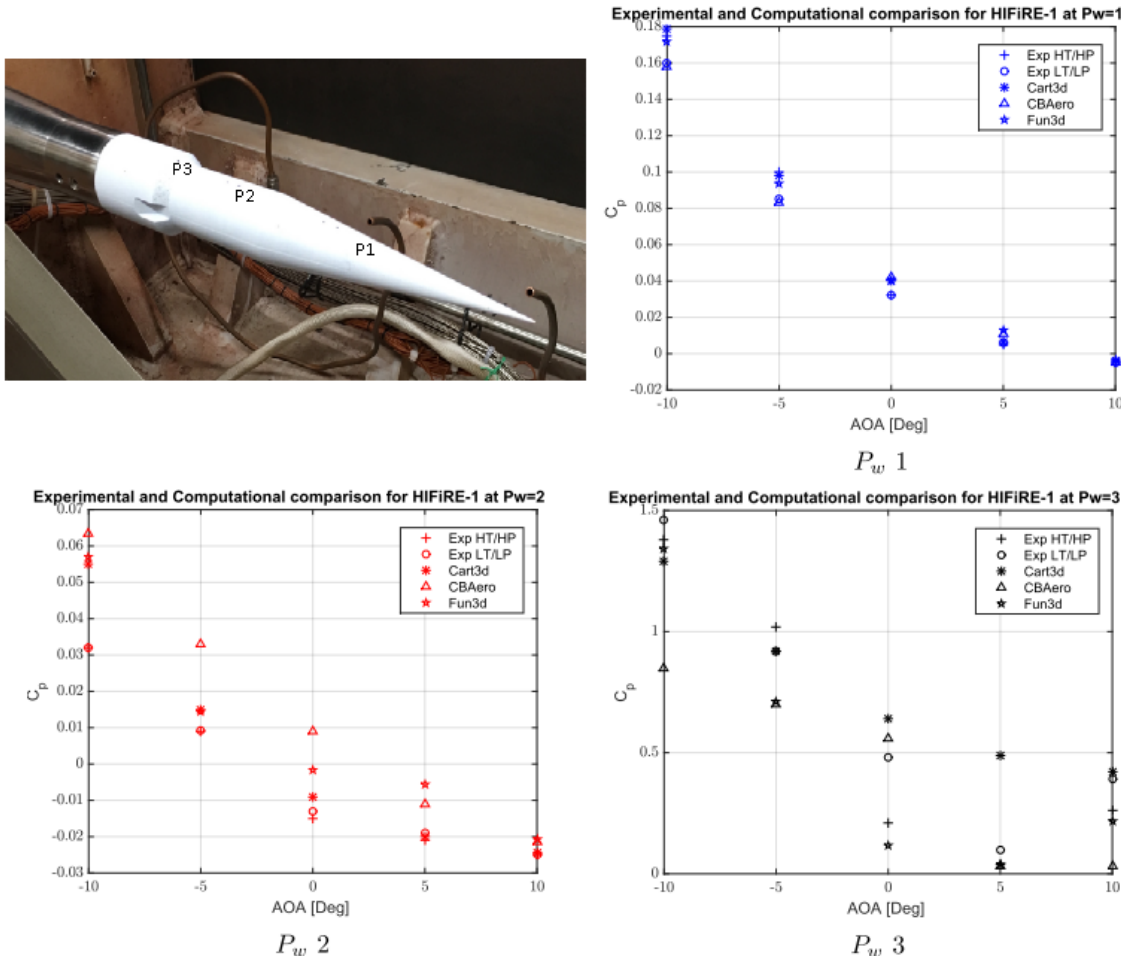


Figure 2.27: Comparisons of CART3D with experimental data and the FUN3D Navier-Stokes CFD solver. P1, P2 and P3 indicate pressure tap locations. Modified from Sagerman et al.[107].

2.10.2 Missile DATCOM

Missile DATCOM is a widely used, semi-empirical, aerodynamic prediction tool for missile configurations. Missile DATCOM uses component-buildup methods by which the aerodynamics of each component of the missile or rocket design are estimated and then added together to determine the aerodynamics of the entire vehicle. Missile DATCOM uses a combination of empirical and theoretical methods and is capable of calculating the aerodynamic forces, stability derivatives and moments over a range of angle of attack and Mach number values. The high efficiency of Missile DATCOM

allows an aerodynamic database to be generated simply and rapidly. Missile DATCOM has been shown to produce close agreement with experimental wind tunnel data for normal force and pitching moment coefficients, and reasonable agreement for axial force coefficients[118].

CHAPTER 3

LAUNCH VEHICLE DESIGN AND SIMULATION

In order to be competitive in the emerging small satellite market, a small satellite launcher must be cost-effective, reliable, and capable of launching on a flexible schedule. The inclusion of airbreathing engines within a small satellite launch system has the potential for improving cost effectiveness compared to disposable rocket-powered launchers, by allowing partial reusability of a launch system. The airbreathing engine most appropriate for small satellite launch systems is the scramjet engine, which operates efficiently within the hypersonic regime, with the capability to operate over a relatively large Mach number range compared to turbojet or ramjet engines. A launch system incorporating scramjets must necessarily include two rocket-powered flight stages; a first stage rocket to accelerate the system from launch to the minimum operational Mach number of the ramjet or scramjet engines; and a third stage rocket to accelerate the payload at exoatmospheric conditions and place it into the correct orbit. This chapter presents the design and modelling of a rocket-scramjet-rocket launch system in which the scramjet stage is reusable for multiple launches. This rocket-scramjet-rocket launch system is designed to launch satellites on the order of 200kg to a 567km altitude sun-synchronous orbit. A sun synchronous orbit is targeted as it is a potentially desirable orbit for small satellite missions, being advantageous for imaging purposes due to its low altitude and consistently timed overpasses. For this launch system to be economically viable, the scramjet stage must be capable of accelerating to a high Mach number, and then returning to its initial launch site for re-use. Returning to the initial launch site removes the need for costly and time-consuming transportation, and allows the refurbishment and refuelling of the scramjet stage to begin immediately. The rocket-scramjet-rocket launch system described in this chapter is used as a representative model for an airbreathing, partially-reusable, multi-stage small satellite launcher.

The rocket-scramjet-rocket launch system used in this study has been designed based on the SPARTAN scramjet accelerator developed by Preller & Smart [CITATIONXX]. The SPARTAN is a scramjet-powered accelerator being developed by The University of Queensland and Hypersonix[citeXX].

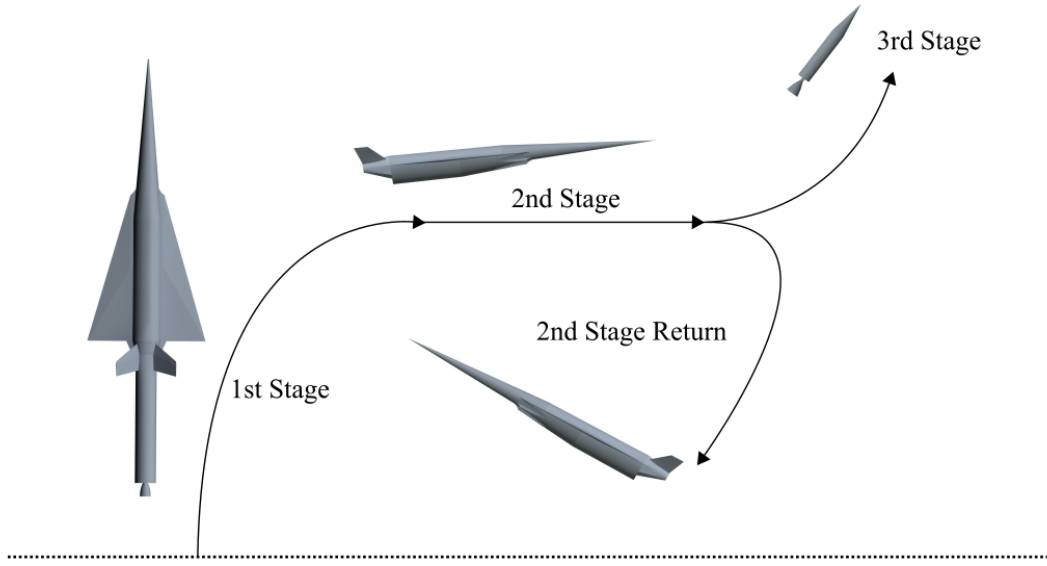


Figure 3.1: The launch process of the rocket-scramjet-rocket launch system, presented in simplified form.

The SPARTAN has been designed for small satellite launches, as part of a rocket-scramjet-rocket launch system. The SPARTAN has been used as the basis for design of the launch system, as it is the most complex stage of the system, and its unique trajectory requirements drive the design of the first and third stages. The trajectory of a launch system involving scramjet propulsion is significantly different to that of a fully rocket-powered launch system. Figure 3.1 shows a simplified representation of the launch trajectory for the vehicle simulated in this study. The operation of the scramjet engine requires in-atmosphere flight, at high dynamic pressure conditions for long periods of time. The launch system must be designed to withstand the high structural loading and heating generated by flight at these conditions. The launch system is launched vertically under rocket power, from a traditional small rocket launch facility. The SPARTAN is mounted to the front of the first stage rocket allowing the SPARTAN to take the brunt of the aerodynamic forces and heating, as well as allowing the use of the control surfaces of the SPARTAN. During first stage rocket operation, the launch system pitches rapidly, reaching close to horizontal flight to allow the SPARTAN to stay at high dynamic pressure conditions. The SPARTAN is accelerated to its minimum operating velocity of approximately Mach 5, at which point separation occurs. The SPARTAN's four scramjet engines are ignited, and The SPARTAN is accelerated through the atmosphere, reaching approximately Mach 9. At this point, the specific impulse of the scramjet engines, and thus the efficiency of the SPARTAN, have decreased, and the third stage rocket is separated. The third stage rocket accelerates and performs a pull-up, before cutting its engine and coasting out of the atmosphere. Once the rocket is

exoatmospheric, the engine is reignited, performing first a circularisation burn, and then a Hohmann transfer to the intended orbit. Meanwhile, the SPARTAN banks and executes a fly-back manoeuvre to return to its initial launch site. The SPARTAN extends landing gear, and lands on a traditional runway in the style of a conventional aircraft. The SPARTAN is able to be rapidly refurbished and remounted for further launches. To fulfil the requirements of this trajectory, The SPARTAN must be able to fly and manoeuvre from velocities greater than Mach 9 to landing, as well as being able to withstand high structural and heating loads without significant deterioration.

The three stage launch system incorporating the SPARTAN is shown in Figures 3.2 & 3.3. The size and external design of the SPARTAN scramjet accelerator are used exactly as defined for the Baseline SPARTAN vehicle designed by Preller & Smart[CITEXX]. The internal layout has been designed for the SPARTAN to carry a large fuel volume while allowing the third stage to fit within the fuselage. The first and third stages have been designed for this study. The third stage rocket replaces the third stage used in previous SPARTAN studies, which was powered by a Pratt & Whitney RL-10-3A engine, with a rocket stage powered by a SpaceX Kestrel engine. The SPARTAN design is presented first, as the design of the SPARTAN drives the design of the first and third stage rockets.

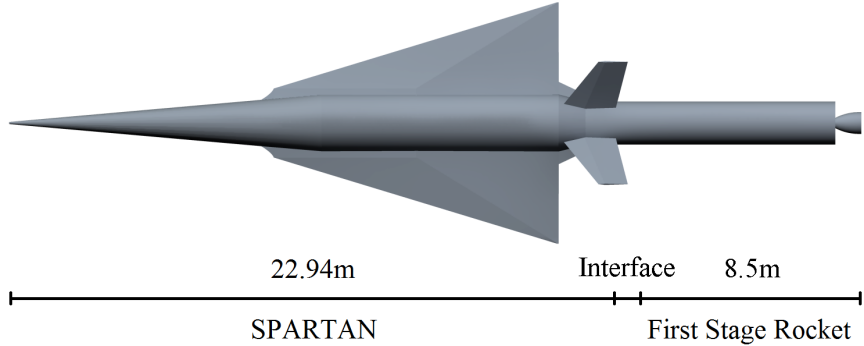


Figure 3.2: The rocket-scramjet-rocket launch system, top view, showing the SPARTAN and first stage.



Figure 3.3: The rocket-scramjet-rocket launch system, side view, showing the SPARTAN and fuel tanks, along with the third and first stages.

3.1 Second Stage Scramjet

3.1.1 The SPARTAN Accelerator

The SPARTAN vehicle in this study is designed based on the work by Preller & Smart CITATION. The SPARTAN is 22.94m long, with a frontal cone half angle of 5° [CITEXX DAWIDS THESIS]. A mass breakdown of the SPARTAN is shown in Table 3.1, adapted from [CITAXX Dawids thesis]. The fuel tank sizes and total fuel mass are sized to accommodate for the Kestrel-powered third stage, described in Section 3.3. This study assumes that the third stage is stored within the fuselage of the

Part	Fuselage	Wings	Tanks	Systems	Landing Gear	Scramjets	Fuel
Mass (kg)	2861.6	350.7	179.4	707.5	188.9	669.0	1562.0

Table 3.1: Mass breakdown of the modified SPARTAN vehicle.

SPARTAN for simplicity. It is assumed that the release mechanism for the third stage is able to be situated within the available space surrounding the third stage, however the release mechanism is not considered further in this study.

The fuel tanks are sized to fit around the kestrel-powered third stage. There are three fuel tanks; two cylindrical tanks situated underneath the third stage; and a truncated conical tank in the nose. The conical fuel tank is designed to fit immediately forward of the third stage. This fuel tank is 8m long, leaving 1.47m^3 of space in the nose for cooling systems, frontal landing gear and any additional systems or sensors which are necessary in the nose cone. The cylindrical tanks are positioned underneath and slightly to either side of the third stage, leaving space underneath for vehicle systems. The cylindrical fuel tanks are designed to be 8.5m long, with diameters of 0.87m, sized to give a nominal total tank volume of 22m^3 . The fuel tanks hold a total of 1562kg of LH2 fuel. This assumes an LH2 density of 71kg/m^3 , slightly denser than LH2 at phase transition point at 1 atm. The mass of the fuel tanks is scaled from Dawid Preller's Baseline vehicle model of the SPARTAN[CITEXX], giving a total fuel tank mass of 179.4kg.

3.1.2 Propulsion

The SPARTAN is powered by four underslung scramjet engines, fuelled by liquid hydrogen. These engines are Rectangular To Elliptical Shape Transition (REST) engines, configured to allow for a conical forebody (C-REST). REST engines have a rectangular to elliptical shape transition inlet, and an elliptical combustor, offering simplicity in design as well as reduced thermal loading and viscous drag compared to scramjets with planar geometries [121]. REST engines are also specifically designed to operate over a wide range of Mach numbers, and at off design conditions, making them particularly applicable to use on scramjet accelerator vehicles.

Propulsion Modelling

The properties of the C-REST scramjet engines must be modelled at every flight condition which the SPARTAN may experience during its flight. The thrust generated by the C-REST engines determines how rapidly the SPARTAN accelerates, and the efficiency of the engines determines the total flight time, and influences the separation point of the third stage rocket. The C-REST engines are simulated separately to the aerodynamic simulations of the SPARTAN, using quasi-1D simulation for simplicity[89, 93]. The engine model takes the conditions at the inlet, and calculates the exit conditions and propulsive properties of the engine. The engine exit conditions are added into the aerodynamic simulations and the propulsive properties are used in the simulated vehicle model.

Before the flow enters the engine, it is affected by the conical shock generated by the forebody of the SPARTAN. Figure 3.4 shows the locations of the flow properties which are necessary to calculate engine performance. The ambient atmospheric conditions are calculated by interpolation using the 1976 NASA Atmospheric properties[77]. The flow properties at the inlet of the engines is calculated using the Taylor-Maccoll analysis method for conical shocks[CitationXX]. This calculation is performed in the cone_shoot program provided for this study by Prof. Michael Smart[CitationXX?]. The flow conditions following the conical shock are shown in Figure 3.5.

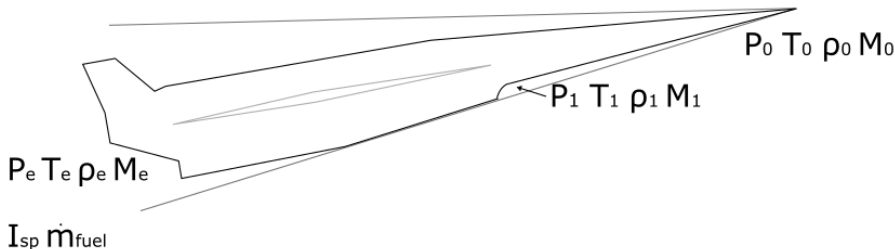


Figure 3.4: The locations of conditions relevant to C-REST engine simulation.

The engine model used is a CRESTM10 database[89, 93], analysed using quasi-1D simulation and provided for this study by Prof. Michael Smart. This database has previously been used in simulations of the SPARTAN, as detailed in Section 2.7.1. This database provides data points of engine performance over inlet conditions within the operational range, at 50kPa dynamic pressure equivalent conditions. The specific impulse data set is shown in Figure 3.6. This data is interpolated between for the given inlet conditions, to calculate specific impulse produced by the engine. As the data points of the C-REST database are unevenly distributed in for inlet Mach and temperature, care must be taken in order to interpolate smoothly to allow the optimal control solver to converge successfully. To ensure that smooth interpolation is achieved, the C-REST database is first interpolated between using linear interpolation, for each 'set' of four nodes which form a square. A uniform grid is created using this linear interpolation, on which a cubic spline interpolation is applied using Matlab's grid-dedInterpolant function. This is explained in detail in Appendix XX. During flight the C-REST inlet

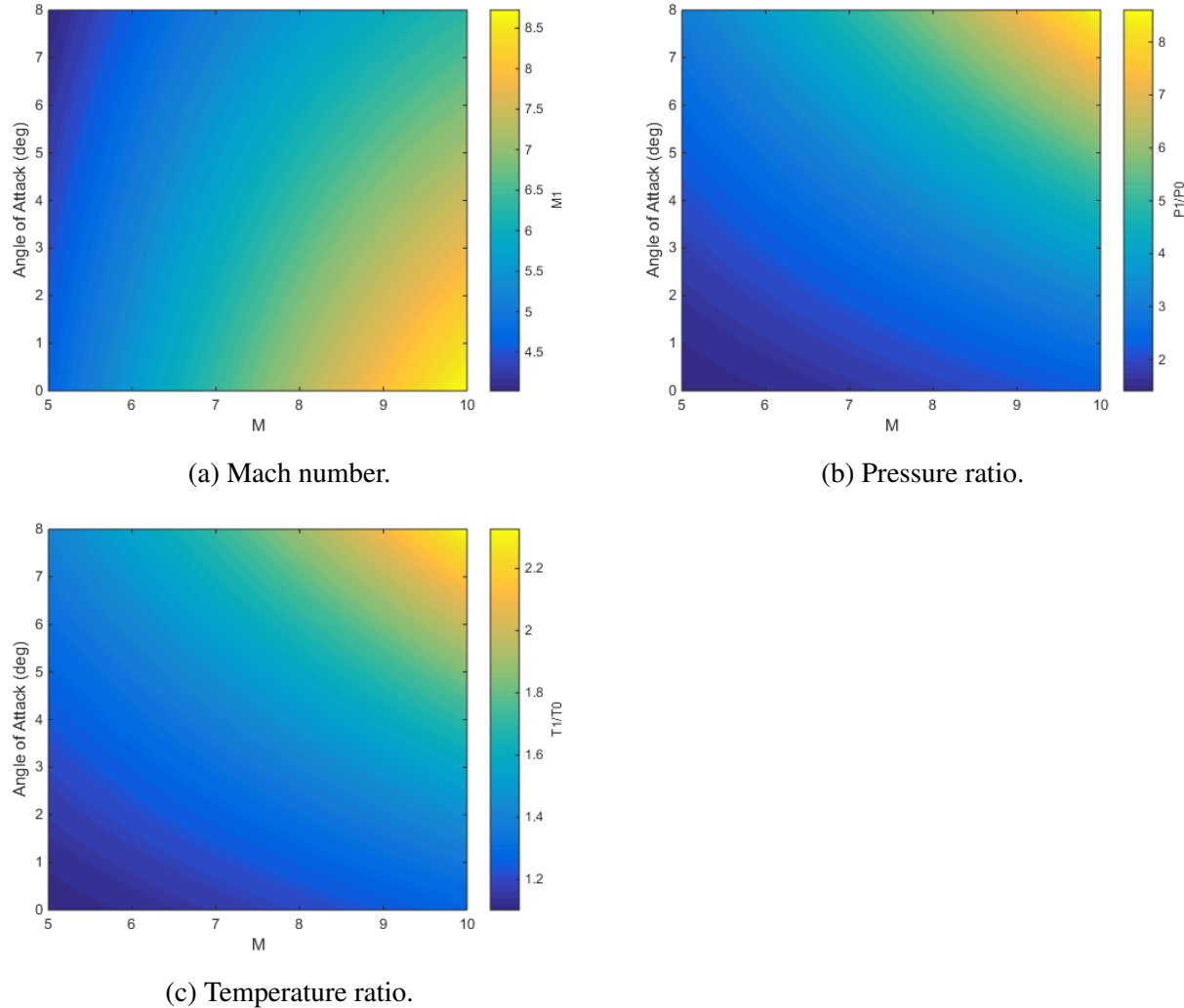


Figure 3.5: Flow conditions after the conical shock generated by the vehicle nose cone. Figure a) shows the Mach number, b) shows the pressure ratio, and c) shows the temperature ratio following the conical shock.

conditions generally stay within the region bounded by the available data. However, for the purposes of the trajectory optimisation, it is necessary for the vehicle model to be able to extrapolate for ISP and equivalence ratio data. This extrapolation is performed in the same manner as the interpolation, a linear extrapolation, followed by a cubic spline interpolation of the extrapolated points. This allows for smooth continuity between the interpolated and extrapolated points, while ensuring that the extrapolated values are reasonable.

For operation at high Mach numbers, the fuel mass flow rate is assumed to be stoichiometric, so that $\dot{m}_f = 0.0291\dot{m}$. This ensures that the scramjet engines are performing at high efficiency throughout the acceleration of the scramjet stage. However, the C-REST engine is a fixed geometry engine,

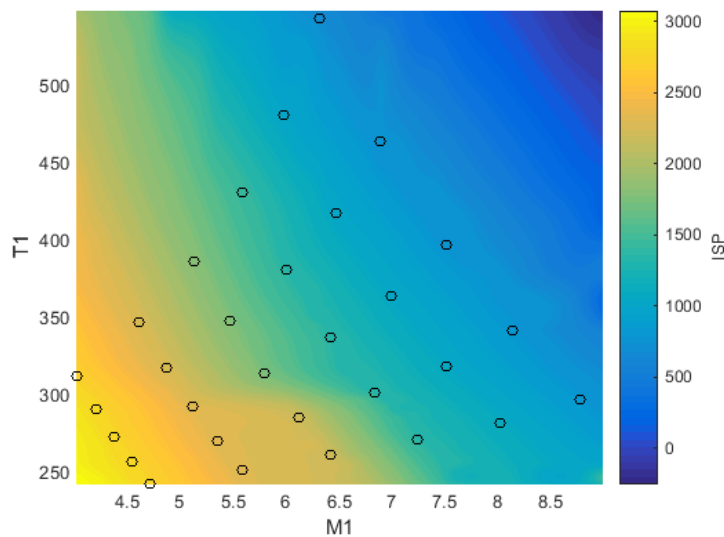


Figure 3.6: Specific impulse of the CRESTM10 engines with input temperature and Mach number. Available data points are indicated.

primarily designed for operability at high Mach numbers[93]. At lower Mach numbers, the addition of excessive fuel may cause the engine to choke and unstart, resulting in total loss of thrust[93]. To avoid unstart, an equivalence ratio (ϕ) of less than 1 is set at low Mach numbers. The equivalence ratio interpolation is linear, as the number of data points available for interpolation is low. The equivalence ratio over the range of SPARTAN operation is shown in Figure 3.7. The fuel mass flow rate is determined by approximating the flow into the inlet as an ideal gas;

$$\dot{m} = 0.9m_c A_{cap} P_0 M_0 \sqrt{\frac{\gamma_0}{R_{air} T_0}}, \quad (3.1)$$

$$\dot{m}_{fuel} = \left(\frac{m_{fuel}}{m_{ox}}\right)_{st} \phi \dot{m}. \quad (3.2)$$

The multiplier of 0.9 is an approximate term included to account for losses due to asymmetry within the engine[89]. The thrust for each engine, T , is obtained by inclusion of the interpolated specific

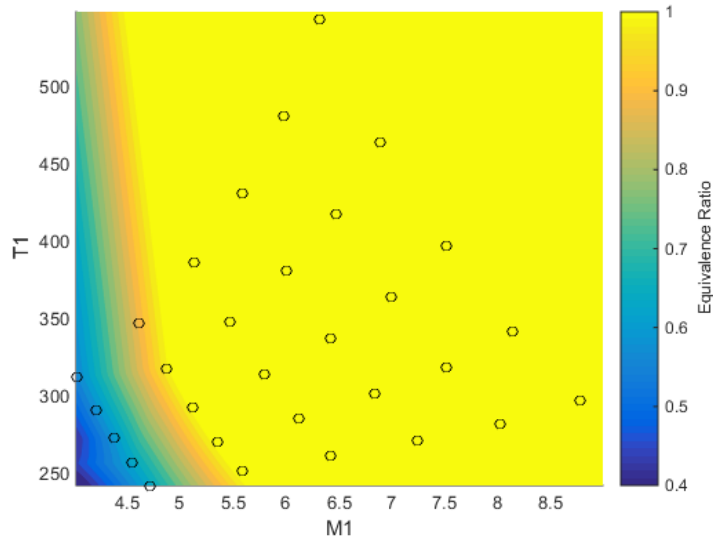


Figure 3.7: Operable equivalence ratio of the CRESTM10 engines with input temperature and Mach number. Available data points are indicated.

impulse, ie.

$$T = g_0 \dot{m} I_{sp}. \quad (3.3)$$

For this database, the C-REST engine was modelled to a nozzle exit area of XXm. This is smaller than the exit area modelled on the version of the SPARTAN used in this work, of XXm. For this reason, additional thrust is obtained from an additional nozzle segment, and the specific impulse of the C-REST engines will be higher than calculated in the database. The modelling of this additional nozzle segment and the thrust obtained are detailed in Section 3.1.3.

3.1.3 The Aerodynamics of the SPARTAN

In order for the trajectory of the SPARTAN to be successfully simulated and optimised, the aerodynamics of the SPARTAN must be calculated for the large range of flight conditions experienced during the acceleration and return flights. The aerodynamics of the SPARTAN are calculated at set flight conditions covering the breadth of necessary conditions, and the results are tabulated in databases. During simulation, the aerodynamics of the SPARTAN are determined by interpolation over the aerodynamic databases using bivariate splines.

The aerodynamics are calculated for Mach numbers between 0-10, angles of attack between 0° and 10° , and for altitudes between 0-40km. Separate aerodynamic simulations are performed for engine-on and engine-off conditions, as the operation of the scramjet engines changes the aerodynamic characteristics of the SPARTAN significantly. When the engines are powered on, the engines are generating thrust on the internal nozzle, as well as on the boat-tail and base. When the scramjet

engines are not operational air flows through the flowpath without fuel injection, generating a large amount of drag. The drag, lift and moment coefficients are determined by interpolating for Mach number, angle of attack, altitude, and centre of gravity as it shifts during flight. The drag and lift produced by each stage of the vehicle are calculated using the standard definition of the aerodynamic coefficients:

$$F_d = \frac{1}{2} \rho c_d v^2 A, \quad (3.4)$$

$$F_L = \frac{1}{2} \rho c_L v^2 A. \quad (3.5)$$

CART3D

The aerodynamics of the SPARTAN have been calculated using CART3D, an inviscid CFD package used in the preliminary design of aerospace vehicles. Cart3D utilises adjoint mesh adaption with a Cartesian cut-cells approach to produce an iteratively refined mesh to fit a flow solution. CART3D is been used to generate the aerodynamic database of the SPARTAN vehicle due to its applicability in both the subsonic and supersonic regimes, and its robustness across multiple flow solutions [16]. CART3D has previously been used to analyse hypersonic vehicles, and has shown good agreement with experimental data across multiple studies CITATIONXX.

The CART3D Meshes are initiated with an outer boundary distance of 40 times the vehicle length. This boundary distance was observed to produce suitable free stream conditions and good mesh convergence. Nine mesh adaption levels are used. Nine levels have been observed to generally produce good convergence, with moderate computation times of 1-3 hours per simulation. The convergence of the residuals and forces are investigated to ascertain if a solution has converged. Figure 3.8 shows an example solution validation for Mach 6, 2° angle of attack, engine-on conditions. Good convergence can be observed in the force functionals, with a corresponding decrease in the error estimate of the functional indicating solution convergence.

Viscous Correction

As Cart3D is an inviscid solver, the aerodynamic database generated by Cart3D lacks the forces generated by skin friction drag. In order for the aerodynamic model to more closely approximate realistic dynamics, a correction for the viscous forces on the SPARTAN is calculated, using the inviscid Cart3D cases. This inviscid correction utilises flat plate correlations for skin friction on each surface cell, employing a simplified running length based on the Euclidean distance to the respective stagnation feature. Further details of this method can be found in Reference [CITEXX]. This method has been shown to significantly improve upon the accuracy of the aerodynamic coefficients calculated by Cart3D for multiple test vehicles [CITEXX]. The viscous drag coefficients are generated for

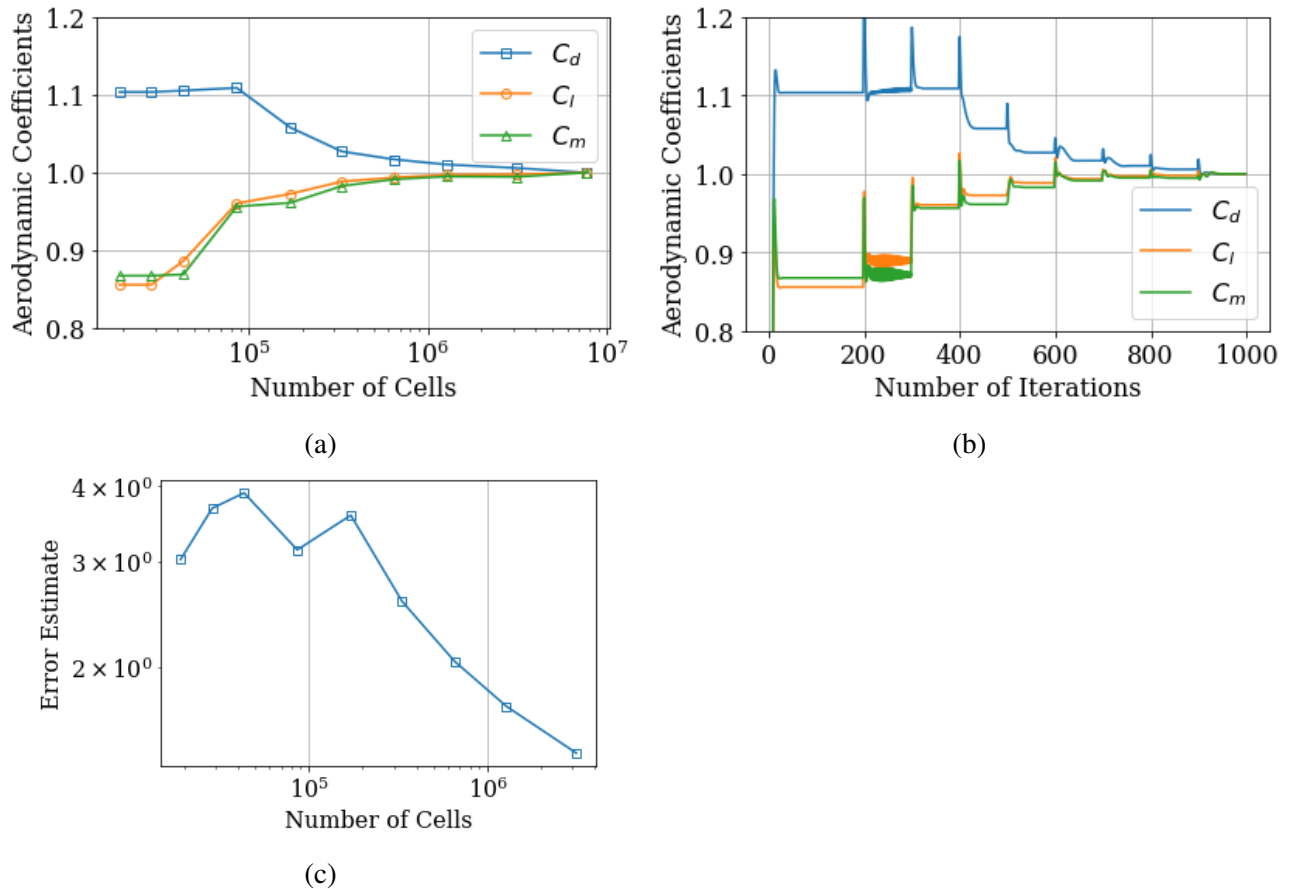


Figure 3.8: Viscous drag coefficient across various Mach numbers.

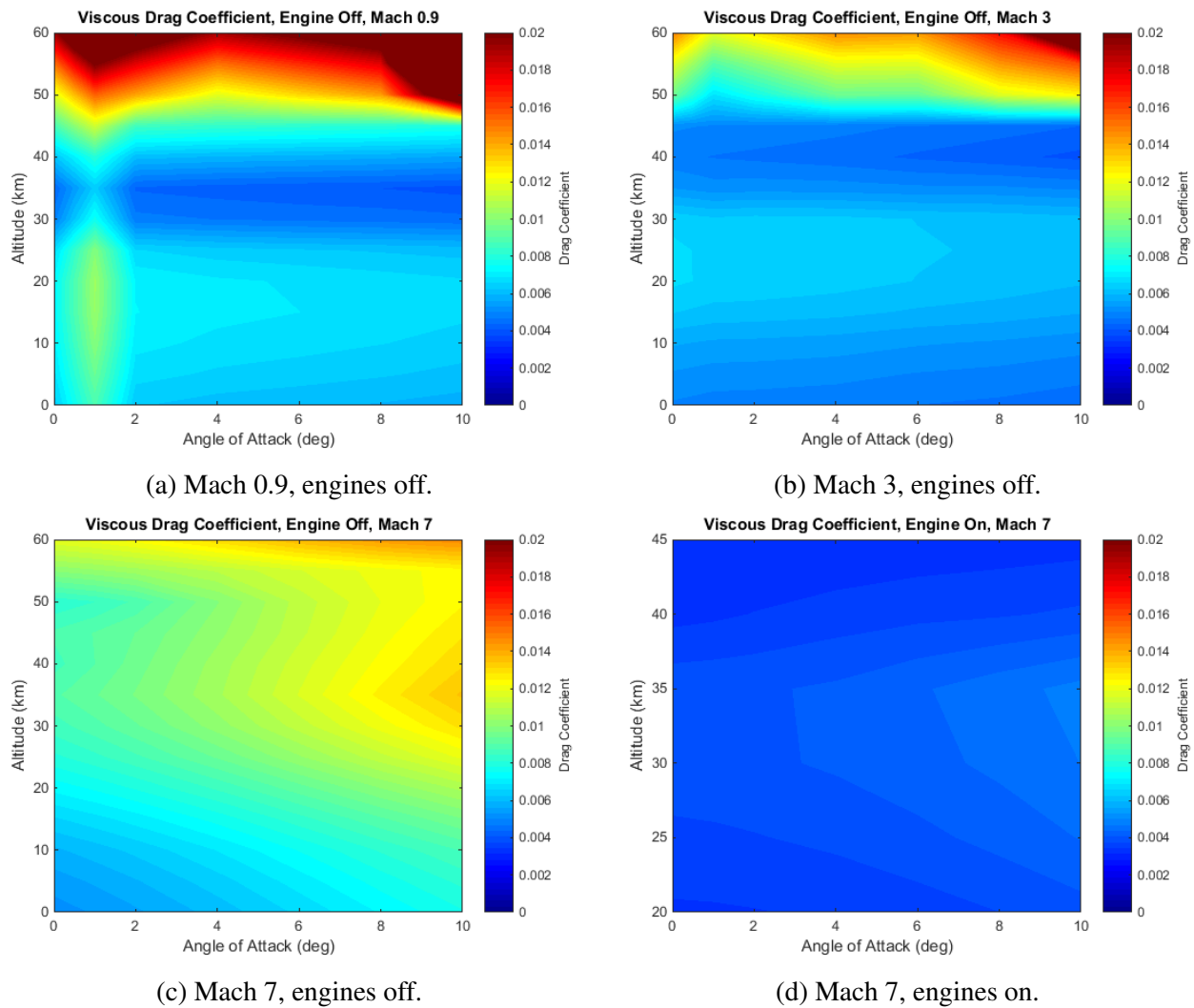


Figure 3.9: Viscous drag coefficient across various Mach numbers.

the SPARTAN at every Mach number and angle of attack which are simulated in Cart3D. Viscous databases are generated for both engine-on and engine-off cases, for altitudes of 20-45km and 20-60km respectively. The viscous drag coefficients for selected flight conditions are shown in Figure 3.9.

Trim Analysis

The SPARTAN is assumed to be trimmed at all conditions during flight. The SPARTAN is trimmed during flight using control surfaces on the wings. The trim is incorporated into the aerodynamic databases prior to trajectory simulation, assuming that the SPARTAN is trimmed at all conditions during flight. The SPARTAN as designed by Preller [CITEXX] is trimmed using control surfaces on the wings, shown in figure 3.10. Trim is determined by calculating the aerodynamic moment coefficient with zero flap deflection, then calculating the flap deflection necessary to balance the

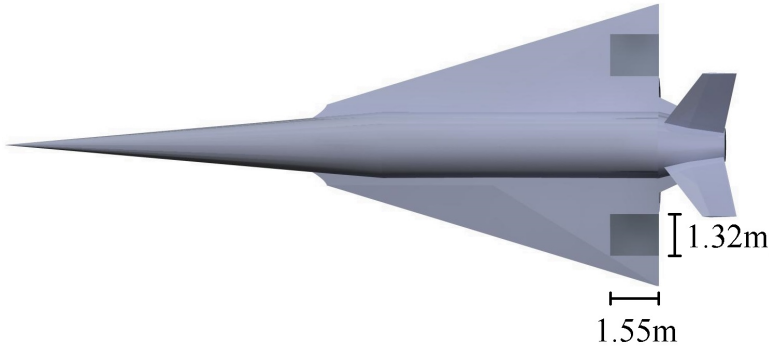


Figure 3.10: SPARTAN model showing control surfaces.

aerodynamic moments to zero. The moment generated by the body and wings of the SPARTAN is balanced by the moment generated by the ailerons, as well as the thrust moments on the engines and boat tail, when the C-REST engines are powered on. The force balance on the SPARTAN is shown in Figure 3.11. This trim balancing is calculated prior to trajectory optimisation for computational efficiency.

The trimmed aerodynamics of the SPARTAN are determined by modelling the flaps at deflected states of -20° , -10° , 10° , and 20° . Each of these deflected states were modelled in CREO and a surface mesh was created in Pointwise. The aerodynamics at each flap deflection were calculated at 0° angle of attack for Mach numbers between 0.2 and 10. For each aerodynamic data point of Mach numbers between 0.2 and 10, and angle of attacks from 0° to 10° , the necessary flap deflection are calculated, and the additional lift and drag produced by the flaps are added. Trimmed aerodynamic databases are calculated for engine on and engine off conditions, as well as at various centre of gravity locations. As the centre of gravity varies during flight, the aerodynamic databases are interpolated between using linear interpolation.

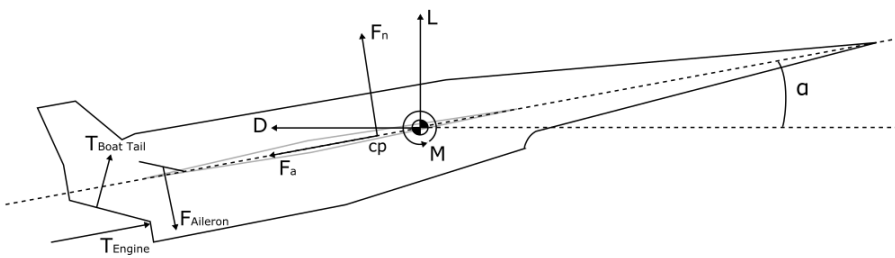


Figure 3.11: The forces on the SPARTAN during flight.

The centre of gravity locations of the SPARTAN are calculated using CREO. For simplicity, it is assumed that structural, systems and landing gear masses are homogeneously distributed throughout the centre fuselage of the SPARTAN. The calculated centre of gravity for the SPARTAN full of fuel

and including the third stage rocket is 15.23m along the body length. The centre of gravity varies as fuel is depleted throughout the acceleration phase, and at third stage release, changing the necessary flap deflections for trim. The cylindrical fuel tanks are depleted first, in order to shift the centre of gravity forward, and improve the aerodynamic stability of the SPARTAN during the majority of flight. Depleting fuel from the cylindrical fuel tanks first would likely also serve to reduce fuel slosh during flight, although the fuel slosh is not modelled in this study. After the cylindrical tanks have been depleted, the fuel in the conical tank within the nose is used. The third stage is released at the end of acceleration, and the centre of gravity changes significantly. When the third stage is released there is still fuel stored in the conical tank for flyback, during which centre of gravity change must also be modelled. Consequently, aerodynamic databases are created for centre of gravity conditions of;

- full of fuel including third stage,
- conical fuel tank full of fuel, including third stage,
- empty of fuel including third stage,
- conical fuel tank full of fuel after third stage release,
- and empty of fuel after third stage release.

Each of these conditions, along with the corresponding centre of gravity, is shown in Figure 3.12. At each of these conditions, aerodynamic coefficients and flap deflections necessary for trim are calculated. A point mass model is used in conjunction with the aerodynamic database, and atmospheric properties obtained from the U.S Standard Atmosphere 1976[26].

Figure 3.13 shows the necessary flap deflections to trim the SPARTAN. Engine-on cases are shown at full-fuel, full conical tank, and empty conditions with the third stage included, and an engine-off case is shown at a fuel-empty condition after third stage release. Additional figures illustrating the variation in moment coefficients are shown in Appendix XX. The flap deflections are designated as negative up. Negative flap deflection necessary for trim indicates that the centre of pressure is aft of the centre of gravity, and that the vehicle has positive static margin. It can be observed that while the cylindrical fuel tanks are being used, the SPARTAN is generally stable at low angles of attack, and the static margin is close to 0, requiring only small flap deflections for trim. As the fuel in the conical tank is depleted, the centre of gravity moves aft, and the SPARTAN develops a negative static margin, requiring larger flap deflections to trim at high Mach numbers. These large flap deflections indicate that the SPARTAN may experience instability issues at the end of its acceleration, however, determining the controllability of the SPARTAN is outside the scope of this study.

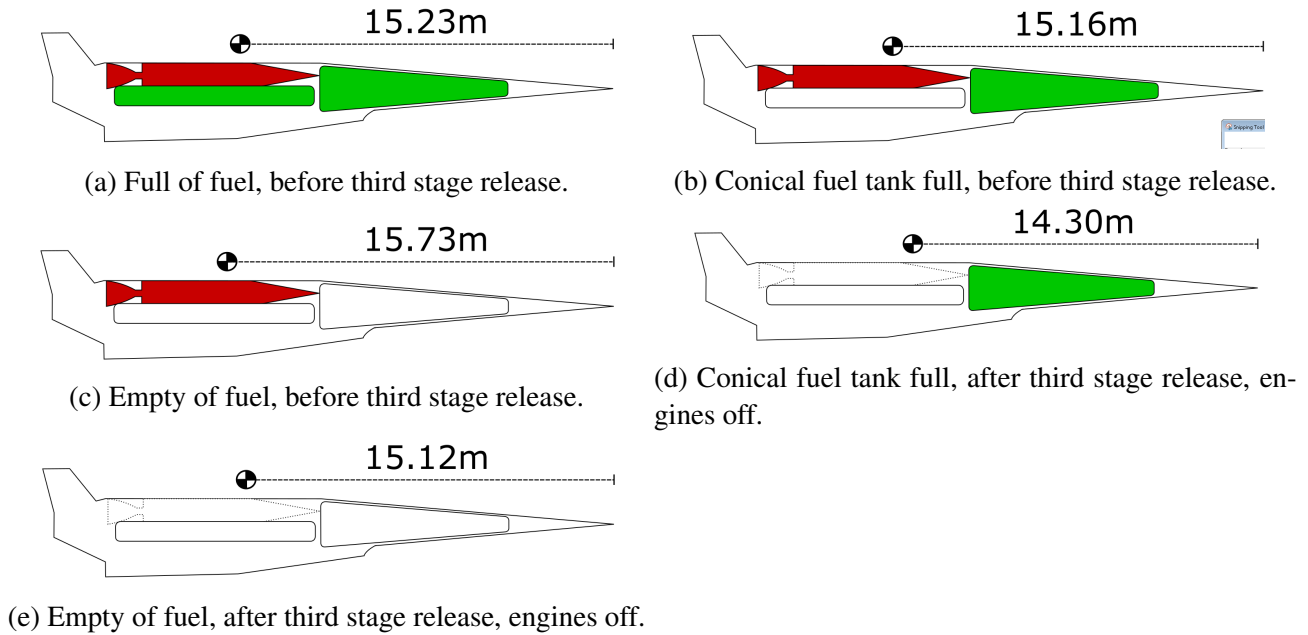


Figure 3.12: Centre of gravity positions throughout the flight of the SPARTAN.

Database Generation

The trimmed aerodynamic databases of the SPARTAN are generated in full prior to trajectory simulation to improve the computational efficiency of the simulation. The aerodynamic coefficients of lift, drag and moment are tabulated, and these tables are interpolated between during simulation. The process for generating the aerodynamic databases is shown in Figure 3.14. An initial surface triangulation of the SPARTAN is created in Pointwise, shown in Figure 3.15. This is then imported into CART3D as a watertight surface.

Following simulation in CART3D over the required flight conditions, the aerodynamic databases are generated. The simulation files are processed using Clic, a subprogram of CART3D used to calculate aerodynamic forces and moments, given surface pressure distributions. The solutions were processed for the necessary centre of gravity positions. At each flight conditions data point, and for each centre of gravity position, the flap deflections necessary for trim are calculated. The additional lift and drag generated by the flap are added to the untrimmed aerodynamics to create a trimmed database.

Engine-On Aerodynamics

The engine-on aerodynamics of the SPARTAN are used during the simulation of the acceleration phase, when the C-REST engines are operational at all times, as well as during the fly-back phase, when the engines are operational for a short time to aid the SPARTAN in returning to its initial launch site. The exhaust of the SPARTAN is simulated using CART3D, using SurfBC boundary conditions

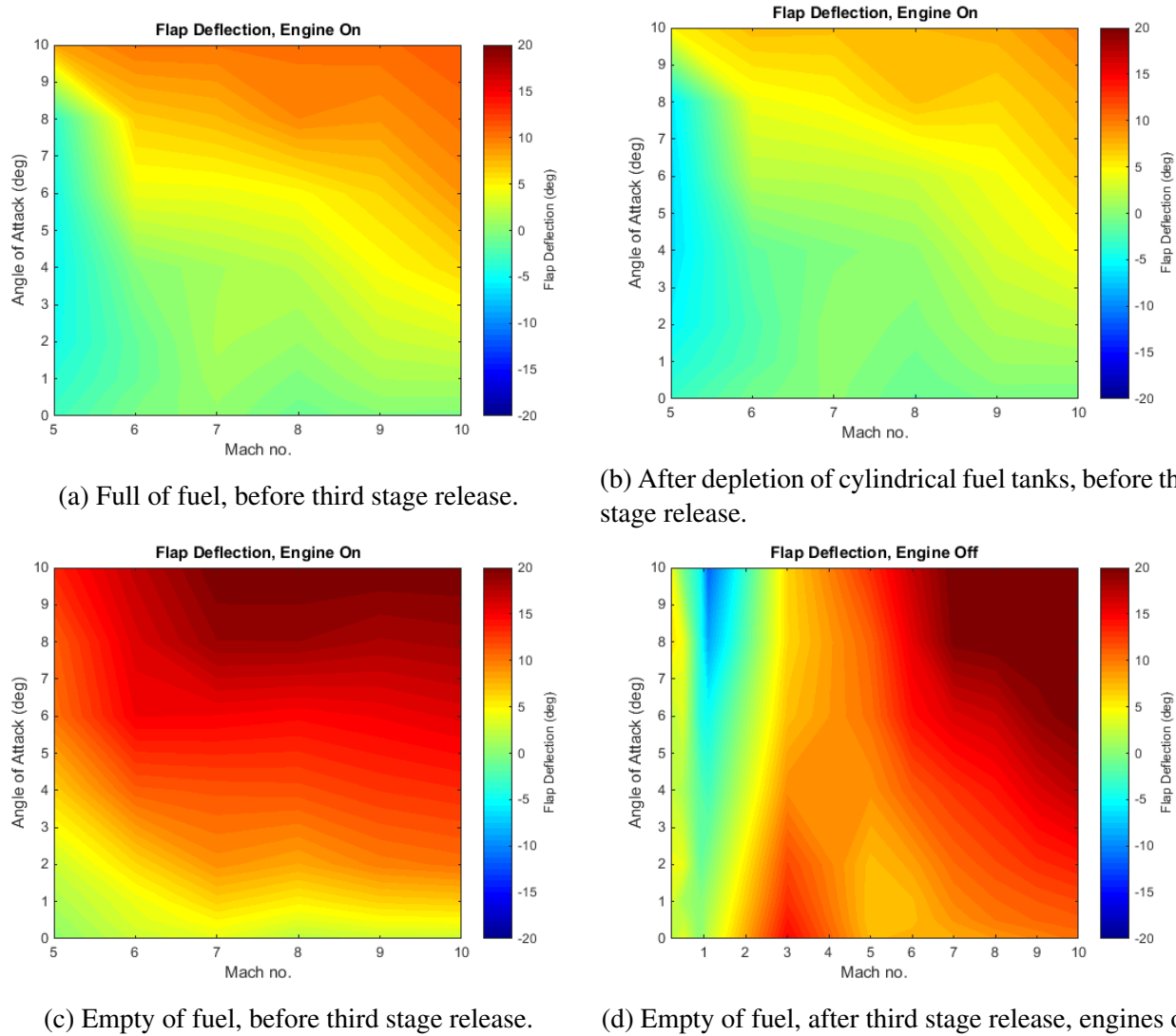


Figure 3.13: Flap deflection required for trim of the SPARTAN. Negative up.

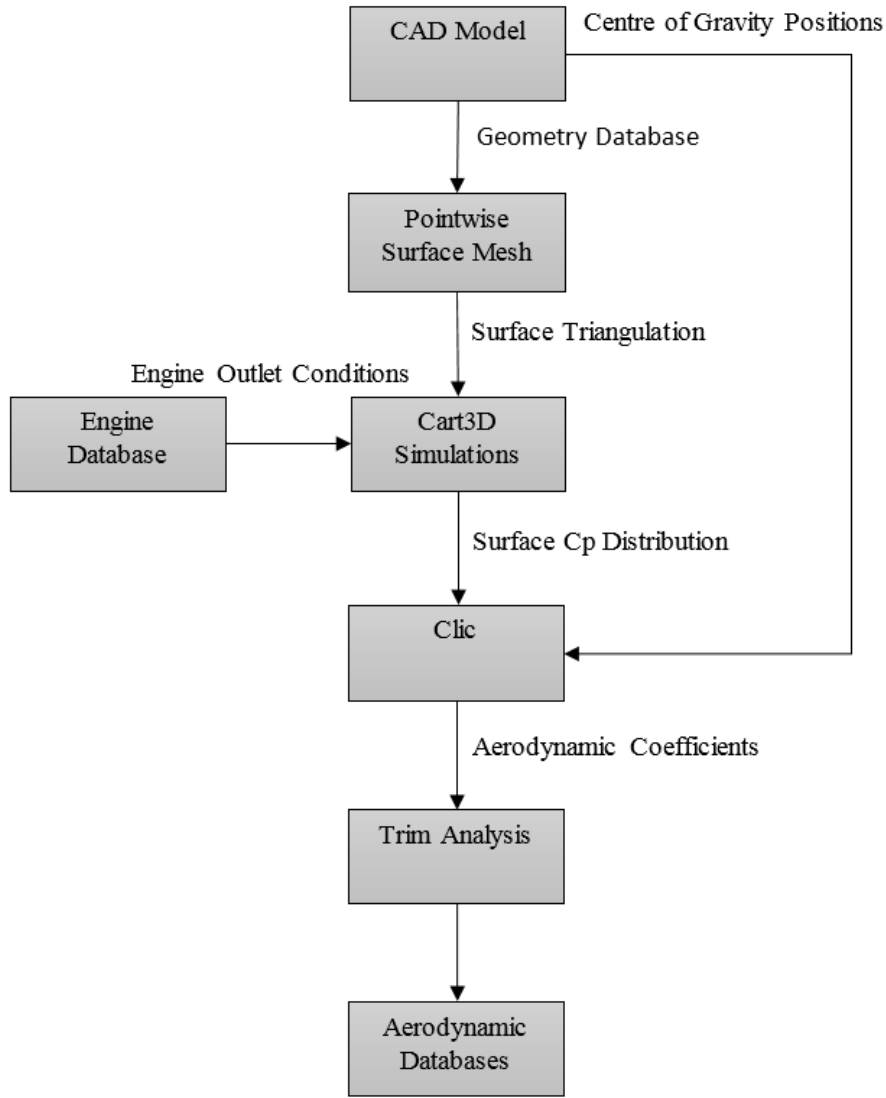


Figure 3.14: Process for generating aerodynamic databases.

which produce inflow and outflow conditions at the inlet and exit of the scramjet engines[84]. The exit conditions calculated by the CRESTM10 database, as defined in Section 3.1.2, are set as the outflow conditions for the CART3D surface. The scaled engine modelled in the CRESTM10 propulsion analysis has an exit area of 0.5586m^2 , smaller than the nozzle exit area on the SPARTAN, of 0.9719m^2 . To accommodate for this, the outflow surfaces are scaled to the exit area of the C-Rest engines simulated by quasi 1-D analysis, to ensure that the outflow conditions match the required nozzle position. The outflow surfaces are positioned inside the nozzle on the SPARTAN model, so that the area of the outflow surface is 0.5586m^2 . The surface triangulation of the SPARTAN with outflow surfaces is shown in Figure 3.16. CART3D performs simulations nondimensionally, and requires the outflow conditions of a boundary to be normalised. The outflow conditions of P_e , ρ_e and M_e given by the CRESTM10 propulsion model are normalised to CART3D nondimensionalised variables as follows

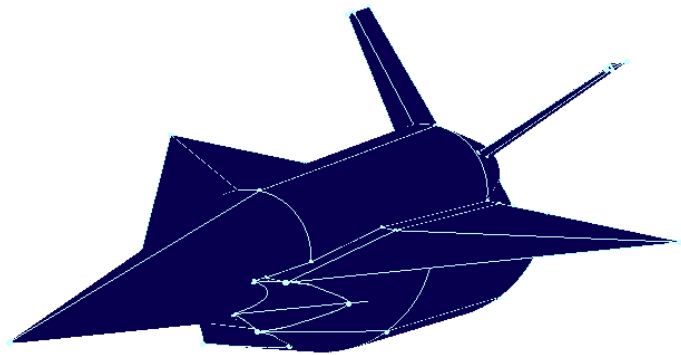


Figure 3.15: Surface triangulation of the Baseline SPARTAN, generated using Pointwise[CITATIONXX].

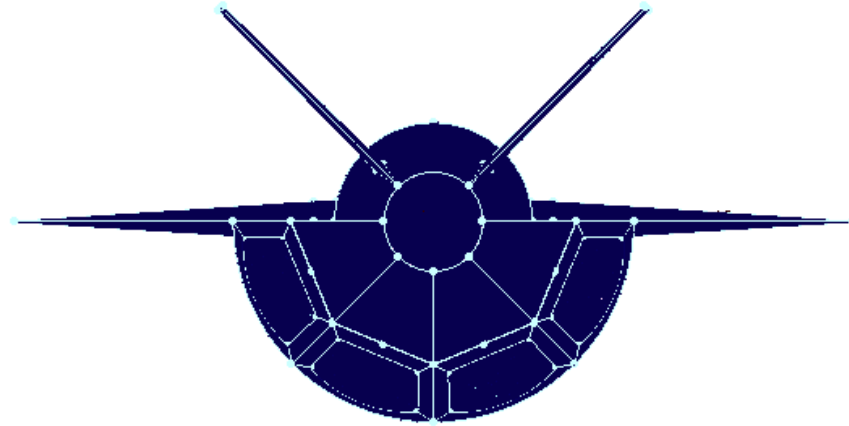


Figure 3.16: View of the SPARTAN surface triangulation showing engine outlet boundaries.

CITATIONXX;

$$P_e^* = P_e / (\gamma_0 P_0), \quad (3.6)$$

$$\rho_e^* = \rho_e / \rho_0, \quad (3.7)$$

$$M_e^* = \sqrt{\gamma_e / \gamma_0} (M_e \sqrt{P_e^* / \rho_e^*})^2. \quad (3.8)$$

Where $*$ indicates the nondimensionalised input to CART3D. This nondimensionalisation includes a correction on the Mach number to account for γ_e variation, which is not possible to include directly in CART3D[73]. The exhaust of the scramjet engines exits the nozzle of the SPARTAN, and is further expanded onto the boat tail on the rear of the SPARTAN fuselage, shown in Figure ???. This expansion

causes significant force on the boat tail of the SPARTAN, generating additional lift, thrust and moment forces. The total thrust generated by the SPARTAN, including the thrust generated by the additional nozzle expansion, and the forces on the boat tail, are shown in Figure 3.17, with the corresponding specific impulse shown in Figure 3.18.

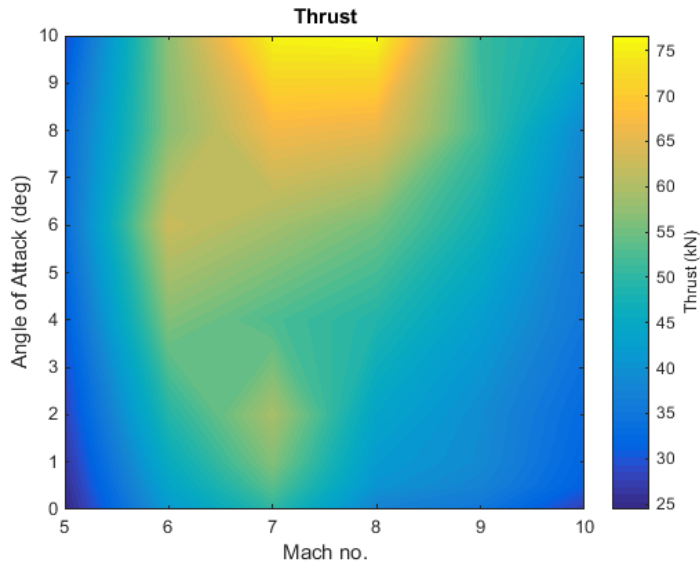


Figure 3.17: The total thrust output of the SPARTAN, including the C-REST database, and Cart3D nozzle and boat tail simulations.

The external aerodynamics of the SPARTAN with the scramjet engines powered on are calculated by removing the engine and boat tail from Cart3D simulations of the SPARTAN with engine flowpaths. Engine-on aerodynamic calculations are performed for Mach numbers 5, 7, 9 and 10. The aerodynamics of the SPARTAN with the scramjet engines powered on are shown in Figure 3.20.

Engine-Off Aerodynamics

During the majority of the return flight, the scramjet engines are not operational, and the SPARTAN is gliding without power. The return phase takes the SPARTAN from third stage separation, at approximately Mach 9, to landing approach at low subsonic speeds. While the engines are not powered on air flows through the flowpath without fuel injection, generating a large amount of drag. The aerodynamics of the SPARTAN are calculated using CART3D for Mach numbers from 0.2 to 10, and angle of attack values from 0° to 10° to cover the range of flight conditions experienced during the fly-back of the SPARTAN. An example CART3D solution is shown for a Mach 7 engine off condition in Figure 3.21. Figure 3.23 shows the engine off aerodynamic characteristics of the SPARTAN vehicle over the range of Mach numbers and angle of attack values analysed. These results show a distinct maximum region in the L/D of the SPARTAN at high Mach numbers, within the hypersonic regime. Below Mach 5, the L/D of the SPARTAN decreases sharply. This is caused by the scramjet

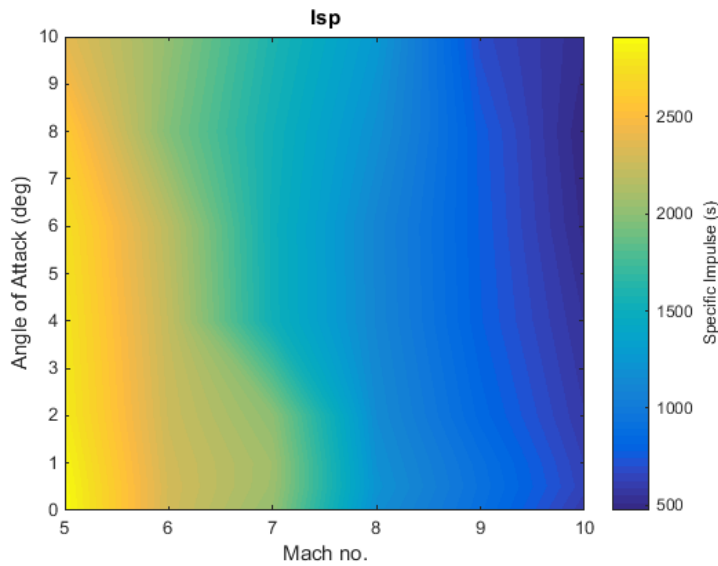


Figure 3.18: The specific impulse of the SPARTAN, including the C-rest database, and Cart3D nozzle and boat tail simulations.

engines unstarting, generating significant drag. The unstarted scramjet engines are shown in Figure 3.24. At low Mach numbers the L/D generally increases, except at very low angle of attack, as the effects of the unstarted engine lessen. Below Mach 1 the L/D of the SPARTAN increases significantly, in part due to not having the significant drag induced from the engines unstarting, as observed in the supersonic regime.

3.2 First Stage Rocket

The first stage rocket is required to deliver the second stage to near horizontal flight at Mach 5.1 flight conditions, after which it is discarded. To achieve this, the first stage rocket is modelled as a Falcon-1e first stage scaled down lengthwise to 8.5m, keeping the original diameter of 1.67m[CITATIONXX]. An additional 1m is added between the first stage and the SPARTAN to allow for any necessary stage interfacing, although this interface is not modelled. The Falcon-1e has been chosen due to its appropriate scale, and the proven flightworthiness of the Falcon-1. The first stage is attached to the rear of the scramjet second stage and is powered by a single LOX-kerosene Merlin 1-C engine. A connecting cowl has been modelled between the first stage rocket and the SPARTAN to improve the aerodynamic profile. The first stage has a structural mass of 1356kg, determined by scaling of the structural mass of the Falcon-1e. The engine mass of the Merlin 1-C is kept constant during scaling at 630kg[CITATIONXX]. The mass of the fuel in the first stage is scaled as part of the optimisation routine, as the dynamics of the vehicle, and its ability to reach a given separation point, are very closely coupled to the available fuel mass.

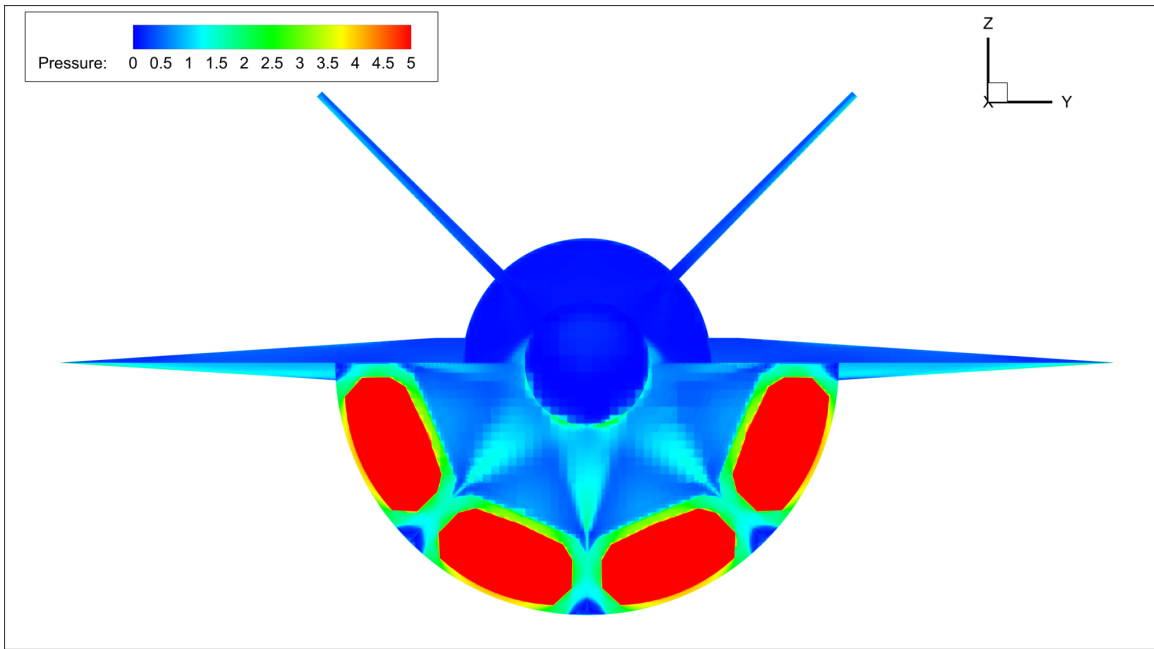


Figure 3.19: Engine-on CART3D simulation at Mach 6, 2° angle of attack, and 25km altitude.

The thrust and specific impulse of the Merlin 1-C are determined by interpolation between the sea level and vacuum specific impulse of the Merlin 1-C, shown in Table 3.2, with pressure. Thrust scaling is determined by linear pressure scaling using nozzle exit area, $T = T_{SL} + (p_e - p_{SL})A_e$. The Merlin 1-C is throttled down to a constant 70% to allow the first stage to pitch over more easily.

$I_{SP_{SL}}$	275s
$I_{SP_{vac}}$	304s
T_{SL}	555.9kN
A_e	$0.552m^2$

Table 3.2: First Stage Engine Properties [CITATIONXX].

3.2.1 Aerodynamics Including First Stage

The aerodynamics of the launch system during first stage flight are calculated in a similar manner to those of the SPARTAN without the first stage rocket, as detailed in Section 3.1.3. The aerodynamics of the SPARTAN and first stage rocket are calculated using CART3D. The first stage aerodynamics are modelled between angles of attack of 0° to -5°, as the first stage will be flying at negative angle of attack to induce faster pitch-over. Mach numbers from 0.2 to 5.1 (second stage separation velocity) are simulated. Figure 3.26 shows an example CART3D simulation case, at Mach 2, -1° angle of attack. The coefficient of lift, drag and aerodynamic moment are tabulated for each simulation. Figure 3.27 shows the lift and drag coefficients of the first stage, as well as the lift-over-drag, across the simulated

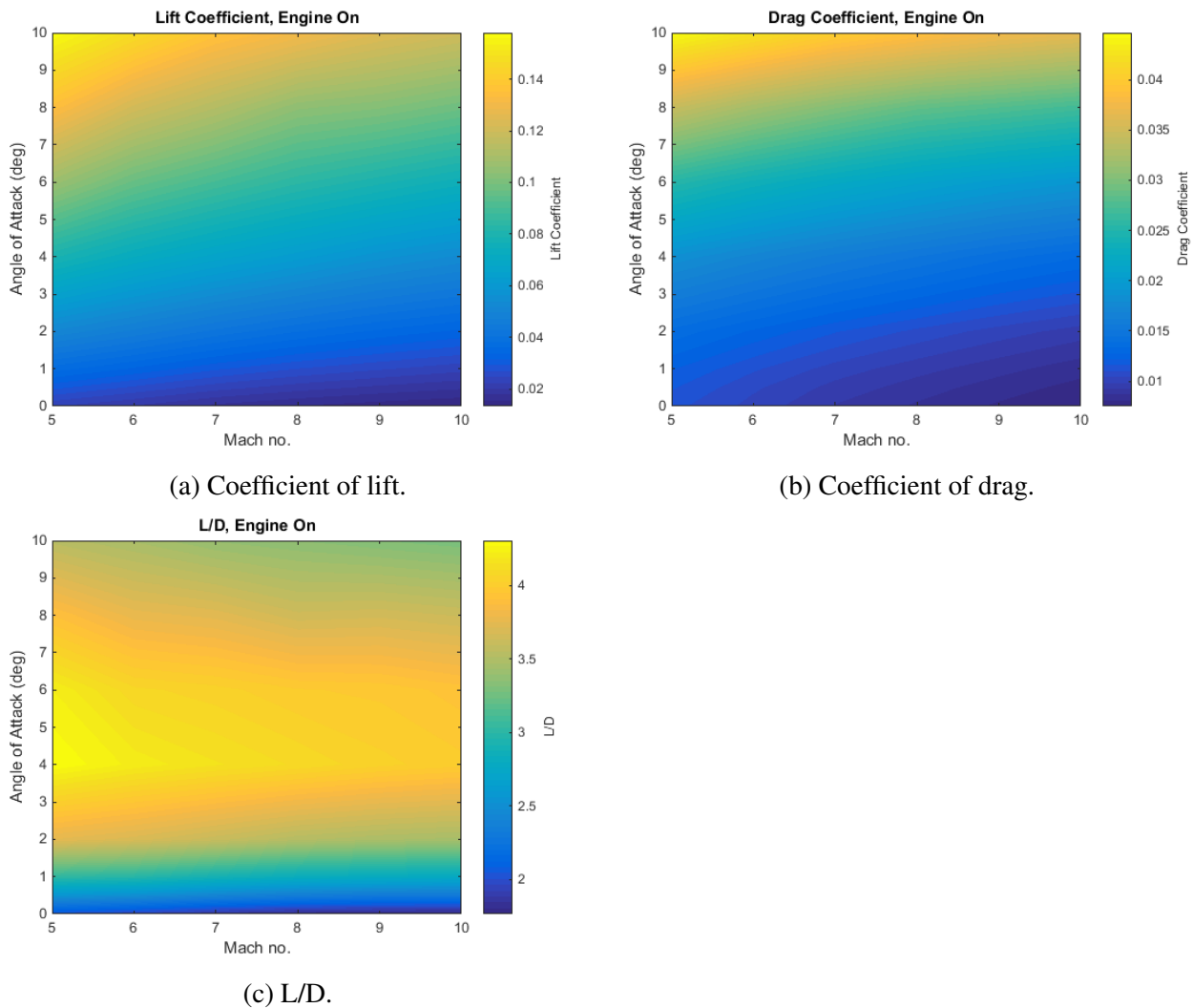


Figure 3.20: Aerodynamic coefficients with the C-REST engines powered on. Coefficients correspond to a reference area of 62.77m^2 .

Mach Numbers and angles of attack. The First stage is trimmed using thrust vectoring of the Merlin 1-C engine during flight.

3.3 Third Stage Rocket - Baseline

The third stage has a total length of 9m, with a 3m long nose, 4.5m long centrebody and 1.5m long engine. In this study the third stage rocket has been designed to accommodate a SpaceX Kestrel engine. In previous studies, the third stage has been designed to be powered by a Pratt & Whitney RL-10-3A pump-fed engine. The Kestrel has been used over the RL-10-3A for its cost effectiveness. As a pressure-fed engine, the Kestrel trades off specific impulse for weight and cost savings when compared to the RL-10-3A. As the only expendable portion of the system; the cost of the third stage

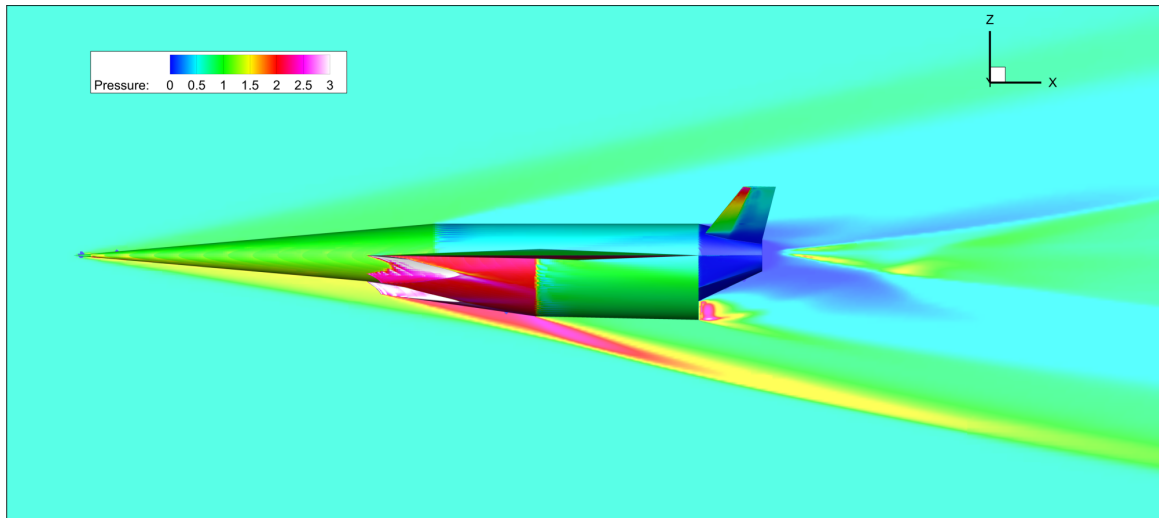


Figure 3.21: Side view of the CART3D flow result for the SPARTAN, at Mach 6, 2° angle of attack.

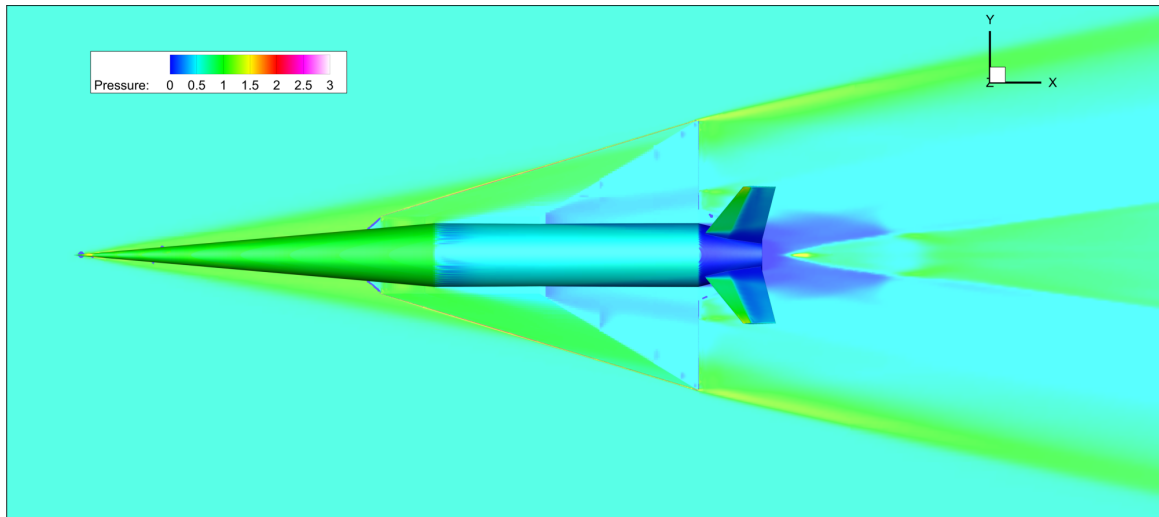
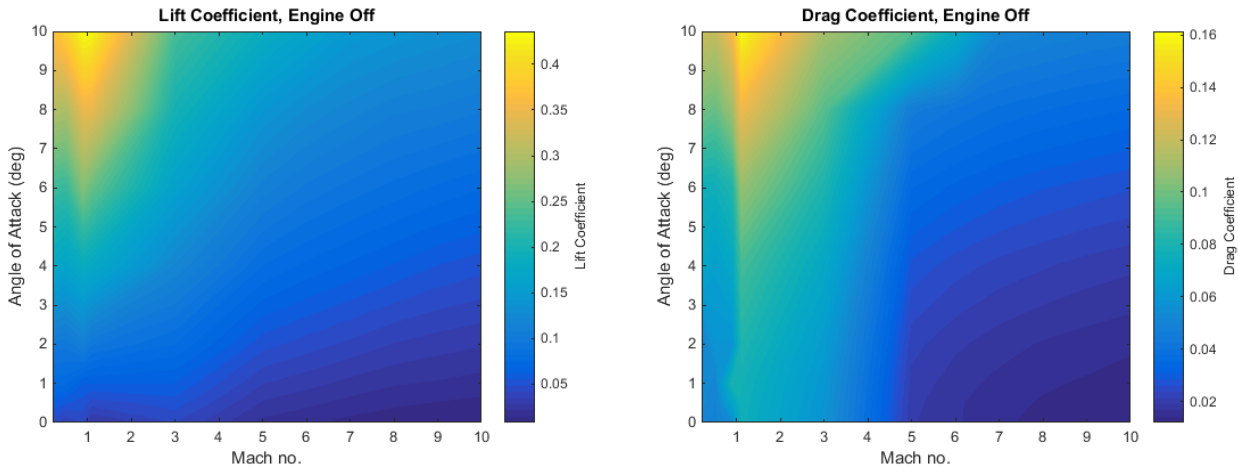


Figure 3.22: Top view of the CART3D flow result for the SPARTAN, at Mach 6, 2° angle of attack.

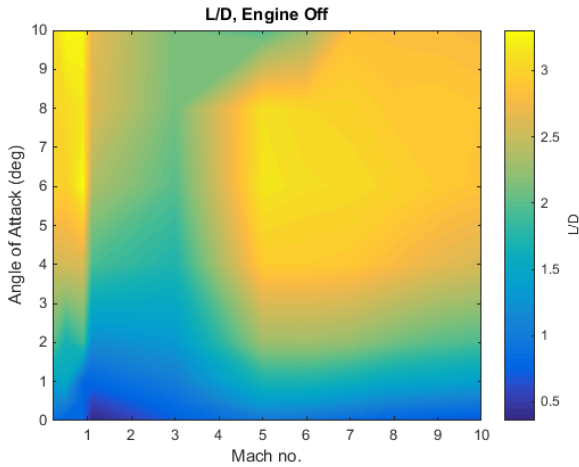
is one of the main drivers of overall system cost. Reducing the cost of the third stage allows the cost of launch to be directly reduced.

The third stage rocket is released at the end of the scramjet accelerator burn, and lifts the payload out of the atmosphere and into the desired orbit. The third stage weighs a total of 3300kg. This has been chosen as a nominal design weight, to satisfy the fuel necessary to achieve orbit with an acceptable payload, while also allowing for ample payload volume. The internal layout of the third stage rocket is shown in Figure 3.28. The third stage has a structural mass fraction of 0.09, similar to the Falcon 1 second stage [119]. This gives a total structural mass (without heat shield) of 285.7kg.

The kestrel engine used in the third stage is modified to have 50% increased propellant mass flow rate, giving a mass flow rate of 14.8kg/s. The nozzle exit of the Kestrel engine has been kept constant at 1.1m diameter. An increase in mass flow necessitates a corresponding increase in throat area. This



(a) Coefficients of lift of the SPARTAN, calculated us- (b) Coefficients of drag of the SPARTAN, calculated us-
ing CART3D.



(c) L/D of the SPARTAN.

Figure 3.23: Aerodynamic Characteristics of the SPARTAN with C-REST engine powered off. Coefficients correspond to a reference area of 62.77m^2 .

increase in throat area decreases the area ratio of the nozzle. The initial area ratio is 60, measured from schematics in the Falcon-1 Users Guide. A 50% mass flow increase corresponds to a 50% throat area increase, which causes the area ratio to decrease to 40. This decrease in area ratio results in a 2% loss of efficiency from the nozzle, measured from the thrust coefficient relationships shown in Figure 3.29[122]. The coefficient of thrust is calculated for a specific heat ratio of 1.20, as this is close to the specific heat ratio of oxygen and RP-1 of 1.24[122]. The modified specific impulse of the engine is 310.7s.

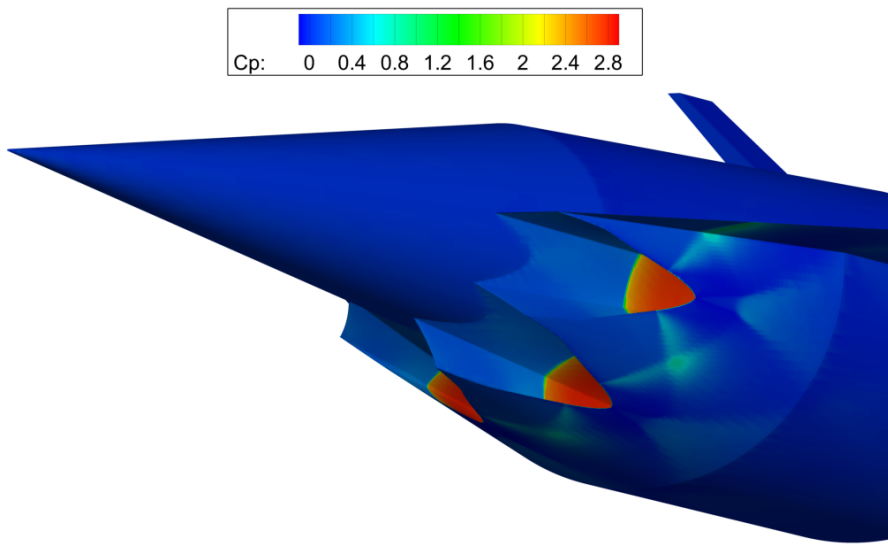


Figure 3.24: Unstarted scramjet engines at mach 3, 2° angle of attack.

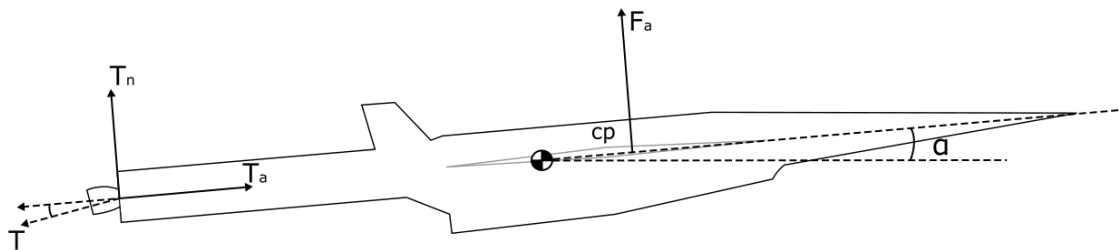


Figure 3.25: Thrust vectoring moment balancing of the first stage.

3.3.1 Heat Shield Sizing

The third stage rocket is separated from the SPARTAN at a high dynamic pressure, after which it spends a considerable amount of time accelerating in-atmosphere before reaching exoatmospheric conditions. The time spent within a high dynamic pressure environment creates a large amount of heat loading, which must be mitigated by heat shielding. The heat shielding must be capable of withstanding the extremely high heat and structural loading necessary to protect the third stage rocket internals and payload, as well as being lightweight, as the payload-to-orbit is extremely sensitive to the mass of the third stage, and cost effective, as increasing the cost of the third stage directly increases launch cost due to it being expendable.

The heat shield used to protect the third stage is constructed from a tungsten nose tip, a reinforced carbon-carbon nose cone, and a phenolic cork cylinder, weighing 130.9kg in total. This heat shield is designed based on the materials and thicknesses defined in [92]. A mass breakdown is shown in Table 3.3. Tungsten is used at the tip of the nose cone, the area of maximum heat loading. Tungsten

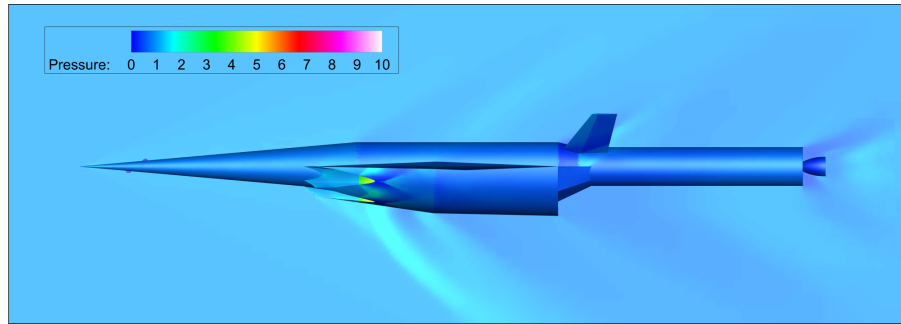


Figure 3.26: CART3D result for the SPARTAN and first stage vehicles at Mach 2, -1° angle of attack.

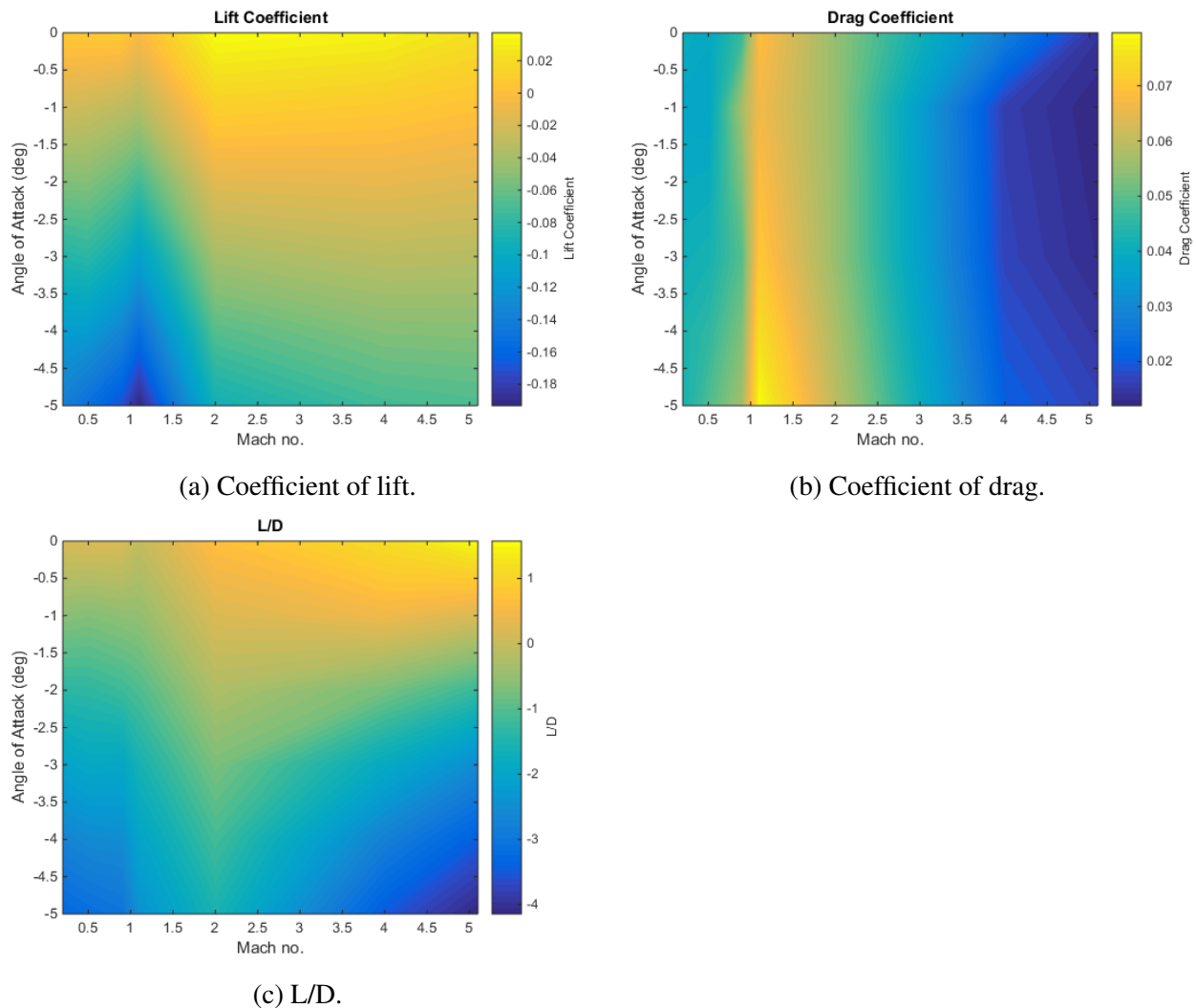


Figure 3.27: Aerodynamic characteristics of the SPARTAN including the first stage rocket.



Figure 3.28: The third stage rocket, showing major internal features.

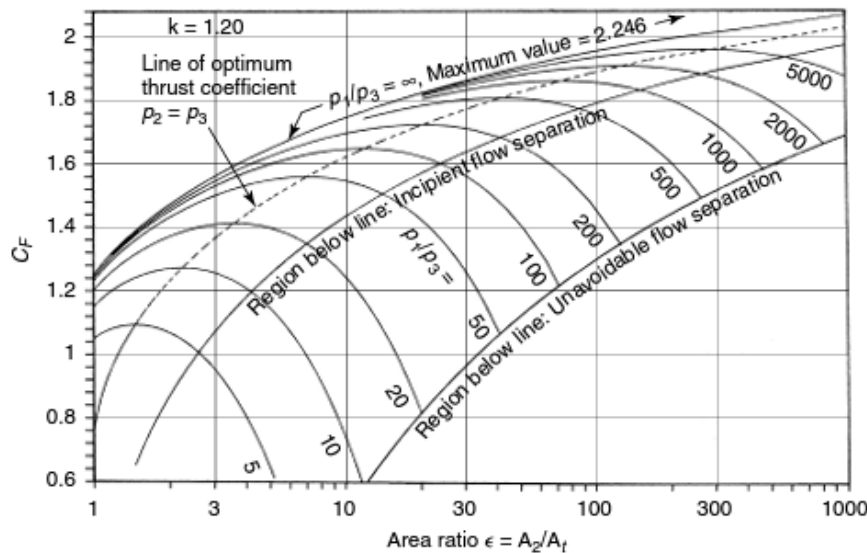


Figure 3.29: Variation in coefficient of thrust with area ratio [122].

has extremely high heat resistivity, and a very low coefficient of thermal expansion[CITATIONXX]. However, tungsten is costly and heavy, and is only used on the very tip of the nose where it is absolutely necessary. Reinforced carbon-carbon is used for the conical section of the heat shield, as this is an area that will be subject to high heat and structural loading. Carbon-carbon is able to withstand high temperatures, as well as being thermal shock resistant and having a low coefficient of thermal expansion[35]. Carbon-carbon is used in rocket and missile nose cones, as well as on aircraft leading edges due to its good heat resistant properties[35]. However, carbon-carbon is expensive, and is used only on the conical section of the heat shield to minimise cost. For the cylindrical section of the heat shield protecting the main body of the third stage, phenolic cork is used. Phenolic cork is a composite of ground cork and phenolic binders which is light and relatively cheap, with good heat resistivity. Phenolic cork has lower tensile strength and heat resistivity than carbon-carbon[19, 35], but is cheaper and lighter, making it appropriate for use on section of the heat shield which experiences lower heating and structural loads.

Part	Density	Geometry	mass
Tungsten Nose	$\rho_{Tungsten} = 19250 \text{ kg/m}^3$	50mm diameter cylinder, spherical tip	12.6kg
C-C Cone	$\rho_{CC} = 1800 \text{ kg/m}^3$	10mm thick, conical	93.4kg
Phenolic Cork Cylinder	$\rho_{PhenolicCork} = 320 \text{ kg/m}^3$	5mm thick, cylindrical	24.9kg

Table 3.3: Third stage heat shield breakdown.

3.3.2 Fuel Tank Sizing

The internal design of the third stage is allowed to be slightly variable as the trajectory is optimised. The third stage mass is fixed at 3300kg, and the calculated payload-to-orbit varies by exchanging leftover fuel mass for effective payload mass. To calculate the dynamics of the third stage, the fuel tanks have been approximately sized, assuming 160kg of payload-to-orbit. Realistically the exchange between fuel and payload mass would cause the fuel tanks to be resized slightly. For the purposes of this study the fuel tanks are assumed to be of constant size for simplicity. Currently this is a reasonable assumption as the internals of the rocket are very simplified. The structural mass is held constant at 9%. The third stage carries a total propellant mass of 2736.7kg. Table 3.4 breaks shows the component break-down of the LOX oxidiser and RP1 fuel.

	LOX	RP1
Ratio	2.56	1
Density	1141kg/m3	813kg/m3 [72]
Volume	1.7248m3	0.9455m3
Mass	1968.0 kg	768.7 kg

Table 3.4: Third stage fuel distribution.

3.3.3 The Aerodynamics of the Third Stage Rocket

The third stage aerodynamics have been calculated using Missile DATCOM [REFXX], a preliminary design tool for estimating the aerodynamic characteristics of missile and rocket vehicles. Missile DATCOM utilises empirical methods, along with various estimation techniques, to compute the aerodynamics of missile and rocket-like vehicles across the subsonic, supersonic and hypersonic regimes. The aerodynamics of the third stage rocket are shown in Figure 3.30. The code used to compute the aerodynamics of the third stage rocket is detailed in Appendix XX.

Thrust Vectoring

The third stage rocket is controlled via thrust vectoring. The centre of pressure is calculated using missile DATCOM. The thrust vector is set so that the moment generated by the engine matches the lift force acting at the centre of pressure, shown in Figure 3.31. The maximum thrust vector limit

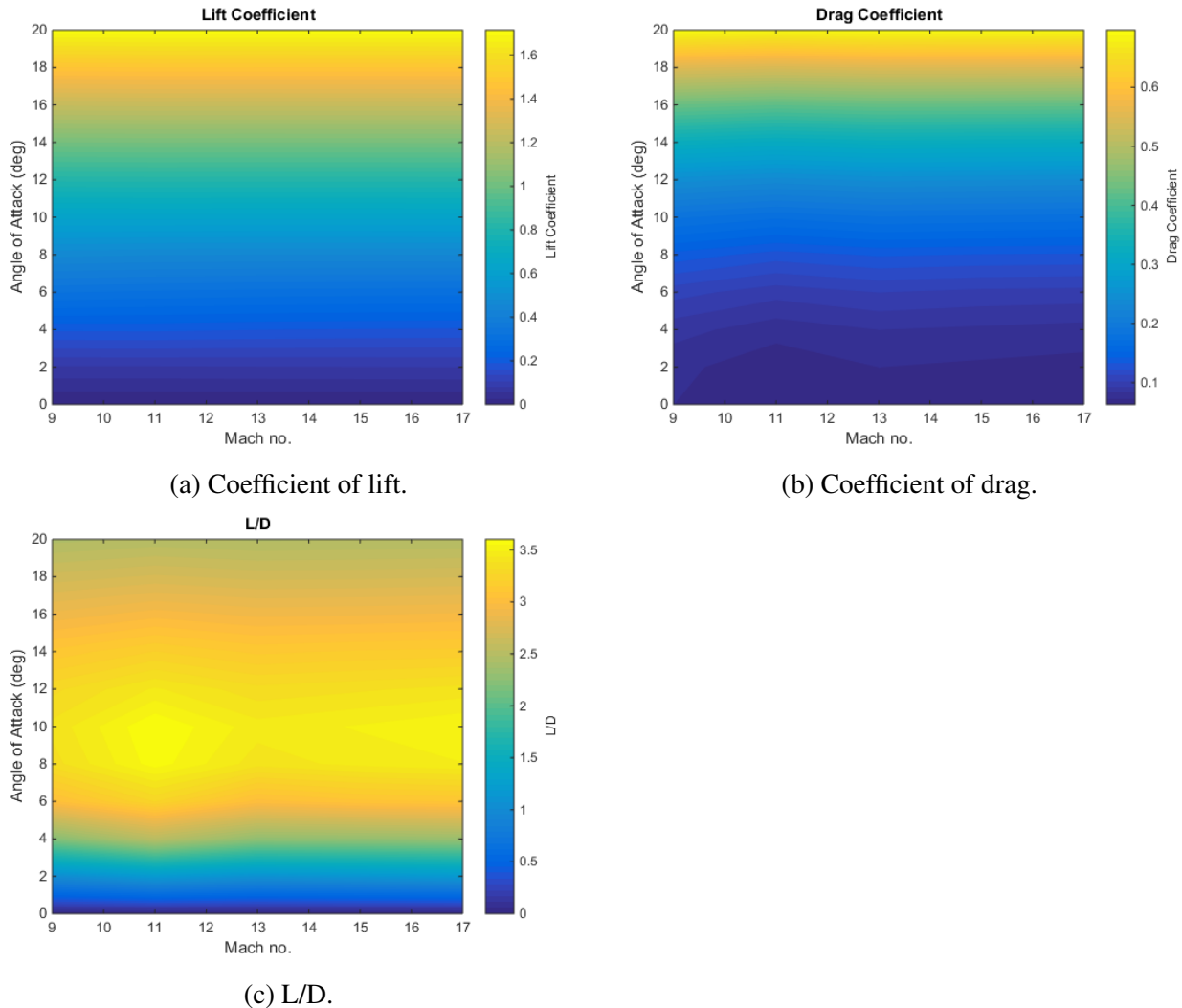


Figure 3.30: Aerodynamic characteristics of the baseline third stage rocket, for a reference area of 0.95m^2 .

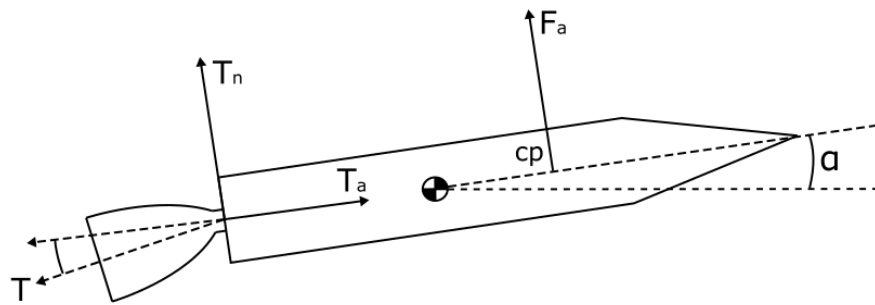


Figure 3.31: Thrust vector moment balancing of the third stage.

has been set to 8° . As no data on the maximum thrust vectoring capabilities of the kestrel engine was able to be found, this was set to the maximum gimbal range of the Aestus pressure-fed engine and Orbital Manoeuvring Engine (OME), which are similarly sized engines, although pressure fed CITATIONXX.

The centre of gravity is determined using CREO, and is at XXm from the nose. It is assumed that the mass of the structure of the rocket (excluding fuel tanks, heat shielding, engine and payload) is distributed homogeneously for simplicity. The third stage rocket is statically unstable. Flying this rocket at an angle of attack will require an advanced automatic controller, as the only control available is produced by thrust vectoring. This study assumes that the third stage rocket controllable as long as the thrust vector limits of the vehicle are not exceeded.

CHAPTER 4

LODESTAR

This chapter covers the package LODESTAR (Launch Optimisation and Data Evaluation for Scramjet Trajectory Analysis Research), which has been used to calculate the optimal trajectories of the rocket-scramjet-rocket system. The structure of LODESTAR is presented, as well as the set-up of LODESTAR for the rocket-scramjet-rocket trajectory optimisation, and the verification methods used to determine if a solution has converged correctly.

LODESTAR optimises a trajectory towards a user-defined objective function, such as maximum payload-to-orbit, subject to constraints which bound the operational region of a vehicle. LODESTAR is MATLAB based and utilises GPOPS-2[CITEXX], a proprietary pseudospectral method optimisation package which utilises an hp-adaptive version of the Radau pseudospectral method, ie. the pseudospectral method with collocation at Legendre-Gauss-Radau points. At these points, the derivatives of the approximating polynomials are constrained to the vehicle dynamics. Between these points, the Legendre polynomials used for approximation ensure that the dynamics of the launch vehicles are interpolated accurately. The operation of the pseudospectral method is described in further detail in Section 3.1.2. LODESTAR provides setup files to configure GPOPS-2 for multiple vehicle launch optimisation, and processing functions to asses the viability of the optimised solutions and plot the solutions effectively. LODESTAR also provides simulations of the vehicles within the launch system including interpolation schemes specifically designed to provide smooth, continuous aerodynamic and engine properties to ensure that the optimisation converges correctly. Both rocket-powered and scramjet-powered vehicles are accurately modelled within LODESTAR in 6 degrees of freedom. LODESTAR contains multiple modes configured for the SPARTAN launch system, which are able to optimise trajectories for,

1. The ascent of the first stage rocket,
2. The ascent of the second stage scramjet-powered accelerator,

3. The flyback of the second stage scramjet-powered accelerator,
4. The ascent of the third stage rocket, and
5. Combined trajectories of multiple stages in any combination.

Figure 4.1 illustrates a simplified iteration of the pseudospectral solver. GPOPS-2 provides an initial guess of the solution to the external modules, over an initial mesh of nodes. The external modules calculate the aerodynamic and engine performance of the launch system at each point along the trajectory, along with atmospheric conditions. This data is then used to calculate the dynamics of the vehicle along the trajectory. The constraints and cost function are then evaluated by GPOPS-2 and passed through to the IPOPT nonlinear optimisation package[132], which updates the guess of the state and control variables. This process is repeated for a set number of iterations, with the solution evaluated at each iteration to compute the feasibility and optimality of the solution. This process repeats until the solver reaches a predefined tolerance of optimality, or a predefined number of iterations. At this point, GPOPS-2 updates the node mesh, clustering nodes and creating mesh segments around key sections of the trajectory to improve accuracy. The process repeats for a number of mesh iterations defined by the user.

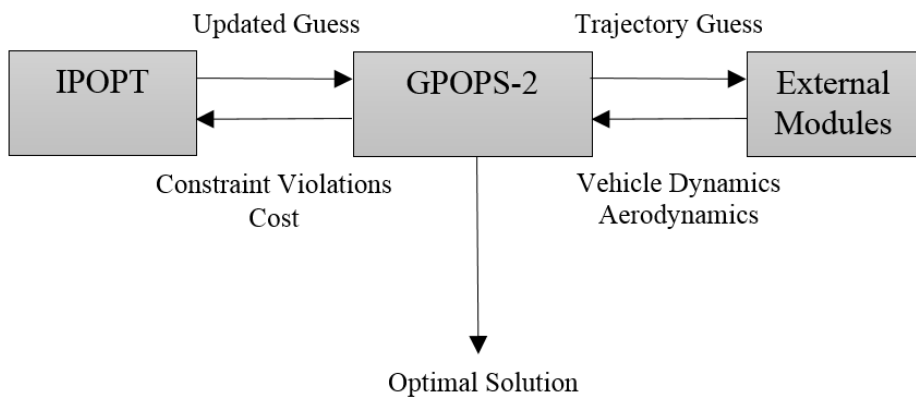


Figure 4.1: The optimisation process.

Due to the nature of the pseudospectral method, it is possible that GPOPS-2 will not be able to converge to a physically valid or optimal solution. LODESTAR contains a number of verification modules which assess the optimised trajectory solution to ensure that the solution has converged sufficiently, and that the dynamics of the solution are accurate. To aid in ensuring that an optimal solution is reached, GPOPS-2 is initiated from four separate initial guesses, with final altitude guess varied by 1km between each guess. These iterations of GPOPS-2 are run in parallel, using Matlab's Parfor function. After all iterations of GPOPS-2 have completed, the state feasibility is calculated

for each solution. The 'best' solution is chosen as the solution with the most accurately modelled dynamics.

4.1 Vehicle Simulation

Each of the vehicles within the rocket-scramjet-rocket launch system are simulated by establishing a set of dynamic equations which fully describe the motion of the vehicle in terms of the time, states (\mathbf{x}), and controls (\mathbf{u}) of the system;

$$\dot{\mathbf{x}}(t) = f[t, \mathbf{x}(t), \mathbf{u}(t)]. \quad (4.1)$$

The states and controls are the variables which define the time dependent physical characteristics of the system. The state variables are dependent on the controls and the system dynamics, while the control variables are the variables which drive the behaviour of the system and are independently variable.

These dynamic equations consist of the equations of motion of the vehicle, as well as other important time varying parameters, such as fuel mass flow rate. The dynamic equations are defined by the coordinate system, and the outputs of each vehicle model. These are nonlinear equations which depend on the interpolation of data sets which supply the atmospheric, aerodynamic and propulsion characteristics of each vehicle. The methods used to interpolate these data sets must be as smooth and continuous as possible, and cover the entire possible operational range of the vehicle. Even if the solution is well within the range of all input data sets, the solver will potentially explore all regions within the user defined bounds. If there are large discontinuities or inaccurate extrapolation effects within the possible solution space, the solver may be unable to converge, or converge to a physically invalid solution.

4.1.1 6DOF Equations of Motion

The dynamics of the vehicle are calculated in six degrees of freedom, illustrated in Figures 4.2 and 4.3, with yaw constrained to zero. The dynamics of all stages are calculated using an geodetic rotational reference frame, written in terms of the angle of attack α , bank angle η , radius from centre of Earth r , longitude ξ , latitude ϕ , flight path angle γ , velocity v and heading angle ζ . The equations of motion are given from [56]:

$$\dot{r} = v \sin \gamma \quad (4.2)$$

$$\dot{\xi} = \frac{v \cos \gamma \cos \zeta}{r \cos \phi} \quad (4.3)$$

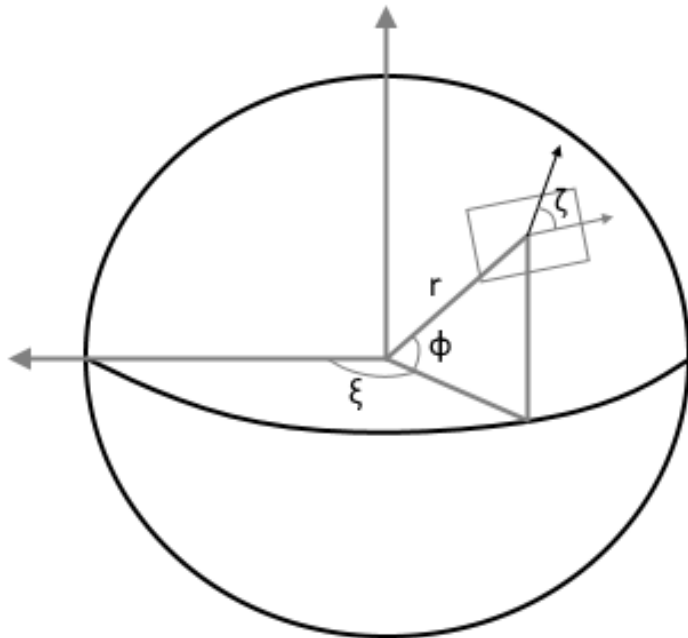


Figure 4.2: The Earth-fixed components of the geodetic rotational coordinate system.

$$\dot{\phi} = \frac{v \cos \gamma \sin \zeta}{r} \quad (4.4)$$

$$\dot{\gamma} = \frac{T \sin \alpha \cos \eta}{mv} + \left(\frac{v}{r} - \frac{\mu_E}{r^2 v} \right) \cos \gamma + \frac{L}{mv} + \cos \phi [2\omega_E \cos \zeta + \frac{\omega_E^2 r}{v} (\cos \phi \cos \gamma + \sin \phi \sin \gamma \sin \zeta)] \quad (4.5)$$

$$\dot{v} = \frac{T \cos \alpha}{m} - \frac{\mu_E}{r^2} \sin \gamma - \frac{D}{m} + \omega_E^2 r \cos \phi (\cos \phi \sin \gamma - \sin \phi \cos \gamma \sin \zeta) \quad (4.6)$$

$$\dot{\zeta} = \frac{T \sin \alpha \sin \eta}{mv \cos \gamma} - \frac{v}{r} \tan \phi \cos \gamma \cos \zeta + 2\omega_E \cos \phi \tan \gamma \sin \zeta - \frac{\omega_E^2 r}{v \cos \gamma} \sin \phi \cos \phi \cos \zeta - 2\omega_E \sin \phi \quad (4.7)$$

4.2 Mission Definition

LODESTAR has been developed to be able to simulate any mission desired of the rocket-scramjet-rocket launch system. However, the configuration of the optimal control routines must be tailored towards the specific mission profile desired. The mission chosen for the optimal trajectory calculation is a launch to sun synchronous orbit. A satellite in sun synchronous orbit is close to polar inclination,

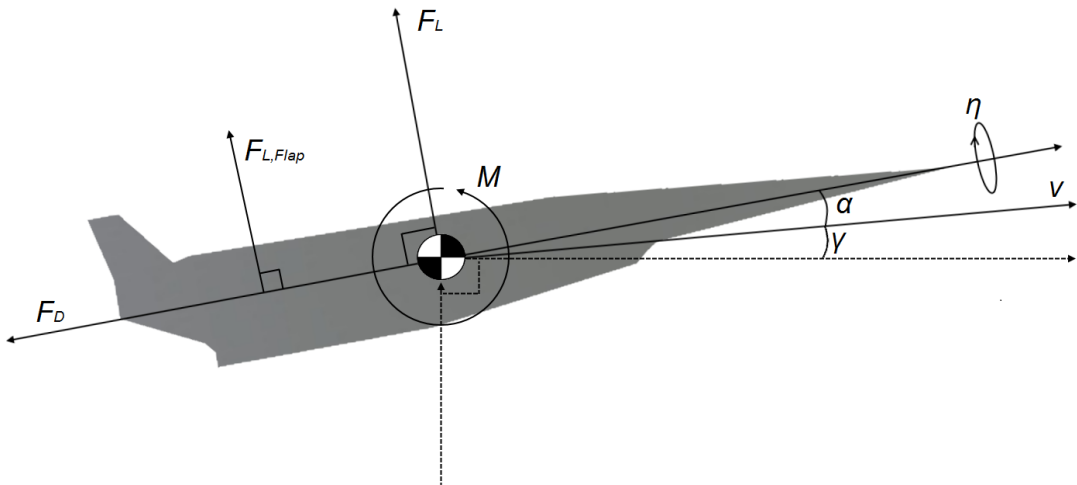


Figure 4.3: The vehicle-based components of the coordinate system.

regressing so that it keeps its orbital alignment to the sun. The sun synchronous is one of the most commonly used types of orbit for space science missions, as it has many useful properties[12]. A sun synchronous orbit allows for global coverage, passing over each latitude at the same time each day, illustrated in Figure 4.4. It also allows for a satellite to either have full sun and have consistent power generation, or alternatively, allows for a satellite to have a consistent 'dark side' each day to alleviate thermal issues[12]. A sun synchronous orbit at 566km has been used in previous studies as the target orbit[92], and this orbit is also used for the current work.

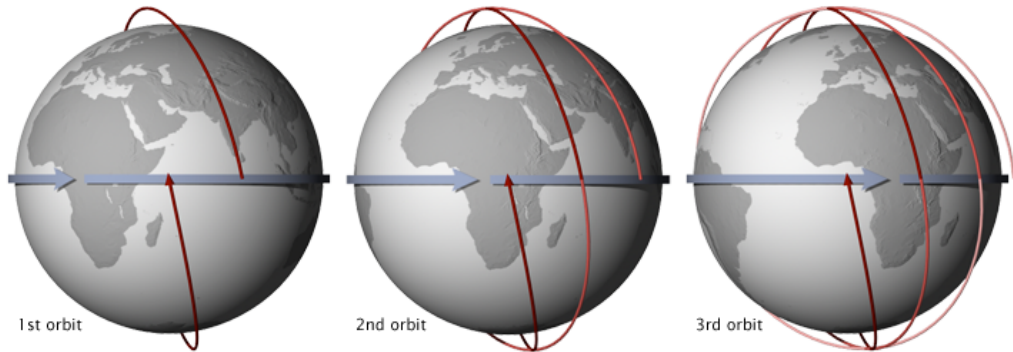


Figure 4.4: Sun synchronous orbit illustration, passing over the equator at the same time each day[111].

The launch site selected for the simulation is the proposed Equatorial Launch Australia launch site near Nhulunbuy in the Northern Territory, Australia[CITEXX]. This proposed launch site looks to take advantage of the remoteness of northern Australia, as well as its close proximity to the equator. While the proximity to the equator of this launch site is slightly disadvantageous for launch to sun synchronous orbits, the possibility of launch directions from this location, and its active development, make it an appropriate choice as a practical launch location within Australia. The site is 'about 30km

south of Nhulunbuy'[CITEXX news.com.au] which places it within the approximate region indicated in Figure 4.5.



Figure 4.5: Approximate location of the ELA launch site. Image from Google maps.

4.3 Optimal Control Problem Structure

The pseudospectral method used by GPOPS-2 is described in detail in section 2.8. Practically, the implementation of optimal control involves the specification of the dynamics of the system to be optimised, as well as the set of constraints and objectives that define the optimisation problem. Together, these define the optimisation problem being solved.

Cost Function

The cost function, J , defines the target of the optimisation problem. This cost function may be any function which is defined by the states or controls of the optimisation problem. The cost function is defined as follows:

$$J(t, \mathbf{x}(t), \mathbf{u}(t)) = M[t, \mathbf{x}(t_f), \mathbf{u}(t_f)] + \int_{t_0}^{t_f} P[\mathbf{x}(t), \mathbf{u}(t)] dt, \quad t \in [t_0, t_f], \quad (4.8)$$

where M is the terminal cost function and P is the time integrated cost.

Dynamic Constraints

The constraints impose various conditions on the optimisation problem. The optimisation problem is subject to a set of dynamic constraints, which describe the behaviour of the system over the solution space:

$$\dot{\mathbf{x}}(t) - f[t, \mathbf{x}(t), \mathbf{u}(t)] = 0. \quad (4.9)$$

These dynamic constraints ensure that the polynomial approximations of the state variables match the physical dynamics of the system. Implementing the dynamics as constraints allows each state variable to be approximated separately, and gives the optimiser some freedom to explore each state variable independently, greatly increasing the robustness of the optimal control problem.

Bounds and Path Constraints

Inequality constraints define the bounds of each state, as well as any path constraints. The bounds directly confine the state and control variables to prescribed values. This serves the purpose of limiting the search space to the physically possible (eg. constraining altitude to be greater than ground level), constraining the vehicle within its performance limits (eg. limiting the angle of attack), and improving computational efficiency by ensuring that the optimiser is constrained to a reasonable solution space:

$$\mathbf{b}_{min} \leq \mathbf{x}(t), \mathbf{u}(t) \leq \mathbf{b}_{max}. \quad (4.10)$$

The path constraints are inequality constraints which consist of functions based on the states and controls of the system. Path constraints are generally used to impose physical limitations on the system such as structural, aerothermodynamic or pathing limitations:

$$\lambda[t, \mathbf{x}(t), \mathbf{u}(t)] \leq \mathbf{0}. \quad (4.11)$$

Event Constraints

The event constraints define the states at the start and end points of a trajectory or phase:

$$\psi_0[\mathbf{x}(t_0), t_0] = \mathbf{0}, \quad (4.12)$$

$$\psi_f[\mathbf{x}(t_f), t_f] = \mathbf{0}. \quad (4.13)$$

These constraints determine the initial and terminal conditions of the optimisation problem. Additionally, if the problem has multiple phases, these constraints are used to couple the states and time of each phase to the preceding and following phases as follows:

$$\mathbf{x}_{f,1} - \mathbf{x}_{0,2} = 0, \quad (4.14)$$

$$\mathbf{t}_{f,1} - \mathbf{t}_{0,2} = 0. \quad (4.15)$$

Together, these objectives, constraints, and variables describe the optimal control problem being

solved, and form the inputs into GPOPS-2. GPOPS-2 uses these inputs, along with a pseudospectral method transcription, to form the constrained optimisation problem that is solved using IPOPT.

4.3.1 Trajectory Connection Points

The optimisation of a large, multi-vehicle launch trajectory requires that the optimal control problem be broken down into multiple segments. This segmentation is performed in order to assist the convergence of the optimal control solver, by ensuring that the dynamics of the underlying model are as smooth and continuous as possible across each segment. For a launch system, discontinuities in the system dynamics generally arise when the aerodynamics, mass and propulsion mode of a launch vehicle change significantly between stages or flight modes. If a vehicle model with large discontinuities is implemented directly into a single phase application of the pseudospectral method, it is likely to cause significant convergence issues, as the system dynamics will be unable to be approximated by the underlying polynomial of the pseudospectral method[CITEXX].

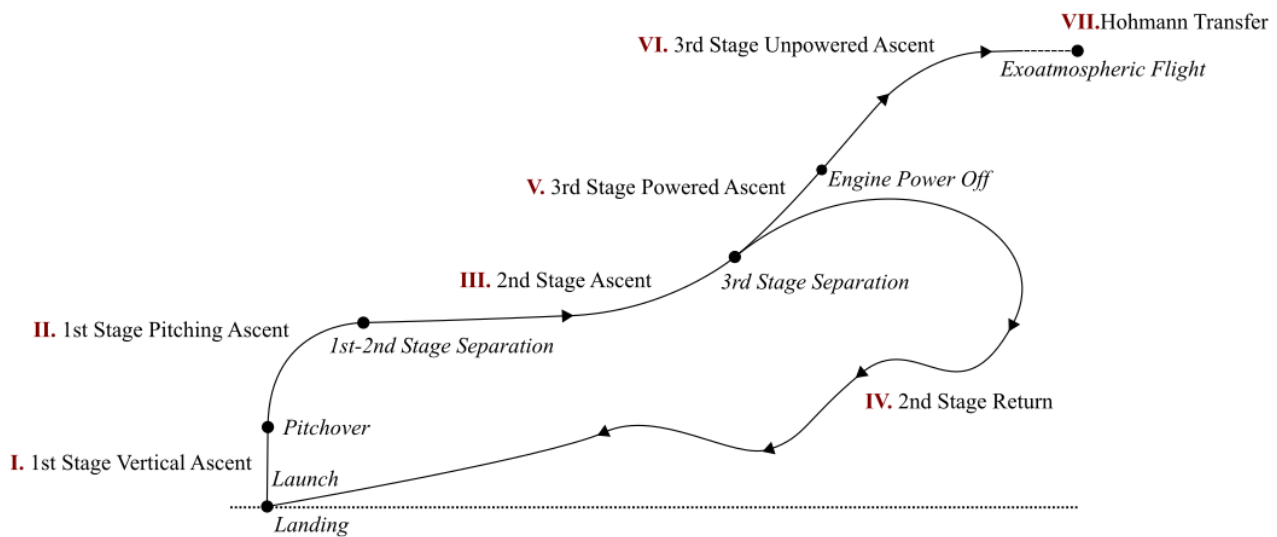


Figure 4.6: Illustration of the segmented launch profile.

To allow the trajectory profile to be formulated as an optimal control problem, the trajectory of the rocket-scramjet-rocket launch system has been broken down into the seven segments shown in Figure 4.6. The segments have been separated into two groups; controlled segments which take the form of phases within the optimal control problem; and segments without control which are either forward simulated at each iteration of the optimiser, or simulated externally to the optimal control problem. If the unpowered segments are simulated within the optimiser, they may be included in the cost and constraint functions of the optimisation problem. The unpowered segments are implemented in this

way in order to increase computational efficiency and improve the convergence of the optimal control solver.

Segments **II-V** are controlled by various combinations of angle of attack, bank angle and throttle, and are implemented as the phases of the optimisation problem. These phases are; The 1st stage pitching ascent; the 2nd stage ascent; the 2nd stage return flight; and the 3rd stage powered ascent. Segments **I, VI** and **VII** are segments without direct control, which are simulated using forward time stepping methods. These phases are; the pre-pitch segment of the first stage; the unpowered section of the third stage ascent; and the final Hohmann transfer to orbit. Each segment is connected through a set of conditions, which ensure that the trajectory of the vehicle is continuous, and that the trajectory that is being simulated is the one that is intended. The optimal control problem phases are connected through the use of initial and end discontinuity constraints on each phase to be coupled, ie $\mathbf{x}_{f1} = \mathbf{x}_{02}, t_{f1} = t_{02}$, while the forward simulated segments are simply initiated and terminated at set conditions. The segment coupling conditions are described in Table 4.1.

Section	Initial Conditions	End Conditions	Controlled
1 st Stage Vertical Ascent (I)	Launches from rest, at the predefined launch site.	Fly until pitchover conditions are met.	no
1 st Stage Pitching Ascent (II)	Start at pitchover conditions	-	yes
2 nd Stage Ascent (III)	Must begin at 1 st stage pitching ascent end conditions.	-	yes
2 nd Stage Return (IV)	Must begin at 2 nd stage ascent end conditions.	Must approach landing conditions at the initial launch site.	yes
3 rd Stage Powered Ascent (V)	Must begin at 2 nd stage ascent end conditions.	Must produce exoatmospheric flight at the termination of stage VI.	yes
3 rd Stage Unpowered Ascent (VI)	Must begin at 3 rd stage powered ascent end conditions.	Terminates when flight is parallel with Earth's surface.	no
3 rd Stage Hohmann Transfer (VII)	Must begin at 3 rd stage unpowered ascent end conditions.	Must attain prescribed orbit.	no

Table 4.1: Segment coupling conditions for combined trajectory optimisation.

I. First Stage Vertical Ascent

LODESTAR optimises the ascent of the first stage rocket in two segments; pre and post-pitchover. These aerodynamics of flight during these segments are simulated using spline interpolation of the databases generated using the method described in Section 3.2.1, and the engine properties are determined using linear pressure scaling as described in Section 3.2.

The pre-pitchover phase is the segment of flight immediately after vertical launch. During this phase, the launch system continues vertically for a short time in order to clear the launch tower and stabilise the vehicle. The pre-pitchover section is not optimised, and is simulated externally to the optimisation to improve computational efficiency, and to allow the dynamics of the system to behave appropriately during the pitching ascent. During vertical flight, the heading angle (Equation 4.7) is meaningless, and vertical flight is allowed during the pitching ascent, the heading angle change rate can tend towards infinity, causing mathematical and scaling errors. Simulating this segment after the optimisation has been completed makes the starting mass and altitude of the first stage slightly variable, but this variation is negligible. The pitchover is defined to occur at 90m altitude and 15m/s velocity. During the vertical launch the rocket is assumed to need no control, and is held at 0° angle of attack.

II. First Stage Pitching Ascent

At 90m altitude and 15m/s velocity, pitchover occurs. The pitchover is a very minor amount of instantaneous pitching (0.01°) which is introduced in order to begin the pitching ascent, allowing the 6DOF dynamics of the vehicle to resolve correctly. The first stage pitching ascent trajectory is an angle of attack controlled phase in the optimisation routine, which is simulated from pitchover until second stage separation. Table 4.2 shows the optimisation setup of this phase. During this phase, the launch system is allowed to fly at negative angles of attack, to assist in pitching. The control of this phase is the second derivative of angle of attack. This is chosen as the control variable to assist in mitigating the first stage's sensitivity to angle of attack, ie. when the trajectory angle is near 90° and at low velocities, the effect of changes in angle of attack is very large. Using the second derivative of angle of attack as the control variable smooths the angle of attack change rate and improves the optimised solution. The initial fuel mass of the first stage rocket is unconstrained, as small variations in the initial fuel mass can have an important effect on the capabilities of the first stage. The fuel mass can influence the velocity achievable at first to second stage separation, as well as the rate at which the rocket is able to pitch, and consequentially, the altitude and flight path angle range of the first stage. Allowing the initial fuel mass to vary increases the flexibility of the optimal control solver, though it is expected that the maximum allowable fuel mass will be used in most cases. The bounds on the latitude and longitude are chosen to cover the possible solution space, and are kept consistent across each phase to ensure that the position of the vehicle is not being unreasonably constrained

between segments. The velocity constraints are chosen to cover the possible solution space, with the lower bound of 10m/s chosen to not allow the velocity to approach 0m/s, which produces singularities within the system dynamics. This velocity limit is true for all phases. The other bounds on the state dynamics are chosen to encompass the solution space, while not being overly expansive, to assist with the convergence and scaling of the optimal control solver, this is true for most of the bounds in all phases.

Variable Group	Associated Variables	Values
Initial Constraints	Velocity Altitude Latitude Longitude Trajectory Angle Angle of Attack	30m/s 90m -12.16° 136.75° 89.9° 0°
Terminal Constraints	$\mathbf{x}_{f,\text{II}} - \mathbf{x}_{0,\text{III}}$ $t_{f,\text{II}} - t_{0,\text{III}}$	0 0
Path Constraints	Dynamic Pressure	0kPa - 50kPa
Control Variables	$\ddot{\alpha}$	$\pm 0.029^\circ/s^2$
State Variables	Altitude Velocity Trajectory Angle Latitude Longitude Heading Angle Total Mass Angle of Attack (α) $\dot{\alpha}$	0 - 30km 10 - 3000m/s $-5.7^\circ - 89.9^\circ$ $\pm 28.6^\circ$ $114.6^\circ - 171.9^\circ$ $\pm 360^\circ$ 11453 - 29388kg $-5^\circ - 0^\circ$ $\pm 5.7^\circ/s$

Table 4.2: Optimisation setup of the first stage phase.

4.3.2 III. Second Stage Ascent Trajectory

The second stage ascent phase consists of the acceleration of the SPARTAN scramjet-powered vehicle. The ascent trajectory of the SPARTAN is controlled using angle of attack and bank angle. The aerodynamics of the SPARTAN are interpolated from the engine on database developed as described in Sections 3.1.3 and 3.1.3. The engine properties are determined as described in Section 3.1.2. During the ascent, the engines are assumed to be operating at the maximum equivalence ratio at all times. This is 1 in most sections of the trajectory, except at low mach numbers where the possibility of unstart and choking necessitates a reduction in equivalence ratio. This trajectory is constrained to a maximum dynamic pressure of 50kPa, corresponding to the maximum structural limits of the vehicle. Aerodynamic and propulsion databases are generated as described in Sections 3.1.2 and 3.1.3.

The lift and drag of the vehicle is interpolated from of the trimmed aerodynamics database and the propulsion is determined from interpolation of the C-REST database. The control variables are set as angle of attack and bank angle change rate. Using the derivatives of the angle of attack and bank angle as the control variables serves to smooth the angle of attack and bank angle by constraining the change rates to reasonable values. The angle of attack is constrained to 10° , approximated as a reasonable upper bound to the angle of attack, and the limit to which the aerodynamic characteristics of the SPARTAN are modelled. The bank angle is constrained to a maximum of 90° , as it is assumed that the SPARTAN is not able to invert. The bank angle is also constrained to positive values only (ie. that the heading angle may only increase) as the SPARTAN is launched from the ELA launch site at Nhulunbuy, and must be launched to the northeast or east to avoid overflying populated areas.

A cost function can be included during this phase, when flying a constant dynamic pressure trajectory is desired. This cost function is configured as a quadratic cost function around 50kPa dynamic pressure, to ensure a smooth cost function, which goes to 0 at the target dynamic pressure. The cost function approaching 0 at the target dynamic pressure allows the cost function of payload mass (which is calculated during the third stage phases) to still be active, while prioritising flying constant dynamic pressure. This cost function is scaled by a constant scalar value, which has been tuned to ensure that the target dynamic pressure is matched closely during the acceleration of the SPARTAN, while still maximising payload-to-orbit during third stage optimisation.

4.3.3 IV. Second Stage Return Trajectory

After releasing the third stage rocket, the scramjet-powered second stage must return back to the initial launch site. During this return flight, the SPARTAN is able to use its engines if necessary to ensure that it is able to return successfully. The aerodynamics of the SPARTAN during fly-back are determined by interpolation of the engine-on and engine-off trimmed data sets described in Section 3.1.3. As the scramjet engines are throttled on, the aerodynamics are assumed to vary linearly between the aerodynamics calculated by the engine-off and engine-on datasets. During the fly-back, the SPARTAN cannot exceed its dynamic pressure limit of 50kPa. The end state is constrained to a minimum of -20° trajectory angle, which is assumed to be an appropriate lower bound on the trajectory angle for approach to a landing strip. The altitude is constrained to less than 1km at the end point to ensure that the SPARTAN is approaching landing altitude. The velocity left unconstrained at the end point. Constraining the end velocity may over constrain the optimisation problem, and it is assumed that for a payload-to-orbit optimised trajectory the SPARTAN will end its return at a low velocity, so that the energy necessary for return is small.

During the return, the C-REST engines are able to be throttled on and off. The throttle is set as a state variable, variable between 0 and 1, where 1 represents the maximum equivalence ratio at that

Variable Group	Associated Variables	Values
Initial Constraints	Fuel Mass	1562kg
Terminal Constraints	Altitude Trajectory Angle Bank Angle η $\mathbf{x}_{f,\text{III}} - \mathbf{x}_{0,\text{IV}}$ $t_{f,\text{III}} - t_{0,\text{IV}}$	0 - 45km 0 - 15° 0° 0 0
Path Constraints	Dynamic Pressure	0 - 50kPa
Target Cost	Dynamic Pressure*	$(q - 50000)^2 / 50000$
Control Variables	$\dot{\alpha}$ $\dot{\eta}$	±0.5°/s ±1°/s
State Variables	Altitude Velocity Trajectory Angle Latitude Longitude Heading Angle Fuel Mass Angle of Attack (α) Bank Angle η	0 - 50km 10 - 3000m/s −28.6° - 15° ±28.6° 114.6° - 171.9° −240° - 360° 0 - 1562kg 0° - 10° −1° - 90°

Table 4.3: Optimisation setup of the second stage ascent. * This is only used in the constant dynamic pressure simulation.

point. The fuel mass flow rate is scaled linearly with the throttle:

$$\dot{m}_{fuel} = \dot{m}_{fuel,max} \text{throttle}, \quad (4.16)$$

and the thrust of the engine is assumed to scale linearly with the fuel mass flow rate. A control variable of throttle change rate is added, to smooth the throttle in the same was as angle of attack and bank angle.

4.3.4 V. Third Stage Powered Ascent

The trajectory of the third stage rocket is separated into the powered and unpowered phases of ascent. During the powered ascent phase, the third stage is manoeuvred out of the atmosphere using one continuous burn of the Kestrel engine. The powered phase is controlled using angle of attack, and trimmed using thrust vectoring of the engine, as described in Section 3.3.3. The aerodynamics of the third stage are determined using interpolation of the aerodynamic dataset developed as described in Section 3.3.3.

The third stage rocket is constrained to an angle of attack of less than 20°. This is assumed to be the maximum controllable angle of attack possible for the third stage rocket. Additionally, a maximum

Variable Group	Associated Variables	Values
Initial Constraints	Bank Angle η	0°
Terminal Constraints	Latitude Longitude	-12.16° 136.75°
Path Constraints	Dynamic Pressure	0 - 50kPa
Control Variables	$\dot{\alpha}$ $\dot{\eta}$ <i>Throttle</i>	±0.5°/s ±1°/s ±0.2/s
State Variables	Altitude Velocity Trajectory Angle Latitude Longitude Heading Angle Fuel Mass Angle of Attack (α) Bank Angle (η) Throttle	0 - 70km 10 - 5000m/s ±80° ±28.6° 114.6° - 171.9° 60° - 500° 0kg - 500kg 0° - 10° 0° - 90° 0 - 1

Table 4.4: Optimisation setup of the second stage return.

normal force restriction is placed on the third stage, to limit the angle of attack of the third stage by the normal force on the vehicle. However, as a detailed structural study of the third stage has not been conducted, the maximum allowable normal force on the third stage is not known. For consistency, the maximum allowable normal force was calculated from the conditions of previous studies. Previous studies flew the third stage rocket at a constant 10° angle of attack, and initially released the rocket at 50kPa[CITEXX]. It is assumed that this condition of 10° angle of attack and 50kpa dynamic pressure produces the maximum allowable normal force to prevent the rocket from being released into an environment which could exceed its structural limitations. The maximum allowable normal force is calculated at the release Mach number, and is set as a path constraint.

The end angle of attack is constrained to 0°, as the angle of attack will not be able to be controlled during the unpowered ascent. The other terminal constraints of this phase correspond to end constraints imposed after the third stage unpowered ascent has been simulated. The altitude at the end of the unpowered ascent (Phase VI) is constrained to a lower limit of 90km, in order to ensure that the circularisation burn is exoatmospheric. The final heading angle is also constrained at this point, so that the orbit of the third stage is circularised into the correct inclination for sun synchronous orbit.

4.3.5 VI. Third Stage Unpowered Ascent

After the burn of the Kestrel engine is complete, the engine is cut and the third stage coasts to a point where it is able to be circularised into a low orbit. The unpowered phase of the ascent is not controlled.

Variable Group	Associated Variables	Values
Initial Constraints	Total Mass $\mathbf{x}_{f,\text{III}} - \mathbf{x}_{0,\text{V}}$ $t_{f,\text{III}} - t_{0,\text{V}}$	3300kg 0 0
Terminal Constraints	Alt _{f,VI} Heading Angle, $\zeta_{f,\text{VI}}$ Angle of Attack (α)	$\geq 90\text{km}$ 97.64° 0°
Path Constraints	Angle of Attack (α) Thrust Vector Angle	Maximum F_N $\pm 8^\circ$
Target Cost	Payload-to-Orbit	Payload Calculated in Phase VII
Control Variables	$\dot{\alpha}$	$\pm 1^\circ$
State Variables	Altitude Velocity Trajectory Angle Latitude Heading Angle Total Mass Angle of Attack (α)	30 - 84km 10 - 8000m/s $-5^\circ - 30^\circ$ $\pm 28.6^\circ$ $80^\circ - 120^\circ$ 0kg - 3300kg $-5^\circ - 0^\circ$

Table 4.5: Optimisation setup of the third stage powered ascent.

After the engine is cut, the third stage does not have sufficient aerodynamic control to manoeuvre, and the trajectory of the third stage is a coast at 0° angle of attack. The trajectory of the third stage rocket is only directly optimised during the powered section of its trajectory, the unpowered section of the trajectory is simulated from the end of the controlled section of the trajectory, using a second order Taylor series approximation. This integration ceases when the flight path angle reaches 0° . During this phase, the heat shield is released once the rocket has reached a dynamic pressure of 10Pa, where it is assumed that atmospheric effects will have ceased to have a major thermal effect. As the third stage is required to deliver the payload into heliosynchronous orbit, the third stage must achieve an inclination of 97.63° at the end of this phase[CITEXX]. These terminal constraints are implemented in Phase V.

4.3.6 **VII. Hohmann Transfer**

After the rocket has attained exoatmospheric flight parallel to the Earth's surface, a circularisation burn is performed. This circularisation burn takes the third stage rocket into low orbit around the Earth. However, in order to reach a heliosynchronous orbit of 567km, the orbit of the third stage rocket must be raised. To this end, the final manoeuvre performed by the third stage rocket is a Hohmann transfer. A Hohmann transfer is the most fuel efficient way to raise a spacecraft from one circular orbit to another[CITEXX]. The orbit of the third stage is first circularised into a low orbit:

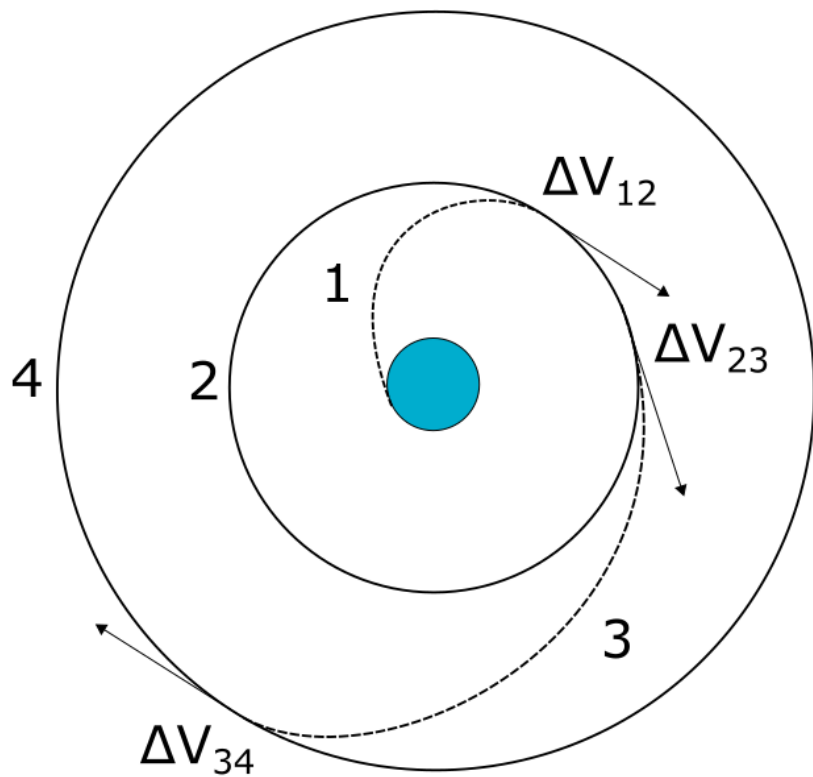


Figure 4.7: The Hohmann transfer manoeuvre.

$$\Delta V_{12} = \sqrt{\frac{\mu}{r_2}} - V_1. \quad (4.17)$$

Following circularisation, the third stage engine is reignited (or remains ignited) and the third stage manoeuvres into an appropriate elliptical orbit:

$$\Delta V_{23} = \sqrt{\frac{\mu}{r_2}} \left(\sqrt{\frac{2r_4}{r_2 + r_4}} - 1 \right). \quad (4.18)$$

At the apogee of the transfer orbit, corresponding to the desired orbital radius, an insertion burn is performed, and the orbit is circularised:

$$\Delta V_{34} = \sqrt{\frac{\mu}{r_4}} \left(1 - \sqrt{\frac{2r_2}{r_2 + r_4}} \right). \quad (4.19)$$

At this point, the payload is separated from the third stage rocket.

The mass of the third stage rocket after each burn is calculated using the Tsiolkovsky rocket equation:

$$m_2 = \frac{m_{1f}}{\exp^{\frac{V_{12}}{I_{SP} \cdot g_0}}} \quad (4.20)$$

$$m_3 = \frac{m_2}{\exp^{\frac{V_{23}}{I_{SP} \cdot g_0}}} \quad (4.21)$$

$$m_4 = \frac{m_3}{\exp^{\frac{V_{34}}{I_{SP} \cdot g_0}}} \quad (4.22)$$

Finally, the payload-to-orbit is determined by removing the structural mass from the total mass of the vehicle at the end of the Hohmann transfer. The remaining mass is taken to be the payload-to-orbit capability of the vehicle.

$$m_{payload} = m_4 - m_{struct} \quad (4.23)$$

4.4 Optimal Solution Analysis

LODESTAR provides the capacity to analyse the optimal solution provided by the pseudospectral method solver to assist in determining whether the pseudospectral method solver has converged close to an optimal solution of the nonlinear programming problem. It is particularly useful to verify that the optimality and constraint tolerances that have been chosen are sufficiently small, or to check whether the pseudospectral method solver has approached an optimal solution in the case that the defined tolerances are not able to be reached. Checking the solution is achieved through the examination of five key metrics; the IPOPT constraint violation and dual infeasibility parameters; the Hamiltonian necessary condition for optimality; the state derivatives; and finally a forward simulation.

The first metrics to be checked are the IPOPT constraint violation (*inf-pr*) and dual infeasibility parameter (*inf-du*)[59]. The constraint violation parameter is a measure of the infinity-norm (*L_∞ -norm*) of the constraints of the problem[59]. This factor must be suitably small in order to indicate that the constraints of the problem have been met. While the permissible magnitude of this factor changes with each individual problem, it is always desirable for this factor to be as small as possible. The dual infeasibility provides an indication of the optimality of the solution. A low dual infeasibility indicates that the solution is dual feasible and is likely to have approached an optimal solution. A dual feasible solution indicates that the dual problem is at least a lower bound on the optimal solution, $p^* \geq g(\lambda, v)$. For more details on duality see Reference [49]. Again, the magnitude of this value is variable with each problem, though as a problem becomes more complex, the ability to converge towards an optimal solution diminishes. It should generally be observable that the *inf-du* term is decreasing by multiple orders of magnitude and is stable at the completion of optimisation for a solution to be approaching optimality. In this study it is accepted that a given solution may not approach the global optimum, and multiple solutions are calculated to mitigate the error caused by the problem complexity, with the 'most optimal' solution selected.

The Hamiltonian of the optimal control problem is defined as

$$H(x(t), u(t), \lambda(t), t) = \lambda^T(t) f(x(t), u(t)) + L(x(t), u(t)). \quad (4.24)$$

The Hamiltonian of the optimal control problem is investigated as a partial verification that the first order necessary conditions hold. Due to the unconstrained end time of the trajectory problems, $H \equiv 0$ [94]. This is calculated using LODESTAR and the Hamiltonian condition is able to be verified. A sufficiently small Hamiltonian indicates that the end solution is likely to have approached an optimal solution.

The pseudospectral method considers the dynamics of the system as constraints on the optimal control problem, and solves across the entire trajectory simultaneously. This causes the physical system dynamics to have an associated margin of error, ie. $\dot{x} = f(x)$ will only hold to a certain degree of accuracy. For a well converged solution, this margin of error will be negligibly small, and the dynamics of the system will be consistent with realistic Newtonian dynamics. However, when the problem is not well converged, the dynamics of the system may have a large error. A check is performed on each state to affirm that the derivative of the approximated state is equal to the derivative supplied by the vehicle model. This checks that the solver has converged to a solution which satisfies the vehicle dynamics at each individual node. The state feasibility of the solution is checked through a comparison of the state derivatives, $\dot{x} = f(x, u)$. \dot{x} is first determined through numerical differentiation of the state variables over the solution time, differentiated at the node points created by GPOPS-2. Then $f(x, u)$ is determined using the dynamics of the system and vehicle model, in the same way that $f(x, u)$ is input to the pseudospectral solver. Examination of the error between the 'expected' state derivatives, and the numerical approximation of the derivatives, $\dot{x} - f(x, u)$, allows the accuracy of the system dynamics to be assessed.

The final verification check is a full forward simulation. This forward simulation starts at the initial conditions prescribed by the pseudospectral method solver, and propagates the dynamics of the system forward in time using the Runge-Kutta method, through Matlab's ODE45 function. The forward simulation uses the optimised control variables as the only input. This checks that the flight path will follow the path computed by GPOPS-2, using only the calculated control inputs. This is the most complete test of the optimal solution. However, in some cases calculating a forward solution may be problematic. The pseudospectral method has a limited number of nodes, potentially spread across relatively large time steps. Due to the high accuracy of the polynomial approximation, the pseudospectral method is able to maintain accuracy over large time steps. However, a forward simulation necessarily has less accuracy than the spectral method, and may interpolate differently when applied to the optimal solution, causing minor deviations. These variations are usually negligibly small, however, this is problematic during the return phase, due to the way the throttling of the engines is modelled, ie. the specific impulse of the engines is set to 0 under Mach 5 or 20kPa inlet conditions during the optimisation process. As the engines are often throttled close to the minimum operable conditions, these restrictions can intensify the effects of otherwise minor deviations in the forward simulation. For this reason, the forward simulation of the return stage is split into three segments, with divisions at 1/6th and 1/3rd of the total trajectory length, chosen to separate the first major

'skip' and bank, and split the 'skipping' section of the trajectory. A forward simulation is initiated at each of these segments, mitigating some of the effects of the engines throttling on and off in the forward simulation. Splitting the forward simulation allows the forward simulation of the return stage to be assessed without the effects of the throttle model having an unreasonably large effect.

4.5 The Optimisation Process

Figure 4.8 shows the flow chart of the optimisation process, including the external simulation modules. The main process is run multiple times, with varying initial guesses, in order to be able to select the most converged solution. This process is parallelised, with green and red arrows in Figure 4.8 indicating the initiation and termination of the parallel loop respectively.

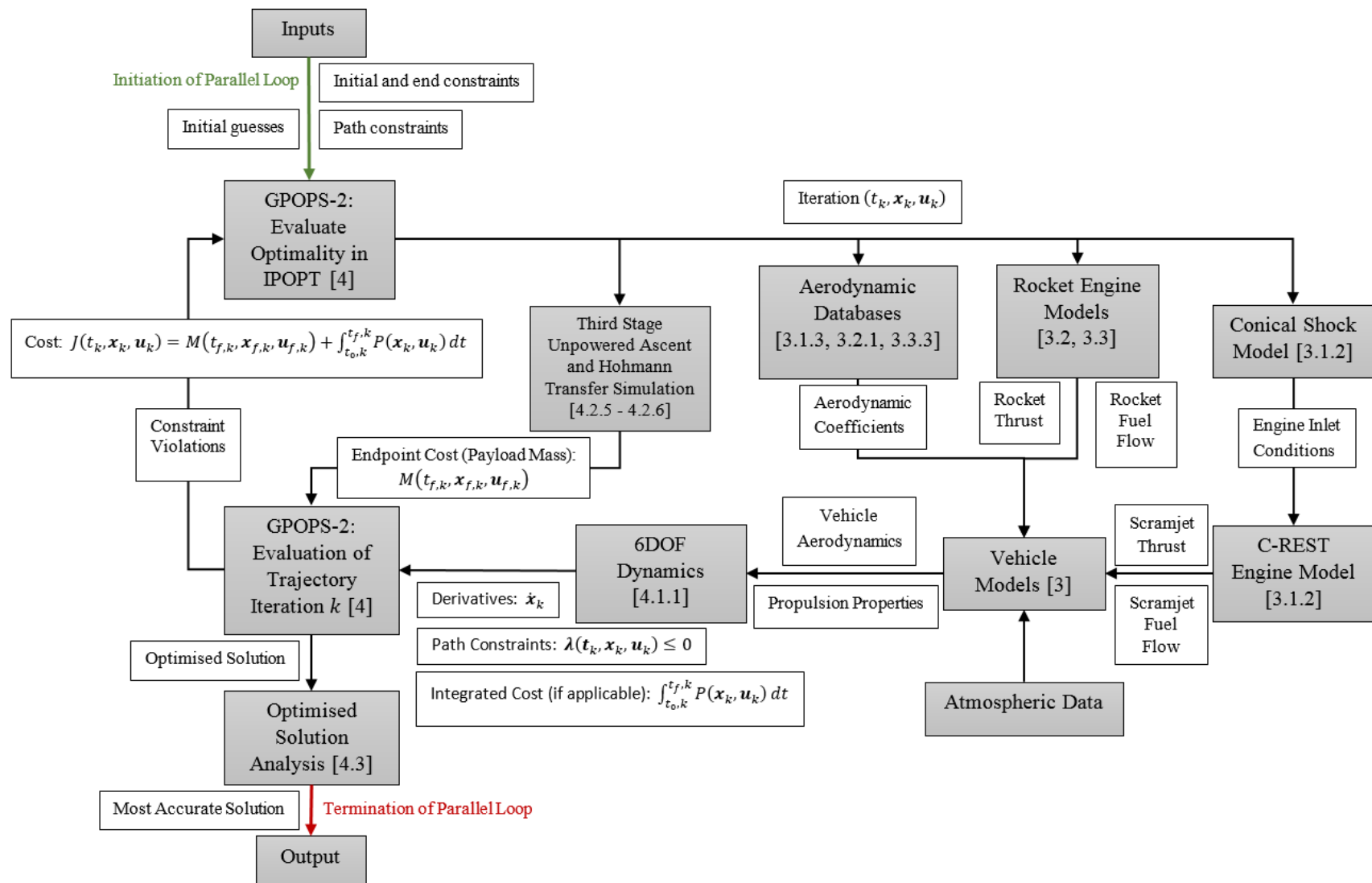


Figure 4.8: The process of the rocket-scramjet-rocket trajectory optimisation. Relevant sections are indicated in square brackets at each process step.

CHAPTER 5

OPTIMISED ASCENT TRAJECTORY

This chapter presents a maximum payload-to-orbit trajectory optimisation for the rocket-scramjet-rocket launch system incorporating the SPARTAN scramjet-powered accelerator. This launch system is simulated being launched from the Equatorial Launch Australia launch site in East Arnhem Land (Detailed in Section XX), and delivers a small satellite into sun synchronous orbit. LODESTAR is used to calculate maximum payload-to-orbit trajectory solutions for a variety of mission profiles. Firstly, a trajectory is calculated for the case in which the SPARTAN flies a constant dynamic pressure. This trajectory is calculated to serve as a baseline for comparisons to be made, as previous studies have assumed that flying the SPARTAN at its maximum allowable dynamic pressure would produce the best overall system performance[CITEXX]. An optimal payload-to-orbit trajectory is then developed, and the trajectory shape compared and contrasted to the constant dynamic pressure trajectory. Lastly, a sensitivity study is performed, varying key performance parameters of the launch system and investigating the effects of each parameter on the performance of the launch system.

The following trajectories are developed:

1. : $q = 50\text{kPa}$ fixed SPARTAN trajectory with minimum pull-up.
→ This trajectory provides a baseline trajectory for comparison purposes.
2. : Trajectory optimised for payload-to-orbit, $q_{max} = 50\text{kPa}$.
→ This trajectory Demonstrates improved performance through coupled trajectory optimisation.
3. : Variation of maximum allowable dynamic pressure between $q_{max} = 40\text{kPa}$ & $q_{max} = 50\text{kPa}$.
→ Comparison of these simulations allows investigation into the effect of q max on payload-to-orbit, and enables inferences about the effects of variation in the structural strength of the SPARTAN on launch system performance.

4. : Variation of the coefficient of drag of the SPARTAN between $C_d = 90\%$ & $C_d = 110\%$.
→ Comparison of optimal trajectories with drag variation allows investigation of the effects of variations in the SPARTAN's external design on launch system performance.
5. : Variation of the specific impulse of the SPARTAN's C-REST engines between $I_{SP} = 90\%$ & $I_{SP} = 110\%$.
→ Comparison of optimal trajectories with specific impulse variation allows investigation of the effects of the efficiency of the C-REST engines on the performance of the launch system.
6. : Variation of the mass of the SPARTAN between $m_2 = 90\%$ & $m_2 = 110\%$.
→ Comparison of optimal trajectories with SPARTAN mass variation allows investigation of the effects of the internal design of the SPARTAN on the launch system performance.
7. : Variation of the fuel mass of the SPARTAN between $m_{fuel} = 90\%$ & $m_{fuel} = 110\%$.
→ Comparison of optimal trajectories with SPARTAN fuel mass variation allows investigation of the effects of the amount of fuel which the SPARTAN is able to carry on the launch system efficiency.
8. : Variation of the mass of the third stage rocket between $m_3 = 90\%$ & $m_3 = 110\%$.
→ Comparison of optimal trajectories with third stage mass variation allows investigation of the effects of the third stage internal layout on the efficiency of the system.
9. : Variation of the thrust of the third stage rocket between $T_3 = 90\%$ & $T_3 = 110\%$.
→ Comparison of optimal trajectories with third stage thrust variation allows investigation of the effects of the output of the third stage engine on the efficiency of the launch system.

5.1 Constant Dynamic Pressure Trajectory

The first trajectory which is produced using LODESTAR is a maximum payload-to-orbit trajectory in which the SPARTAN flies a constant dynamic pressure path, at its maximum allowable dynamic pressure of 50kPa. In order to drive the SPARTAN towards a constant dynamic pressure path, the cost function described in Table 4.3 is utilised. In addition to the dynamic pressure cost function, the maximum payload-to-orbit cost function is also active on the third stage phase, so that when the SPARTAN is close to 50kPa, the third stage will fly a maximum payload-to-orbit trajectory from the termination of the SPARTAN's constant dynamic pressure path. A constant dynamic pressure trajectory is produced to serve as a baseline for comparison with the maximum payload-to-orbit optimised trajectory, as previous studies have assumed that flying at constant dynamic pressure will produce the best possible system performance [CITEXX]. Producing a constant dynamic pressure trajectory also serves to verify that LODESTAR is able to calculate a trajectory in which the SPARTAN flies

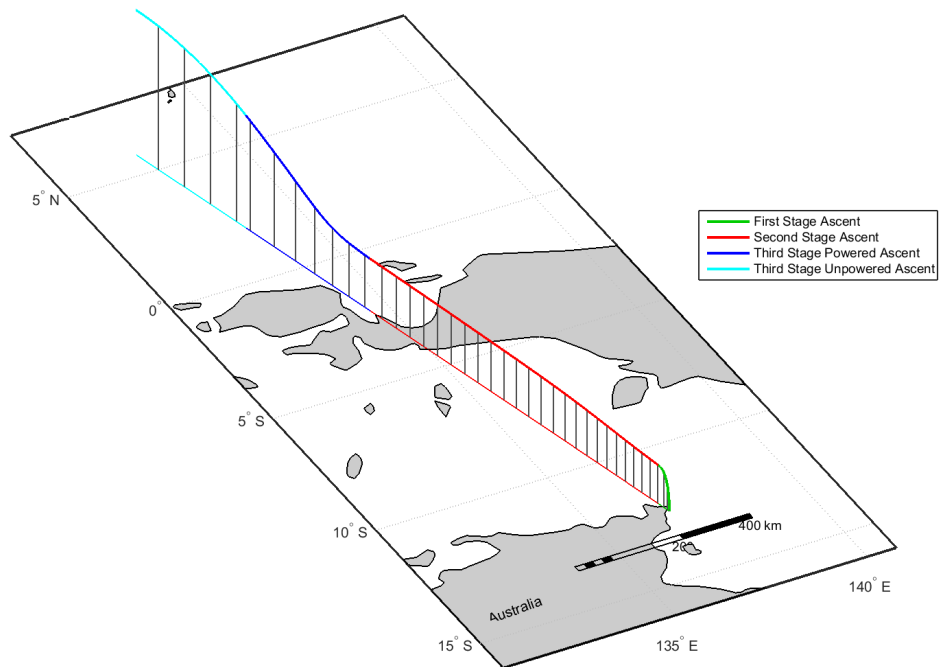


Figure 5.1: Maximum payload-to-orbit trajectory path with the SPARTAN flying at constant dynamic pressure.

at the maximum possible dynamic pressure for the duration of its flight. As the aerodynamics and design of the vehicle have been changed from previous studies[CITEXX], It must be ensured that any deviations from a constant dynamic pressure path in the payload-to-orbit optimised trajectory serve to improve the performance of the system, rather than being a result of the problem setup or design constraints.

LODESTAR is able to successfully simulate the trajectory of the rocket-scramjet-rocket system, with the SPARTAN flying at constant dynamic pressure, achieving a payload-to-orbit of 135.1kg. Figure 5.1 shows the simulated trajectory path, and Table 5.1 provides a summary of the key parameters of the trajectory. The rocket-scramjet-rocket system launches vertically, flying a fixed vertical trajectory for XXs, after which a pitchover is initiated. Under power of the first stage rocket, the launch system begins pitching, flying north-west, over the Arafura Sea. After pitchover the angle of attack stays constant at 0° for 56.2s. At this point, the angle of attack is reduced, reaching a minimum of

Trajectory Condition	Constq
Payload to Orbit (kg)	135.1
Separation Alt, 1→2 (km)	23.70
Separation v, 1→2 (m/s)	1436
Separation γ, 1→2 (m/s)	0.7
Separation Alt, 2→3 (km)	32.25
Separation v, 2→3 (m/s)	2799
Separation γ, 2→3 (deg)	0.5
Separation q, 2→3(kPa)	49.8
2nd Stage L/D, 2→3	5.4
2nd Stage Flight Time (s)	620.7
3rd Stage $t, q > 5\text{kpa}$ (s)	104.2
3rd Stage max α (deg)	11.3
3rd Stage final v (m/s)	6360.3
3rd Stage final m (kg)	895.4

Table 5.1

4.80°, before increasing back up to 0° for stage separation. The SPARTAN is separated at a trajectory angle of 0.7° at an altitude of 23.70km, a total flight time of XXs, with a total ground distance of XXkm covered under power of the first stage rocket.

The constant dynamic pressure trajectory for the SPARTAN stage is shown in Figure 5.3 with key results summarised in Table 5.1. After the separation of the first stage rocket, the SPARTAN flies north west over the Arafura Sea, and crosses West Papua before releasing the third stage rocket. Due to the clear objective of a constant dynamic pressure trajectory, any deviations from the target dynamic pressure are readily apparent, allowing the efficacy of the optimiser to be verified. These results show very close adherence to 50kPa dynamic pressure (maximum XX% deviation). Third stage release occurs at 620.7s at 32.25km altitude. Over the trajectory the Mach no. increases from XX to XX and the velocity from 1436m/s to 2799m/s. The flap deflection shows an overall increase from XX° to XX° over the trajectory. The net specific impulse ($I_{sp,net} = \frac{T-D}{m_f g}$) generally decreases over the trajectory, as the efficiency of the scramjet engines decreases. However, at the beginning of the trajectory the equivalence ratio increases as the capture limitations are relaxed with increasing Mach number. This causes the net specific impulse to increase, to a maximum of XX, during the first XXs flight time.

Figure 5.4 shows the corresponding third stage atmospheric exit trajectory after release, evaluated as described in Chapter 4. The third stage released from a constant dynamic pressure trajectory, shown in Figure XX, is limited by the maximum thrust vector angle for the first XXs of flight. This places significant limitations on the maximum allowable angle of attack. This angle of attack limitation reduces the lift of the rocket, causing it to spend a large amount of time at low altitude, in a high drag environment. The angle of attack increases gradually to a maximum of XX° at XXs before decreasing

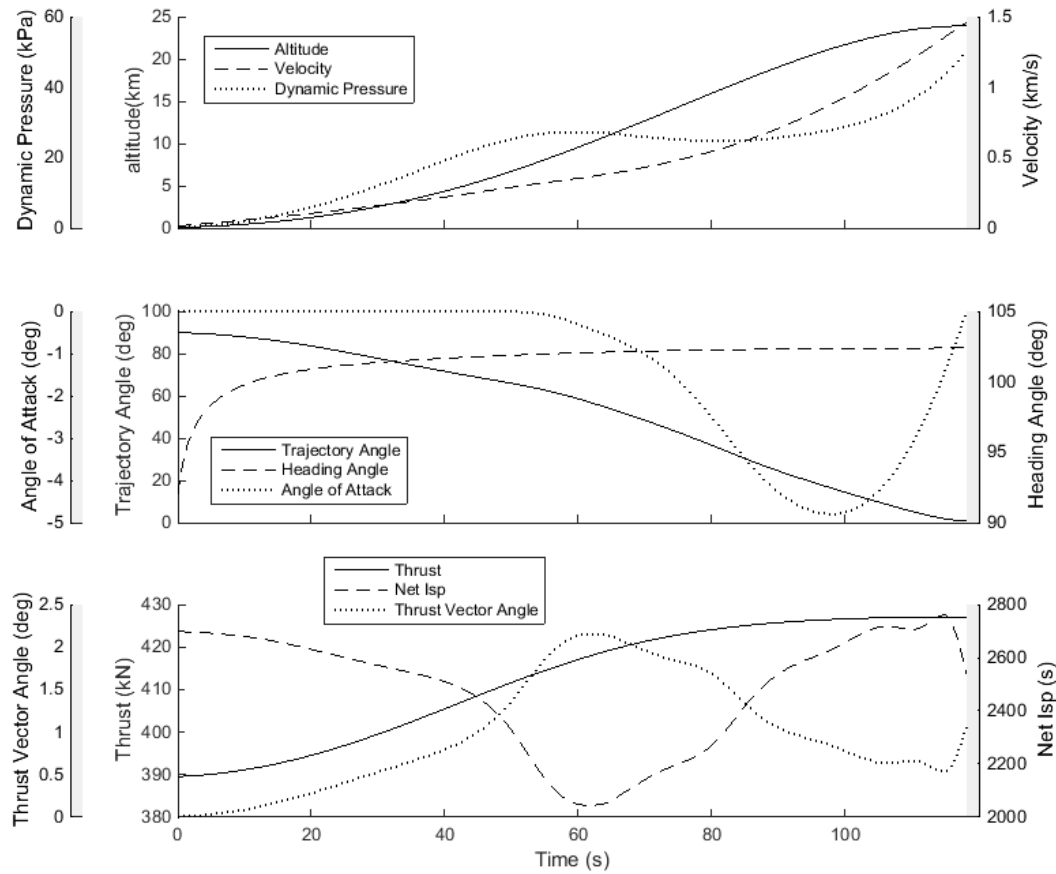


Figure 5.2: The first stage trajectory of the launch system, with the SPARTAN constrained to flight at constant dynamic pressure.

until burnout at XXs. The third stage rocket reaches XX dynamic pressure at XXs, and the heat shield is discarded. The rocket coasts to a trajectory angle of 0° , which is reached at a total flight time of XXs. The trajectory terminates at 90km, the lowest allowable altitude for circularisation. When this altitude is reached, the trajectory is circularised and performs a Hohmann transfer manoeuvre to reach sun synchronous orbit.

5.2 Optimised Ascent Trajectory

This section presents the maximum payload-to-orbit trajectory for the rocket-scramjet-rocket launch system. The optimal trajectory shape for a $q = 50\text{kPa}$ limited, maximum payload-to-orbit trajectory is shown in Figure 5.5 with key results summarised in Table 5.2. The maximum payload-to-orbit trajectory shape involves flying the SPARTAN away from its maximum dynamic pressure at multiple points along the trajectory, with altitude raising manoeuvres. These manoeuvres serve either to

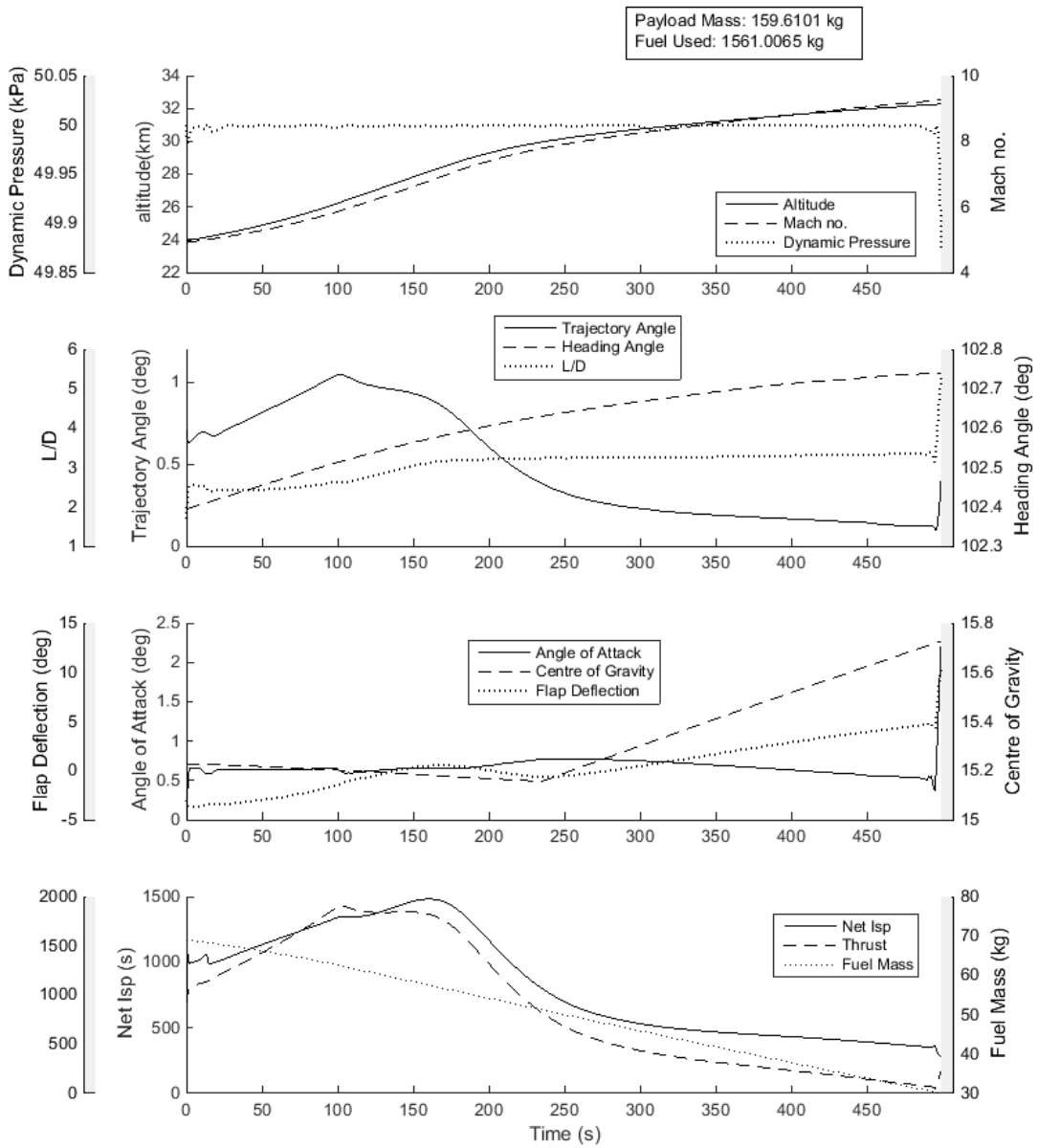


Figure 5.3: The constant dynamic pressure flight path of the SPARTAN.

increase the net specific impulse of the SPARTAN, or to trade-off the efficiency of the SPARTAN in order to increase the efficiency of the first and third stages. This payload-to-orbit optimised trajectory is able to deliver 189.2kg of payload to heliocentric orbit, an increase of XX over the constant dynamic pressure result.

The first stage trajectory, shown in Figure 5.6, has a very similar trajectory shape to that of the first stage releasing the SPARTAN onto a constant dynamic pressure trajectory. However, the trajectory angle at the separation of the SPARTAN is 10.8° , rather than the separation angle of 0.5° required

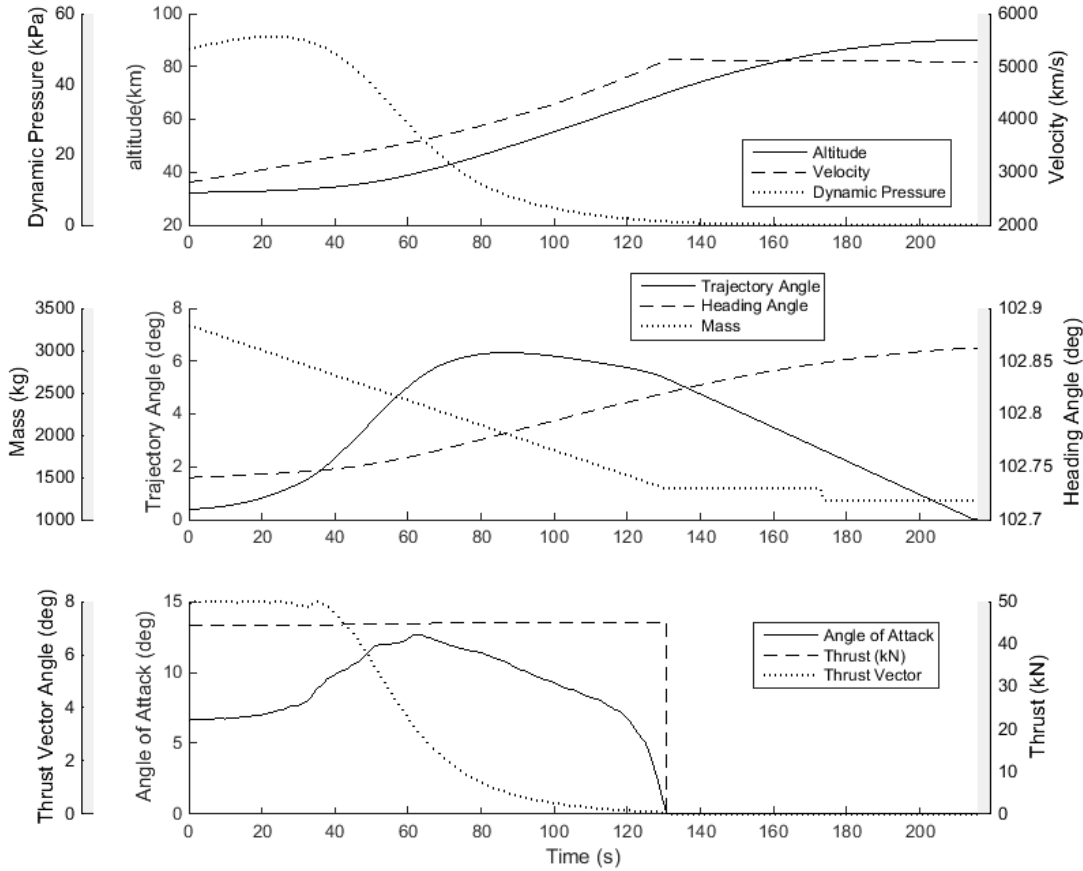


Figure 5.4: The third stage trajectory of the launch system, with the SPARTAN constrained to flight at constant dynamic pressure.

for the SPARTAN to fly a constant dynamic pressure trajectory. This higher release angle causes the altitude of the SPARTAN to immediately increase, and consequently for its dynamic pressure to decrease. This trajectory angle at release is the consequence of a trade-off of the efficiency of the SPARTAN for first stage efficiency. In order to release the SPARTAN at a lower trajectory angle, the first stage must launch with a lower fuel mass, to allow it to pitch in the correct manner. During the maximum payload-to-orbit trajectory, the first stage launches with a fuel mass of 17185kg, in contrast to the first stage segment of the constant dynamic pressure trajectory, which launches with a fuel mass of 17010kg. During the maximum payload-to-orbit trajectory, the first stage rocket releases the SPARTAN at a velocity of 1484.3m/s, an increase of XX m/s compared to the first stage releasing the SPARTAN onto a constant dynamic pressure trajectory. Neither first stage utilises the full amount of allowable fuel mass, 17934kg, indicating that using the full fuel mass would necessitate separation conditions which would reduce the efficiency of the SPARTAN unfavourably. These results indicate that the fuel mass utilised by the first stage has a distinct optimal magnitude, and that including

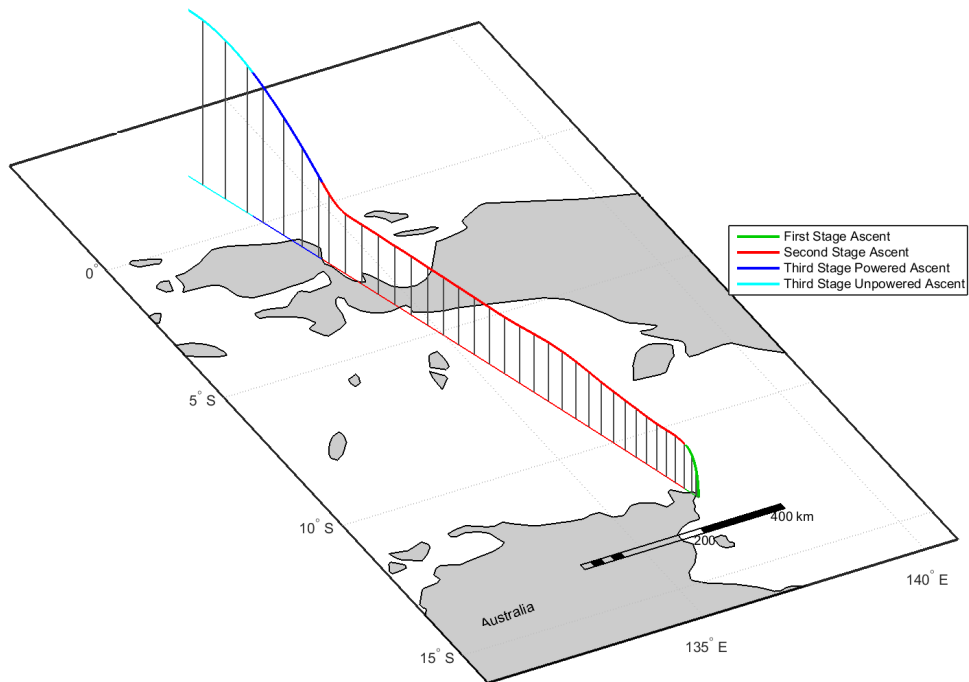


Figure 5.5

additional fuel over a certain amount may not increase the performance of the system. This implies that the size of the first stage is closely linked to the optimal trajectory of the system, and that future first stage designs should be sized so that optimal pitching is achieved.

After the initial deviation from the maximum dynamic pressure, the SPARTAN returns to 50kPa dynamic pressure for a time. At 122.5 seconds, the altitude of the trajectory is again raised, and the dynamic pressure decreased, to a minimum of 35.6kPa. In this region the net specific impulse of the SPARTAN is relatively homogeneous. This homogeneous region can be observed in Figure 5.8, in the Mach 7 and 8 contour plots. This is caused by the homogeneity which can be observed in the specific impulse of the C-REST engines in Figure 5.9, between M1 values of 6 and 7. This homogeneity means that flying at the maximum dynamic pressure in this region does not necessarily produce the maximum specific impulse from the C-REST engines. Figure 5.8 shows the altitude and angle of attack of the optimised and constant dynamic pressure trajectories at each Mach number. The optimised trajectory is flying in similar or higher net specific impulse regions, with the exception

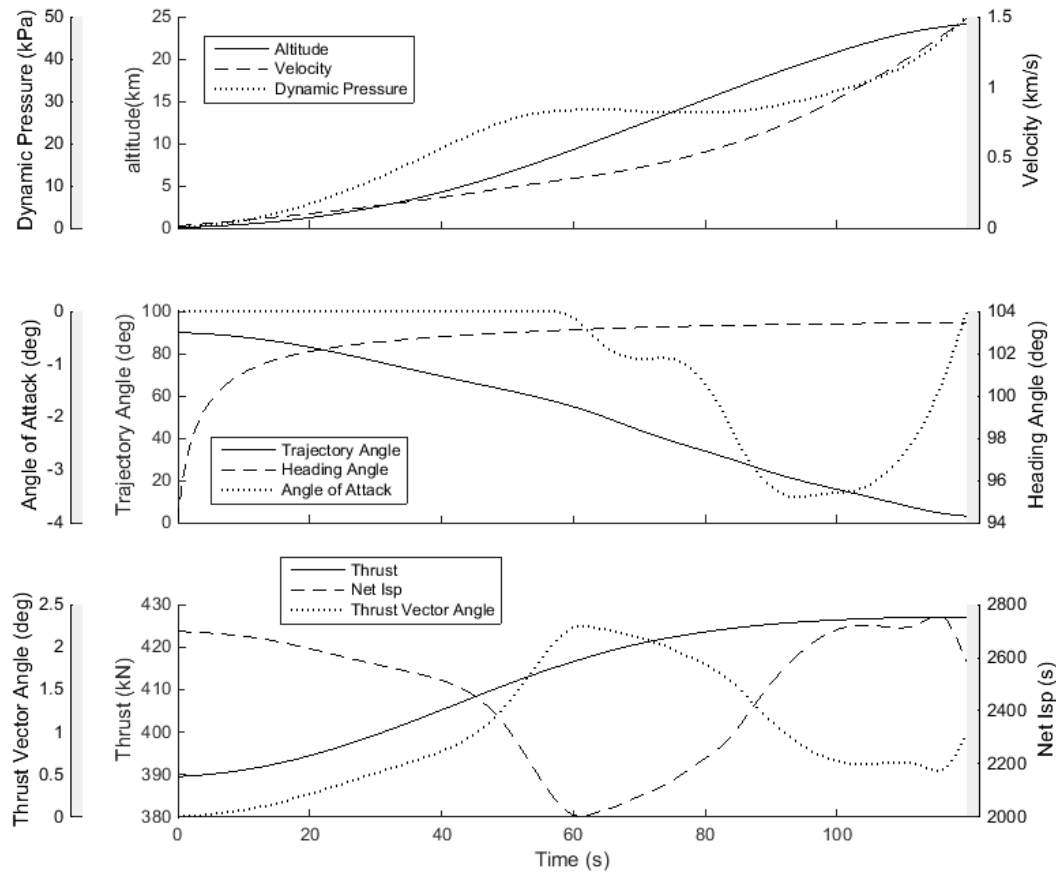


Figure 5.6

of the initial trajectory conditions at Mach 5. This is when the optimised trajectory shape requires a lower than optimal angle of attack, as the SPARTAN trades off efficiency with the first stage rocket. As a result, this manoeuvre results in a slight increase the in the net specific impulse of the SPARTAN.

At 314.3s, the SPARTAN returns to flight at close to 50kPa dynamic pressure until 494.1s at which point a pull-up manoeuvre is performed, gaining altitude until the third stage rocket is released at 528.4s SPARTAN flight time. The point at which the pull-up manoeuvre begins is the optimisation result that takes into account the best combination of velocity, altitude and release angle for scramjet stage performance and the release of the rocket stage. This pull-up indicates the region at which increasing altitude and release angle becomes more important than extracting maximum thrust from the scramjet (which is generally attained at high q and low flight angle at an equivalence ratio of 1). Flight in a lower dynamic pressure environment results in less thrust output from the scramjet engines, as well as an increase in angle of attack and flap deflection angle to compensate for the additional lift required. Due to this, less overall acceleration is obtained compared to the constant dynamic pressure result with minimum pull-up. Separation occurs at a velocity of 2687m/s, a decrease of XXm/s.

Trajectory Condition	Standard
Payload to Orbit (kg)	189.2
Separation Alt, 1→2 (km)	24.12
Separation v, 1→2 (m/s)	1484
Separation γ, 1→2 (m/s)	3.1
Separation Alt, 2→3 (km)	41.73
Separation v, 2→3 (m/s)	2687
Separation γ, 2→3 (deg)	10.8
Separation q, 2→3(kPa)	10.8
2nd Stage L/D, 2→3	4.0
2nd Stage Flight Time (s)	648.1
3rd Stage t, $q > 5$kpa (s)	14.2
3rd Stage max α (deg)	16.2
3rd Stage final v (m/s)	3718.0
3rd Stage final m (kg)	2202.8

Table 5.2: Summary of key results from the maximum payload-to-orbit trajectory.

However, at the same time separation altitude increases by XXkm to 41.73km, resulting in a decrease in separation dynamic pressure to 10.8kPa.

The larger scramjet stage pull-up assists the rocket in manoeuvring to exoatmospheric altitude by increasing the altitude and angle at separation by virtue of the increased L/D ratio and manoeuvrability of the scramjet vehicle. Even a small increase in release angle, to the optimal angle of XX°, significantly reduces the turning that is required by the rocket as evident from comparing Fig 5.4 and 5.10.

Compared to studies considering vehicles with a scramjet-rocket transition within a single stage[71, 127][CITEXX], the maximum payload to orbit trajectory of the multi-stage system shows a scramjet-rocket transition point at much lower altitudes. This lower transition point is a consequence of the stage separation creating an energy trade-off, which does not occur in a single stage vehicle. Single-stage vehicles must necessarily transport all components to exoatmosphere, and so utilise the scramjet engines until higher altitude to take advantage of their high efficiency. A multi-stage vehicle is able to separate the scramjet stage. This separation occurs when the performance benefits provided by the superior aerodynamics and engine efficiency of the scramjet stage are offset by the energy required to lift the extra mass to higher altitude. The beneficial ability to separate the scramjet stage results in a lower altitude scramjet-rocket transition point, when compared to single stage vehicle designs.

The trajectory of the third stage rocket after release from an optimised scramjet trajectory is shown in Figure 5.10. Release at a higher, more optimal angle mitigates the effects of the aerodynamic moment, and the thrust vector limit is not reached. The rocket increases flight path angle and gains altitude rapidly. Due to the higher altitude and release angle, the third stage rocket is released at a lower dynamic pressure, 10.8kPa compared to 49.8kPa, and spends much less time flying in a high

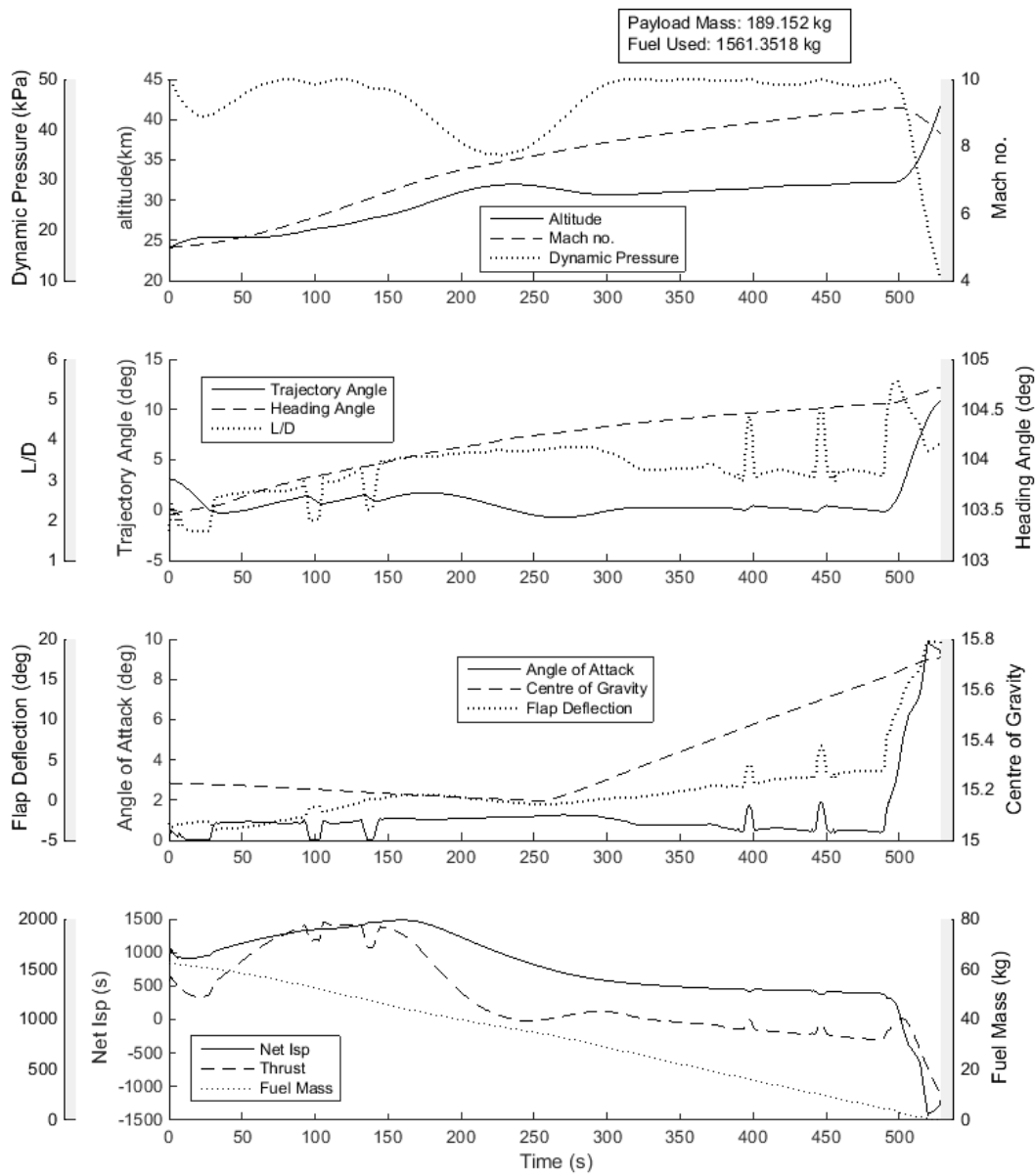


Figure 5.7

dynamic pressure environment, 13.3s at over 5kPa dynamic pressure rather than 104.2s. The reduced time that the rocket must spend in a high dynamic pressure environment and decrease in the maximum dynamic pressure that the rocket stage experiences may allow the structural mass and heat shielding necessary to achieve exoatmospheric flight to be decreased. This may enable higher payload to orbit, though it is beyond the scope of this study to investigate these design changes.

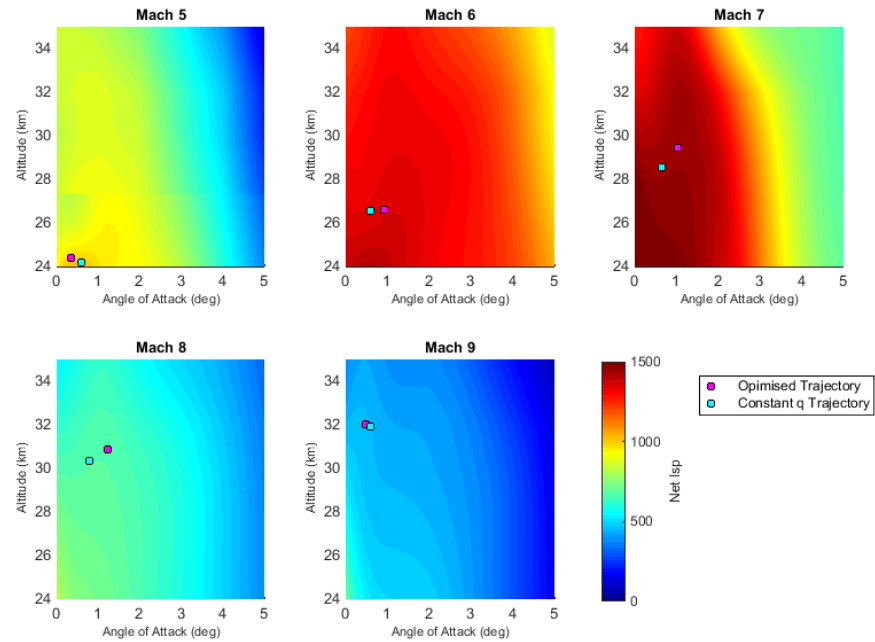


Figure 5.8: Net Isp contours for the SPARTAN at Mach numbers from 5-9, showing optimised trajectory and constant dynamic pressure trajectory.

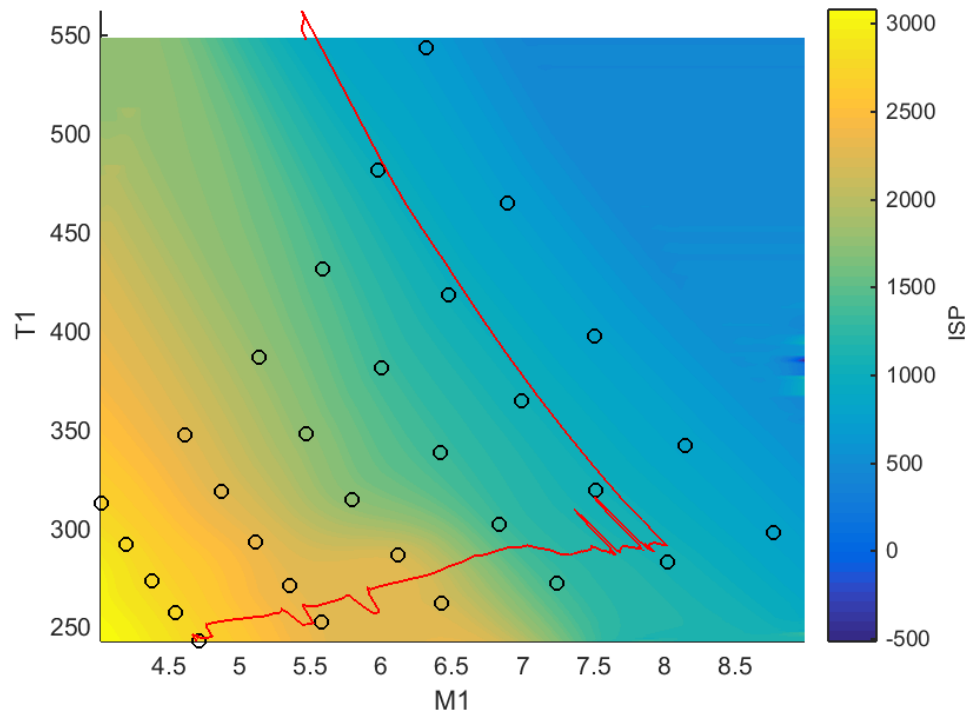


Figure 5.9

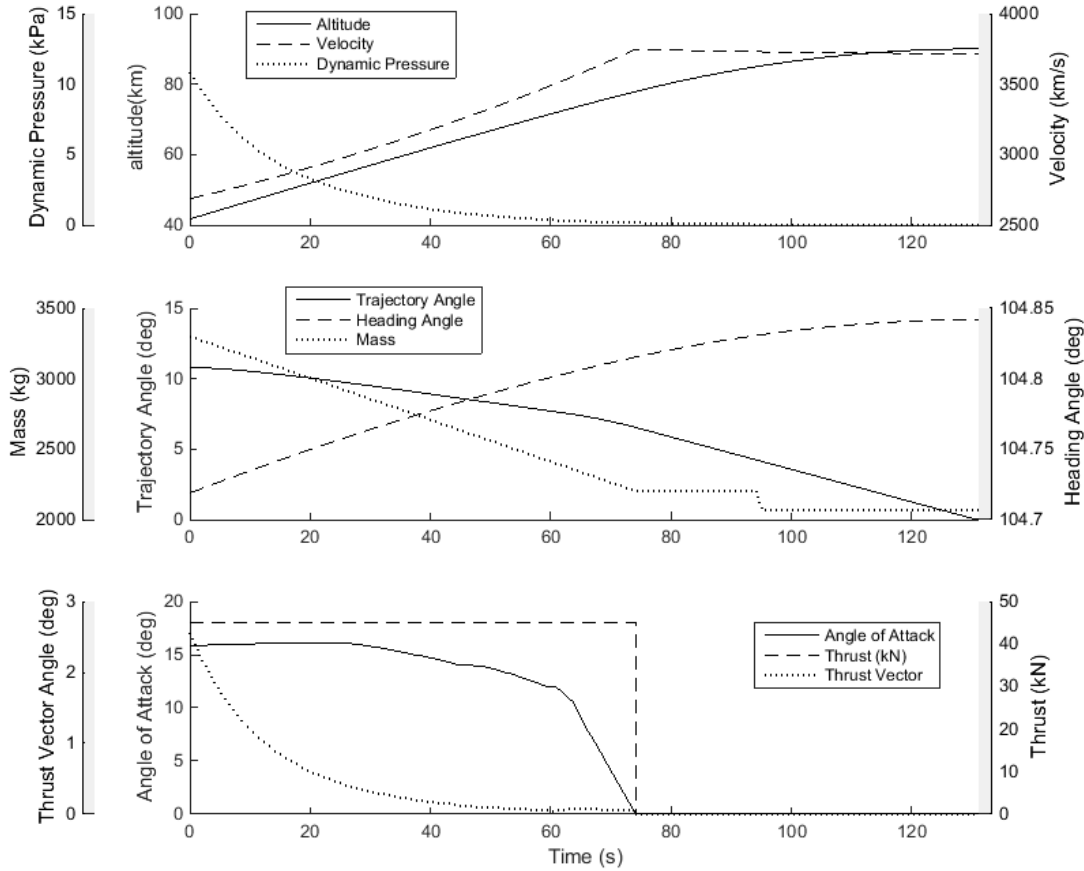


Figure 5.10

5.3 Sensitivity Analysis

A sensitivity analysis is conducted, in which selected design parameters of the launch system are varied, and the effects on the optimised maximum payload-to-orbit trajectory of the launch system are investigated. This study is performed in order to determine the relative impact of the design parameters on the efficiency of the system, as well as investigating how the maximum payload-to-orbit trajectory changes as the performance of the launch system is varied. The investigation of the key design parameters of the launch system provides a metric which can be used to quantify the relative impact of vehicle design parameters. Likewise, the optimal trajectory variation can be used to investigate the performance trade-offs between the stages. The information obtained from this study can be used to inform future launch system designs.

5.3.1 Dynamic Pressure Sensitivity

To investigate the sensitivity of the vehicle to changes in q_{max} , the maximum dynamic pressure is varied by $\pm 10\text{kPa}$ and the flight trajectory optimised, with results shown in Table 5.3. The variation in maximum dynamic pressure has only a small effect on the payload mass delivered to heliocentric orbit. Varying the maximum dynamic pressure by $\pm 20\%$ from causes a variation of only $+7.2\text{kg}$ ($+3.8\%$) or -7.8kg (-4.1%) in payload to orbit. Separation altitudes of 42.00km and 41.39km are reached for 40kPa and 60kPa limited cases respectively, with separation velocities of 2657m/s and 2720m/s. The 40kPa limited case flies for 731.6s, significantly longer than the 60kPa case which flies for 587.8s. Both trajectories pull-up to similar altitudes, with relatively small variation in separation velocity. This small variation in velocity is despite the increase in air density and decrease in angle of attack required for flight at higher dynamic pressures, both of which increase the mass flow into the engine. Although the thrust output of the REST engines increases with dynamic pressure, so does the drag on the vehicle, and the net increase in performance is small.

Trajectory Condition	q40	q45	q50	q55	q60	/%
Payload to Orbit (kg)	181.4	185.7	189.2	192.8	196.4	0.36
Separation Alt, 1→2 (km)	25.49	24.77	24.12	23.51	23.00	-0.12
Separation v, 1→2 (m/s)	1480	1483	1484	1483	1485	-
Separation γ, 1→2 (m/s)	5.5	4.4	3.1	1.1	0.8	-0.25
Separation Alt, 2→3 (km)	42.00	41.90	41.73	41.61	41.39	-0.03
Separation v, 2→3 (m/s)	2657	2673	2687	2703	2720	3.12
Separation γ, 2→3 (deg)	10.1	10.5	10.8	11.0	11.2	0.06
Separation q, 2→3(kPa)	10.2	10.4	10.8	11.1	11.6	0.07
2nd Stage L/D, 2→3	3.9	3.9	4.0	4.0	4.3	-
2nd Stage Flight Time (s)	731.6	686.1	648.1	611.2	587.8	-7.25
3rd Stage $t, q > 5\text{kpa}$ (s)	12.7	12.4	14.2	12.6	13.3	-
3rd Stage max α (deg)	17.8	16.6	16.2	15.5	14.7	0
3rd Stage final v (m/s)	3773.2	3756.1	3718.0	3718.2	3716.2	-
3rd Stage final m (kg)	2131.8	2161.9	2202.8	2218.4	2235.6	5.28

Table 5.3

Only a small variation in optimal payload mass is observed, without modification of vehicle design to account for the dynamic pressure limit. This indicates that designing and operating a vehicle at lower dynamic pressures may be preferable. Flying at a lower maximum dynamic pressure allows reduction of the structural weight and heat shielding of the vehicle. While it is outside the scope of this study to directly estimate the thermal shielding mass increase necessary when increasing the maximum allowable dynamic pressure, it can be observed from Section 5.3.4 that the influence of the SPARTAN's mass on the performance of the system is large. It can be inferred that the decrease in thermal protection system mass due to the decrease in maximum allowable dynamic pressure, which is likely to be significant, will serve to partially offset the negative effects on performance.

5.3.2 Drag Sensitivity Analysis

To investigate the effect of vehicle design and uncertainty in aerodynamic performance on the optimal trajectory the drag on the vehicle is varied by $\pm 10\%$, and an optimised trajectory calculated with dynamic pressure limited to 50kpa. Results are compared to the 100% drag result in 5.4 with the trajectory comparison shown in Appendix XX. These results show that when drag is varied the optimal trajectories are similar to the base-line case, with a similarly sized pull-up, though as the drag is increased (ie. L/D is decreased), the second stage follows a slightly slower and hence lower flight path. The similar flight path shape of the high drag case suggests that sacrificing velocity to increase separation altitude in a pull-up manoeuvre is optimal for multiple vehicle designs.

Trajectory Condition	Cd90	Cd95	Cd100	Cd105	Cd110	/%
Payload to Orbit (kg)	209.8	198.1	189.2	180.4	172.0	-1.9
Separation Alt, 1→2 (km)	25.24	25.00	24.12	23.89	23.65	-0.09
Separation v, 1→2 (m/s)	1528	1505	1484	1457	1430	-4.87
Separation γ, 1→2 (m/s)	5.1	4.8	3.1	1.9	1.2	-0.22
Separation Alt, 2→3 (km)	41.04	41.20	41.73	41.47	40.85	-
Separation v, 2→3 (m/s)	2804	2741	2687	2637	2589	-10.69
Separation γ, 2→3 (deg)	10.7	10.7	10.8	11.0	11.1	-
Separation q, 2→3(kPa)	13.0	12.1	10.8	10.8	11.4	-
2nd Stage L/D, 2→3	3.8	3.9	4.0	4.1	4.2	0.02
2nd Stage Flight Time (s)	668.8	661.5	648.1	650.6	653.3	-
3rd Stage $t, q > 5\text{kpa}$ (s)	16.1	14.1	14.2	14.4	14.6	-
3rd Stage max α (deg)	14.7	15.7	16.2	16.0	16.1	-
3rd Stage final v (m/s)	3815.9	3770.0	3718.0	3688.0	3650.9	-8.24
3rd Stage final m (kg)	2224.0	2205.9	2202.8	2185.0	2172.9	-2.46

Table 5.4

5.3.3 ISP

The specific impulse of the C-REST scramjet engines is varied by $\pm 10\%$ to directly investigate the effects of the efficiency of the scramjet engines on the performance of the launch vehicle. The additional efficiency allows the SPARTAN to accelerate more over the flight time, increasing the velocity at SPARTAN-third stage separation significantly. The velocity added to the end of the SPARTAN's trajectory directly contributes to the final velocity of the third stage at circularisation. Varying the specific impulse does not change the optimal SPARTAN-third stage separation altitude significantly, however the increased velocity allows this altitude to be reached by the SPARTAN with less trajectory angle variation during the pull-up, and allows the third stage to reach orbit from this release point release at a lower trajectory angle.

Trajectory Condition	Is90	Isp95	Isp100	Isp105	Isp110	/%
Payload to Orbit (kg)	168.7	179.1	189.2	199.5	213.4	2.2
Separation Alt, 1→2 (km)	24.12	24.12	24.12	24.12	25.28	-
Separation v, 1→2 (m/s)	1484	1484	1484	1484	1480	-
Separation γ, 1→2 (m/s)	3.2	3.4	3.1	3.3	5.5	-
Separation Alt, 2→3 (km)	41.58	41.64	41.73	41.07	41.53	-
Separation v, 2→3 (m/s)	2553	2622	2687	2752	2831	13.74
Separation γ, 2→3 (deg)	11.9	11.3	10.8	10.6	10.2	-0.08
Separation q, 2→3(kPa)	10.0	10.4	10.8	12.5	12.4	-
2nd Stage L/D, 2→3	3.9	4.2	4.0	3.9	3.8	-
2nd Stage Flight Time (s)	677.1	665.6	648.1	645.9	668.0	-
3rd Stage $t, q > 5\text{kpa}$ (s)	10.7	11.7	14.2	14.9	14.8	-
3rd Stage max α (deg)	15.6	16.0	16.2	15.9	15.8	-
3rd Stage final v (m/s)	3573.9	3645.0	3718.0	3786.2	3861.3	14.32
3rd Stage final m (kg)	2210.4	2208.3	2202.8	2200.9	2207.7	-

5.3.4 mSPARTAN

The mass of the SPARTAN is varied by $\pm 5\%$, to investigate the effects of the structural, thermal shielding, and system mass of the SPARTAN on the performance of the launch system. For this mass variation, it is assumed that the scramjet engines are operable at velocities slightly under Mach 5, in order to allow assessment of the effect of higher mass values without modification of the first stage rocket. Only a total mass variation of 5% is used, in order to prevent the first stage-SPARTAN separation velocity from dropping unacceptably low. Increasing the structural mass of the SPARTAN has a significant effect on both the first stage-SPARTAN and SPARTAN-third stage separation velocities, which in turn lessen the final velocity of the third stage rocket. However, most other trajectory conditions are relatively unaffected, with a pull-up of similar magnitude being performed at the end of each trajectory. A higher SPARTAN mass affects the first stage-SPARTAN separation velocity significantly, which would potentially affect the necessary sizing of the first stage rocket significantly.

5.3.5 mFuel SPARTAN

The available fuel mass of the SPARTAN is varied by $\pm 10\%$, to investigate the effects of variation in the available fuel tank size within the SPARTAN. As previously, it is assumed that the SPARTAN is operable at velocities slightly under Mach 5. The addition of extra fuel mass allows the SPARTAN to accelerate for longer, directly increasing the velocity at SPARTAN-third stage separation, and requiring slightly less pull-up angle. As the increased fuel mass directly increases the velocity at the end of the SPARTAN's trajectory, the beneficial effects of additional fuel are likely to exhibit diminishing returns as the velocity at the end of the SPARTAN's trajectory increases, and Isp decreases. The significant effects of the variation in fuel mass indicates that it is beneficial to maximise the available

Trajectory Condition	m295	m297.5	m2100	m2102.5	m2105	/%
Payload to Orbit (kg)	196.6	192.5	189.2	185.2	181.3	-1.5
Separation Alt, 1→2 (km)	25.70	25.06	24.12	23.86	23.55	-0.22
Separation v, 1→2 (m/s)	1540	1509	1484	1454	1418	-11.97
Separation γ, 1→2 (m/s)	5.1	4.7	3.1	2.7	1.8	-0.34
Separation Alt, 2→3 (km)	41.56	41.75	41.73	41.71	41.77	-
Separation v, 2→3 (m/s)	2733	2709	2687	2662	2637	-9.54
Separation γ, 2→3 (deg)	10.6	10.6	10.8	11.0	11.1	0.06
Separation q, 2→3(kPa)	11.4	10.9	10.8	10.6	10.4	-0.1
2nd Stage L/D, 2→3	3.9	4.0	4.0	4.0	4.1	-
2nd Stage Flight Time (s)	671.5	674.4	648.1	650.8	652.6	-
3rd Stage $t, q > 5\text{kpa}$ (s)	14.4	14.3	14.2	13.3	11.9	-0.24
3rd Stage max α (deg)	16.1	16.2	16.2	16.0	16.0	-
3rd Stage final v (m/s)	3757.8	3754.0	3718.0	3689.0	3669.5	-9.67
3rd Stage final m (kg)	2207.8	2192.7	2202.8	2205.5	2201.4	-

volume of fuel tanks within the SPARTAN.

Trajectory Condition	mF90	mF95	mF100	mF105	mF110	/%
Payload to Orbit (kg)	181.9	185.6	189.2	192.6	196.1	0.7
Separation Alt, 1→2 (km)	25.21	25.06	24.12	23.95	23.80	-0.08
Separation v, 1→2 (m/s)	1520	1501	1484	1465	1446	-3.65
Separation γ, 1→2 (m/s)	4.7	4.7	3.1	2.9	2.9	-
Separation Alt, 2→3 (km)	41.76	41.79	41.73	41.20	41.59	-
Separation v, 2→3 (m/s)	2639	2662	2687	2712	2734	4.78
Separation γ, 2→3 (deg)	11.2	11.0	10.8	10.6	10.4	-0.04
Separation q, 2→3(kPa)	10.4	10.5	10.8	11.9	11.4	-
2nd Stage L/D, 2→3	3.9	3.9	4.0	3.9	4.0	-
2nd Stage Flight Time (s)	611.9	637.9	648.1	674.7	703.8	4.41
3rd Stage $t, q > 5\text{kpa}$ (s)	11.8	14.1	14.2	14.3	14.3	0.11
3rd Stage max α (deg)	15.9	16.0	16.2	16.0	16.4	-
3rd Stage final v (m/s)	3669.8	3686.9	3718.0	3756.8	3781.5	5.87
3rd Stage final m (kg)	2204.1	2208.4	2202.8	2190.9	2189.3	-

5.3.6 m3

The mass of the third stage rocket is varied by $\pm 10\%$ to investigate the effect of having greater combined payload, fuel and structural mass within the third stage rocket. The structural mass fraction is kept constant at 9% of total mass (without heat shield) and the heat shield mass is unchanged. This mass variation primarily investigates the effects of the third stage internal layout on the trajectory of the launch system, quantifying the consequences of fitting additional fuel, payload and structure within the available space.

As the mass of the third stage increases, acceleration of the first stage and SPARTAN are decreased, and a larger trajectory angle is required during SPARTAN pull-up. Nevertheless, as the third stage mass increases, the payload to orbit increases significantly. The majority of the additional mass is used for fuel and additional structural mass, with 11.5% of the added mass utilised for payload. This mass fraction change rate is greater than the payload mass fraction of the standard third stage without heat shield, 6.0%, indicating that as more payload, fuel and structural mass is added to the internals of the third stage, the efficiency of the third stage increased.

Trajectory Condition	m390	m395	m3100	m3105	m3110	/%
Payload to Orbit (kg)	149.1	169.5	189.2	208.0	226.0	3.8
Separation Alt, 1→2 (km)	26.93	25.39	24.12	23.77	23.39	-0.17
Separation v, 1→2 (m/s)	1556	1521	1484	1444	1400	-7.79
Separation γ, 1→2 (m/s)	6.9	4.9	3.1	2.7	2.0	-0.24
Separation Alt, 2→3 (km)	41.37	41.30	41.73	41.48	42.14	-
Separation v, 2→3 (m/s)	2751	2723	2687	2651	2611	-7.05
Separation γ, 2→3 (deg)	10.4	10.5	10.8	11.2	11.6	0.06
Separation q, 2→3(kPa)	11.9	11.8	10.8	10.9	9.6	-
2nd Stage L/D, 2→3	3.9	3.9	4.0	4.0	4.2	-
2nd Stage Flight Time (s)	681.5	660.3	648.1	653.0	656.1	-
3rd Stage t, q > 5kpa (s)	14.7	14.2	14.2	12.4	10.5	-0.2
3rd Stage max α (deg)	14.7	15.6	16.2	16.3	16.9	0
3rd Stage final v (m/s)	3780.8	3764.9	3718.0	3684.2	3633.7	-7.5
3rd Stage final m (kg)	1989.0	2086.3	2202.8	2309.2	2427.1	21.98

5.3.7 T3

The thrust of the third stage rocket is varied between 90-110% in order to investigate the effect of the tank pressure on the payload to orbit. The specific impulse is not altered, so that the fuel mass rate is effectively the parameter being modified. This allows an indirect assessment of the effects of the third stage tank pressure on the performance of launch system. The constant Isp means that only the in-atmosphere portion of the trajectory is directly affected, with the circularisation burn and Hohmann transfer not being directly influenced.

The thrust variation has a significant effect on the trajectory of the system, and the payload-to-orbit. As the thrust increases, the SPARTAN-third stage separation altitude and separation angle decrease significantly, and the SPARTAN-third stage velocity increases. The third stage thrust variation is the only design parameter which has a significant effect on the altitude of the pull-up manoeuvre. This significant variance is caused by the third stage rocket requiring higher initial angle of attack with lower thrust values. As the maximum allowable angle of attack of the third stage increases as the SPARTAN-third stage release altitude increases, the altitude of release significantly affects the performance of the third stage rocket. The lower the third stage is able to be released, the more efficient

the trajectory path, however, the third stage can reach the required circularisation altitude more easily from a higher release point.

The lower, faster release point also indicates that increasing the thrust of the third stage rocket engine allows the SPARTAN to have a smaller pull-up, resulting in a more efficient SPARTAN trajectory. The L/D of the SPARTAN at SPARTAN-third stage separation generally increases as the third stage thrust increases. At lower values of third stage thrust, the L/D is constant due to the SPARTAN hitting the angle of attack limit of 10° during pull-up.

Trajectory Condition	T390	T395	T3100	T3105	T3110	/%
Payload to Orbit (kg)	172.0	179.6	189.2	202.8	224.4	2.6
Separation Alt, 1→2 (km)	24.11	24.11	24.12	24.13	24.13	-
Separation v, 1→2 (m/s)	1484	1483	1484	1485	1486	-
Separation γ, 1→2 (m/s)	3.2	3.2	3.1	3.2	3.2	-
Separation Alt, 2→3 (km)	44.46	43.91	41.73	40.02	38.61	-0.31
Separation v, 2→3 (m/s)	2636	2647	2687	2725	2746	5.96
Separation γ, 2→3 (deg)	12.5	12.1	10.8	9.2	8.2	-0.23
Separation q, 2→3(kPa)	7.0	7.7	10.8	14.3	17.9	0.56
2nd Stage L/D, 2→3	4.0	4.0	4.0	4.5	4.8	-
2nd Stage Flight Time (s)	650.1	651.1	648.1	647.6	647.5	-
3rd Stage t, $q > 5\text{kpa}$ (s)	5.0	6.3	14.2	20.0	31.0	1.31
3rd Stage max α (deg)	20.0	18.0	16.2	14.0	11.6	-0.01
3rd Stage final v (m/s)	3178.7	3310.5	3718.0	4554.4	5875.8	132.76
3rd Stage final m (kg)	2518.7	2454.7	2202.8	1747.6	1223.0	-65.97

5.4 Cd3

The coefficient of drag of the third stage rocket is varied by ±20% to investigate the effects of the third stage design and sizing on the performance of the launch system. The third stage drag is found to have only a very small effect on the performance of the launch system. This indicates that the aerodynamic properties of the third stage rocket do not contribute significantly to the performance of the system.

5.5 Comparison of Design Parameters

Figure 5.11 shows the payload change per percent for each design parameter of the launch system. The influence of the third stage on the payload-to-orbit performance of the launch system is large, with the third stage mass and thrust having the largest percentile sensitivities of any of the design parameters tested. This indicates that the performance of the system is particularly sensitive to the third stage design. However, the aerodynamic performance of the third stage is shown to have negligible

Trajectory Condition	Cd380	Cd390	Cd3100	Cd3110	Cd3120	/%
Payload to Orbit (kg)	190.1	189.6	189.2	188.8	188.4	0
Separation Alt, 1→2 (km)	24.12	24.12	24.12	24.12	24.12	-
Separation v, 1→2 (m/s)	1485	1484	1484	1484	1484	-
Separation γ, 1→2 (m/s)	3.1	3.2	3.1	3.1	3.2	-
Separation Alt, 2→3 (km)	40.68	41.02	41.73	41.96	42.24	0.04
Separation v, 2→3 (m/s)	2704	2695	2687	2684	2677	-0.64
Separation γ, 2→3 (deg)	10.2	10.6	10.8	10.9	11.2	0.02
Separation q, 2→3(kPa)	12.7	12.0	10.8	10.4	10.0	-0.07
2nd Stage L/D, 2→3	4.0	3.9	4.0	4.0	4.0	-
2nd Stage Flight Time (s)	646.4	647.6	648.1	647.9	648.9	-
3rd Stage t, $q > 5\text{kpa}$ (s)	16.7	14.8	14.2	11.9	11.8	-0.13
3rd Stage max α (deg)	17.6	16.2	16.2	15.9	15.3	0
3rd Stage final v (m/s)	3757.0	3748.6	3718.0	3723.5	3719.1	-
3rd Stage final m (kg)	2180.3	2183.7	2202.8	2197.3	2198.7	-

impact on the performance of the launch system. This implies that designing the shape of the third stage rocket to maximise the fuel mass, payload mass, and tank strength may be beneficial. However, a detailed thermal analysis would be required to assess the impact of changing the third stage design on the heat shielding, which is outside the scope of this study.

The influence of maximum dynamic pressure on the performance of the launch system is very low, particularly when compared to the influence of closely linked the SPARTAN mass parameter. The SPARTAN's thermal protective properties and structural strength define the maximum dynamic pressure, so the low variance in performance with maximum dynamic pressure will likely be offset by the variation in the mass of the SPARTAN, ie. a lower maximum dynamic pressure requires less structural and thermal protection system mass. This indicates that in the future it may be beneficial to design the SPARTAN towards a lower maximum dynamic pressure.

The influence of the fuel mass of the SPARTAN is also low, however, the fuel mass is only a fraction of the total mass of the SPARTAN (24.0%). This means that relatively small mass changes in fuel mass are still significant. Comparing the impact of the fuel mass and structural mass of the SPARTAN along with their relative magnitudes (1562kg of fuel mass and 4957kg of structural mass), the absolute impact of each is 0.044 and 0.030kg_{payload}/kg respectively. This implies that so long as fuel mass can be added to the SPARTAN with less than 1.47kg of structural mass incorporated for each kg of fuel mass, adding additional fuel mass will be beneficial. However, the fuel mass is constrained considerably by the available internal space within the SPARTAN, which is likely to be the main limiting factor.

The design parameters which increase the velocity at SPARTAN-third stage separation do not cause the SPARTAN to pull-up to higher altitude before third stage release, rather the higher velocity is utilised to allow for a lower release angle at the end of the pull-up manoeuvre. The third stage thrust

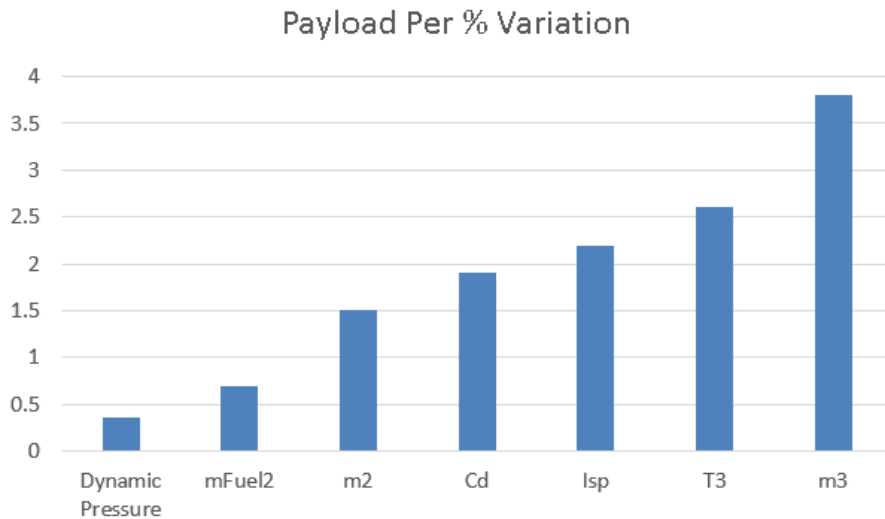


Figure 5.11

and drag coefficient are the only parameters which has a significant effect on the release altitude, indicating that it is the third stage performance which is primarily driving the pull-up.

When the velocity at SPARTAN-third stage separation is varied, the magnitude of the velocity variation carries through in similar magnitude to the third stage velocity at circularisation. This indicates that the Δv of the third stage before circularisation is relatively consistent. However, the benefits of increased velocity at SPARTAN-third stage separation may potentially be offset slightly by an increase in necessary thermal protection mass, though this is beyond the scope of this study.

5.6 Summary

In this chapter, LODESTAR was used to design the trajectory of the rocket-scramjet-rocket multi-stage system. A trajectory was simulated in which the SPARTAN stage flies at a constant dynamic pressure, producing 135.1kg of payload-to-orbit. Trajectory optimisation for maximum payload indicates that the optimal scramjet flight path for a system transitioning between separate airbreathing and rocket-powered stages is for the first stage-SPARTAN separation to occur at a higher trajectory angle than in the constant dynamic pressure trajectory, causing the SPARTAN to fly at lower dynamic pressure initially. The SPARTAN exhibits two more altitude raising manoeuvres, one to improve the specific impulse of the C-REST engines, and finally a pull-up manoeuvre. The optimal pull-up manoeuvre trades off velocity (a decrease of 24m/s) for altitude (an increase of 1.32km) and improved flight path angle (an increase of 1.41°), when compared to the constant dynamic pressure case. The optimal flight path increases payload mass to heliocentric orbit by XXkg (XX%) compared to a constant dynamic pressure trajectory. The pull up manoeuvre in the payload-optimised trajectory also reduces third stage dynamic pressure to XX kPa, a decrease of XX compared to a trajectory with

minimum pull-up.

A sensitivity study was conducted, to determine the relative effects of key vehicle design parameters on the optimised trajectory. It was found that the maximum dynamic pressure has a relatively small effect on the payload-to-orbit performance of the launch system, and the negative efficiency effects which are present are likely to be offset by the benefits of lower dynamic pressure flight. It was found that the third stage contributes significantly, and that the efficiency of the third stage is the major driving factor of the pull-up manoeuvre.

CHAPTER 6

OPTIMISED TRAJECTORY INCLUDING FLY-BACK

This chapter presents the optimised trajectory of the launch system, including the fly-back of the SPARTAN. The combined optimisation for the ascent/fly-back and third stage trajectory is currently operational in LODESTAR. Figures ??-?? show an example of a combined optimised trajectory for the ascent/return of the SPARTAN and the ascent of the third stage, for maximum payload-to-orbit. However, the aerodynamic and propulsive databases are currently being updated, and will change the optimised results slightly. It is not expected that the major points of interest in the trajectory will change.

The ascent trajectory will be compared to the optimised ascent without fly-back calculated in Section 5. The SPARTAN compensates for the fly-back by banking during ascent. This requires additional angle of attack, and results in less velocity and a smaller pull-up. A small deviation from 50kPa dynamic pressure is observed directly before pull-up, accompanied by a rise in bank angle. This manoeuvre reduces the total range during ascent for minimal velocity losses, decreasing the fuel necessary for the return flight.

The return flight analysis consists of a modified form of the paper 'Fly-Back of a Scramjet-Powered Accelerator', presented at Scitech 2018. Currently, this analysis is for a standalone optimised fly-back from a fixed point. The results will be modified to be for the fly-back portion of the combined optimisation. The analysis in this section is expected to change little.

The sensitivity analysis in this chapter will be expanded, and will be compared against the sensitivity analysis without fly-back, presented in Chapter 5, to determine how the fly-back changes the sensitivity of the trajectory to the design parameters of the SPARTAN. As in Chapter 5, the validation of each case will be discussed, with forward simulation comparisons and optimality condition validations provided in appendices.

6.1 Combined SPARTAN Ascent-Descent & Third Stage

Trajectory Condition	Standard
Payload to Orbit (kg)	173.1
Separation Alt, 1→2 (km)	25.79
Separation v, 1→2 (m/s)	1554
Separation γ, 1→2 (m/s)	3.8
Separation Alt, 2→3 (km)	41.18
Separation v, 2→3 (m/s)	2599
Separation γ, 2→3 (deg)	10.9
Separation q, 2→3(kPa)	10.9
2nd Stage L/D, 2→3	4.8
2nd Stage Flight Time (s)	505.2
3rd Stage $t, q > 5\text{kpa}$ (s)	13.3
3rd Stage max α (deg)	16.6
3rd Stage final v (m/s)	3684.3
3rd Stage final m (kg)	2155.3

The trajectory of the rocket-scramjet-rocket launch system has been optimised in LODESTAR, including the return of the SPARTAN to its initial launch site. The optimised trajectory is shown in Figure 6.1. The successful computation of this optimised trajectory indicates that it is possible to launch a small satellite using the rocket-scramjet-rocket launch system, while returning the SPARTAN to the initial launch site location, and approaching the landing at appropriately low altitude and velocity. This optimised trajectory attains a payload mass to SSO of 173.1kg.

The maximum payload-to-orbit is reduced by XX% compared to the optimised trajectory result without flyback. This is a relatively small reduction in payload, and the benefits of flying back the SPARTAN to its initial launch site are likely to far outweigh this associated reduction in payload. This result indicates that flying back the SPARTAN to its initial launch site is possible, and is likely to be desirable as the most cost efficient way to operate the rocket-scramjet-rocket launch vehicle.

The optimised trajectory shape is significantly different from that of the optimised trajectory without flyback. The initial launch is to the East, with the SPARTAN manoeuvring during its acceleration so that the heading angle is pointed close to North. The SPARTAN releases the third stage, and executes a banking turn, with a sequence of 'skipping' manoeuvres. The scramjet engine is ignited three times during the return flight, using a total of 238.3kg of fuel, 15.2% of the total fuel mass.

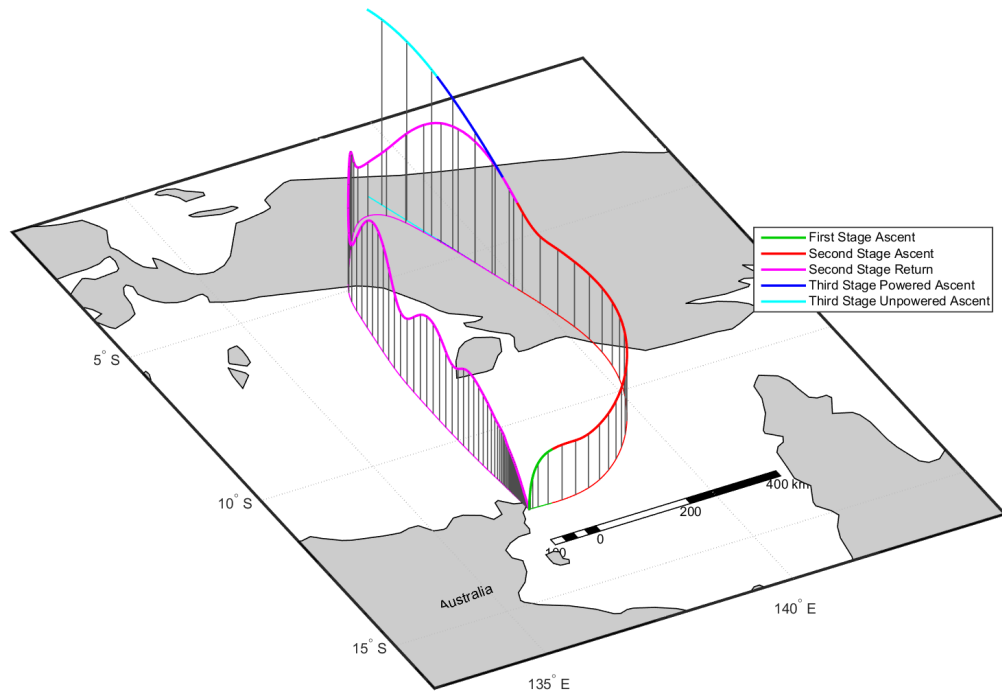


Figure 6.1

6.2 First Stage Trajectory

6.3 Second Stage Trajectory

-higher AoA (maybe pinpoint location on Isp graphs)

with no return case: -compare L/D Net Isp and thrust history

-compare end trajectory angle/altitude

-compare eq ratio (plot of both together? dont use normalised time scale)

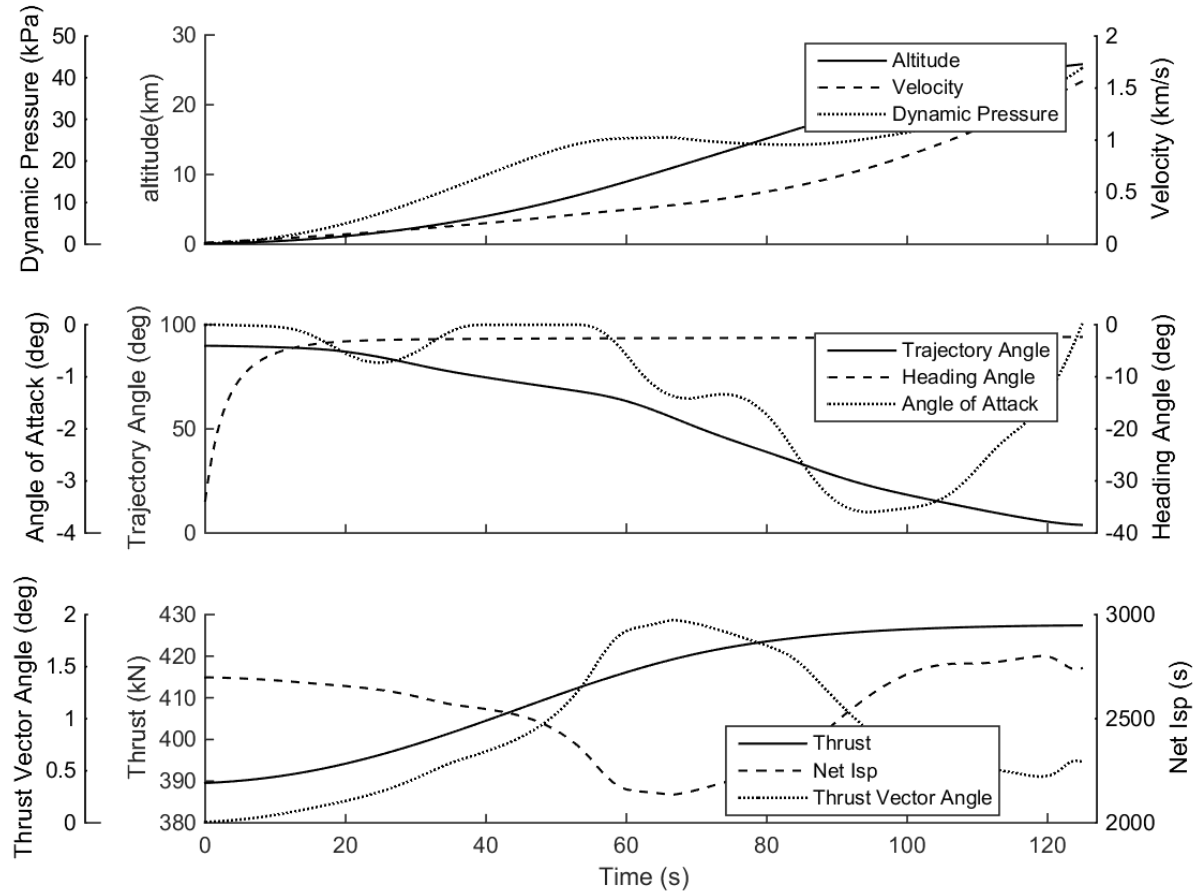


Figure 6.2

6.4 Third Stage Trajectory

6.5 Fly-Back Trajectory

-as below, explain why the ascent banks

6.6 Fly-Back Trajectory Analysis - paper

The fly-back of the SPARTAN is optimised using LODESTAR. The fly-back is optimised for minimum fuel usage, with initial conditions constrained to be similar to the intended third stage release point, and end position constrained within 12.7km of the initial launch site, at 15.3°S, 144.9°E[37]. The margin of 12.7km is allowed so as to not over-constrain the end position within LODESTAR, and it is assumed that the landing strip will not be at the exact location of the launch site. The angle of attack is limited to 10°, to ensure vehicle stability. The bank angle is limited to 90° to produce

a conservative solution and to limit any possible design complications that may arise from inverted flight. The dynamic pressure is limited to 50kPa, the structural limit of the vehicle. The scramjet engines are limited to only operate above 20kPa dynamic pressure, an estimated lower limit on the operable mass flow rate. The end of the trajectory is constrained to sub-200m altitude, and a trajectory angle range between -10° and 0° to ensure that the SPARTAN can perform a landing manoeuvre. These constraints ensure that the vehicle is approaching the landing site at the end of the optimised trajectory. The end velocity is only limited to be greater than 0m/s. It can be assumed that the optimal fly-back trajectory minimises end velocity as shown in the optimised trajectory results. It is also assumed that the vehicle is able to carry any necessary fuel in addition to the fuel required during the ascent trajectory, allowing the initial conditions to be kept constant. The potential specific impulse is shown along the trajectory, this is the specific impulse obtainable from the C-REST engines should they be powered on.

6.6.1 Return Trajectory

The optimised fly-back trajectory is shown in Figures ?? and ???. The fly-back is initiated from the optimised second-third stage separation point at 7.7°S, 145.0°E, 34.5km altitude, 2.9° trajectory angle, 2881m/s velocity and 102° heading angle, corresponding to the conditions of optimal third stage release described in Section ???. The SPARTAN is shown to be capable of fly-back, using 166.0kg of fuel, a total increase in the fuel usage of the SPARTAN of 10.6%. The optimised trajectory has four distinct parts; 1. initial turn, 2. boost phase, 3. hop-glide, and 4. approach.

Initial Turn

The SPARTAN starts at the maximum bank angle of 90° , and sustains this bank angle for 34.4s. At this point, the altitude of the SPARTAN decreases, and the vehicle is close to hitting the dynamic pressure of 50kPa. To avoid exceeding this limit, the bank angle is reduced to 71.2° , allowing the vehicle to generate sufficient lift to slow its descent. The bank angle is then increased again, to 80.7° at 70.8s. After this time, the bank angle is gradually reduced.

Boost Phase

Soon after the bank angle begins to reduce, at 118.7s flight time and Mach 5.71, the scramjet engines are ignited. The C-REST engines are powered-on at a point of high potential specific impulse, at a low Mach number, and burn for 119.8s. The altitude of the SPARTAN is raised during the majority of the burn, ensuring that the Mach number is kept low for maximum efficiency[93], as shown in Figure ???. The maximum altitude is limited by the lower dynamic pressure limit of the C-REST engines of 20kPa. The bank angle of the vehicle is reduced to produce increased lift, so as to increase the altitude

of the SPARTAN, while also maximising the specific impulse of the scramjet engines by keeping the angle of attack low. Low angle of attack decreases the temperature and raises the Mach number, at the inlet of the C-REST engines. While these effects partially offset each other[93], the temperature increase is more significant, and decreasing angle of attack has the net effect of increasing the specific impulse of the C-REST engines. This increase in specific impulse is balanced by a decrease in the L/D of the SPARTAN at angle of attack values lower than 4° , as illustrated in Figure 3.23c. However, the specific impulse has a more significant impact than L/D during this phase, resulting in the optimised angle of attack being kept low. At 204s the angle of attack is increased, bringing the L/D of the vehicle towards maximum and initiating the first 'skip' of the skip-glide phase.

Skip-Glide

During the unpowered trajectory after the burn phase, the angle of attack is controlled so that the L/D of the SPARTAN is close to the maximum. Initially, the SPARTAN performs several 'skips' after the scramjet burn. These are due to the high L/D of the SPARTAN above Mach 4, and are aided by the angle of attack, which is controlled to emphasize the size of the skips. These skips are consistent with research which has shown that a periodic skipping trajectory increases the downrange distance achievable by hypersonic vehicles[29, 57].

Approach

After the skip phase, as the vehicle is approaching Mach 1, the angle of attack is reduced gradually to bring the SPARTAN down to 1km altitude, in a controlled manner. At the end of the trajectory the SPARTAN levels out, and reaches 1km altitude at $-XX^\circ$ trajectory angle and XXm/s velocity. These conditions are similar to those of the space shuttle at landing[106], and it is assumed that the SPARTAN is able to perform a landing manoeuvre after this point.

6.6.2 Design Sensitivity Analysis

During the preliminary stages of launch vehicle design, it is important to characterise the effects of changes in the design of a vehicle. Quantifying the effects of variations within the vehicle design allows the vehicle performance to be improved. However, the complete assessment of the effects of vehicle design variations requires every critical feature of the design to be modified, and the new vehicle design to be investigated. This method of investigation is prohibitively time consuming and computationally expensive for a complex launch system. Consequently, it is important to first understand the effects of the key performance parameters of the vehicle, so that when the design of the launch system is to be iterated, the design of each vehicle and subsystem may be tailored towards improving the overall performance. To this end, a sensitivity study is performed to investigate the variations in the optimal trajectory when key performance parameters of the vehicle are modified.

The performance parameters modified are:

- Maximum dynamic pressure.
- Specific Impulse of the C-REST engines.
- SPARTAN aerodynamic drag.
- SPARTAN mass.
- SPARTAN fuel mass.
- Third stage mass.
- Third stage thrust.
- SPARTAN viscous drag.

These parameters are varied and the new optimal fly-back trajectories are calculated using LODESTAR. These optimised trajectories are detailed in the following sections.

The consistency of the trajectory shape indicates that the optimal solution is robust with variation in the aerodynamic parameters and specific impulse of the SPARTAN. The optimised trajectories show clear trends with variation in vehicle parameters.

6.7 dynamic pressure

6.8 Isp

Increasing the specific impulse causes the fuel necessary for fly-back to decrease by -XXkg (-XX%), while decreasing the specific impulse causes the fuel necessary to rise by +XXkg (+XX%). The start of scramjet burn is consistent across different specific impulse test cases. Due to the increase in thrust, the SPARTAN accelerates more rapidly for the higher specific impulse case. As a consequence, the initial 'skip' is performed sooner, and subsequent skips are larger.

-check this

Trajectory Condition	Isp90	Isp95	Isp100	Isp105	Isp110	/%
Payload to Orbit (kg)	155.8	164.0	173.1	181.0	188.8	1.7
Separation Alt, 1→2 (km)	25.83	25.97	25.79	25.93	25.81	-
Separation v, 1→2 (m/s)	1554	1553	1554	1553	1553	-
Separation γ, 1→2 (m/s)	3.9	4.1	3.8	4.1	3.9	-
Separation Alt, 2→3 (km)	41.12	40.95	41.18	41.24	41.43	-
Separation v, 2→3 (m/s)	2478	2536	2599	2651	2699	11.1
Separation γ, 2→3 (deg)	11.9	11.5	10.9	10.4	10.2	-0.09
Separation q, 2→3(kPa)	10.0	10.8	10.9	11.3	11.4	0.06
2nd Stage L/D, 2→3	4.7	4.7	4.8	4.8	4.8	-
2nd Stage Flight Time (s)	500.4	504.4	505.2	506.7	505.3	-
3rd Stage t, q > 5kpa (s)	13.0	12.3	13.3	14.8	14.7	-
3rd Stage max α (deg)	16.2	17.1	16.6	17.1	17.0	-
3rd Stage final v (m/s)	3522.1	3622.1	3684.3	3737.0	3776.3	12.46
3rd Stage final m (kg)	2186.0	2156.3	2155.3	2154.3	2161.5	-

6.9 Cd

Increasing the drag coefficient causes the fuel necessary for fly-back to increase by +XXkg (+XX%). Conversely, decreasing the drag coefficient by 10% causes the fuel necessary for fly-back to decrease by -XXkg (-XX%). When the drag is increased (ie. L/D is decreased), the scramjet engine burn phase begins earlier, and continues for longer. The greater burn time allows the maximum altitude attained during the initial 'skip' to be higher. This additional altitude is necessary as the greater drag causes the velocity, and consequentially altitude, of the SPARTAN to decrease more rapidly.

-check all this

Trajectory Condition	Cd90	Cd95	Cd100	Cd105	Cd110	/%
Payload to Orbit (kg)	188.3	180.3	173.1	164.1	156.7	-1.6
Separation Alt, 1→2 (km)	25.96	25.85	25.79	25.96	25.88	-
Separation v, 1→2 (m/s)	1590	1572	1554	1534	1517	-3.67
Separation γ, 1→2 (m/s)	4.0	3.9	3.8	4.2	4.1	-
Separation Alt, 2→3 (km)	41.97	41.54	41.18	40.74	40.56	-0.07
Separation v, 2→3 (m/s)	2685	2639	2599	2542	2490	-9.75
Separation γ, 2→3 (deg)	10.6	10.8	10.9	11.3	11.7	0.05
Separation q, 2→3(kPa)	10.4	10.7	10.9	11.2	11.0	-
2nd Stage L/D, 2→3	4.8	4.8	4.8	4.7	4.4	-
2nd Stage Flight Time (s)	509.9	504.1	505.2	502.8	498.8	-
3rd Stage t, q > 5kpa (s)	14.3	13.2	13.3	15.1	13.7	-
3rd Stage max α (deg)	16.8	16.4	16.6	17.1	16.3	-
3rd Stage final v (m/s)	3722.6	3711.6	3684.3	3661.5	3547.8	-7.99
3rd Stage final m (kg)	2196.0	2168.5	2155.3	2130.5	2172.8	-

6.10 m SPARTAN

Trajectory Condition	m295	m297.5	m2100	m2102.5	m2105	/%
Payload to Orbit (kg)	177.9	174.1	173.1	168.3	165.7	-1.2
Separation Alt, 1→2 (km)	26.12	26.09	25.79	25.88	25.66	-
Separation v, 1→2 (m/s)	1594	1573	1554	1533	1512	-8.09
Separation γ, 1→2 (m/s)	3.9	4.1	3.8	4.2	4.1	-
Separation Alt, 2→3 (km)	41.28	40.99	41.18	40.79	40.83	-
Separation v, 2→3 (m/s)	2624	2606	2599	2565	2551	-7.47
Separation γ, 2→3 (deg)	10.9	10.8	10.9	11.2	11.2	-
Separation q, 2→3(kPa)	11.0	11.3	10.9	11.3	11.1	-
2nd Stage L/D, 2→3	4.7	4.7	4.8	4.6	4.6	-
2nd Stage Flight Time (s)	499.7	500.5	505.2	501.1	508.4	-
3rd Stage t, q > 5kpa (s)	13.7	13.7	13.3	14.7	13.8	-
3rd Stage max α (deg)	16.0	16.3	16.6	16.1	16.6	-
3rd Stage final v (m/s)	3687.7	3733.7	3684.3	3638.9	3617.7	-
3rd Stage final m (kg)	2174.1	2126.5	2155.3	2164.0	2167.0	-

6.11 m Fuel

Trajectory Condition	mF90	mF95	mF100	mF105	mF110	/%
Payload to Orbit (kg)	164.4	168.2	173.1	174.2	180.3	0.8
Separation Alt, 1→2 (km)	25.75	25.95	25.79	26.07	26.24	-
Separation v, 1→2 (m/s)	1578	1565	1554	1539	1527	-2.58
Separation γ, 1→2 (m/s)	3.6	4.0	3.8	4.5	4.8	-
Separation Alt, 2→3 (km)	41.21	40.86	41.18	41.00	41.14	-
Separation v, 2→3 (m/s)	2535	2566	2599	2607	2647	5.3
Separation γ, 2→3 (deg)	11.6	11.2	10.9	10.8	10.5	-0.05
Separation q, 2→3(kPa)	10.4	11.2	10.9	11.3	11.4	-
2nd Stage L/D, 2→3	4.7	4.8	4.8	4.7	4.8	-
2nd Stage Flight Time (s)	457.8	480.6	505.2	527.0	555.0	4.82
3rd Stage t, q > 5kpa (s)	12.1	14.7	13.3	14.9	14.9	-
3rd Stage max α (deg)	16.1	16.2	16.6	16.6	17.0	-
3rd Stage final v (m/s)	3585.2	3642.4	3684.3	3708.0	3740.9	7.54
3rd Stage final m (kg)	2182.9	2161.3	2155.3	2143.9	2148.8	-

Trajectory Condition	m390	m395	m3100	m3105	m3110	/%
Payload to Orbit (kg)	161.3	166.3	173.1	176.1	181.3	1
Separation Alt, 1→2 (km)	26.40	26.29	25.79	25.78	25.49	-0.05
Separation v, 1→2 (m/s)	1607	1579	1554	1526	1501	-5.27
Separation γ, 1→2 (m/s)	4.2	4.4	3.8	4.1	3.9	-
Separation Alt, 2→3 (km)	40.90	40.95	41.18	41.06	41.21	-
Separation v, 2→3 (m/s)	2651	2618	2599	2561	2537	-5.71
Separation γ, 2→3 (deg)	10.1	10.5	10.9	11.3	11.7	0.08
Separation q, 2→3(kPa)	11.9	11.5	10.9	10.8	10.4	-0.07
2nd Stage L/D, 2→3	5.0	4.8	4.8	4.7	4.5	-0.02
2nd Stage Flight Time (s)	501.4	502.8	505.2	503.8	505.8	-
3rd Stage $t, q > 5\text{kpa}$ (s)	15.2	14.6	13.3	12.9	13.3	-
3rd Stage max α (deg)	16.6	16.1	16.6	17.1	17.8	-
3rd Stage final v (m/s)	3715.0	3726.4	3684.3	3647.0	3588.9	-
3rd Stage final m (kg)	1953.2	2032.6	2155.3	2259.9	2392.5	22.12

Trajectory Condition	T390	T395	T3100	T3105	T3110	/%
Payload to Orbit (kg)	152.8	161.1	173.1	184.0	208.1	2.7
Separation Alt, 1→2 (km)	26.19	25.94	25.79	25.78	25.88	-
Separation v, 1→2 (m/s)	1551	1552	1554	1553	1554	-
Separation γ, 1→2 (m/s)	4.5	4.1	3.8	4.0	4.0	-
Separation Alt, 2→3 (km)	42.84	42.52	41.18	39.11	37.94	-0.26
Separation v, 2→3 (m/s)	2543	2550	2599	2628	2664	6.41
Separation γ, 2→3 (deg)	12.5	12.2	10.9	9.0	7.9	-0.25
Separation q, 2→3(kPa)	8.3	8.7	10.9	15.2	18.6	0.54
2nd Stage L/D, 2→3	4.1	4.4	4.8	5.1	5.2	0.06
2nd Stage Flight Time (s)	504.8	501.9	505.2	503.3	508.7	-
3rd Stage $t, q > 5\text{kpa}$ (s)	7.2	8.9	13.3	26.1	32.2	1.34
3rd Stage max α (deg)	19.9	18.5	16.6	14.2	12.1	-0.01
3rd Stage final v (m/s)	3181.6	3283.5	3684.3	4818.3	5778.8	134.59
3rd Stage final m (kg)	2416.0	2381.7	2155.3	1555.8	1222.6	-64.26

6.12 m3

6.13 T3

6.14 Viscous Drag

6.15 Comparison of Sensitivities

-check this (from paper)

These results indicate that the aerodynamic performance of the SPARTAN has significantly more

Trajectory Condition	Alternate
Payload to Orbit (kg)	176.0
Separation Alt, 1→2 (km)	25.87
Separation v, 1→2 (m/s)	1551
Separation γ, 1→2 (m/s)	3.8
Separation Alt, 2→3 (km)	41.28
Separation v, 2→3 (m/s)	2583
Separation γ, 2→3 (deg)	10.9
Separation q, 2→3(kPa)	10.7
2nd Stage L/D, 2→3	4.8
2nd Stage Flight Time (s)	505.5
3rd Stage t, $q > 5\text{kpa}$ (s)	14.7
3rd Stage max α (deg)	16.6
3rd Stage final v (m/s)	3656.5
3rd Stage final m (kg)	2162.7

impact than the efficiency of the scramjet engines on the optimised fly-back trajectory. During the fly-back trajectory, the specific impulse is effecting performance only whilst the scramjet engines are operating, compared with the aerodynamics of the vehicle, which effect performance throughout the trajectory. This suggests that, for maximum fly-back performance, the aerodynamic performance should be given preference over engine efficiency in the design of fly-back hypersonic accelerators.

6.16 Sonic Boom Ground Effects

6.17 Alternate Launch Locations

Southern Launch

note potential for sonic booms and safety issues

6.18 Summary

The fly-back trajectory of the SPARTAN hypersonic vehicle is investigated, from separation at $7.7^\circ\text{S}, 145.0^\circ\text{E}$ to landing at $15.3^\circ\text{S}, 144.9^\circ\text{E}$, corresponding to a near 180° turn and a fly-back of 878km. The aerodynamics of the SPARTAN are calculated using CART3D, an inviscid CFD package, over the range of Mach numbers and angle of attack values of flight. The optimal trajectory of the SPARTAN is calculated, to fly-back to the initial launch position with minimum fuel. The optimal trajectory is calculated using the launch vehicle optimal control program LODESTAR. It is found that the SPARTAN is capable of returning to its initial launch position, using 166.0kg of fuel. The optimal trajectory terminates when SPARTAN reaches 200m altitude at a velocity of 119.8m/s. After this point, it is

assumed that the SPARTAN lands on a traditional runway, at similar conditions to the space shuttle. This result indicates that the fly-back of a hypersonic launch vehicle from high velocity separation at a Mach number greater than nine, returning to its initial launch site using scramjet hypersonic air-breathing engines, is feasible. This fly-back to the the original launch site is a crucial component for low cost access-to-space using scramjets.

The coefficient of drag of the SPARTAN and specific impulse of the scramjet engines were independently varied by $\pm 10\%$ and the new optimal trajectories calculated to assess the robustness of the fly-back trajectory to uncertainties in vehicle aerodynamics and scramjet performance. It was found that a $\pm 10\%$ variation in C_D results in a $+31.0\%$ or -34.9% variation in fuel mass burned during fly-back, while a $\pm 10\%$ variation in I_{SP} results in a much smaller variation of -6.9% or $+13.8\%$. These results indicate that the aerodynamics of a fly-back hypersonic accelerator are much more significant to the fly-back fuel usage than the performance of the scramjet engine.

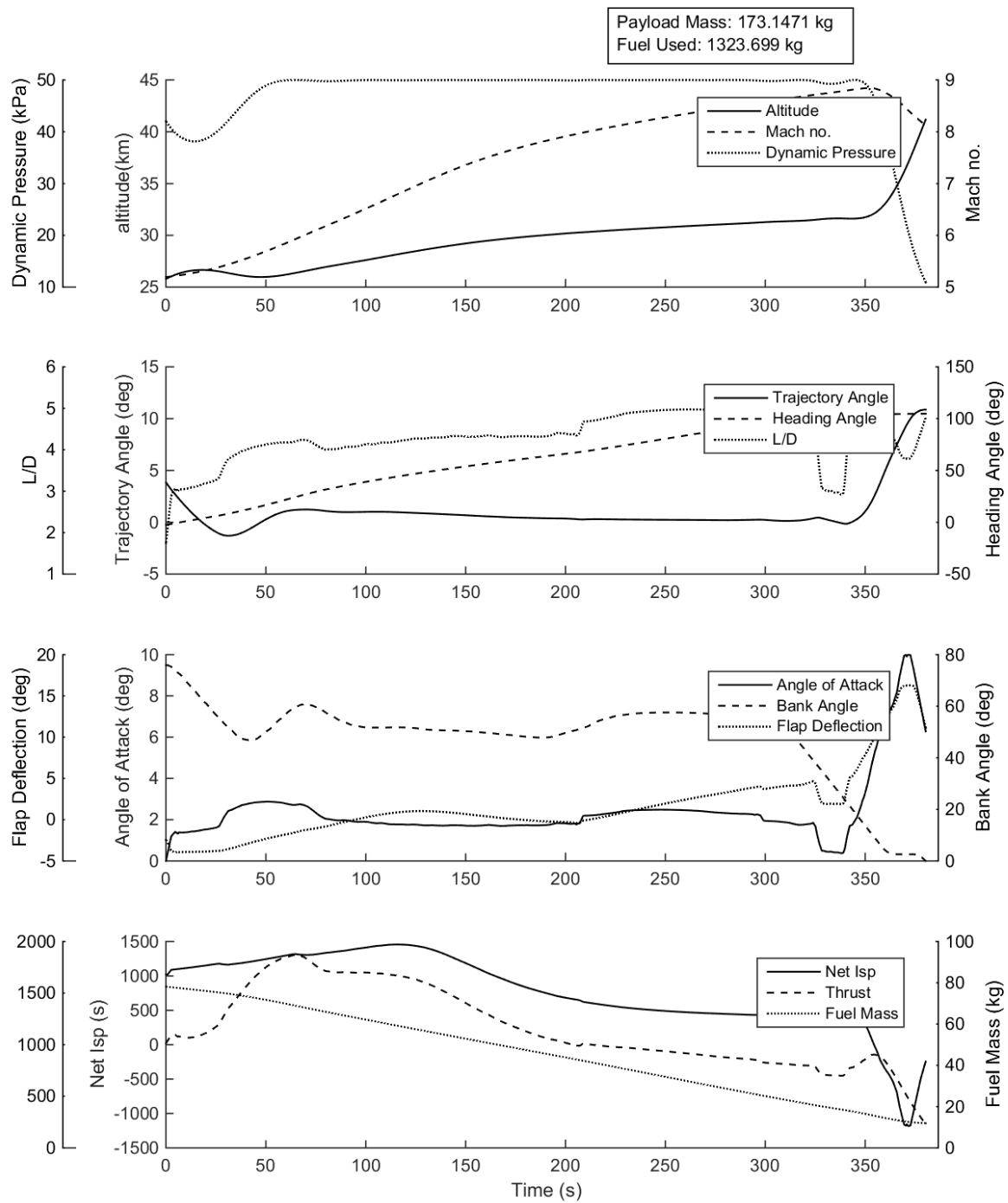


Figure 6.3

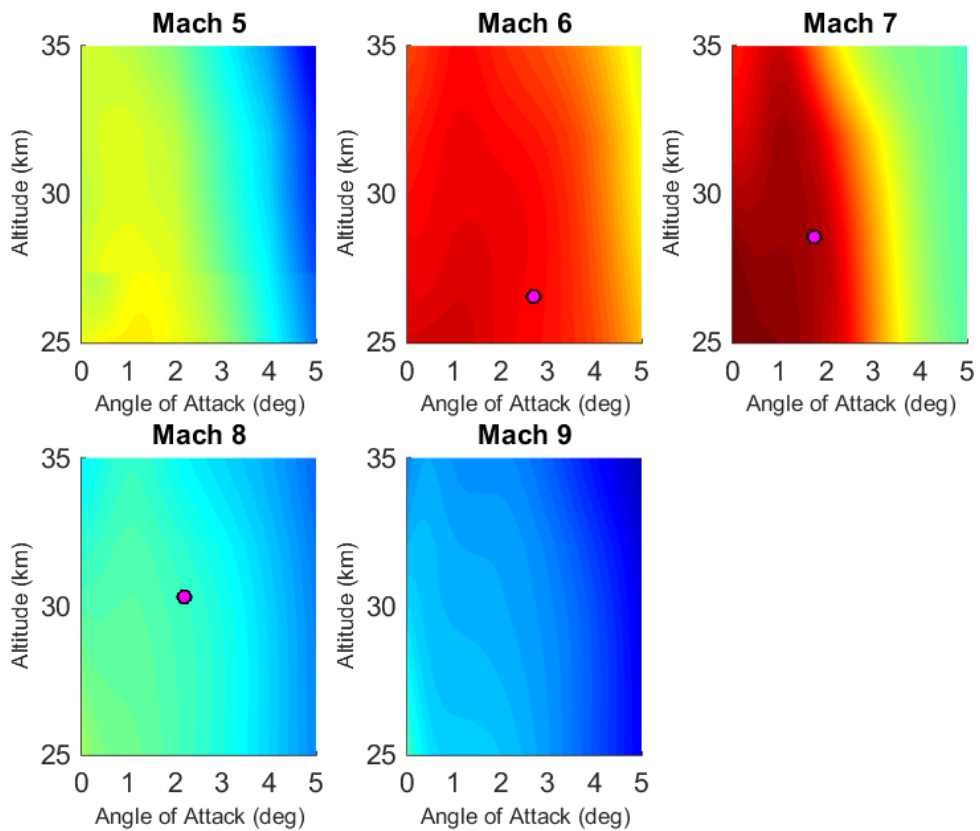


Figure 6.4

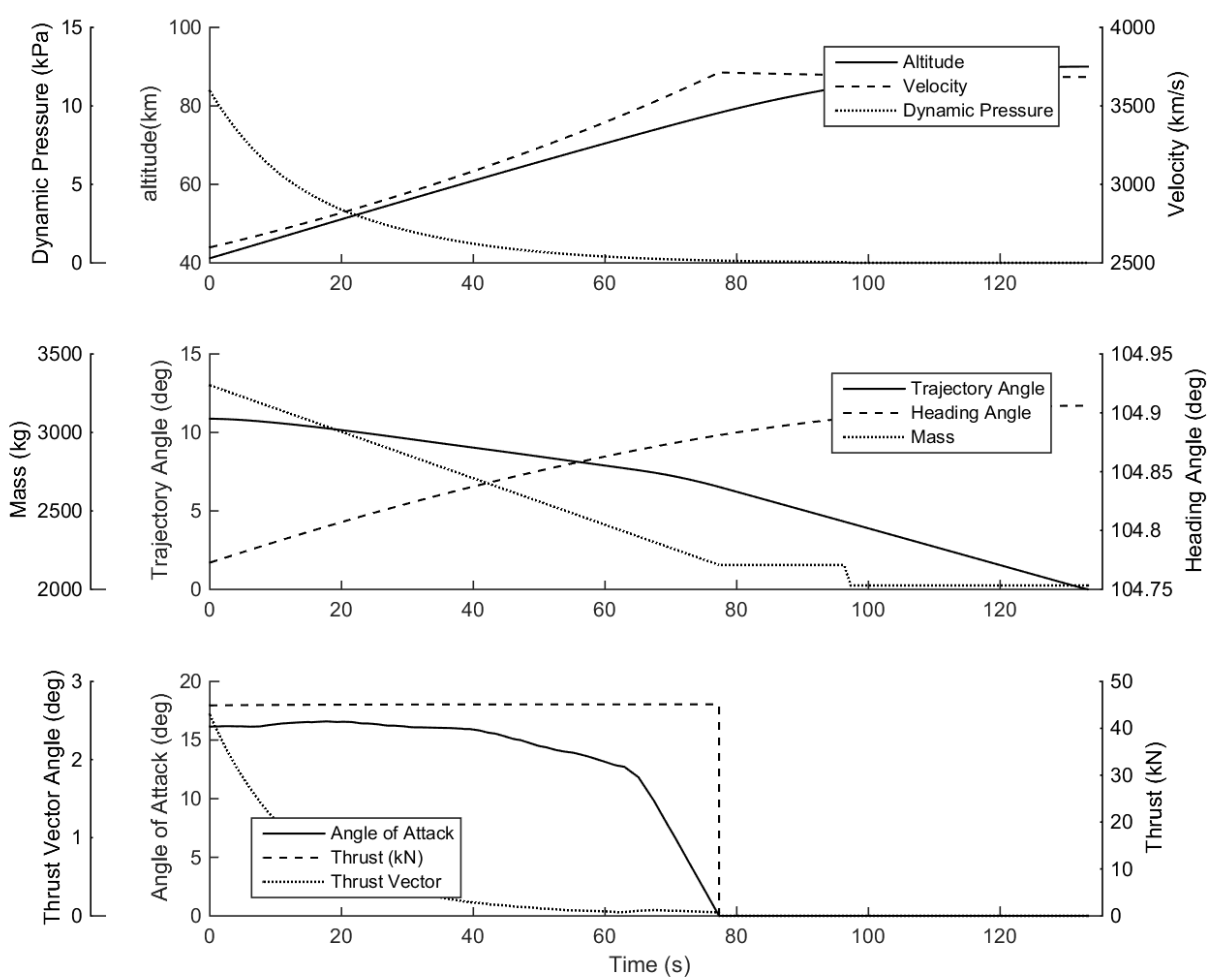


Figure 6.5

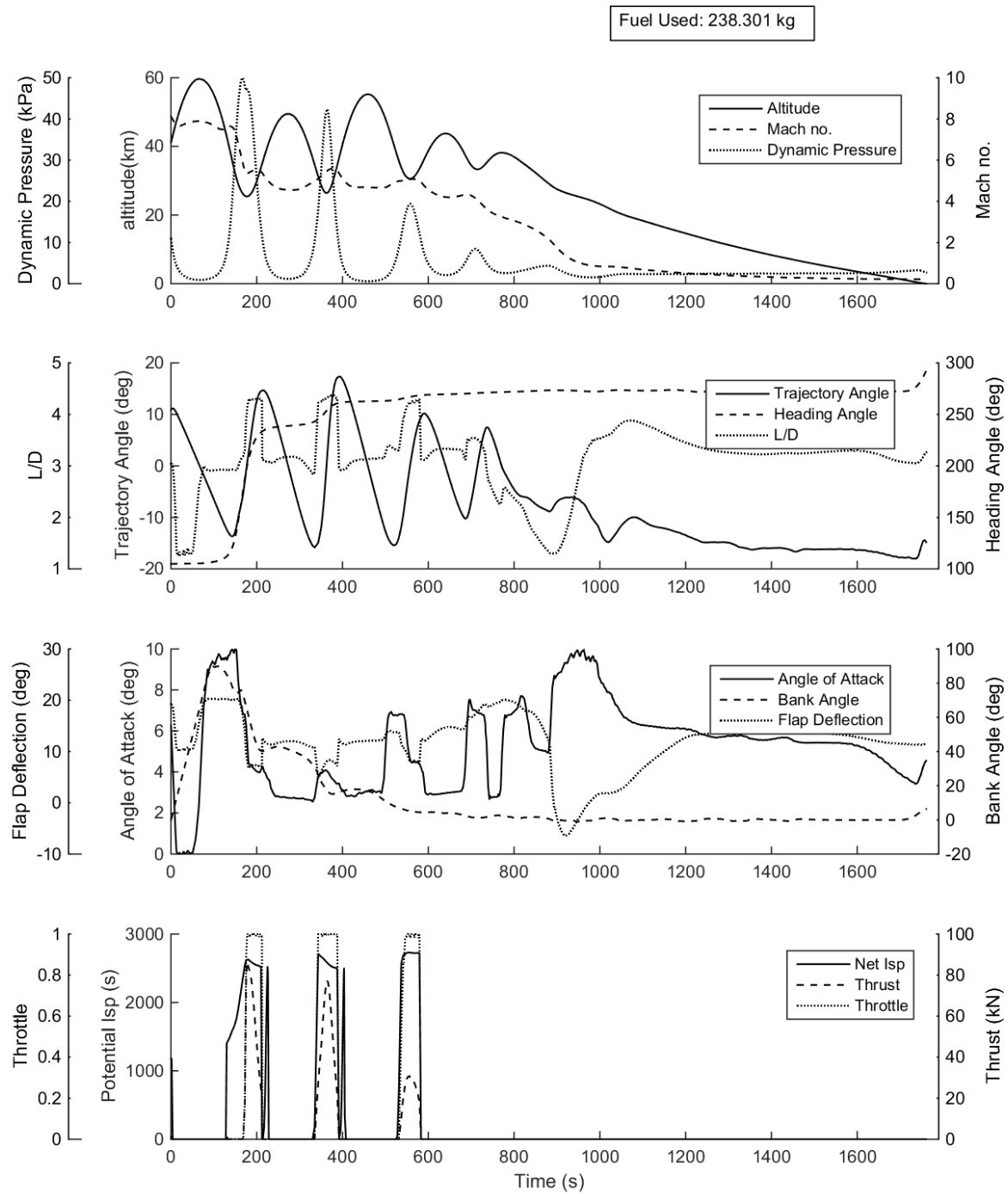


Figure 6.6

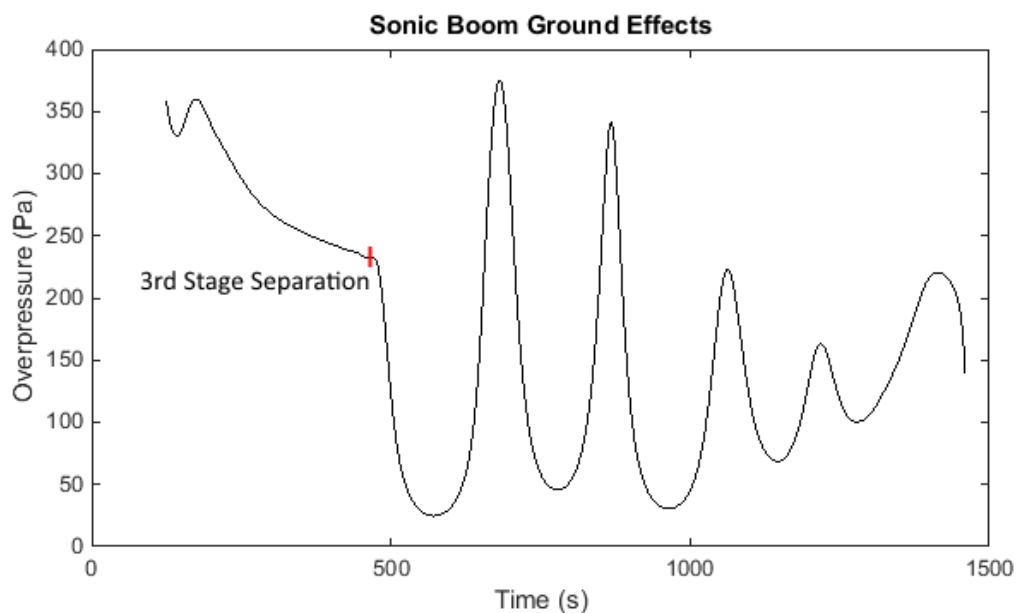


Figure 6.7

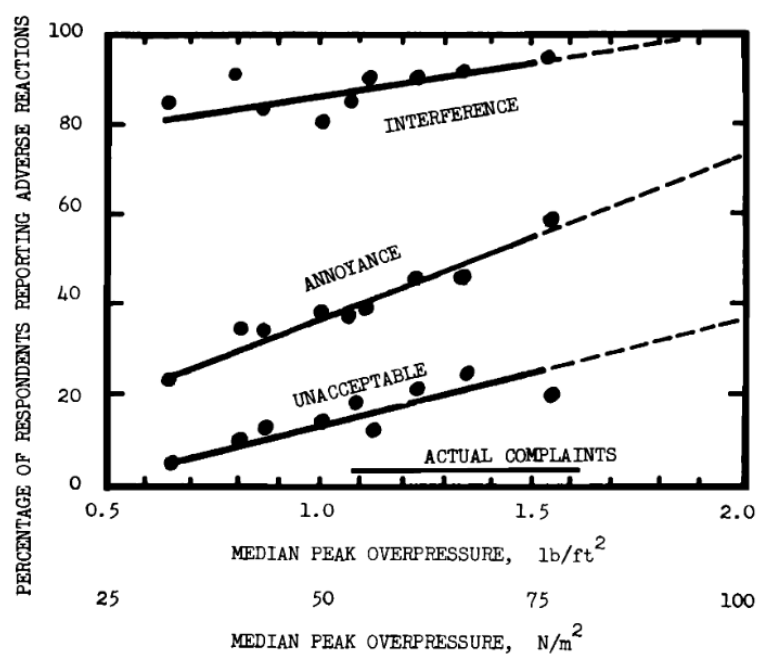


Figure 6.8

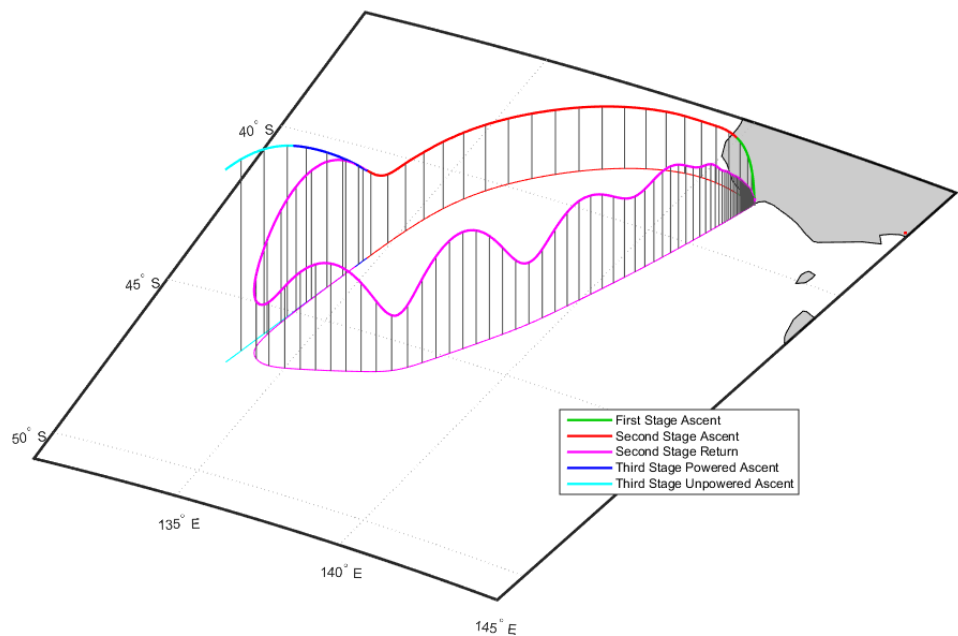


Figure 6.9

CHAPTER 7

CONCLUSIONS

- The optimal ascent trajectory for the rocket-scramjet-rocket three stage launch system involves a pull-up before third stage release.
- The optimal fly-back of the SPARTAN involves several distinct stages, including a boost phase, skip phase and glide phase.
- Description of conclusions from the combined ascent/fly-back trajectory. The combined ascent and fly-back trajectory involves the SPARTAN banking during ascent, to mitigate the distance flown during the ascent trajectory.
- Summary of conclusions from third stage sizing analysis.

7.1 Recommendations for future work

- Further design optimisation incorporating trajectory optimisation.
- Sizing of entire system for optimal monetary cost efficiency.

LIBRARY

- [1] Dineth Abeynayake and Alan Agon. “Comparison of computational and semi-empirical aerodynamics tools for making fit-for-purpose modelling decisions”. In: *20th International Congress on Modelling and Simulation*. December. Adelaide, Australia, 2013, pp. 1–6.
- [2] Michael J. Aftosmis, Marian Nemec, and Susan E. Cliff. “Adjoint-based low-boom design with Cart3D”. In: *29th AIAA Applied Aerodynamics Conference 2011*. June. 2011, pp. 1–17. ISBN: 9781624101458. DOI: [doi:10.2514/6.2011-3500](https://doi.org/10.2514/6.2011-3500). URL: <http://www.scopus.com/inward/record.url?eid=2-s2.0-84872373928&partnerID=tZ0tx3y1>.
- [3] *Airbus Defence and Spaces solution to reuse space Launchers*. 2017. URL: <https://airbusdefenceandspace.com/reuse-launchers/> (visited on 11/23/2017).
- [4] D Almosnino. “Assessment of an inviscid euler-adjoint solver for prediction of aerodynamic characteristics of the NASA HL-20 lifting body”. In: *34th AIAA Applied Aerodynamics Conference, 2016* June (2016). DOI: [10.2514/6.2016-3266](https://doi.org/10.2514/6.2016-3266). URL: [https://www.scopus.com/inward/record.uri?eid=2-s2.0-84980371959&partnerID=40&md5=1b304aabaa2976daf4d0742d5bdc6ba](http://www.scopus.com/inward/record.uri?eid=2-s2.0-84980371959&partnerID=40&md5=1b304aabaa2976daf4d0742d5bdc6ba).
- [5] Dan Almosnino. “A Low Subsonic Study of the NASA N2A Hybrid Wing-Body Using an Inviscid Euler-Adjoint Solver”. In: *34th AIAA Applied Aerodynamics Conference* June (2016), pp. 1–18. DOI: [doi:10.2514/6.2016-3267](https://doi.org/10.2514/6.2016-3267). URL: <http://dx.doi.org/10.2514/6.2016-3267>.
- [6] Astos Solutions. *Astos Solutions*. 2018. URL: <https://www.astos.de/> (visited on 07/24/2018).
- [7] *Australia’s hypersonic plane for a new space race*. URL: <http://www.bbc.com/future/story/20161117-australias-hypersonic-spaceplane-for-a-new-space-race> (visited on 06/21/2018).

- [8] Mokhtar S. Bazaraa, Hanif D. Sherali, and C. M. Shetty. *Nonlinear Programming: Theory and Algorithms*. John Wiley & Sons, 2013.
- [9] Nazareth Bedrossian, Bastion Technologies, and Louis Nguyen Nasa. “Zero Propellant Manoeuvre Flight Results For 180 Degree ISS Rotation”. In: *20th International Symposium on Space Flight Dynamics*. Annapolis, MD, 2007.
- [10] John T. Betts. “Survey of Numerical Methods for Trajectory Optimization”. In: *Journal of Guidance, Control, and Dynamics* 21.2 (1998), pp. 193–207. ISSN: 0731-5090. DOI: [10.2514/2.4231](https://doi.org/10.2514/2.4231).
- [11] F. S. Billig. “Research on supersonic combustion”. In: *Journal of Propulsion and Power* 9.4 (1993), pp. 499–514. ISSN: 0748-4658. DOI: [10.2514/3.23652](https://doi.org/10.2514/3.23652).
- [12] Ronald J Boain. “A-B-Cs of Sun-Synchronous Orbit Mission Design 14 AAS / AIAA Space Flight Mechanics Conference”. In: *14th AAS/AIAA Space Flight Mechanics Conference* (2004), pp. 1–19.
- [13] Pt Boggs and Jw Tolle. “Sequential quadratic programming for large-scale nonlinear optimization”. In: *Journal of Computational and Applied Mathematics* 124.1-2 (2000), pp. 123–137. ISSN: 03770427. DOI: [10.1016/S0377-0427\(00\)00429-5](https://doi.org/10.1016/S0377-0427(00)00429-5). URL: <http://linkinghub.elsevier.com/retrieve/pii/S0377042700004295> \$ \backslash backslash \$ <http://www.sciencedirect.com/science/article/pii/S0377042700004295>.
- [14] John Bradford et al. “Exploration of the design space for the ABLV-GT SSTO reusable launch vehicle”. In: *Space 2000 Conference and Exposition* September (2000). DOI: [doi:10.2514/6.2000-5136](https://doi.org/10.2514/6.2000-5136). URL: <http://dx.doi.org/10.2514/6.2000-5136>.
- [15] R Bulirsch et al. “Combining direct and indirect methods in optimal control: Range maximization of a hang glider”. In: *Optimal Control (Calculus of Variations, Optimal Control Theory and Numerical Methods)* 111 (1993), pp. 273–288.
- [16] Dong Chai et al. “Boost-skipping trajectory optimization for air-breathing hypersonic missile”. In: *Aerospace Science and Technology* 46 (2015), pp. 506–513. ISSN: 12709638. DOI: [10.1016/j.ast.2015.09.004](https://doi.org/10.1016/j.ast.2015.09.004). URL: <http://dx.doi.org/10.1016/j.ast.2015.09.004>.
- [17] Stephen Clark. *Falcon 9 rocket launching Sunday sports fin upgrade*. 2018. URL: <https://spaceflightnow.com/2017/06/25/falcon-9-rocket-launching-sunday-sports-fin-upgrade/> (visited on 06/21/2018).
- [18] William Colson. *Program to Optimize Simulated Trajectories* 2. 2017. URL: <https://post2.larc.nasa.gov/> (visited on 07/24/2018).

- [19] a. C. Composites. “<http://www.corkcomposites.amorim.com/images/livraria/TPS%20brochure.pdf>”. In: *Consultado em Março de 2014* ().
- [20] Stephen Cook and Uwe Hueter. “NASA’s Integrated Space Transportation Plan 3rd generation reusable launch vehicle technology update”. In: *Acta Astronautica* 53.4-10 (2003), pp. 719–728. ISSN: 00945765. DOI: [10.1016/S0094-5765\(03\)00113-9](https://doi.org/10.1016/S0094-5765(03)00113-9).
- [21] Edward T. Curran. “Scramjet Engines: The First Forty Years”. In: *Journal of Propulsion and Power* 17.6 (2001), pp. 1138–1148. ISSN: 0748-4658. DOI: [10.2514/2.5875](https://doi.org/10.2514/2.5875). URL: <http://arc.aiaa.org/doi/10.2514/2.5875>.
- [22] Edward T. Curran. “Scramjet Engines: The First Forty Years”. In: *Journal of Propulsion and Power* 17.6 (2001), pp. 1138–1148. ISSN: 0748-4658. DOI: [10.2514/2.5875](https://doi.org/10.2514/2.5875).
- [23] E.T. Curran. *Scramjet Propulsion*. Progress in Astronautics and Aeronautics, 2001. ISBN: 978-1-60086-660-9.
- [24] F. Curran et al. “The Benefits of Hypersonic Airbreathing Launch Systems for Access to Space”. In: *39th AIAA/ASME/SAE/ASEE Joint Propulsion Conference and Exhibit* July (2003), pp. 1–14. DOI: [10.2514/6.2003-5265](https://doi.org/10.2514/6.2003-5265). URL: <http://arc.aiaa.org/doi/10.2514/6.2003-5265>.
- [25] Derek Dalle, Sean Torrez, and James Driscoll. “Turn Performance of an Air-Breathing Hypersonic Vehicle”. In: *AIAA Atmospheric Flight Mechanics Conference* August (2011). DOI: [10.2514/6.2011-6300](https://doi.org/10.2514/6.2011-6300). URL: <http://arc.aiaa.org/doi/10.2514/6.2011-6300>.
- [26] Derek J. Dalle et al. “Minimum-Fuel Ascent of a Hypersonic Vehicle Using Surrogate Optimization”. In: *Journal of Aircraft* 51.6 (2014), pp. 1973–1986. ISSN: 0021-8669. DOI: [10.2514/1.C032617](https://doi.org/10.2514/1.C032617). URL: <http://arc.aiaa.org/doi/10.2514/1.C032617>.
- [27] Christopher L. Darby, William W. Hager, and Anil V. Rao. “An hp-adaptive pseudospectral method for solving optimal control problems”. In: *Optimal Control Applications and Methods* 32.3 (2011), pp. 476–502. DOI: [10.1002/oca.957](https://doi.org/10.1002/oca.957). URL: <http://doi.wiley.com/10.1002/oca.957>.
- [28] Christopher L. Darby, William W. Hager, and Anil V. Rao. “Direct Trajectory Optimization Using a Variable Low-Order Adaptive Pseudospectral Method”. In: *Journal of Spacecraft and Rockets* 48.3 (2011), pp. 433–445. ISSN: 0022-4650. DOI: [10.2514/1.52136](https://doi.org/10.2514/1.52136).
- [29] By Alfred J Eggers, H Julian Allen, and Stanford E Neice. “Technical Note 4046”. In: October (1957).
- [30] Thino Eggers. “Aerodynamic Analysis of the Dual-Mode Ramjet Vehicle JAPHAR”. In: *Notes on Numerical Fluid Mechanics and Multidisciplinary Design*. Vol. 115. 2011, pp. 137–140. ISBN: 9783642177699.

- [31] F. Fahroo and I.M. Ross. “Direct trajectory optimization by a Chebyshev pseudospectral method”. In: *Proceedings of the 2000 American Control Conference*. Chicago, IL, 2000, pp. 3860–3864. ISBN: 0-7803-5519-9. DOI: [10.1109/ACC.2000.876945](https://doi.org/10.1109/ACC.2000.876945).
- [32] Fariba Fahroo and I. Michael Ross. “Costate Estimation by a Legendre Pseudospectral Method”. In: *Journal of Guidance, Control, and Dynamics* 24.2 (2001), pp. 270–277. ISSN: 0731-5090. DOI: [10.2514/2.4709](https://doi.org/10.2514/2.4709).
- [33] Rob Falck. *OTIS*. 2016. URL: <https://otis.grc.nasa.gov/index.html> (visited on 07/24/2018).
- [34] Giorgio Fasano and Janos Pinter. *Modelling and Optimisation in Space Engineering*. New York, NY: Springer, 2013. DOI: [10.1007/978-1-4614-4469-5](https://doi.org/10.1007/978-1-4614-4469-5).
- [35] E. Fitzer and L.M. Manocha. *Carbon Reinforcements and Carbon/Carbon Composites*. Berlin, Heidelberg: Springer Berlin Heidelberg, 1998. ISBN: 3-642-58745-3.
- [36] Kevin W. Flaherty, Katherine M. Andrews, and Glenn W. Liston. “Operability Benefits of Airbreathing Hypersonic Propulsion for Flexible Access to Space”. In: *Journal of Spacecraft and Rockets* 47.2 (2010), pp. 280–287. ISSN: 0022-4650. DOI: [10.2514/1.43750](https://doi.org/10.2514/1.43750). URL: <http://arc.aiaa.org/doi/abs/10.2514/1.43750>.
- [37] Sholto O. Forbes-Spyratos et al. “Trajectory Design of a Rocket-Scramjet-Rocket Multi-Stage Launch System”. In: *Journal of Spacecraft and Rockets - Under Consideration* TBD (2018).
- [38] S.O. Forbes-Spyratos et al. “Trajectory design of a rocket-scramjet-rocket multi-stage launch system”. In: *21st AIAA International Space Planes and Hypersonics Technologies Conference, Hypersonics 2017*. Xiamen, China, 2017. ISBN: 9781624104633.
- [39] Jeff Foust. *SpaceX achievements generate growing interest in reusable launchers*. 2018. URL: <http://spacenews.com/spacex-achievements-generate-growing-interest-in-reusable-launchers/> (visited on 06/21/2018).
- [40] Ronald S. Fry. “A Century of Ramjet Propulsion Technology Evolution”. In: *Journal of Propulsion and Power* 20.1 (2004), pp. 27–58. ISSN: 0748-4658. DOI: [10.2514/1.9178](https://doi.org/10.2514/1.9178). URL: <http://arc.aiaa.org/doi/10.2514/1.9178>.
- [41] D Garg, Ma Patterson, and Ww Hager. “An Overview of Three Pseudospectral Methods for the Numerical Solution of Optimal Control Problems”. In: *Advances in thAstronautical Sciences* 135 (2009), pp. 1–17. URL: <http://vdol.mae.ufl.edu/ConferencePublications/unifiedFrameworkAAS.pdf>.
- [42] Adam Gilmour. *ROCKET STARTUP SHOOTS FOR THE STARS WITH AUD 5 MILLION (USD 3 . 7 MILLION) SERIES A FUNDING*. 2017.

- [43] Reynaldo Gomez et al. “STS-107 Investigation Ascent CFD Support”. In: *34th AIAA Fluid Dynamics Conference and Exhibit* (2004), pp. 1–15. DOI: [10.2514/6.2004-2226](https://doi.org/10.2514/6.2004-2226). URL: <http://arc.aiaa.org/doi/10.2514/6.2004-2226>.
- [44] Chunlin Gong, Bing Chen, and Liangxian Gu. “Design and Optimization of RBCC Powered Suborbital Reusable Launch Vehicle”. In: *19th AIAA International Space Planes and Hypersonic Systems and Technologies Conference* June (2014), pp. 1–20. DOI: [10.2514/6.2014-2361](https://doi.org/10.2514/6.2014-2361). URL: <http://arc.aiaa.org/doi/abs/10.2514/6.2014-2361>.
- [45] Qi Gong, I. Michael Ross, and Friba Fahroo. “Costate Computation by a Chebyshev Pseudospectral Method”. In: *Journal of Guidance, Control, and Dynamics* 33.2 (2010), pp. 623–628. ISSN: 0731-5090. DOI: [10.2514/1.45154](https://doi.org/10.2514/1.45154).
- [46] William Heiser et al. *Hypersonic Airbreathing Propulsion*. the American Institute of Aeronautics and Astronautics, 1994. ISBN: 978-1-56347-035-6.
- [47] Heiser H. H. and D T Pratt. *Hypersonic Airbreathing Propulsion*. Washington, D.C: American Institute of Aeronautics and Astronautics, 1994, p. 11. ISBN: 1-56347-035-7. DOI: [10.2514/4.470356](https://doi.org/10.2514/4.470356).
- [48] Barry Mark Hellman. *Comparison of Return to Launch Site Options for a Reusable Booster Stage*. Tech. rep. Space Sytems Design Lab, Georgia Institute of technology, 2005, pp. 1–18.
- [49] H. Hindi. “A tutorial on convex optimization II: duality and interior point methods”. In: *2006 American Control Conference* 1 (2006), 11 pp. ISSN: 07431619. DOI: [10.1109/ACC.2006.1655436](https://doi.org/10.1109/ACC.2006.1655436). URL: <http://ieeexplore.ieee.org/document/1655436/>.
- [50] Horizon. *Black Arrow* 2. 2017. URL: <http://www.horizonsas.com/products/> (visited on 12/01/2017).
- [51] B Houska, H.J Ferrau, and M. Diehl. “ACADO Toolkit – An Open Source Framework for Automatic Control and Dynamic Optimization”. In: *Optimal Control Applications and Methods* 32.3 (2011), pp. 298–312.
- [52] Gt Huntington, David Benson, and Av Rao. “A Comparison of Accuracy and Computational Efficiency of Three Pseudospectral Methods”. In: *AIAA Guidance, Navigation and Control Conference and Exhibit* (2007), pp. 1–43. DOI: [10.2514/6.2007-6405](https://doi.org/10.2514/6.2007-6405). URL: <http://arc.aiaa.org/doi/abs/10.2514/6.2007-6405>.
- [53] Thomas Jazra, Dawid Preller, and Michael K. Smart. “Design of an Airbreathing Second Stage for a Rocket-Scramjet-Rocket Launch Vehicle”. In: *Journal of Spacecraft and Rockets* 50.2 (2013), pp. 411–422. ISSN: 0022-4650. DOI: [10.2514/1.A32381](https://doi.org/10.2514/1.A32381). URL: <http://arc.aiaa.org/doi/abs/10.2514/1.A32381>.

- [54] D. Jezewski. “An Optimal, Analytic Solution to the Linear-Gravity, Constant-Thrust Trajectory Problem”. In: *Journal of Spacecraft and Rockets* July (1971), pp. 793–796.
- [55] *JModelica.org*. URL: <https://jmodelica.org/> (visited on 07/24/2018).
- [56] Scott Josselyn and I Michael Ross. “Rapid Verification Method for the Trajectory Optimization of Reentry Vehicles”. In: *Notes* 26.3 (2002), pp. 505–508. ISSN: 0731-5090. DOI: [10.2514/2.5074](https://doi.org/10.2514/2.5074).
- [57] Takeshi Kanda and Tetsuo Hiraiwa. “Evaluation of Effectiveness of Periodic Flight by a Hypersonic Vehicle”. In: *Journal of Aircraft* 44.6 (2007), pp. 2076–2077. ISSN: 0021-8669. DOI: [10.2514/1.31143](https://doi.org/10.2514/1.31143).
- [58] Takeshi Kanda and Kenji Kudo. “Payload to Low Earth Orbit by Aerospace Plane with Scramjet Engine Summary”. In: *Journal of Propulsion and Power Technical Notes* 13.1 (1996), pp. 164–166. ISSN: 0748-4658. DOI: [10.2514/2.7641](https://doi.org/10.2514/2.7641).
- [59] Yoshiaki Kawajir, Carl D Laird, and Andreas Waechter. “Introduction to IPOPT: A tutorial for downloading, installing, and using IPOPT .” In: *Most* (2010), pp. 1–68. ISSN: 00981354. DOI: http://web.mit.edu/ipopt_v3.8/doc/documentation.pdf. arXiv: [arXiv:1011.1669v3](https://arxiv.org/abs/1011.1669v3).
- [60] Matthew P Kelly. “Transcription Methods for Trajectory Optimization A beginners tutorial”. In: (2015), pp. 1–14.
- [61] Randy Kendall and Pete Portanova. *Launch Vehicles Then and Now: 50 Years of Evolution*. 2010. URL: <http://www.aerospace.org/crosslinkmag/spring-2010/launch-vehicles-then-and-now-50-years-of-evolution/> (visited on 06/21/2018).
- [62] Andrew D Ketsdever et al. “Overview of Advanced Concepts for Space Access”. In: *Journal of Spacecraft and Rockets* 47.2 (2010), pp. 238–250. ISSN: 0022-4650. DOI: [10.2514/1.46148](https://doi.org/10.2514/1.46148).
- [63] RI Kimmel et al. “HIFiRE-5 flight vehicle design”. In: *AIAA paper* July (2010), pp. 1–17. DOI: [10.2514/6.2010-4985](https://doi.org/10.2514/6.2010-4985). URL: <http://arc.aiaa.org/doi/pdf/10.2514/6.2010-4985>.
- [64] Masatoshi Kodera et al. “Multi-Objective Design and Trajectory Optimization of Space Transport Systems with RBCC Propulsion via Evolutionary Algorithms and Pseudospectral Methods”. In: *52nd Aerospace Sciences Meeting* January (2014), pp. 1–14. DOI: [10.2514/6.2014-0629](https://doi.org/10.2514/6.2014-0629). URL: <http://arc.aiaa.org/doi/10.2514/6.2014-0629>.
- [65] Heinz-Otto Kreiss and Joseph Oliger. “Comparison of accurate methods for the integration of hyperbolic equations”. In: *Tellus A* 1971 (1972). ISSN: 0280-6495. DOI: [10.3402/tellusa.v24i3.10634](https://doi.org/10.3402/tellusa.v24i3.10634).

- [66] *Kuai Zhou (Fast Vessel)*. URL: <https://chinaspacereport.com/launch-vehicles/kuaizhou/> (visited on 12/01/2017).
- [67] Markus Kuhn et al. “Innovative European Launcher Concept SMILE”. In: *21st AIAA International Space Planes and Hypersonics Technologies Conference* March (2017), pp. 1–14. DOI: [10.2514/6.2017-2441](https://arc.aiaa.org/doi/10.2514/6.2017-2441). URL: <https://arc.aiaa.org/doi/10.2514/6.2017-2441>.
- [68] Roger D. Launius. “Assessing the legacy of the Space Shuttle”. In: *Space Policy* 22.4 (2006), pp. 226–234. ISSN: 02659646. DOI: [10.1016/j.spacepol.2006.08.008](https://doi.org/10.1016/j.spacepol.2006.08.008).
- [69] Sarah Lewin. *Blue Origin Announces Big 'New Glenn' Rocket for Satellite & Crew Launches*. 2016. URL: <https://www.space.com/34034-blue-origin-new-glenn-rocket-for-satellites-people.html> (visited on 06/21/2018).
- [70] Huifeng Li et al. “Footprint problem with angle of attack optimization for high lifting reentry vehicle”. In: *Chinese Journal of Aeronautics* 25.2 (2012), pp. 243–251. ISSN: 10009361. DOI: [10.1016/S1000-9361\(11\)60384-1](https://doi.org/10.1016/S1000-9361(11)60384-1). URL: [http://dx.doi.org/10.1016/S1000-9361\(11\)60384-1](http://dx.doi.org/10.1016/S1000-9361(11)60384-1).
- [71] Ping Lu. “Inverse dynamics approach to trajectory optimization for an aerospace plane”. In: *Journal of Guidance, Control, and Dynamics* 16.4 (1993), pp. 726–732. ISSN: 0731-5090. DOI: [10.2514/3.21073](https://doi.org/10.2514/3.21073). URL: <http://arc.aiaa.org/doi/abs/10.2514/3.21073>.
- [72] J W Magee Bruno, T.J., Friend, D. G., Huber, M.L., Laesecke, A., Lemmon, E.W., McLinden, M.O., Perkins, R.A., Baranski, J., Widegren, J.A. *Thermophysical Properties Measurements and Models for Rocket Propellant RP-1: Phase I, NIST- IR 6644*, National Institute of Standards and Technology (U.S.) Tech. rep. 2006.
- [73] Unmeel Mehta et al. “Skylon Aerospace Plane and Its Aerodynamics and Plumes”. In: *Journal of Spacecraft and Rockets* 53.2 (2016), pp. 340–353. ISSN: 0022-4650. DOI: [10.2514/1.A33408](https://doi.org/10.2514/1.A33408). URL: <http://arc.aiaa.org/doi/10.2514/1.A33408>.
- [74] Unmeel B. Mehta and Jeffrey V. Bowles. “Two-Stage-to-Orbit Spaceplane Concept with Growth Potential”. In: *Journal of Propulsion and Power* 17.6 (2001), pp. 1149–1161. ISSN: 0748-4658. DOI: [10.2514/2.5886](https://doi.org/10.2514/2.5886).
- [75] Dave Mosher. *SpaceX faces a growing list of competitors in the new space race*. 2018. URL: <https://www.businessinsider.com.au/spacex-elon-musk-competition-companies-rockets-2018-3> (visited on 06/21/2018).
- [76] Nathan D. Moshman and Ronald J. Proulx. “Range Improvements in Gliding Reentry Vehicles from Thrust Capability”. In: *Journal of Spacecraft and Rockets* 51.5 (2014), pp. 1681–1694. ISSN: 0022-4650. DOI: [10.2514/1.A32764](https://doi.org/10.2514/1.A32764). URL: <http://arc.aiaa.org/doi/10.2514/1.A32764>.

- [77] NASA. *U.S. Standard Atmosphere, 1976*. U.S. Government Printing Office, Washington, D.C., 1976, pp. 1–243. URL: <http://ntrs.nasa.gov/archive/nasa/casi.ntrs.nasa.gov/19770009539.pdf>.
- [78] NASA Glenn Research Center. *Euler Equations*. URL: <https://www.grc.nasa.gov/WWW/k-12/airplane/eulereqs.html> (visited on 07/24/2018).
- [79] Yuanbo Nie, Omar Faqir, and Eric Kerrigan. *ICLOCS2*. 2018. URL: <http://www.ee.ic.ac.uk/ICLOCS/> (visited on 07/24/2018).
- [80] Carlos Niederstrasser and Warren Frick. “Small Launch Vehicles A 2015 State of the Industry Survey”. In: *Proceedings of the 29th Annual AIAA/USU Conference on Small Satellites* (2015).
- [81] J.R. Olds and I.a. Budianto. “Constant Dynamic Pressure Trajectory Simulation with POST”. In: *Aerospace Sciences Meeting & Exhibit*. Reno, NV, 1998, pp. 1–13. DOI: [10.2514/6.1998-302](https://doi.org/10.2514/6.1998-302). URL: <http://citeserx.ist.psu.edu/viewdoc/download?doi=10.1.1.25.6506&rep=rep1&type=pdf>.
- [82] Orbital Access. *The Orbital 500R*. 2017. URL: <http://www.orbital-access.com/the-orbital-500/> (visited on 12/01/2017).
- [83] DARPA Outreach. *DARPA Picks Design for Next-Generation Spaceplane*. 2017. URL: <https://www.darpa.mil/news-events/2017-05-24> (visited on 11/16/2017).
- [84] Shishir Pandya, Scott Murman, and Michael Aftosmis. “Validation of Inlet and Exhaust Boundary Conditions for a Cartesian Method”. In: *22nd Applied Aerodynamics Conference and Exhibit January* (2004), pp. 1–16. ISSN: 10485953. DOI: [10.2514/6.2004-4837](https://doi.org/10.2514/6.2004-4837). URL: <http://arc.aiaa.org/doi/10.2514/6.2004-4837>.
- [85] A Paull, R.J Stalker, and D Mee. “Thrust Measurements of a Complete Axisymmetric Scramjet in an Impulse Facility”. In: *5TH INTERNATIONAL AEROSPACE PLANES AND HYPERSONICS TECHNOLOGIES CONFERENCE*. 1993.
- [86] Fabrizio Pescetelli et al. “Ascent Trajectory Optimisation for a Single-Stage-to-Orbit Vehicle with Hybrid Propulsion”. In: *18th AIAA/3AF International Space Planes and Hypersonic Systems and Technologies Conference*. September. 2012, pp. 1–18. ISBN: 978-1-60086-931-0. DOI: [10.2514/6.2012-5828](https://doi.org/10.2514/6.2012-5828). URL: <http://arc.aiaa.org/doi/abs/10.2514/6.2012-5828>.
- [87] Harry Pettit. *The galaxy's fastest car*. 2018. URL: <http://www.dailymail.co.uk/sciencetech/article-5361789/Ride-Elon-Musks-Starman-travels-space.html> (visited on 06/21/2018).

- [88] Richard W. Powell et al. “Ascent performance of an air-breathing horizontal-takeoff launch vehicle”. In: *Journal of Guidance, Control, and Dynamics* 14.4 (1991), pp. 834–839. ISSN: 0731-5090. DOI: [10.2514/3.20719](https://doi.org/10.2514/3.20719).
- [89] Dawid Preller. “Multidisciplinary Design and Optimisation of a Pitch Trimmed Hypersonic Airbreathing Accelerating Vehicle”. PhD thesis. University of Queensland, 2018.
- [90] Dawid Preller and Michael Smart. “Reusable Launch of Small Satellites using Scramjets”. In: *Journal of Spacecraft and Rockets* (2017).
- [91] Dawid Preller and Michael K Smart. “Longitudinal Control Strategy for Hypersonic Accelerating Vehicles”. In: *Journal of Spacecraft and Rockets* 52.3 (2015), pp. 1–6. ISSN: 0022-4650. DOI: [10.2514/1.A32934](https://doi.org/10.2514/1.A32934). URL: <http://dx.doi.org/10.2514/1.A32934>.
- [92] Dawid Preller and Michael K. Smart. “Reusable Launch of Small Satellites Using Scramjets”. In: *Journal of Spacecraft and Rockets* 54.6 (2017), pp. 1–13. ISSN: 0022-4650. DOI: [10.2514/1.A33610](https://doi.org/10.2514/1.A33610). URL: <https://arc.aiaa.org/doi/10.2514/1.A33610>.
- [93] Dawid Preller and Michael K. Smart. “Scramjets for Reusable Launch of Small Satellites”. In: *Journal of Spacecraft and Rockets Advance On* (2017), pp. 1–13. ISSN: 0022-4650. DOI: [10.2514/6.2015-3586](https://doi.org/10.2514/6.2015-3586). URL: <http://arc.aiaa.org/doi/10.2514/6.2015-3586>.
- [94] Patrizia Pucci and James B Serrin. *The maximum principle*. Tech. rep. 2007, pp. 80–104.
- [95] Ligy Susan Punnoose, Madan Lal, and V Brinda. “On-Line Trajectory Optimization of a Typical Air-Breathing Launch Vehicle using Energy State Approximation Approach”. In: *Advances in Control and Optimization of Dynamical Systems* (2007), pp. 296–302.
- [96] Anil V. Rao et al. “Algorithm 902”. In: *ACM Transactions on Mathematical Software* 37.2 (2010), pp. 1–39. ISSN: 00983500. DOI: [10.1145/1731022.1731032](https://doi.org/10.1145/1731022.1731032).
- [97] Av Rao. “A survey of numerical methods for optimal control”. In: *Advances in the Astronautical Sciences* 135 (2009), pp. 497–528. URL: <http://vdol.mae.ufl.edu/ConferencePublications/trajectorySurveyAAS.pdf>.
- [98] Richard Webb. “Is It Worth It? The Economics of Reusable Space Transportation”. In: *ICEAA 2016 International Training Symposium, Bristol, UK* (2016), pp. 1–19.
- [99] S. Tauqeer Ul Islam Rizvi, Lin Shu He, and Da Jun Xu. “Optimal trajectory and heat load analysis of different shape lifting reentry vehicles for medium range application”. In: *Defence Technology* 11.4 (2015), pp. 350–361. ISSN: 22149147. DOI: [10.1016/j.dt.2015.06.003](https://doi.org/10.1016/j.dt.2015.06.003). URL: <http://dx.doi.org/10.1016/j.dt.2015.06.003>.
- [100] Joseph M Roche and Daniel N Kosareo. *Structural Sizing of a 25000-Lb Payload , Air-Breathing Launch Vehicle for Single-Stage-To-Orbit*. Tech. rep. January 2001. 2000.

- [101] Rocket Lab. *Electron*. 2016. URL: <https://www.rocketlabusa.com/electron/> (visited on 11/30/2017).
- [102] RocketCrafters. *Intrepid-1*. 2017. URL: <http://rocketcrafters.space/products-services/intrepid-launcher-family/intrepid-1/> (visited on 12/01/2017).
- [103] I M Ross and F Fahroo. “A direct method for solving nonsmooth optimal control problems”. In: *Proceedings of the 2002 {IFAC World Congress}* (2002).
- [104] I. Michael Ross and Fariba Fahroo. “Pseudospectral Knotting Methods for Solving Nonsmooth Optimal Control Problems”. In: *Journal of Guidance, Control, and Dynamics* 27.3 (2004), pp. 397–405. ISSN: 0731-5090. DOI: [10.2514/1.3426](https://doi.org/10.2514/1.3426).
- [105] P E Rutquist and M M Edvall. “PROPT - Matlab Optimal Control Software”. In: *Tomlab Optimization Inc* 260 (2010), pp. –.
- [106] Jeanne Ryba. *Space Shuttle*. 2017. URL: https://www.nasa.gov/mission_pages/shuttle/launch/landing101.html (visited on 11/27/2017).
- [107] Denton G. Sagerman et al. “Comparisons of Measured and Modeled Aero-thermal Distributions for Complex Hypersonic Configurations”. In: *55th AIAA Aerospace Sciences Meeting* January (2017), pp. 1–22. DOI: [10.2514/6.2017-0264](https://doi.org/10.2514/6.2017-0264). URL: <http://arc.aiaa.org/doi/10.2514/6.2017-0264>.
- [108] Marti Sarigul-Klijn and Nesrin Sarigul-Klijn. “Flight Mechanics of Manned Sub-Orbital Reusable Launch Vehicles with Recommendations for Launch and Recovery”. In: *41st Aerospace Sciences Meeting and Exhibit, Aerospace Sciences Meetings*. Reno, NV, 2003.
- [109] Corin Segal. *The Scramjet Engine: Processes and Characteristics*. Cambridge, UK: Cambridge University Press, 2009, p. 229. ISBN: 9780521838153.
- [110] John D Shaughnessy, S Zane Pinckney, and John D McMinn. “Hypersonic Vehicle Simulation Configuration Model : Winged-Cone Configuration”. In: (1990).
- [111] Robert Simmon. *Three Classes of Orbit*. 2009. URL: <https://earthobservatory.nasa.gov/Features/OrbitsCatalog/page2.php>.
- [112] M Smart. “Scramjets”. In: 3219 (2007).
- [113] Michael Smart. *Scramjet Inlets*. Tech. rep. 9. The University of Queensland, 2010, pp. 1–24. DOI: [10.2514/5.9781600866609.0447.0511](https://doi.org/10.2514/5.9781600866609.0447.0511).
- [114] Michael K. Smart. “How Much Compression Should a Scramjet Inlet Do?” In: *AIAA Journal* 50.3 (2012), pp. 610–619. ISSN: 0001-1452. DOI: [10.2514/1.J051281](https://doi.org/10.2514/1.J051281). URL: <http://arc.aiaa.org/doi/10.2514/1.J051281>.

- [115] Michael K Smart and Edward G Ruf. “Free-jet testing of a {REST} scramjet at off-design conditions”. In: *Collection of Technical Papers - 25th AIAA Aerodynamic Measurement Technology and Ground Testing Conference* AIAA 2006-2955 (2006), pp. 190–201. DOI: [doi: 10.2514/6.2006-2955](https://doi.org/10.2514/6.2006-2955).
- [116] Michael K. Smart and Matthew R. Tetlow. “Orbital Delivery of Small Payloads Using Hypersonic Airbreathing Propulsion”. In: *Journal of Spacecraft and Rockets* 46.1 (2009), pp. 117–125. ISSN: 0022-4650. DOI: [10.2514/1.38784](https://doi.org/10.2514/1.38784).
- [117] Michael K. Smart and Matthew R. Tetlow. “Orbital Delivery of Small Payloads Using Hypersonic Airbreathing Propulsion”. In: *Journal of Spacecraft and Rockets* 46.1 (2009), pp. 117–125. ISSN: 0022-4650. DOI: [10.2514/1.38784](https://doi.org/10.2514/1.38784). URL: <http://arc.aiaa.org/doi/abs/10.2514/1.38784>.
- [118] Thomas J. Sooy and Rebecca Z. Schmidt. “Aerodynamic Predictions, Comparisons, and Validations Using Missile DATCOM (97) and Aeroprediction 98 (AP98)”. In: *Journal of Spacecraft and Rockets* 42.2 (2005), pp. 257–265. ISSN: 0022-4650. DOI: [10.2514/1.7814](https://doi.org/10.2514/1.7814).
- [119] Space Exploration technologies. *Falcon 1 Launch Vehicle Payload Users Guide*. Tech. rep. Hawthorne, CA: Space Exploration Technologies, 2008, p. 65.
- [120] O. Stryk and R. Bulirsch. “Direct and indirect methods for trajectory optimization”. In: *Annals of Operations Research* 37 (1992), pp. 357–373. ISSN: 0254-5330. DOI: [10.1007 / BF02071065](https://doi.org/10.1007/BF02071065).
- [121] M Suraweera and M K Smart. “Shock Tunnel Experiments with a Mach 12 {REST} Scramjet at Off-Design Conditions”. In: *Journal of Propulsion and Power* 25.3 (2009), pp. 555–564. ISSN: 0748-4658. DOI: [10.2514/1.37946](https://doi.org/10.2514/1.37946).
- [122] George Sutton and Oscar Biblarz. *Rocket propulsion Elements*. 8th. John Wiley & Sons, 2010, p. 67. ISBN: 978-0470080245. DOI: [10.1017 / S0001924000034308](https://doi.org/10.1017/S0001924000034308).
- [123] M R Tetlow et al. “Comparison of Glideback and Flyback Boosters”. In: *Journal of Spacecraft and Rockets* 38.5 (1992), pp. 752–758. ISSN: 0022-4650. DOI: [10.2514/2.3742](https://doi.org/10.2514/2.3742). URL: <http://dx.doi.org/10.2514/2.3742>.
- [124] Bailing Tian and Qun Zong. “Optimal guidance for reentry vehicles based on indirect Legendre pseudospectral method”. In: *Acta Astronautica* 68.7-8 (2011), pp. 1176–1184. ISSN: 00945765. DOI: [10.1016 / j.actaastro.2010.10.010](https://doi.org/10.1016/j.actaastro.2010.10.010). URL: <http://linkinghub.elsevier.com/retrieve/pii/S0094576510003899>.
- [125] *To Challenge SpaceX, Rockets Get Wings*. 2016. URL: <http://www.spacesafetymagazine.com/news/to-challenge-spacex-rockets-get-wings/> (visited on 06/21/2018).

- [126] Federico Toso et al. “Optimisation of ascent and descent trajectories for lifting body space access vehicles”. In: *66th International Astronautical Congress*. Jerusalem, 2015.
- [127] Charles Trefny. “An Air-Breathing Concept Launch Vehicle for Single-Stage-to-Orbit”. In: *35th Joint Propulsion Conference and Exhibit*. May. Los Angeles, CA, 1999. DOI: [10.2514/6.1999-2730](https://doi.org/10.2514/6.1999-2730).
- [128] Takeshi Tsuchiya and Takashige Mori. “Optimal Design of Two-Stage-To-Orbit Space Planes with Airbreathing Engines”. In: *Journal of Spacecraft and Rockets* 42.1 (2005), pp. 90–97. ISSN: 0022-4650. DOI: [10.2514/1.8012](https://doi.org/10.2514/1.8012).
- [129] Richard Varvill and Alan Bond. “THE SKYLON SPACEPLANE : PROGRESS TO REALISATION”. In: *Journal of the British Interplanetary Society* 61 (2008), pp. 412–418.
- [130] Vector Space. *Vector Launch Vehicle Family*. 2017. URL: <https://vectorspacesystems.com/technology/> (visited on 12/01/2017).
- [131] VirginOrbit. *LauncherOne*. 2017. URL: <https://virginorbit.com/> (visited on 11/30/2017).
- [132] a Wächter and L T Biegler. *On the Implementation of a Primal-Dual Interior Point Filter Line Search Algorithm for Large-Scale Nonlinear Programming*. Vol. 106. 1. 2006, pp. 25–57. ISBN: 1010700405.
- [133] Mark Wade. *Encyclopedia Astronautica*. 2017. URL: <http://www.astronautix.com/> (visited on 07/24/2018).
- [134] Dennis Wassel et al. “the Esa Nlp-Solver Worhp Recent Developments and Applications”. In: *Modeling and Optimization in Space Engineering* x (2013).
- [135] Alan W. Wilhite et al. “Technology and staging effects on two-stage-to-orbit systems”. In: *Journal of Spacecraft and Rockets* 31.1 (1991), pp. 31–39. ISSN: 0022-4650. DOI: [10.2514/3.26399](https://doi.org/10.2514/3.26399).
- [136] Shengbo Yang et al. “Trajectory optimization for a ramjet-powered vehicle in ascent phase via the Gauss pseudospectral method”. In: *Aerospace Science and Technology* 67 (2017), pp. 88–95. ISSN: 12709638. DOI: [10.1016/j.ast.2017.04.001](https://doi.org/10.1016/j.ast.2017.04.001). URL: <http://dx.doi.org/10.1016/j.ast.2017.04.001>.
- [137] David Young et al. “Lazarus: A SSTO Hypersonic Vehicle Concept Utilizing RBCC and HEDM Propulsion Technologies”. In: *14th AIAA/AHI Space Planes and Hypersonic Systems and Technologies Conference*. 2006, pp. 1–15. ISBN: 978-1-62410-050-5. DOI: [10.2514/6.2006-8099](https://doi.org/10.2514/6.2006-8099). URL: <http://arc.aiaa.org/doi/10.2514/6.2006-8099>.
- [138] Zero2Infinity. *Bloostar*. 2016. URL: <http://www.zero2infinity.space/bloostar/> (visited on 11/30/2017).

- [139] Jiang Zhao and Rui Zhou. “Reentry trajectory optimization for hypersonic vehicle satisfying complex constraints”. In: *Chinese Journal of Aeronautics* 26.6 (2013), pp. 1544–1553. ISSN: 10009361. DOI: [10.1016/j.cja.2013.10.009](https://doi.org/10.1016/j.cja.2013.10.009). URL: <http://dx.doi.org/10.1016/j.cja.2013.10.009>.

APPENDIX A

PROPULSION INTERPOLATION SCHEME

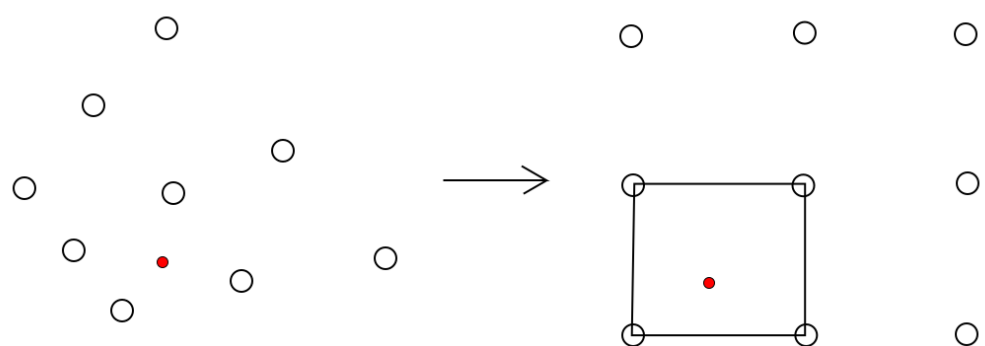


Figure A.1

APPENDIX B

GPOPS-2 EXAMPLE - BRACHISTOCHRONE PROBLEM

This section describes a short example of an optimal control problem solved in GPOPS-II. The purpose of this example is to demonstrate the effectiveness of the pseudospectral method and GPOPS-II, and to provide a simple example case to establish the terminology of an optimal control problem.

The brachistochrone (from the Greek for 'shortest time') problem is a simple optimal control problem, which describes a ball rolling in two dimensions under gravity. The objective is to find the curve of descent which will minimise the time from point a , where the ball is at rest, to point b . It is assumed that gravity is constant and that there is no forces other than gravity acting on the ball. The analytical solution of this problem can be computed using the Euler-Lagrange equation as the equations describing a cycloid:

$$x = A(\theta + \sin \theta),$$

$$y = A(1 - \cos \theta)$$

This problem is included within GPOPS-2 as an example problem, and has been solved to illustrate the GPOPS-2 solution set-up[cite Gpops XX]. Table XX describes the set-up of the optimal control problem in GPOPS-2. The dynamic equations for the Brachistochrone problem are:

$$\dot{x} = v * \cos(u),$$

$$\dot{y} = v * \sin(u),$$

$$\dot{v} = g * \sin(u).$$

These equations are provided to GPOPS-2 as the time-variant system model in this form. The control variable is set to be the descent angle. The initial constraints are defined to initiate the ball at rest at the origin, and the terminal constraints are defined to terminate the problem at coordinates of XX XX. The cost is set to minimum time, so that the solution will be the descent angle which minimises the time to get from the initial position, to the end position.

The GPOPS-2 solution to the Brachistochrone problem is shown in Figure B.1, matching the analytical solution almost exactly. This is expected in this case, as the dynamics of the basic Brachis-

Primal Variables	x Position y Position Velocity
Control Variables	Angle of Descent
Initial Constraints	Velocity x Position y Position
Terminal Constraints	x Position y Position
Path Constraints	None
Target Cost	Minimum Time

tochrone problem are very simple. As the dynamics become more complex, it is no longer possible to obtain an analytical solution. For more complex problems, various methods must be used to verify the optimal solution. These methods are outlined later in this chapter, in Section XX.

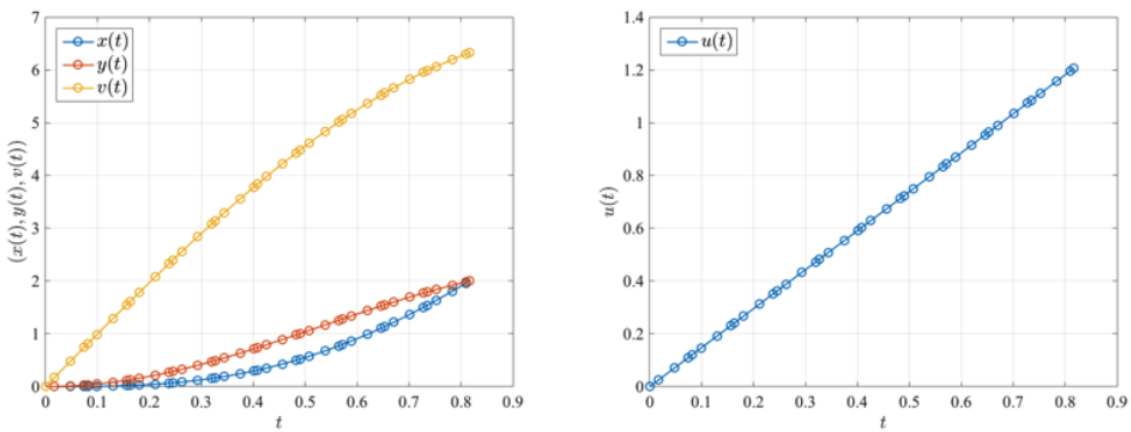


Figure B.1: The solution to the brachistochrone problem, solved in GPOPS-2[CITATIONXX].

APPENDIX C

INITIAL GUESSES

APPENDIX D

TRAJECTORY RESULTS

-engine data with trajectory paths

-mesh histories

APPENDIX E

CART3D RESULTS

E.1 Engine-On Plume Check

-simulate engine-on conditions to check that the plumes do not adversely affect the tail of the vehicle
(justify that I can just remove engines/boattail)

-Mach 5,7,9 at 50kPa

E.2 CART3D Results

-include mesh here

E.3 verification

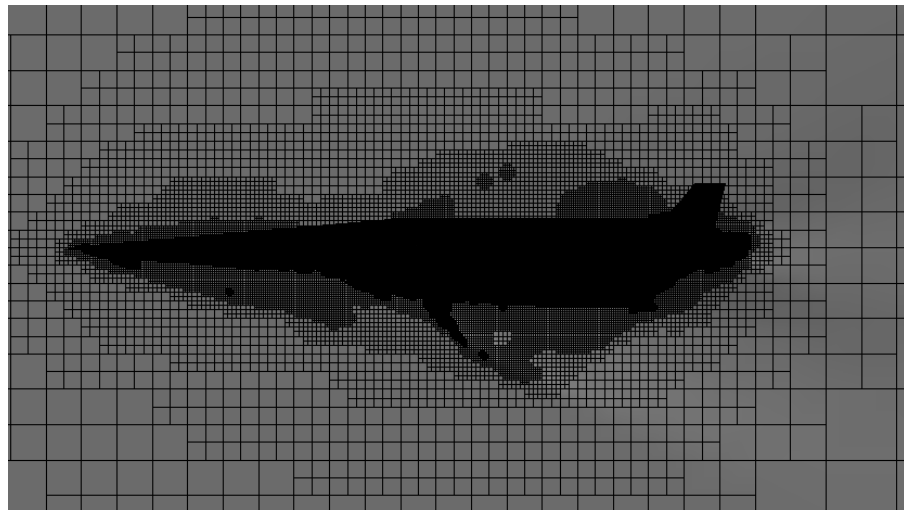


Figure E.1

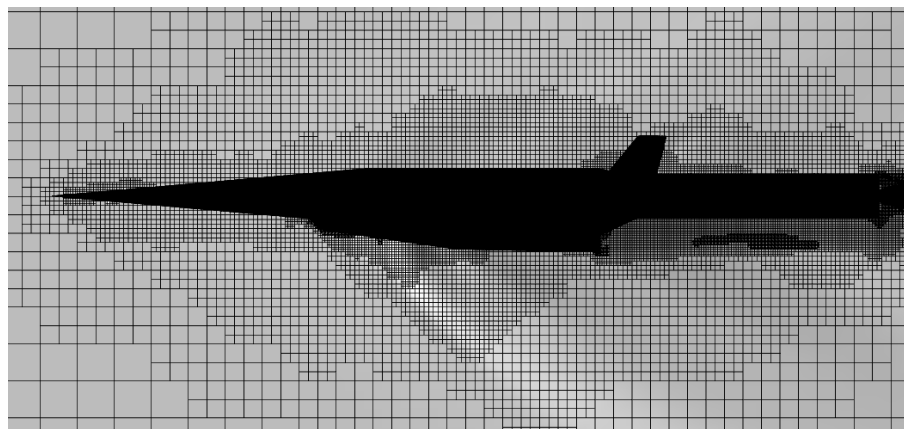


Figure E.2: Mesh generated by CART3D around the SPARTAN and first stage vehicles.

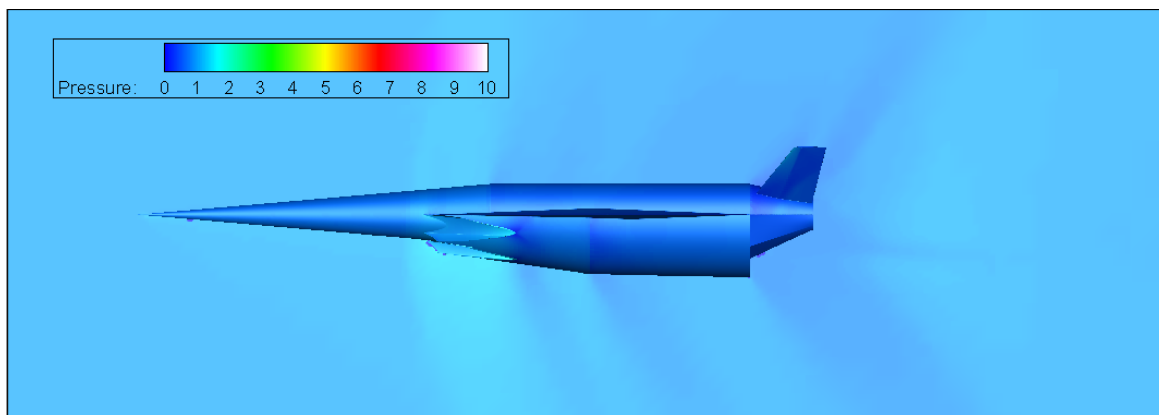


Figure E.3: CART3D flow result for the SPARTAN, at Mach 1.1, 6° angle of attack.

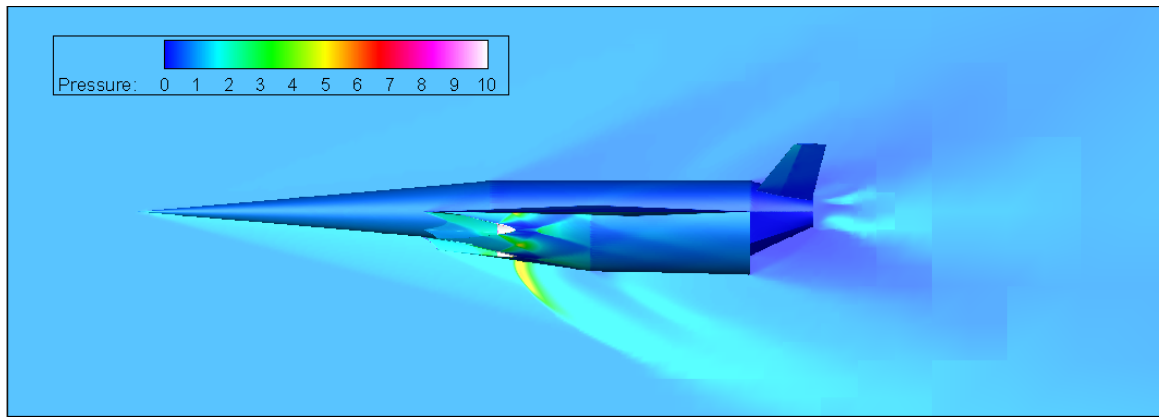


Figure E.4: CART3D flow result for the SPARTAN, at Mach 3, 6° angle of attack.

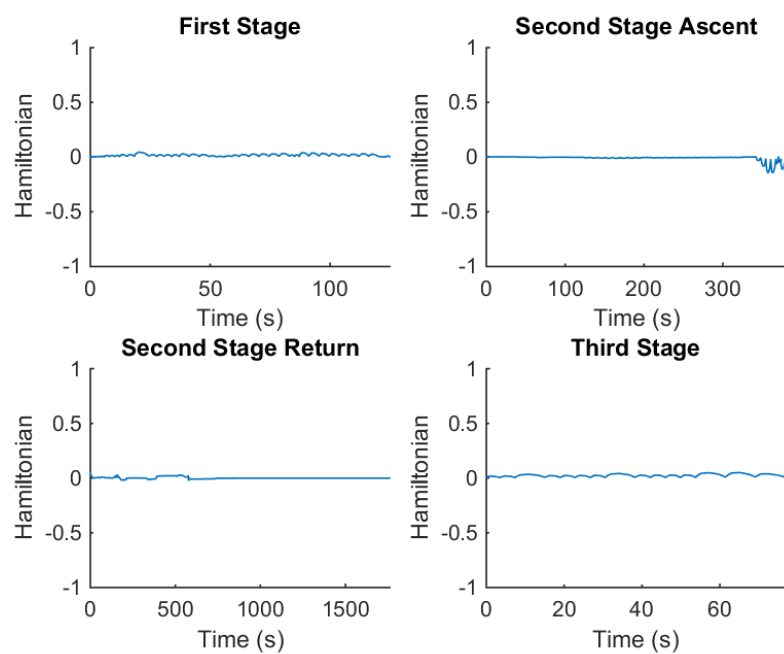


Figure E.5

APPENDIX E. CART3D RESULTS

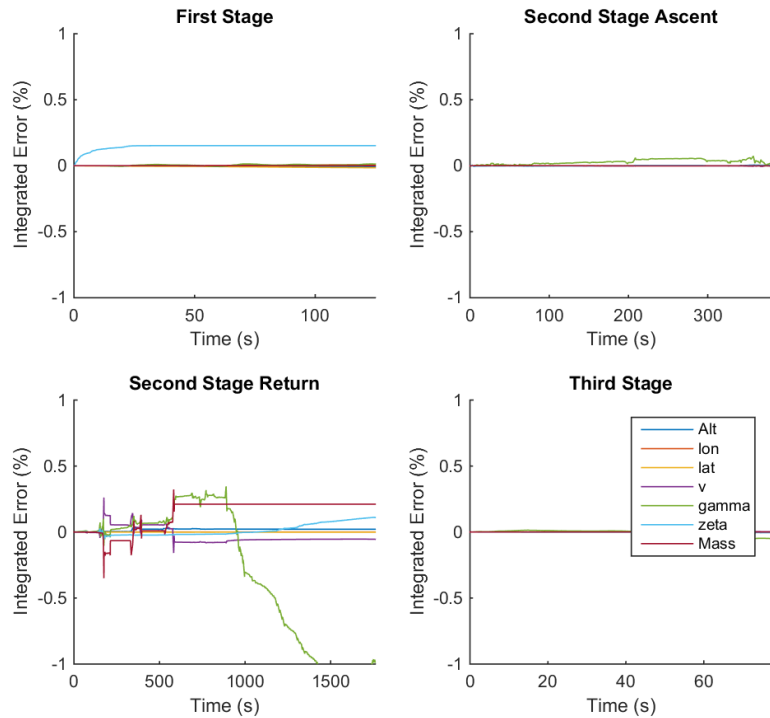


Figure E.6

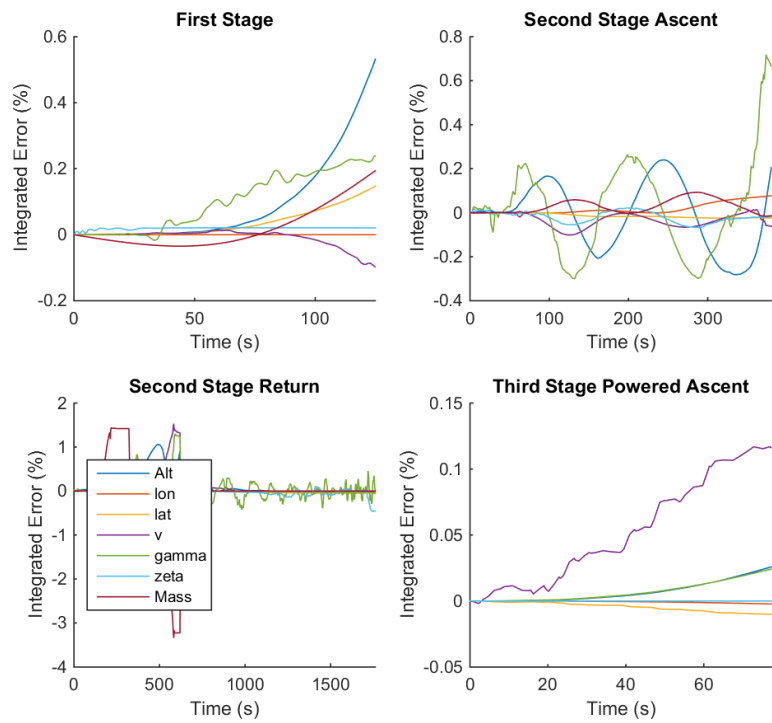


Figure E.7

APPENDIX F

TITLE

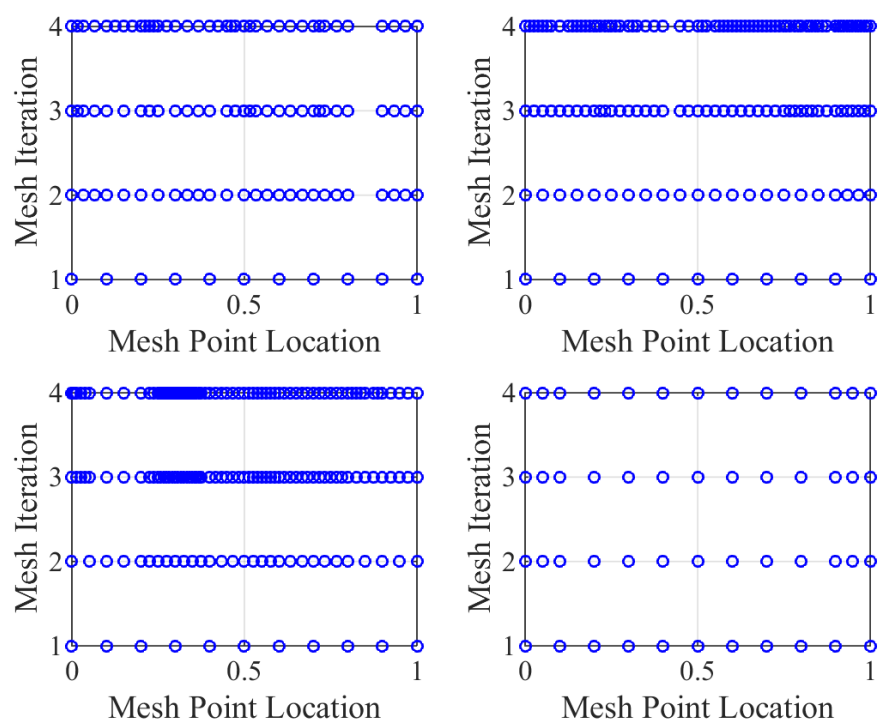


Figure F.1

APPENDIX G

TRAJECTORY PLOT COMPARISONS

G.1 Cases With No Fly-Back

G.1.1 Dynamic Pressure Variation

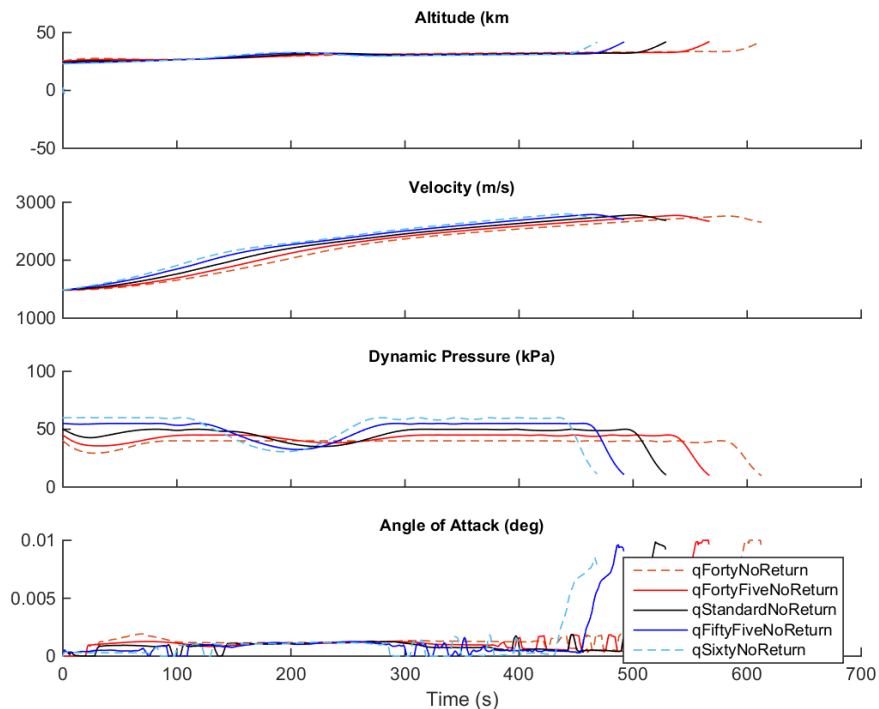


Figure G.1

APPENDIX G. TRAJECTORY PLOT COMPARISONS

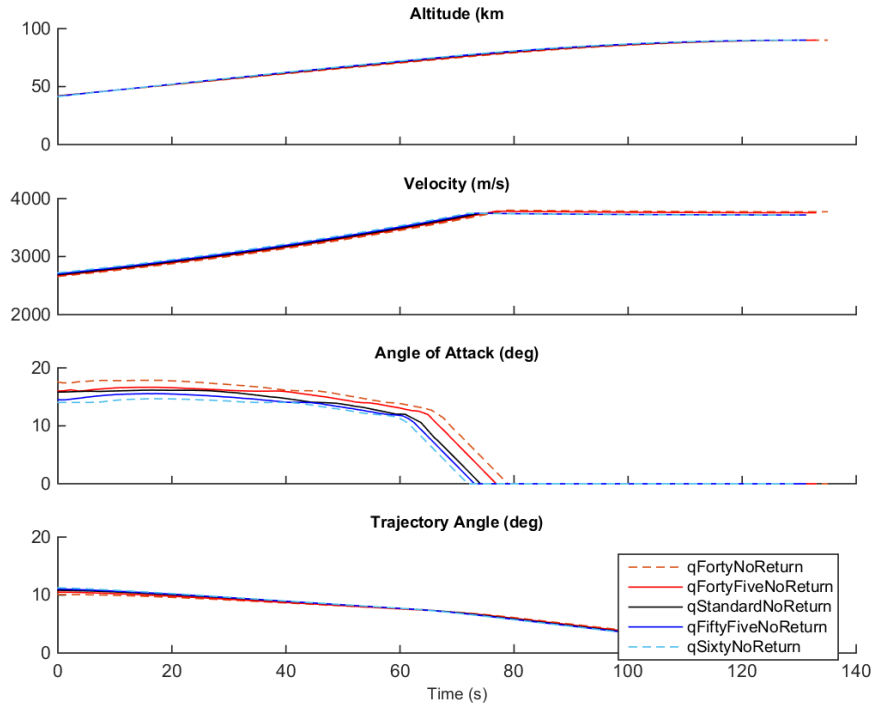


Figure G.2

G.1.2 Specific Impulse

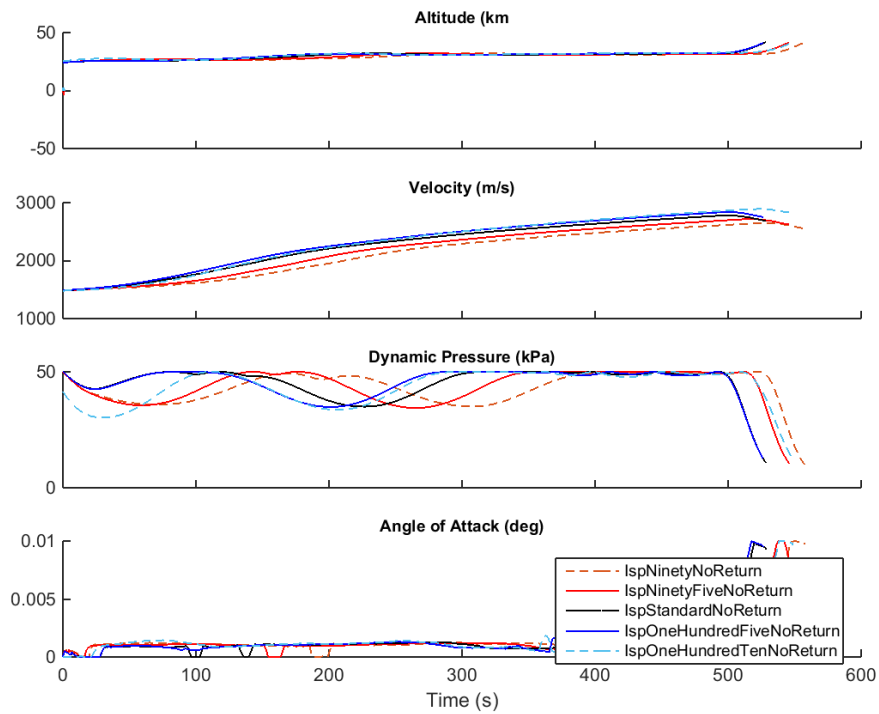


Figure G.3

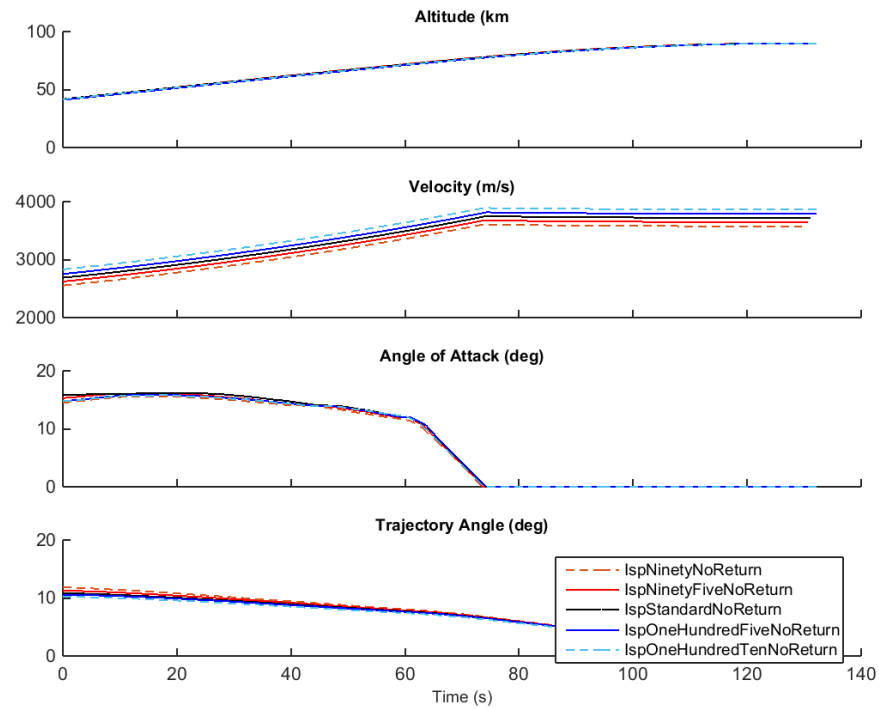


Figure G.4

G.1.3 Drag

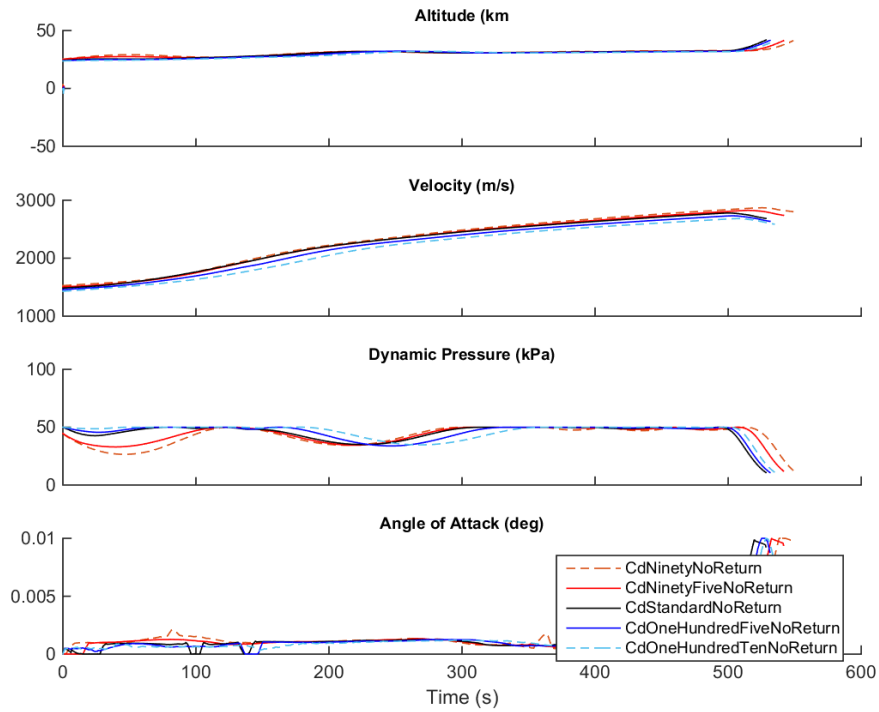


Figure G.5

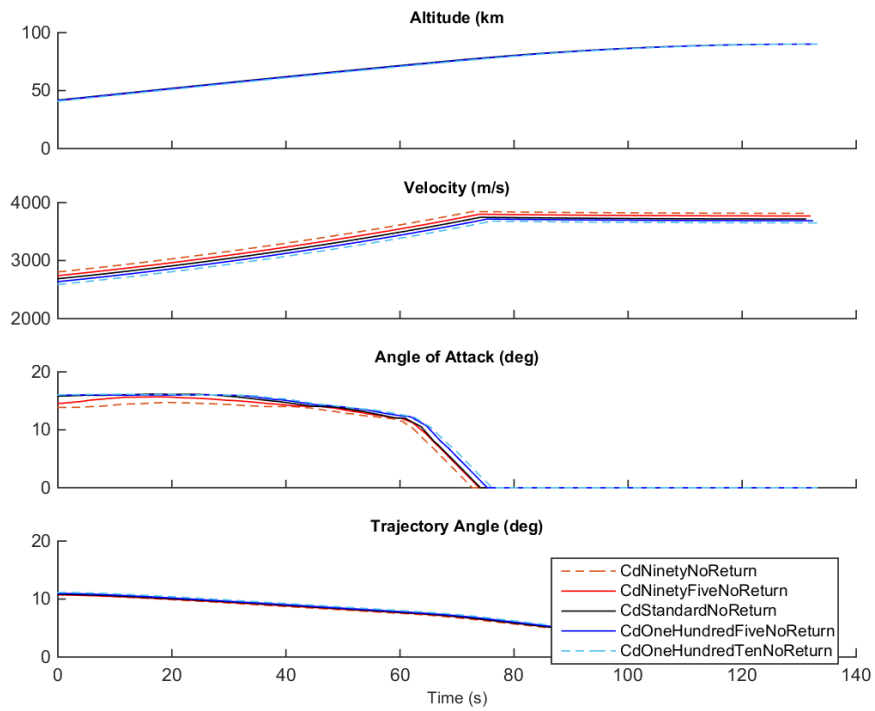


Figure G.6

G.1.4 SPARTAN Mass

APPENDIX G. TRAJECTORY PLOT COMPARISONS

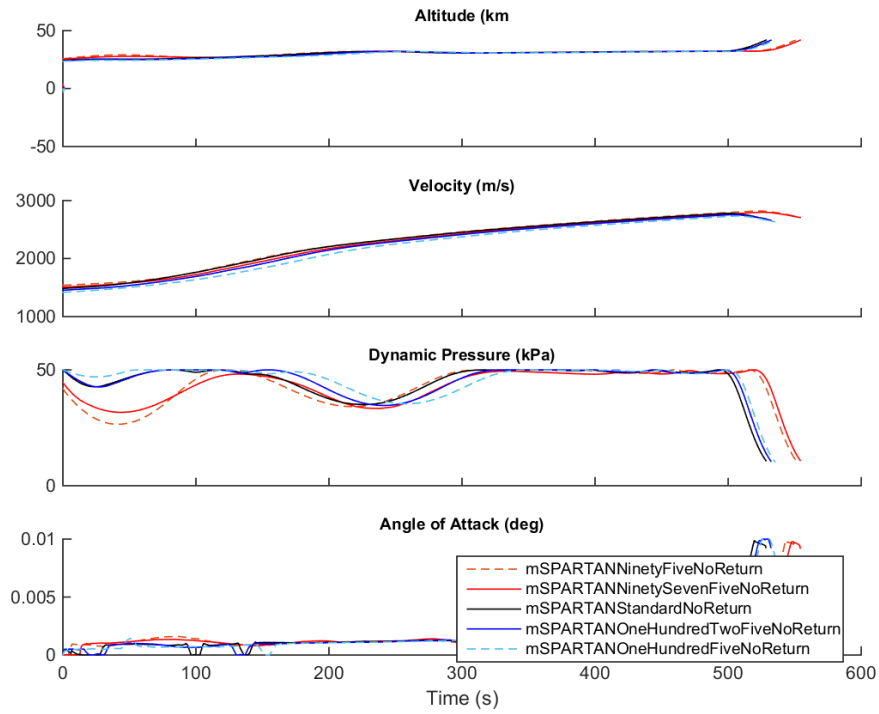


Figure G.7

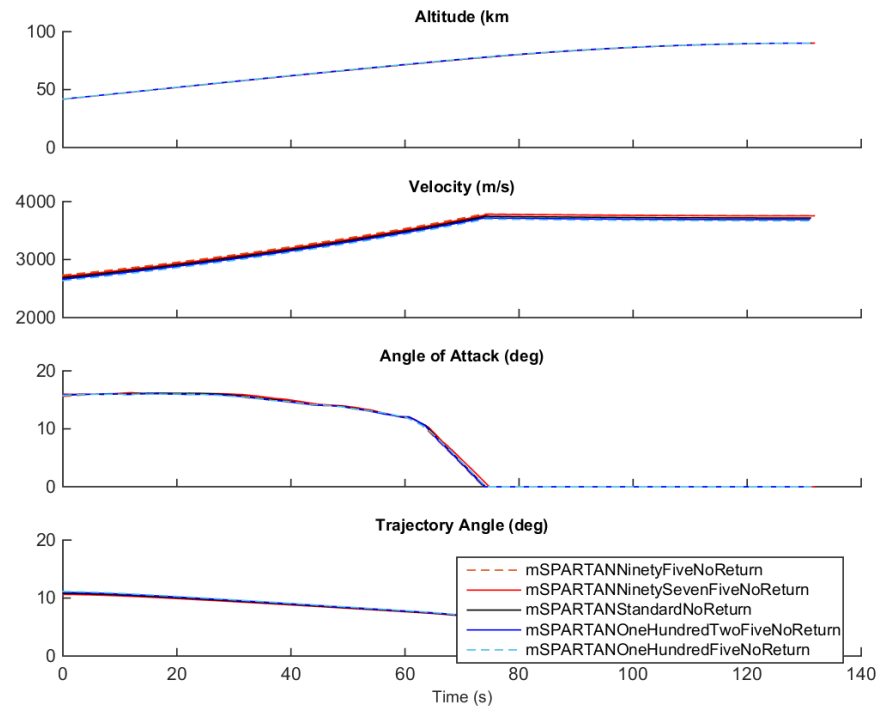


Figure G.8

G.1.5 Fuel Mass

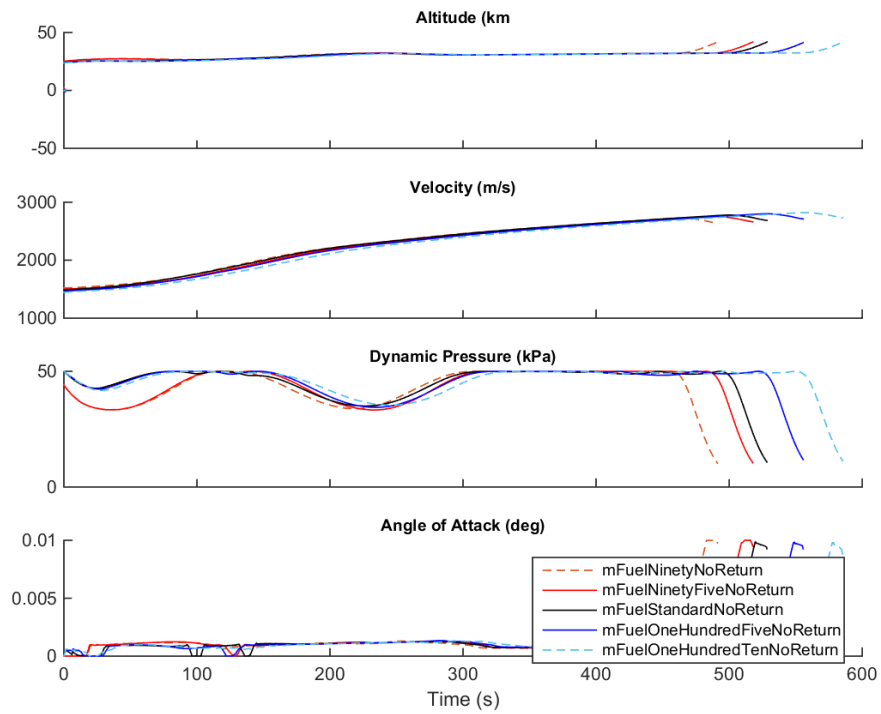


Figure G.9

APPENDIX G. TRAJECTORY PLOT COMPARISONS

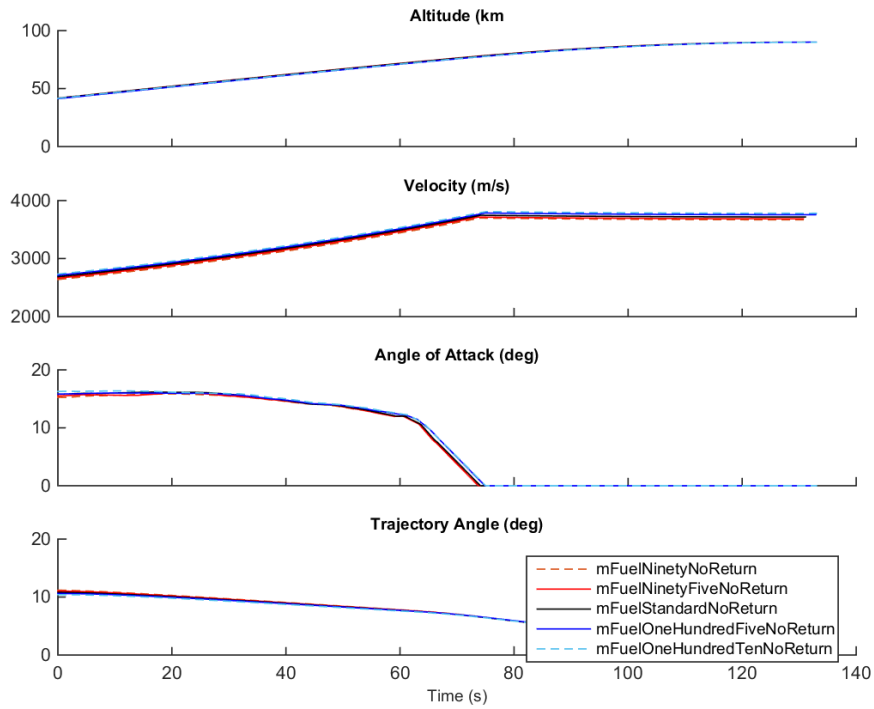


Figure G.10

G.1.6 Third Stage Mass

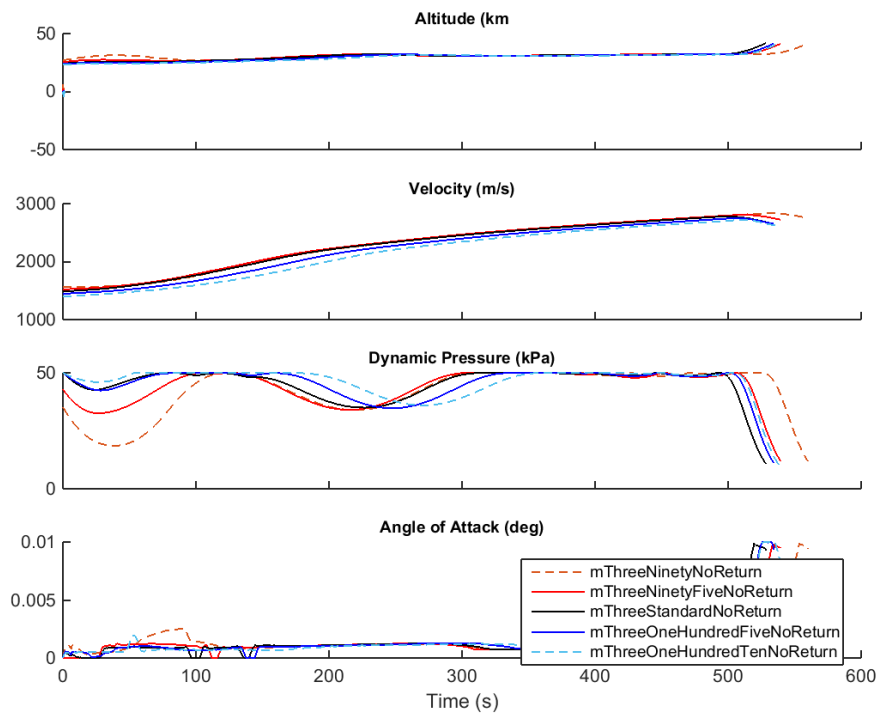


Figure G.11

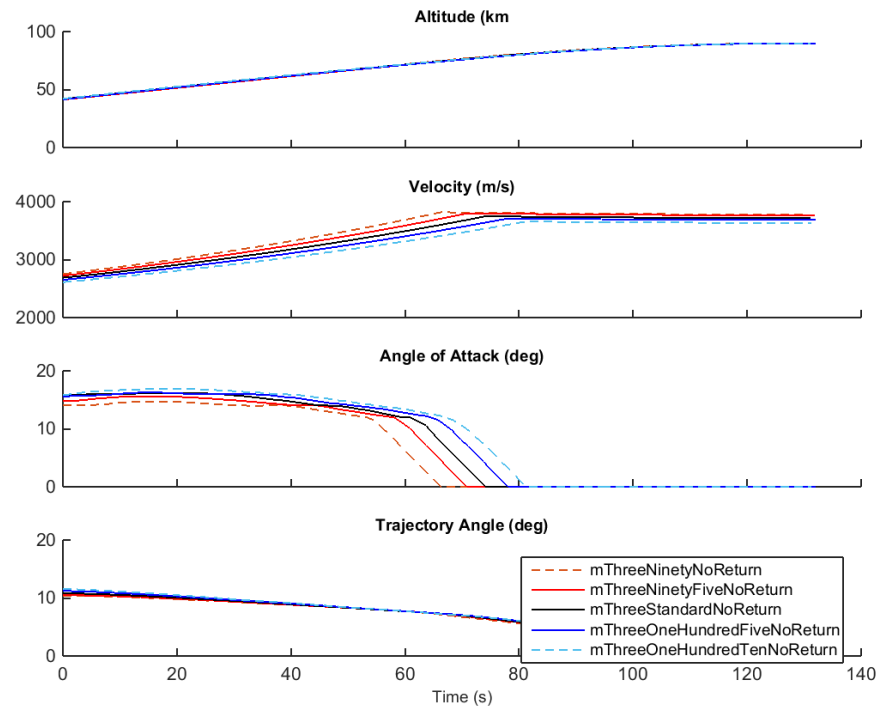


Figure G.12

G.1.7 Third Stage Thrust

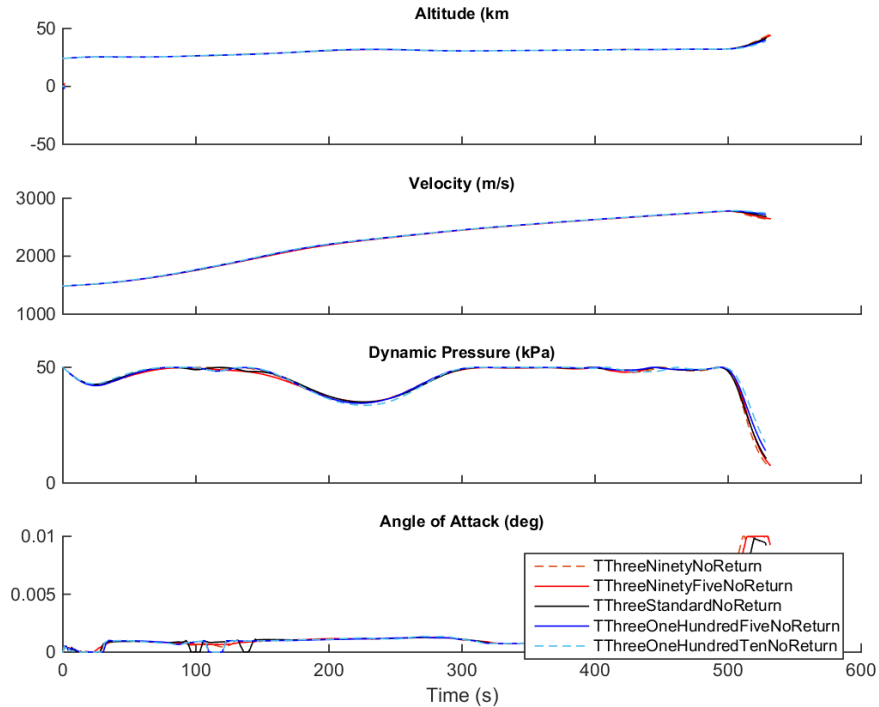


Figure G.13

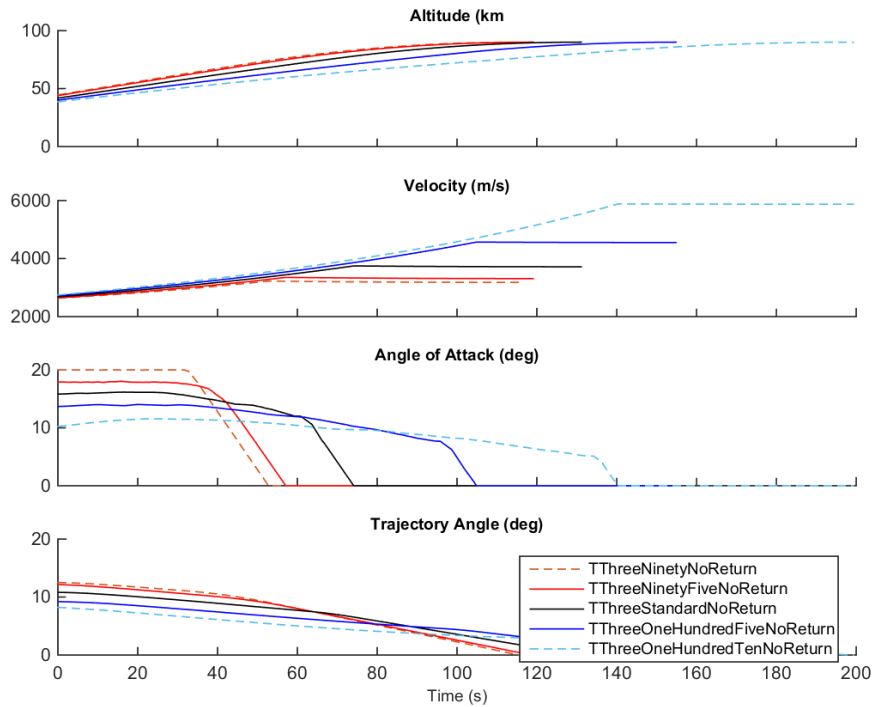


Figure G.14

G.1.8 Third Stage Drag

G.2 Cases With Fly-Back

G.2.1 Dynamic Pressure Variation

G.2.2 Specific Impulse

G.2.3 Drag

G.2.4 SPARTAN Mass

G.2.5 Fuel Mass

G.2.6 SPARTAN Viscous Drag

G.2.7 Third Stage Mass

G.2.8 Third Stage Thrust

APPENDIX G. TRAJECTORY PLOT COMPARISONS

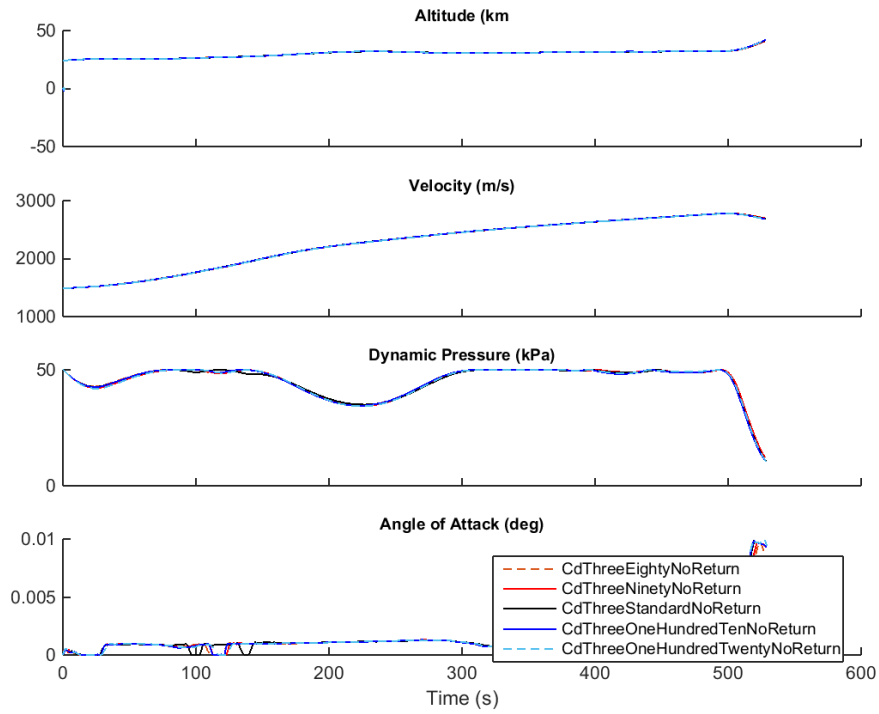


Figure G.15

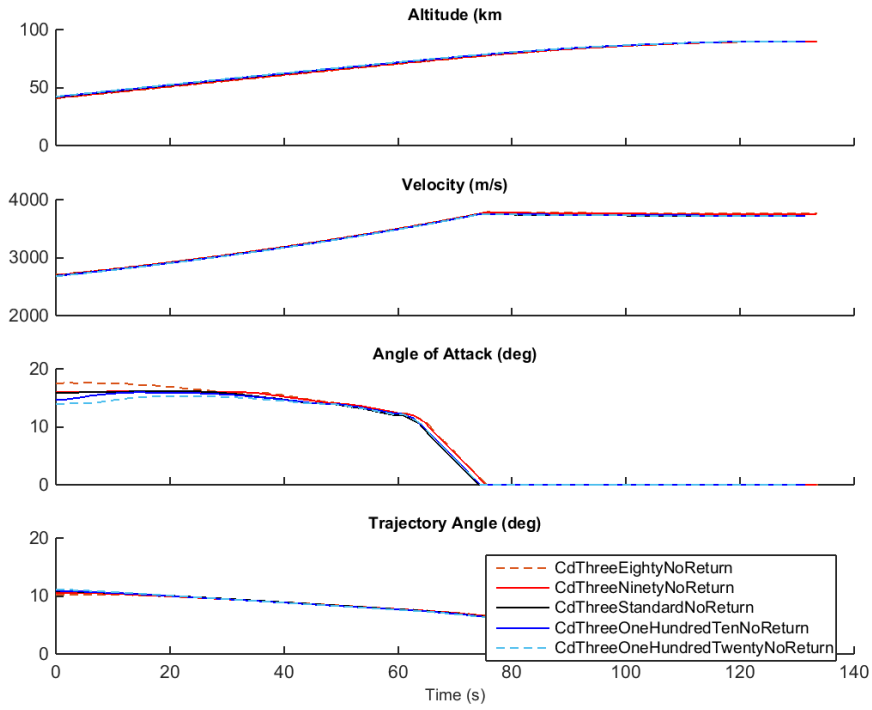


Figure G.16

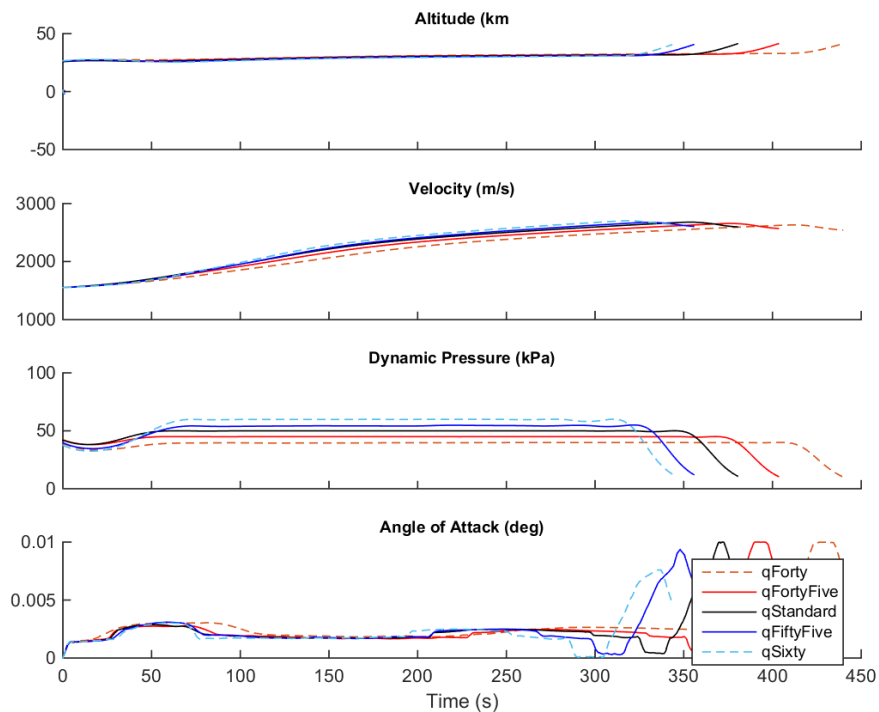


Figure G.17

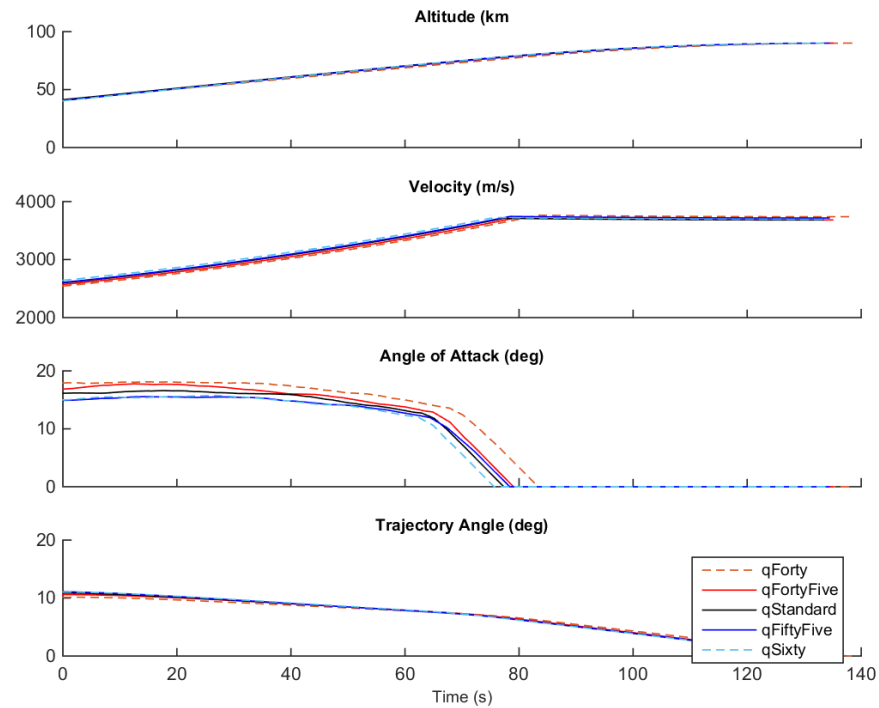


Figure G.18

APPENDIX G. TRAJECTORY PLOT COMPARISONS

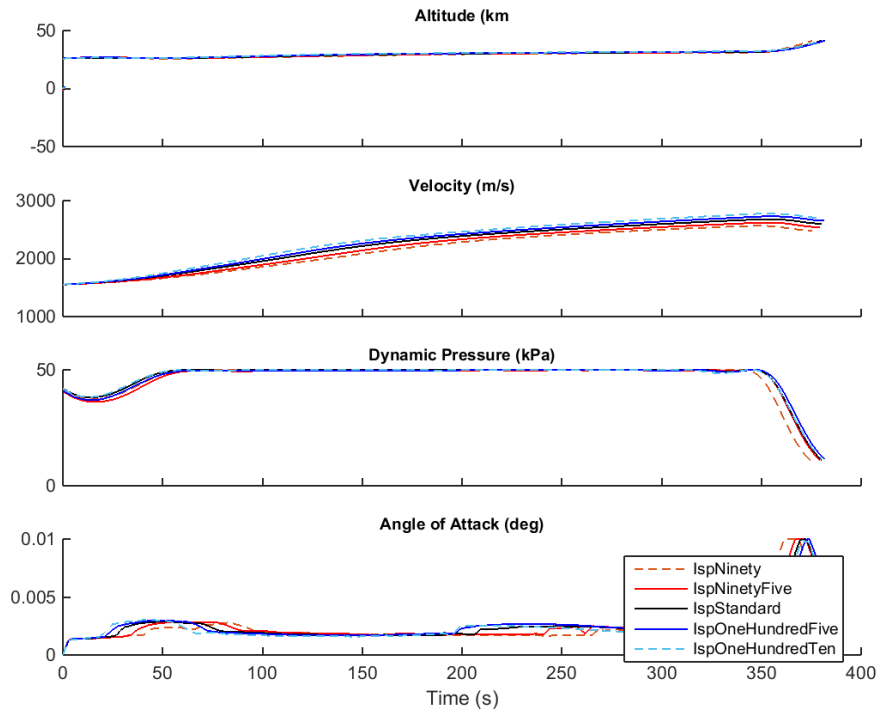


Figure G.19

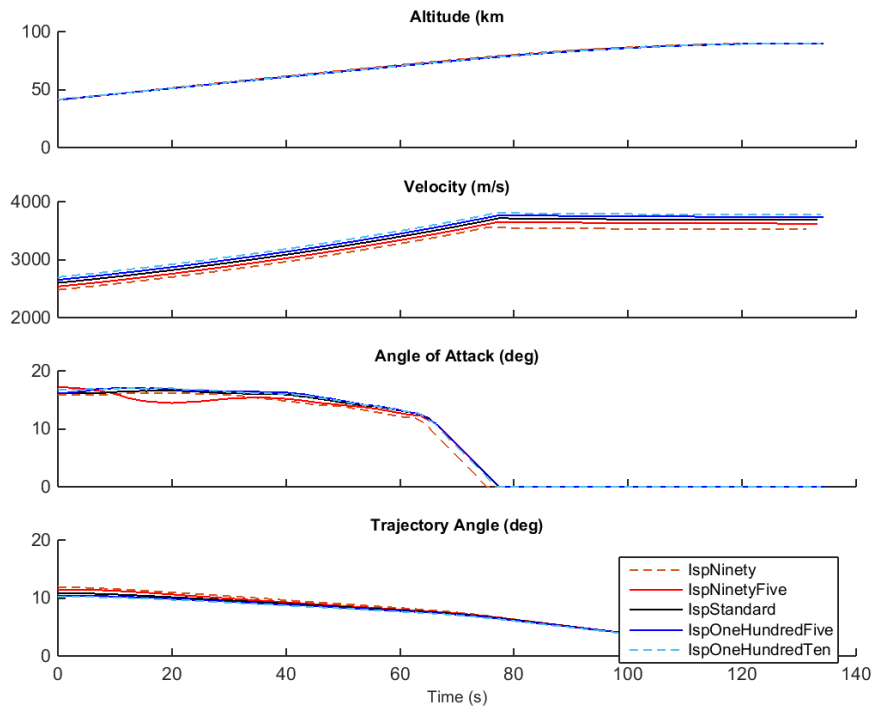


Figure G.20

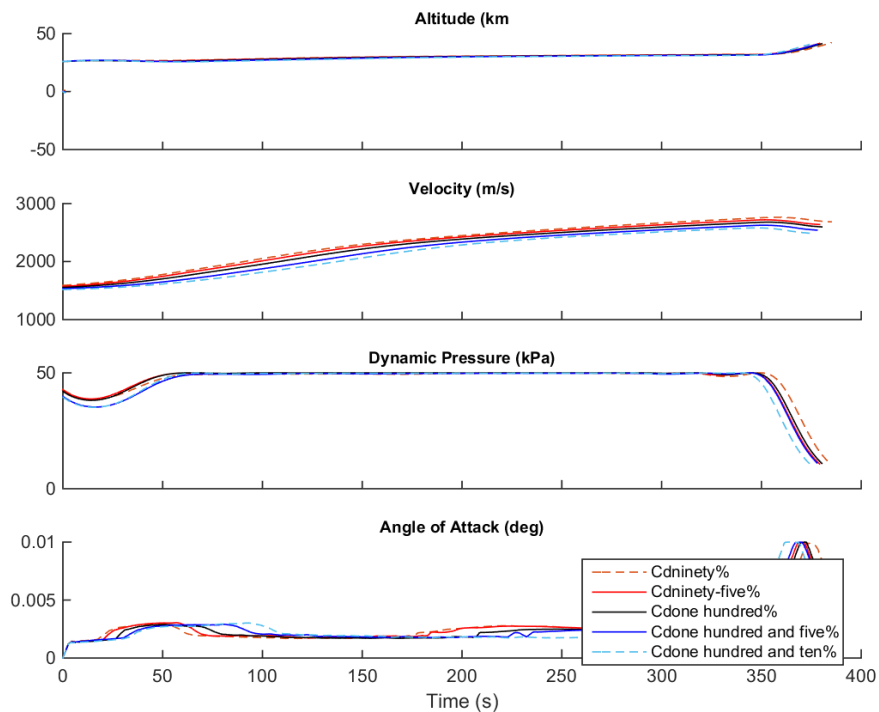


Figure G.21

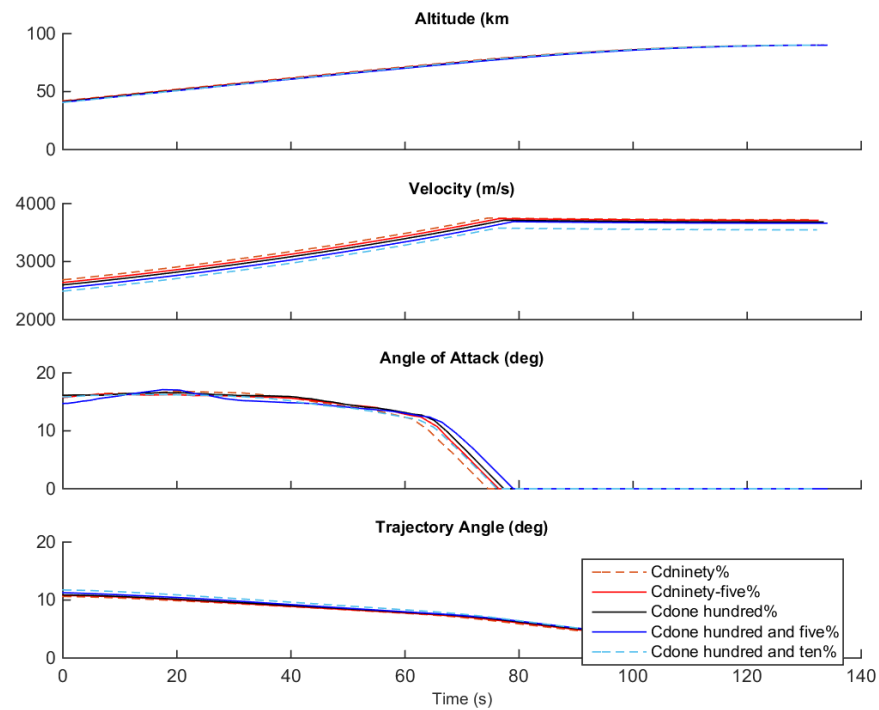


Figure G.22

APPENDIX G. TRAJECTORY PLOT COMPARISONS

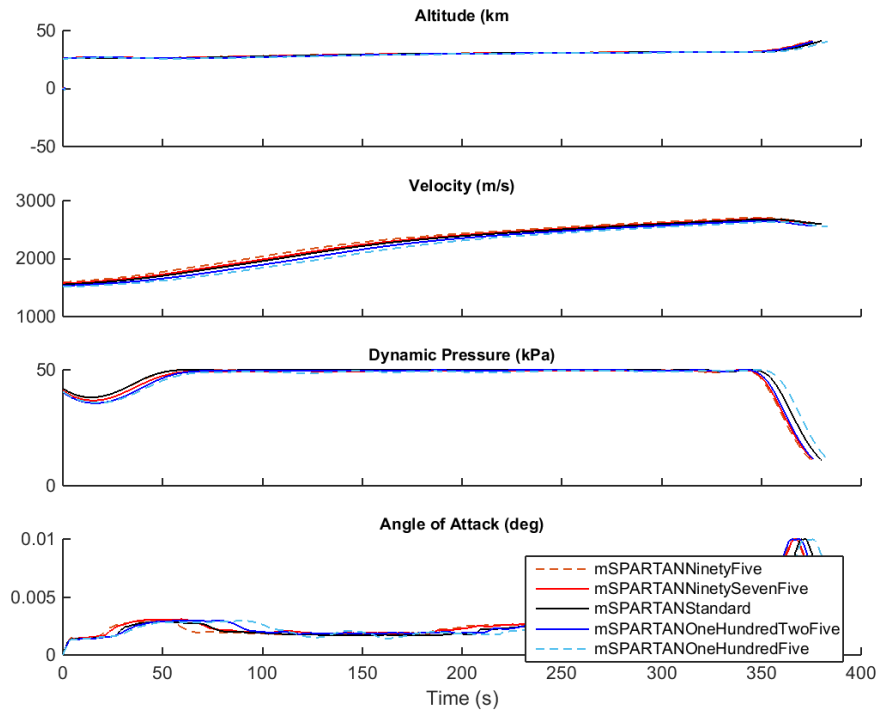


Figure G.23

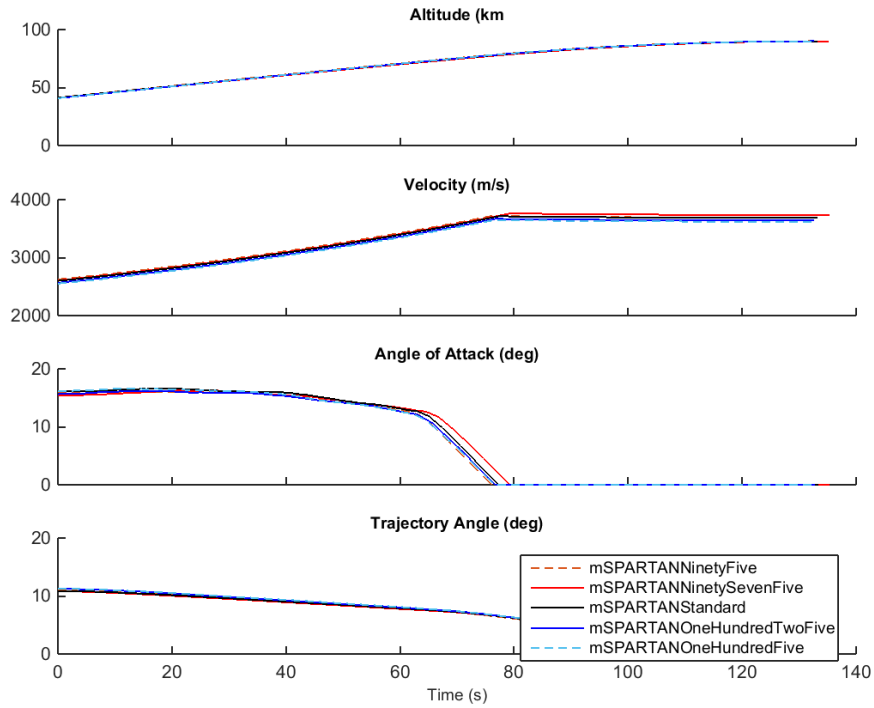


Figure G.24

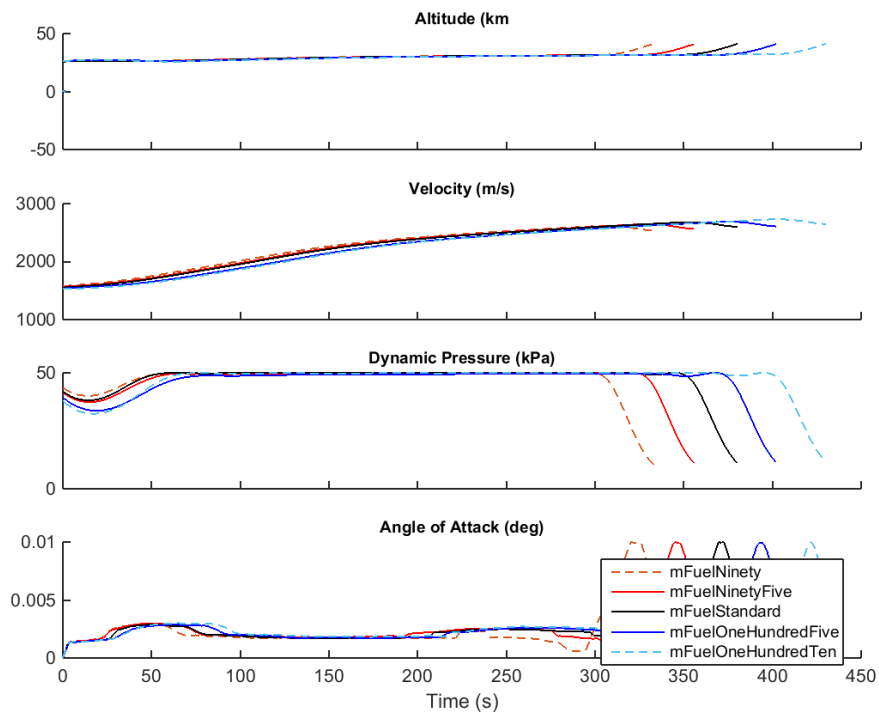


Figure G.25

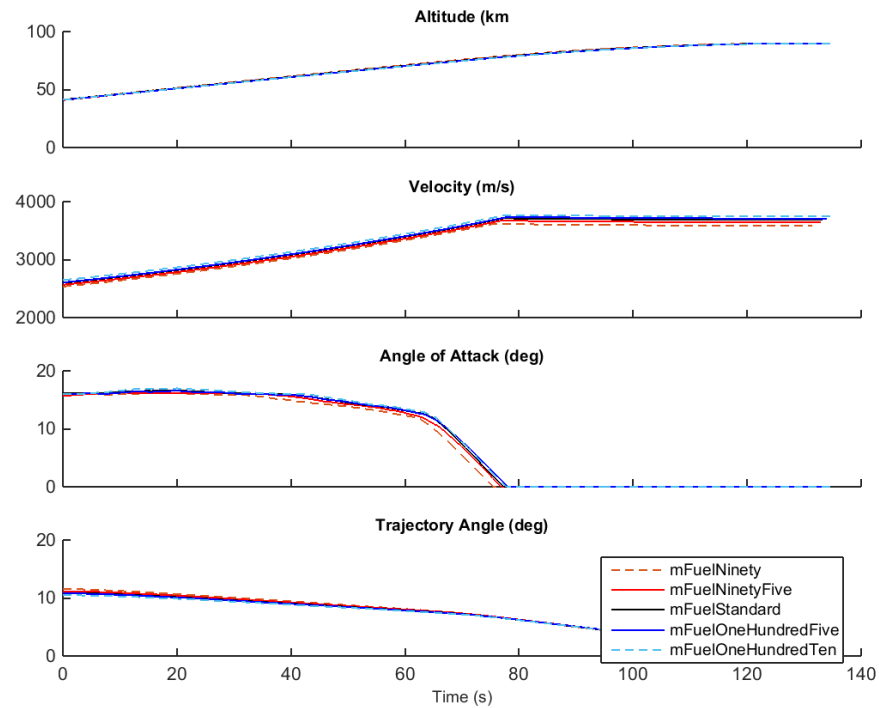


Figure G.26

APPENDIX G. TRAJECTORY PLOT COMPARISONS

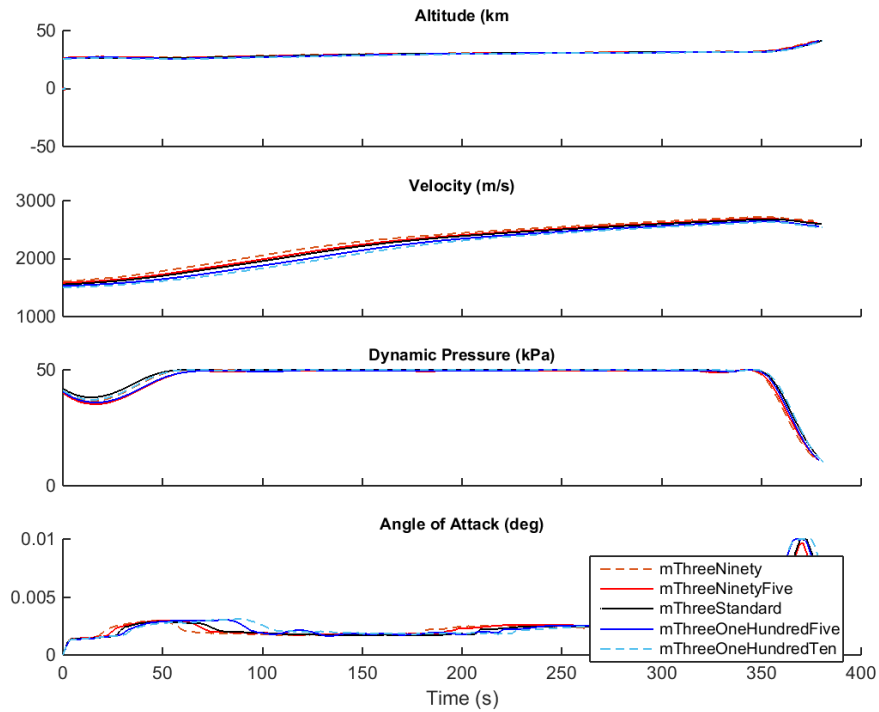


Figure G.27

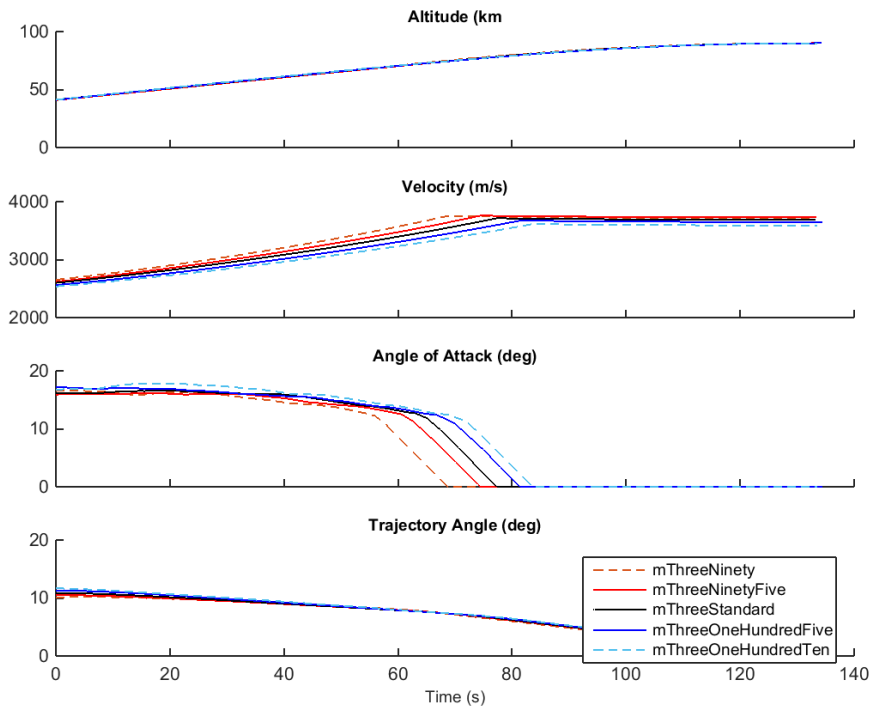


Figure G.28

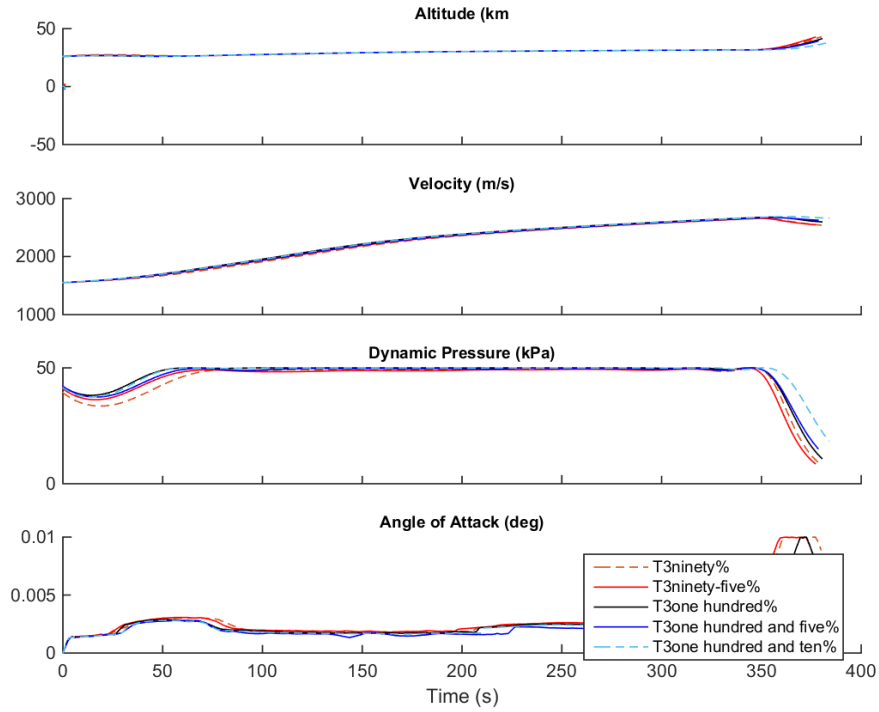


Figure G.29

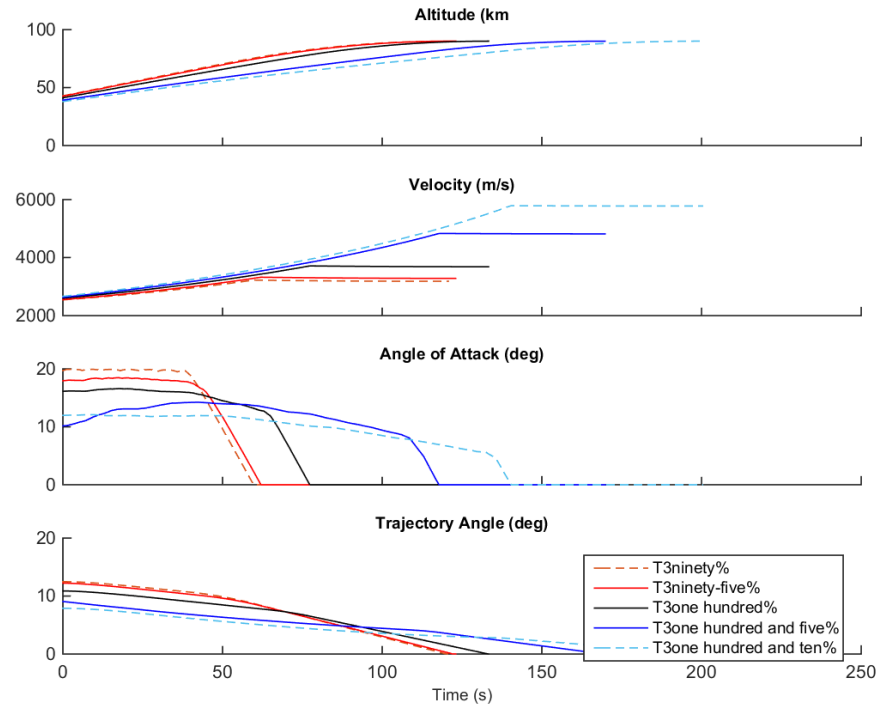


Figure G.30